


# Knowledge-Guided Microwave Diplexers and Multiplexers Design based on Computational Intelligent Techniques

By

Yang Yu

A thesis submitted to the University of Birmingham for the degree of
DOCTOR OF PHILOSOPHY

Emerging Device Technology Group
College of Engineering and Physical Sciences
University of Birmingham
September 2021

UNIVERSITY OF
BIRMINGHAM

## University of Birmingham Research Archive

### e-theses repository

This unpublished thesis/dissertation is copyright of the author and/or third parties. The intellectual property rights of the author or third parties in respect of this work are as defined by The Copyright Designs and Patents Act 1988 or as modified by any successor legislation.

Any use made of information contained in this thesis/dissertation must be in accordance with that legislation and must be properly acknowledged. Further distribution or reproduction in any format is prohibited without the permission of the copyright holder.

# Abstract

This thesis focuses on new techniques in synthesis, design, and fabrication for microwave diplexers and multiplexers. Coupling matrix theories are employed with design knowledge to guide computational intelligent techniques to realize complex microwave multiplexers. To achieve compact size and lightweight multiplexers, novel design concepts and emerging fabrication technologies are proposed and implemented. The main contributions of the thesis are:

1) A general all-resonator diplexer/multiplexer coupling matrix synthesis method (GACMS) is presented. Classic filter design knowledge and advanced optimisation techniques are combined to generate high-quality coupling matrices for diplexers/multiplexers with complex topologies.
2) A novel electromagnetic (EM) optimisation method is presented for diplexers. A systematic physical dimensioning method is proposed for a high-quality initial design. A key performance-based objective function is proposed. Together with a powerful optimizer, the diplexer optimisation can achieve a high success rate in a fully automatic process.
3) A resonant manifold multiplexer is proposed based on an all-resonator structure. Different from the traditional transmission line-based manifold-junction, coupled-resonators constitute the manifold-junction. Tailored methods are proposed to synthesis and optimize the multiplexers. The new multiplexer structure offers a more compact footprint.
4) A D-band diplexer is designed based on all-resonator structure. Two commercial fabrication techniques, high-resolution micro laser sintering 3D printing and high precision CNC milling, are employed to the same diplexer design, respectively. Comprehensive measurements and comparisons are conducted for the fabricated diplexers.

# Acknowledgment

Throughout my Ph.D. study period, I have received much support and assistance. First and foremost, I would like to express my deepest appreciation to my academic supervisors. I would like to thank Prof. Michael Lancaster who introduces me to the area of microwave filters. His expert guidance, encouragement, and supervision motivate me to work on the research projects in this thesis. By the way, I wish him a happy retirement life. I would like to thank Prof. Yi Wang for his broad knowledge and patience guidance, and inspiration. Without frequent and valuable discussions with him, the research works in this thesis cannot go smoothly. I would like to thank Prof. Qingsha S. Cheng for his encouragement and high-quality suggestions on my research work. His positive attitude and careful inspection play important roles in this thesis. I am also grateful to Prof. Bo Liu, University of Glasgow, for his instructions and many constructive discussions on intelligent algorithms in this thesis.

I would like to express my sincerest thanks to my colleagues at the University of Birmingham, Dr. Cheng Guo, Dr. Milan Salek, Dr. Talal Skaik, Dr. Fan Zhang, and Xun Chen for their academic assistance. I would also like to thank the colleagues at Southern University of Science and Technology, Dr. Zhen Zhang, and Dr. Fan Zhang for their encouragement and assistance. Thanks to Mr. Xiaoxiang Hou for his support in measurements.

Finally, I would like to thank my family and all my friends for their support and encouragement.

# Publications

## Journal Papers

1. **Y. Yu**, Yi Wang, T. Skaik, T. Starke, X. Shang, M. J. Lancaster, P. Hunyor, P. Huggard, H. Wang, Q. S. Cheng, "D-band Waveguide Diplexer Fabricated Using Micro Laser Sintering," IEEE Transactions on Microwave Theory and Techniques, Major revision
2. **Y. Yu**, B. Liu, Y. Wang, and Q. S. Cheng, "Automated Diplexer Design with Key Performance Indicator-Based Objectives," IEEE Microwave and Wireless Components Letters, accepted for publication.
3. **Y. Yu**, Y. Wang, C. Guo, Q. S. Cheng and M. Yu, "Resonant Manifold Multiplexer," IEEE Transactions on Microwave Theory and Techniques, vol. 70, no. 2, pp. 1059-1071, Feb. 2022.
4. **Y. Yu**, B. Liu, Y. Wang, M. J. Lancaster and Q. S. Cheng, "A General Coupling Matrix Synthesis Method for All-Resonator Diplexers and Multiplexers," IEEE Transactions on Microwave Theory and Techniques, vol. 68, no. 3, pp. 987-999, Mar. 2020.

## Conference Papers

1. **Y. Yu**, Z. Zhang, Q. S. Cheng, B. Liu, and Y. Wang, "Surrogate-based Design and Tuning Methods for RF/Microwave Devices," 2022 IEEE MTT-S International Microwave Symposium (IMS), Denver, Colorado, USA, 2022, accepted.
2. **Y. Yu**, J. Li, C. Guo, G. Huang, Q. S. Cheng, and A. Zhang, "A Connectorised X-Band

3-D Printed Air-Filled Self-Suspended Rectangular Coaxial Transmission Line," 2019 49th European Microwave Conference (EuMC), Paris, France, 2019, pp. 690-693.

# Table of Contents

**Abstract** ..... **iii**

**Acknowledgment** ..... **v**

**Publications** ..... **vii**

Journal Papers ..... vii

Conference Papers ..... vii

**Lists of Acronyms** ..... **xv**

**Chapter 1 Introduction** ..... **1**

1.1 Overview of Microwave Diplexers and Multiplexers ..... 1

1.2 Thesis Motivations ..... 5

1.3 Novelty and Contributions of the Thesis ..... 8

1.4 Thesis Overview ..... 8

Reference ..... 10

**Chapter 2 Literature Review** ..... **15**

2.1 Configurations of Diplexers and Multiplexers ..... 15

2.2 Synthesis Methods for Diplexers and Multiplexers ..... 19

2.3 Physical Dimensioning Methods ..... 22

2.3.1 Design Curve Method ..... 22

2.3.2 Metamodeling Method ..... 23

2.3.3 Inverse Modelling Method ..... 24

2.4 Optimisation Methods for Diplexers and Multiplexers ..... 24

2.4.1 Computer-aided Design Methods for Multiplexers ..... 24

2.4.2 Direct Optimisation and Surrogate-assisted Optimisation ..... 27

2.4.3 Optimisation Algorithms in SAO ..... 30

2.4.4 Objective Functions ..... 36

2.5 Fabrication Technologies for Waveguide Components ..... 38

2.5.1 Computerised Numerically Controlled (CNC) Milling Technology ..... 39

2.5.2 Micro-fabrication Technologies ..... 39

2.5.3 3D Printing Technologies ..... 40

2.6 Summary of this Chapter ..... 43

Reference ..... 44

**Chapter 3 Theoretical Background ..... 51**

3.1 Filter Network and Polynomials ..... 51

3.1.1 General Characteristics for Filter Network ..... 51

3.1.2 Filter Polynomial Synthesis ..... 54

3.2 Circuit Representation of Resonator-coupled Filter ..... 57

3.2.1 Lowpass Prototype Lumped Circuits ..... 57

3.2.2 Immittance Inverters ..... 59

3.2.3 Frequency Transformation ..... 61

3.3 Coupling Matrix Theory ..... 63

3.3.1 *N*×*N* Coupling Matrix ..... 63

3.3.2 Synthesis of a Bandpass Filter with a Chebyshev Response ..... 66

3.3.3 *N*+*X* Coupling Matrix ..... 67

3.4 Microwave Filter Design ..... 70

3.4.1 Rectangular Waveguide ..... 70

3.4.2 Rectangular Cavity Resonator ..... 72

3.4.3 Discontinuity between Rectangular Resonators ..... 73

3.4.4 External Quality Factor Extraction in Rectangular Waveguide ..... 74

3.4.5 Mutual Coupling Extraction between Rectangular Resonators ..... 76

3.4.6 Example of a 3rd order Filter Design ..... 78

3.5 Summary of this Chapter ..... 80

Reference ..... 80

**Chapter 4 Coupling Matrix Optimisation Method for All-resonator Multiplexers ..... 81**

4.1 Challenges in Optimisation ..... 81

4.2 The Proposed GACMS Optimisation Workflow ..... 83

4.3 Optimisation Techniques ..... 87

4.3.1 Objective Function ..... 87

4.3.2 Optimisation Methods ..... 87

4.4 Multiplexer Examples ..... 90

4.5 Numerical Results and Comparison ..... 94

4.5.1 Performance of the CM Optimisation Framework ..... 94

4.5.2 Comparisons with State-of-the-art Methods ..... 96

4.5.3 Advantages of Memetic Optimizer ..... 98

4.6 Summary of this Chapter ..... 98

Reference ..... 99

**Chapter 5 Global Optimisation of Microwave Diplexers Based on a Design Knowledge-Guided Approach ..... 101**

5.1 Challenges and Motivations ..... 101

5.2 The GDODK Method ..... 106

5.3 Numerical Results and Comparisons ..... 119

5.3.1 Example 1 ..... 120

5.3.2 Example 2 ..... 126

5.3.3 Example 3 ..... 130

5.3.4 Discussion ..... 135

5.4 Summary of this Chapter ..... 136

References ..... 136

**Chapter 6 Resonant Manifold Multiplexers ..... 139**

6.1 Introduction ..... 139

6.2 Resonant Manifold Triplexer ..... 141

6.2.1 Coupling Matrix Synthesis ..... 142

6.2.2 Physical Realization of the 9th-order Triplexer ..... 148

6.3 Resonant Manifold Pentaplexer ..... 154

6.3.1 Coupling Matrix Synthesis ..... 154

6.3.2 Physical Realization for 20th-order Multiplexer ..... 158

6.4 Fabrication and Measurements ..... 160

6.4.1 Triplexer ..... 160

6.4.2 Five-channel Multiplexer ..... 161

6.4.3 Discussion ..... 164

6.5 Summary of this Chapter ..... 165

References ..... 166

**Chapter 7 D-band Waveguide Diplexers Fabricated Using Micro Laser Sintering and CNC Machining ..... 169**

7.1 Introduction ..... 169

7.2 Diplexer Design ..... 170

7.2.1 Filtering Topology and Synthesis ..... 170

7.2.2 Structural Design and Simulation ..... 172

7.3 Fabrication and Surface Treatment ..... 176

7.3.1 Diplexer Fabricated by MLS and CNC ..... 176

7.3.2 Surface Treatment ..... 178

7.4 Measurement and Discussion ..... 181

7.4.1 Electrical Performance ..... 181

7.4.2 Surface Characterisation and Dimensional Measurement ..... 182

7.4.3 Fabrication Tolerance Analysis ..... 186

7.4.4 Measurement After Gold Plating ..... 188

7.4.5 Measurement of CNC Milled Diplexer ..... 190

7.5 Summary of this Chapter ..... 192

References ..... 193

**Chapter 8 Conclusions and Future Work ..... 195**

8.1 Conclusions ..... 195

8.2 Future Work ..... 198

**Appendix ..... 201**

A. Recursive Techniques ..... 201

B. Resonant Frequencies of Denormalized Resonators ..... 205

C. Frequency Allocation Schemes for Resonant Manifold Triplexer ..... 206

C.1 Scheme 1: (a) $CH_1$-$CH_2$-$CH_3$ or (b) $CH_3$-$CH_2$-$CH_1$ ..... 206

C.2 Scheme 2: (a) $CH_2$-$CH_1$-$CH_3$ or (b) $CH_2$-$CH_3$-$CH_1$ ..... 206

C.3 Scheme 3: (a) $CH_1$-$CH_3$-$CH_2$ or (b) $CH_3$-$CH_1$-$CH_2$ ..... 207

# Lists of Acronyms

| | |
|---|---|
| 3-D | Three Dimensional |
| 3DP | Three-Dimensional Printing |
| 5G | Fifth Generation communications technologies |
| 6G | Sixth Generation communications technologies |
| ANN | Artificial Neural Network |
| BW | Bandwidth |
| CAD | Computer-Aided Design |
| CF | Centre Frequency |
| CI | Computational Intelligent |
| CM | Coupling Matrix |
| CNC | Computerised Numerical Control |
| DC | Direct Current |
| DE | Differential Evolution |
| DLP | Digital Light Processing |
| DO | Direct Optimisation |
| DRIE | Deep Reactive Ion Etching |
| EDM | Electrical Discharge Machining |
| EIRP | Equivalent Isotropic Radiated Power |

| | |
|---|---|
| EM | Electromagnetic |
| FDM | Fused Deposition Modelling |
| GACMS | General All-resonator Diplexer/multiplexer Coupling Matrix Synthesis |
| GDODK | General Diplexer global Optimisation method guided by Design Knowledge |
| HPA | High Power Amplifier |
| I/O | Input/Output |
| IL | Insertion Loss |
| KPI | Key Performance Indicator |
| LIGA | LIthographie, Galvanoformung, Abformung – lithography, electroplating, and moulding |
| LNA | Low Noise Amplifier |
| MLS | Micro Laser Sintering |
| MSADEC | Memetic Self-Adaptive Differential Evolution for Coupling matrix synthesis |
| PB | Passband |
| PBF | Powder Bed Fusion |
| PCB | Printed Circuit Board |
| QP | Quadratic Programming |

| | |
|---|---|
| RF | Radio Frequency |
| RL | Return Loss |
| RLL | Return Loss Level |
| RP | Reflection Pole |
| RZ | Reflection Zero |
| SADEC | Self-Adaptive Differential Evolution for Coupling matrix synthesis |
| SAO | Surrogate-Assisted Optimisation |
| S-parameter | Scattering-parameter |
| SLA | Stereolithography |
| SLM | Selective Laser Melting |
| SLS | Selective Laser Sintering |
| SMEAFO | Surrogate Model-assisted Evolutionary Algorithm for Filter Optimisation |
| SQP | Sequential Quadratic Programming |
| ST network | Singly Terminated network |
| STD | Standard Deviation |
| TE | Transverse Electric |
| TM | Transverse Magnetic |
| TZ | Transmission Zero |
| UV | Ultraviolet |

| | |
|---|---|
| VNA | Vector Network Analyser |

# Chapter 1 Introduction

## 1.1 Overview of Microwave Diplexers and Multiplexers

Microwave diplexers and multiplexers are indispensable components in transceiver or multiple radio frequency (RF) channel applications, e.g., cellular base stations, and satellite communication payload systems. With the filtering characteristics, they separate a wideband signal into multiple narrowband signals or combine multiple narrowband signals into a single wideband signal [1]. So, the multiplexers are often called channelizers/combiners. A wideband channel in a satellite payload system usually carries more information than a narrowband channel, which means that it requires more power to transmit the signal. The equivalent isotropic radiated power (EIRP) limits in terminals cannot allow wideband transmission. Narrowband transmissions in a multiple-access way are widely applied in the return link of satellite applications [2]. Fig. 1.1 shows a block diagram incorporating the multiplexers in a satellite communication payload system. The

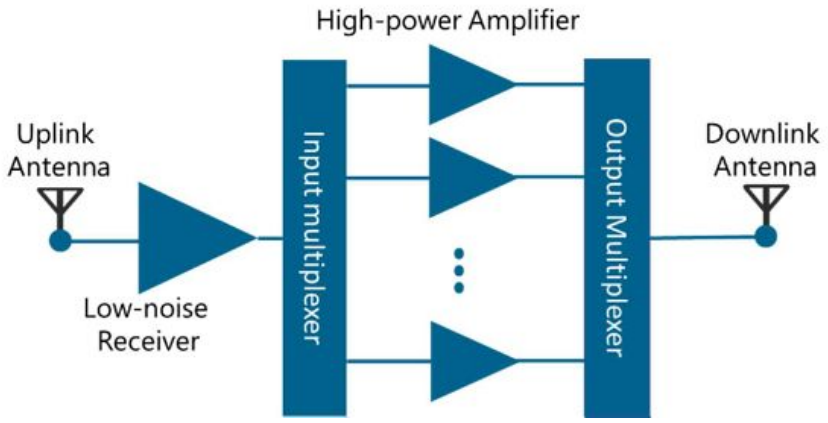



Fig. 1.1. Block diagram of multiplexers used in a payload system.

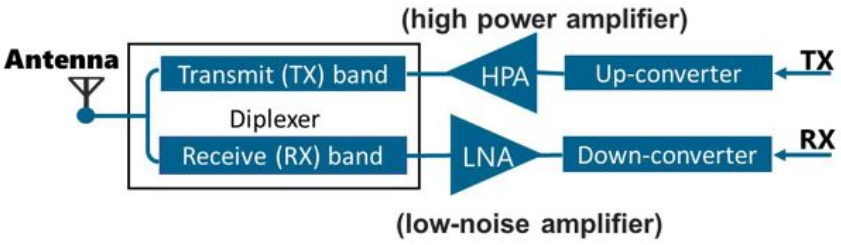



Fig. 1.2. Block diagram of a diplexer in a communication system.

input multiplexer and output multiplexer are separately employed to channelize and recombine the signals with multiple channels. Since they define the RF channels, their performance has a huge impact on the overall communication system.

Diplexers are multiplexers with two channels often called receive and transmit channels. A simple diagram of a diplexer operating in the communication systems is shown in Fig. 1.2. The transmit and receive channels are two filters connecting to a common node with an antenna. The signal received from the antenna is transferred to the receive band while the signal coming from the internal devices should be isolated from the receive bands and directly goes to the antenna [1]. So, isolation is a key performance indicator for diplexers.

It is usually not straightforward to design a usable component from a design specification. The designer first needs to determine the viable fabrication technique and microwave structures they use [3]. The choices of these techniques and structures are highly dependent on the specification or requirements, e.g., loss, bandwidth, and operating frequency. After a technique and a structure are selected, a succession of design and prototyping steps should be implemented to realize the filter components. This could be a

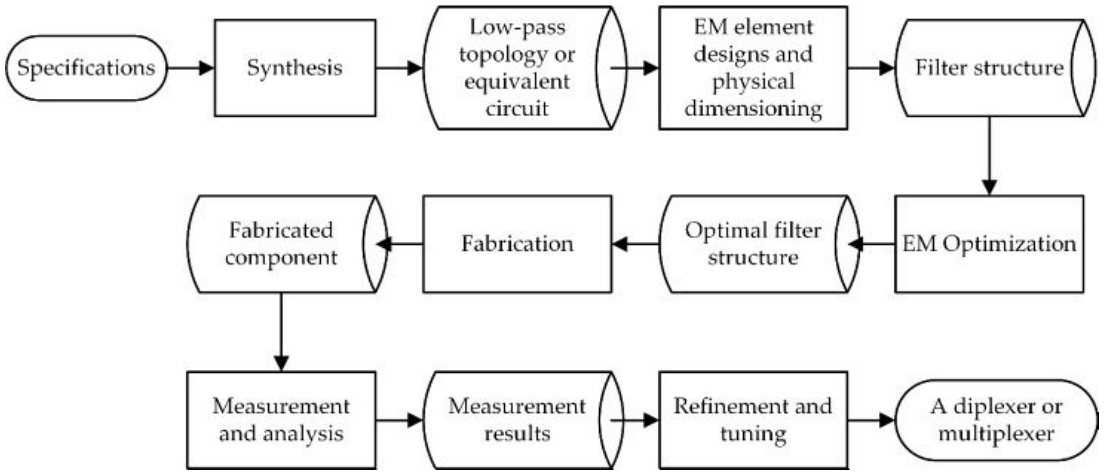



Fig. 1.3. A design flow for a diplexer or multiplexer.

time-consuming process. With a complex structure, the design of a diplexer or a multiplexer could be much more complicated than a microwave filter. It would take even longer when the number of channels increases. Fig. 1.3 illustrates the main procedures during a typical design routine. These are briefly introduced in the following:

***Synthesis***. This step aims to generate useful element values related to specific filtering performance in the normalized frequency domain, i.e., coupling matrix or a lumped-element equivalent circuit. To begin with, ideal channel filtering responses of the multiplexer are firstly represented by using mathematical polynomials according to the selected topology and preassigned specifications [4]. Then, the element values are obtained by using analytical or optimisation-based synthesis methods to realize the filtering performance fulfilling the specifications.

***Electromagnetic (EM) element design and physical dimensioning***. The obtained element values are translated into physical structures in this step. Often, EM simulation is

started from this step. Based on the element values, the designer extracts the initial geometrical dimensions for each specified physical element, e.g., resonators or coupling structures [5]-[6]. A filtering structure with an initial design can be generated.

***3-D EM optimisation***. The initial design is often far from the desired. They are optimized or refined to satisfy the specified requirements. Usually, a large number of EM simulations are required [7] to reach an optimal structure with desired responses.

***Fabrication***. The fabrication technique is selected at beginning of the component design since it often adds constraints to the design options or even dictates some design features. There are various fabrication techniques as well as utilized materials. The commonly used fabrication techniques include computerised numerical control (CNC) [8]-[11] milling on metals (e.g., copper and aluminium) for waveguides and printed circuit board (PCB) for planar circuits. For some very high-frequency applications, high precision micro-fabrication techniques are employed, e.g., SU-8 photoresist [12]-[14], silicon deep reactive ion etching (DRIE) [15]-[19] and LIGA-based thick resist electroplating [20]-[21]. In recent years, additive manufacturing techniques, also known as 3-D printing, have become increasingly popular for microwave devices [3].

***Measurement and analysis***. As a communication device, the RF performance is the main design drive for diplexers/multiplexers. Scattering parameter (S-parameter) is measured by using a vector network analyser (VNA). Designers need to identify the reasons and refine the design if there are significant disagreements between the simulation and

measurement. Moreover, reliability tests may be carried out [22]-[24], e.g., temperature testing, humidity testing, and salt atmosphere testing.

***Refinement and tuning***. Due to the tolerance in the manufacturing and material, post-fabrication refinement or tuning are often required [25]. For one thing, fabricated components may be subject to post-processing, such as polishing and gold plating to improve the surface quality of the cavity components and reduce loss. For another, filters may be tuned to fulfil the required performance. The filters are traditionally manually tuned by technicians while computer-aided tuning has been increasingly developed in recent years [26]. Also, a tolerance analysis can be executed based on the fabricated filters and multiplexers. With the knowing the tolerance and fabrication, the current filter design can be slightly revised to adapt to the fabrication. Then, another round filter optimization and fabrication will be required.

## 1.2 Thesis Motivations

The filter theory has been well-studied over decades. It is still a heated topic in the communication engineering area. New applications (e.g., 5G communication and 6G satellite system) require new design methods and fabrication techniques to implement smaller, lighter, multi-functional, and higher frequency high-performance microwave devices. Among various implementation techniques, coupled-resonator-based microwave filters are extensively used for their general design technique. Theoretically, it can be applied to any type of resonator regardless of its physical structure. This technology has

greatly facilitated the development of the filter/multiplexer.

In recent years, with the development of computer-aided-design technology, the research and development of microwave filters and multiplexers have gradually become a routine of computer-aided processes [27]-[32]. Various commercial electromagnetic (EM) simulation tools have provided convenience for engineers and researchers, e.g., CST Studio Suite [33], and Ansys HFSS [34]. Filter design becomes more accessible and efficient. However, the time cost of full-wave simulation is directly linked to the complexity of the filter structure. When it comes to filters with very complex structures and multiplexers, an iterative brute-force optimisation of such a complete component is often prohibitive. On the other hand, the computer is not yet smart and user-friendly enough to free designers from input and intervention. In fact, more often than not, designers have to "teach computers" (e.g., manually tuning) step by step to realize their design goals. This is usually a time-consuming, unreliable, or even unsuccessful process.

Diplexer/multiplexer is one of the largest passive components in the RF front end. Smaller sizes and less weight are always desired. Diplexers and multiplexers with novel configurations are heavily pursued. In [35], a diplexer with an all-resonator configuration removing the common junction is proposed to reduce the size of the diplexer. This configuration was later extended to multiplexers with more channels and various complex topologies [36]. Comprised by only resonators, the multiplexers with this topology can be represented by a single coupling matrix. In this thesis, novel multiplexers based on all-

resonator structures will be proposed and investigated.

Manufacturing technologies are a driving force for the development of microwave filters/multiplexers. With the help of high precision CNC machining and micromachining techniques, the operation frequency of waveguide-type of filters has been pushed to sub-terahertz frequencies, e.g., the WR-1.5 band [37]. In recent years, 3D-Printing (3DP) technology provides a fresh choice in microwave component fabrications. It could fabricate special geometric resonators (e.g., spherical resonator [38] and depressed super ellipsoid resonator [39]) with better performance (high unloaded quality factor), which cannot be easily fabricated by traditional technology. Also, the monolithic structures enabled by 3DP [38] could greatly reduce the weight of complex parts by removing screws and connectors.

This thesis focuses on the design methodologies, novel circuit topology, and fabrication techniques for diplexers and multiplexers.

For the design methodologies, two aspects will be concerned – synthesis of diplexers and multiplexers with all-resonator structures and their EM optimisation. Filter-design-knowledge and advanced computational techniques are combined to deal with the synthesis and optimisation tasks of diplexers and multiplexers in a general and reliable way.

As for the circuit topology design, a new concept of the manifold multiplexer is presented using the all-resonator structure. We coined the name of 'resonant manifold multiplexer'. Resonators are utilized to replace the traditional manifold junction, a transmission line-based frequency distribution network. The innovation aims to reduce the

overall size of the multiplexers. Both the synthesis and design approaches are presented.

Finally, new fabrication techniques for diplexers over 100 GHz are investigated. D-band diplexer is designed and fabricated by a high-precision micro metal 3D printing technique, the so-called micro laser sintering (MLS).

## 1.3 Novelty and Contributions of the Thesis

The novelty of the research work and the contribution of this thesis are summarised as follows.

(1) Proposed a general optimisation-based coupling matrix synthesis method for all-resonator diplexers and multiplexers. This has been published in IEEE Transactions on Microwave Theory and Techniques.

(2) Proposed a general EM optimisation method for microwave diplexers. This has been accepted by IEEE Microwave and Wireless Components Letters

(3) Proposed a new multiplexer design concept, called resonant manifold multiplexers. This has been published in IEEE Transactions on Microwave Theory and Techniques.

(4) Designed a D-band waveguide diplexer based on all resonator structure. Comprehensive measurements and comparisons are implemented on the commercially fabricated diplexers using micro laser sintering and CNC machining.

## 1.4 Thesis Overview

The thesis contains eight chapters.

Chapter 1 introduces the research background, the main objects of the work, and the motivation of the thesis.

Chapter 2 reviews the existing methodologies and theories related to the work in this thesis. The literature review covers the state-of-the-art synthesis methods, EM optimisation methods, and fabrication techniques for the diplexers and multiplexers.

Chapter 3 lays down the theoretical foundation for the design of diplexers and multiplexers. It starts from the general filter theory and design methodologies and extends to the diplexers and multiplexers.

Chapter 4 proposes a general optimisation-based coupling matrix synthesis method for all-resonator diplexers and multiplexers. This is the general all-resonator multiplexer coupling matrix synthesis (GACMS) method. The method hybrids the classic filter knowledge with advanced optimisation techniques to generate a high-quality coupling matrix for the all-resonator diplexers and multiplexers. Numerical coupling matrix examples for diplexers and multiplexers are illustrated to demonstrate the proposed method.

Chapter 5 proposes an EM optimisation method for diplexers. This method is called a general diplexer global optimisation method guided by design knowledge (GDODK). It is an automatic optimisation method for resonator-coupled diplexers containing two aspects. The initial physical dimensions are generated based on a local optimisation procedure. On the other, the filtering features, such as reflection zeros and transmission zeros, are extracted

to formulate a performance-based objective function. With a powerful global optimizer, the diplexer optimisation achieves a high success rate. Three diplexer examples are implemented to demonstrate the proposed method.

Chapter 6 presents two novel resonant manifold multiplexers based on an all-resonator structure. A coupling matrix synthesis method and an optimisation method are presented. A triplexer and a pentaplexer are designed and fabricated using the rectangular waveguide technique.

Chapter 7 presents a D-band diplexer design. It is fabricated by using MLS and high precision CNC milling technique for comparative study. The synthesis and design methodologies are detailed. Comprehensive characterization and measurements of the geometry structures and the surfaces are conducted to the MLS diplexer.

Chapter 8 concludes the thesis. Future work is suggested.

## Reference

[1] R. J. Cameron, C. M. Kudsia, and R. R. Mansour, "Multiplexer theory and design," Microwave Filters for Communication Systems: Fundamentals, Design, and Applications, Wiley, 2018, pp.569-608, ch18.

[2] O. Kodheli, E. Lagunas, N. Maturo, S. K. Sharma, B. Shankar, J. F. M. Montoya, J. C. M. Duncan, D. Spano, S. Chatzinotas, S. Kisseleff, J. Querol, L. Lei, T. X. Vu, and G. Goussetis, "Satellite Communications in the New Space Era: A Survey and Future Challenges," IEEE Communications Surveys & Tutorials, vol. 23, no. 1, pp. 70–109, 2021.

[3] R. V. Snyder, G. Macchiarella, S. Bastioli, and C. Tomassoni, "Emerging Trends in Techniques and Technology as Applied to Filter Design," IEEE Journal of Microwaves, vol. 1, no. 1, pp. 317-344, Jan. 2021.

[4] G. Macchiarella and S. Tamiazzo, "Cooking Microwave Filters: Is Synthesis Still Helpful in Microwave Filter Design?," IEEE Microwave Magazine, vol. 21, no. 3, pp. 20-33, Mar. 2020.

[5] Richard J. Cameron, Chandra M. Kudsia, and Raafat R. Mansour, "Design and Physical Realization of Coupled Resonator Filters," Microwave Filters for Communication Systems: Fundamentals, Design, and Applications, Wiley, 2018, pp.457-484. ch14.

[6] Jia-Shen G. Hong and Michael J. Lancaster, Microstrip filters for RF/microwave applications, John Wiley & Sons, 2001.

[7] J. W. Bandler, Qingsha S. Cheng, Sameh A. Dakroury, Ahmed S. Mohamed, Mohamed H. Bakr, Kaj Madsen, and Jacob Søndergaard, "Space mapping: the state of the art," IEEE Transactions on Microwave Theory and Techniques, vol. 52, no. 1, pp. 337-361, Jan. 2004.

[8] C. A. Leal-Sevillano, J. R. Montejo-Garai, J. A. Ruiz-Cruz, and J. M. Rebollar, "Low-loss elliptical response filter at 100 GHz," IEEE Microwave Wireless Components Letters, vol. 22, no. 9, pp. 459–461, Sep. 2012.

[9] X. Liao, L. Wan, Y. Yin, and Y. Zhang, "W-band low-loss bandpass filter using rectangular resonant cavities," IET Microwave, Antennas Propagation,vol. 8, no. 15, pp. 1440–1444, Jul. 2014.

[10] C. A. Leal-Sevillano, T. J. Reck, G. Chattopadhyay, J. A. Ruiz-Cruz, J. R. Montejo-Garai, and J. M. Rebollar, "Development of a widebandcompact orthomode transducer for the 180–270 GHz band," IEEE Transactions on Terahertz Science and Technology, vol. 4, no. 5, pp. 634–636, Sep. 2014.

[11] Jian-Xing Zhuang, Wei Hong, and Zhang-Cheng Hao, "Design and analysis of a terahertz bandpass filter," 2015 IEEE International Wireless Symposium (IWS 2015), 2015, pp. 1-4.

[12] C. A. Leal-Sevillano, J. R. Montejo-Garai, M. Ke, M. J. Lancaster, J. A. Ruiz-Cruz, and J. M. Rebollar, "A pseudo-elliptical response filter at W-band fabricated with thick SU-8 photo-resist technology," IEEE Microwave Wireless Components Letters, vol. 22, no. 3, pp. 105–107, Mar. 2012.

[13] X. Shang, Y. Tian, M. J. Lancaster, and S. Singh, "A SU8 micromachined WR-1.5 band waveguide filter," IEEE Microwave Wireless Components Letters, vol. 23, no. 6, pp. 300–302, Jun. 2013.

[14] X. Shang, M. Ke, Y. Wang, and M. J. Lancaster, "Micromachined W-band waveguide and filter with two embedded H-plane bends," IET Microwave, Antennas Propagation, vol. 5, no. 3, pp. 334–339, Feb. 2011.

[15] Y. Li, B. Pan, C. Lugo, M. Tentzeris, and J. Papapolymerou, "Design and characterization of a W-band micromachined cavity filter including a novel integrated transition from CPW feeding lines," IEEE Transactions on Microwave Theory and Techniques, vol. 55, no. 12, pp. 2902–2910, Dec. 2007.

[16] X. H. Zhao, J. F. Bao, G. C. Shan, Y. J. Du, Y. B. Zhen, Y. Wen, and C. H. Shek, "D-band micromachined silicon rectangular waveguide filter," IEEE Microwave and Wireless Components Letters, vol. 22, no. 5, pp. 230–232, May 2012.

[17] C. A. Leal-Sevillano,T. J. Reck, C. Jung-Kubiak, G. Chattopadhyay, J. A. Ruiz-Cruz, J. R. Montejo-Garai, and J. M. Rebollar, "Silicon micromachined canonical E-plane and H-plane

bandpass filters at the terahertz band," IEEE Microwave Wireless Components Letters, vol. 23, no. 6, pp. 288–290, Jun. 2013.

[18] T. J. Reck, C. Jung-Kubiak, J. Gill, and G. Chattopadhyay, "Measurement of silicon micromachined waveguide components at 500–750 GHz," IEEE Transactions on Terahertz Science and Technology, vol. 4, no. 1, pp. 33–38, Jan. 2014.

[19] X. Zhao, O. Glubokov, J. Campion, A. Gomez-Torrent, A. Krivovitca, U. Shah, and J. Oberhammer, "Silicon Micromachined D-Band Diplexer Using Releasable Filling Structure Technique," IEEE Transactions on Microwave Theory and Techniques, vol. 68, no. 8, pp. 3448-3460, Aug. 2020.

[20] J. R. Stanec and N. S. Barker, "Fabrication and integration of micromachined submillimetre-wave circuits," IEEE Microwave Wireless Components Letters, vol. 21, no. 8, pp. 409–411, Aug. 2011.

[21] E. D. Cullens, L. Ranzani, K. J. Vanhille, E. N. Grossman, N. Ehsan, and Z. Popovic, "Micro-fabricated 130–180 GHz frequency scanning waveguide arrays," IEEE Transactions on Antennas and Propagation, vol. 60, no. 8, pp. 3647–3653, Aug. 2012.

[22] P. K. Ambati, V. Singh, S. Soni, and V. D. Parekh, "Accurate Prediction, Validation of Ambient Microwave Breakdown Threshold in High Power Very Narrowband Microwave Filters and Novel Design Techniques to Establish Sufficient Margins," 2017 IEEE MTT-S International Microwave and RF Conference (IMaRC), 2017, pp. 1-5.

[23] T. Pinheiro-Ortega, J. Monge, S. Marini, J. Sanz, E. Sorolla, M. Mattes, C. Vicente, J. Gil, V. E. Boria, and B. Gimeno, "Microwave Corona Breakdown Prediction in Arbitrarily-Shaped Waveguide Based Filters," IEEE Microwave and Wireless Components Letters, vol. 20, no. 4, pp. 214-216, April 2010.

[24] R. R. Mansour, B. Jolley, Shen Ye, F. S. Thomson, and V. Dokas, "On the power handling capability of high temperature superconductive filters," IEEE Transactions on Microwave Theory and Techniques, vol. 44, no. 7, pp. 1322-1338, July 1996.

[25] N. Zahirovic, R. R. Mansour and M. Yu, "Scalar Measurement-Based Algorithm for Automated Filter Tuning of Integrated Chebyshev Tunable Filters," IEEE Transactions on Microwave Theory and Techniques, vol. 58, no. 12, pp. 3749-3759, Dec. 2010.

[26] J. C. Melgarejo, J. Ossorio, S. Cogollos, M. Guglielmi, V. E. Boria, and J. W. Bandler, "On Space Mapping Techniques for Microwave Filter Tuning," IEEE Transactions on Microwave Theory and Techniques, vol. 67, no. 12, pp. 4860-4870, Dec. 2019.

[27] G. T. Roan and K. A. Zaki, "Computer-aided design of microstrip filters by iterated analysis," IEEE Transactions on Microwave Theory and Techniques, vol. 36, no. 11, pp. 1482-1487, Nov. 1988.

[28] N. Leszczynska, A. Lamecki, and M. Mrozowski, "Fast Full-Wave Multilevel Zero-Pole Optimisation of Microwave Filters," IEEE Microwave and Wireless Components Letters, vol. 26, no. 11, pp. 867-869, Nov. 2016.

[29] V. Miraftab and R. R. Mansour, "A robust fuzzy-logic technique for computer-aided diagnosis of microwave filters," IEEE Transactions on Microwave Theory and Techniques, vol. 52, no. 1, pp. 450-456, Jan. 2004.

[30] H. Kabir, Y. Wang, M. Yu, and Q. Zhang, "Neural Network Inverse Modelling and Applications to Microwave Filter Design," IEEE Transactions on Microwave Theory and Techniques, vol. 56, no. 4, pp. 867-879, April 2008.

[31] A. A. Melcon, J. R. Mosig, and M. Guglielmi, "Efficient CAD of boxed microwave circuits based on arbitrary rectangular elements," IEEE Transactions on Microwave Theory and Techniques, vol. 47, no. 7, pp. 1045-1058, July 1999.

[32] J. E. Rayas-Sanchez and V. Gutierrez-Ayala, "EM-Based Monte Carlo Analysis and Yield Prediction of Microwave Circuits Using Linear-Input Neural-Output Space Mapping," IEEE Transactions on Microwave Theory and Techniques, vol. 54, no. 12, pp. 4528-4537, Dec. 2006.

[33] CST studio suite 2021, available: https://www.3ds.com/products-services/simulia/products/cst-studio-suite/.

[34] Ansys HFSS, Available: https://www.ansys.com/products/electronics/ansys-hfss.

[35] T. Skaik, M. Lancaster, and F. Huang, "Synthesis of multiple outputcoupled resonator microwave circuits using coupling matrix optimiza-tion," IET Microwave, Antennas Propagation, vol. 5, no. 9, pp. 1081–1088,Jun. 2011.

[36] X. Shang, Y. Wang, W. Xia, and M. J. Lancaster, "Novel Multiplexer Topologies Based on All-Resonator Structures," IEEE Transactions on Microwave Theory and Techniques, vol. 61, no. 11, pp. 3838-3845, Nov. 2013.

[37] D. Wang, M. J. Lancaster, Y Wang, K. M. Shum, and Q. Zhang, "WR-1.5 (500–750 GHz) waveguide bandpass filter fabricated using high precision computer numerically controlled machining," Microwave Optical Technology Letter, vol. 63, no. 3, pp: 1160– 1164, Dec. 2021.

[38] C. Guo, X. Shang, M. J. Lancaster, and J. Xu, "A 3-D Printed Lightweight X-Band Waveguide Filter Based on Spherical Resonators," IEEE Microwave and Wireless Components Letters, vol. 25, no. 7, pp. 442-444, July 2015.

[39] P. A. Booth and E. Valles Lluch, "Realising advanced waveguide bandpass filters using additive manufacturing," IET Microwave, Antennas Propagation, vol. 11, no. 14, pp: 1943-1948, Nov. 2017.

# Chapter 2 Literature Review

This chapter reviews microwave diplexers and multiplexers focusing on the following aspects: configurations and topologies, synthesis methods, physical dimensioning methods, EM optimisation methods, and micro-fabrication techniques.

## 2.1 Configurations of Diplexers and Multiplexers

There are several typical configurations for multiplexers. Four types are mostly used: hybrid coupler based, circulator based, manifold based, and directional-filter based configuration [1]. Fig. 2.1 illustrates the four types of multiplexers. They are separately briefed in the following.

***The hybrid-coupler-based configurations*** (Fig. 2.1 (a)) employ two identical narrowband filters and two wideband quadrature hybrid couplers in each channel operating at a frequency band with the centre frequency $f_i$ $(i = 1, \ldots, n)$. Using this configuration, the filter design is suitable for high-power applications [1]. As shown in Fig. 2.1(a), two filters are incorporated in each channel, only half of the input channel power passes through each filter. Also, the directional property of the hybrid coupler contributes to the low interaction between channel filters.

***The circulator-coupled multiplexer*** (Fig. 2.1 (b)) utilizes a set of circulators and channel filters to define each channel. It has a similar advantage of good isolation between channels as the hybrid-coupled multiplexers because of the directional nature of the circulators.

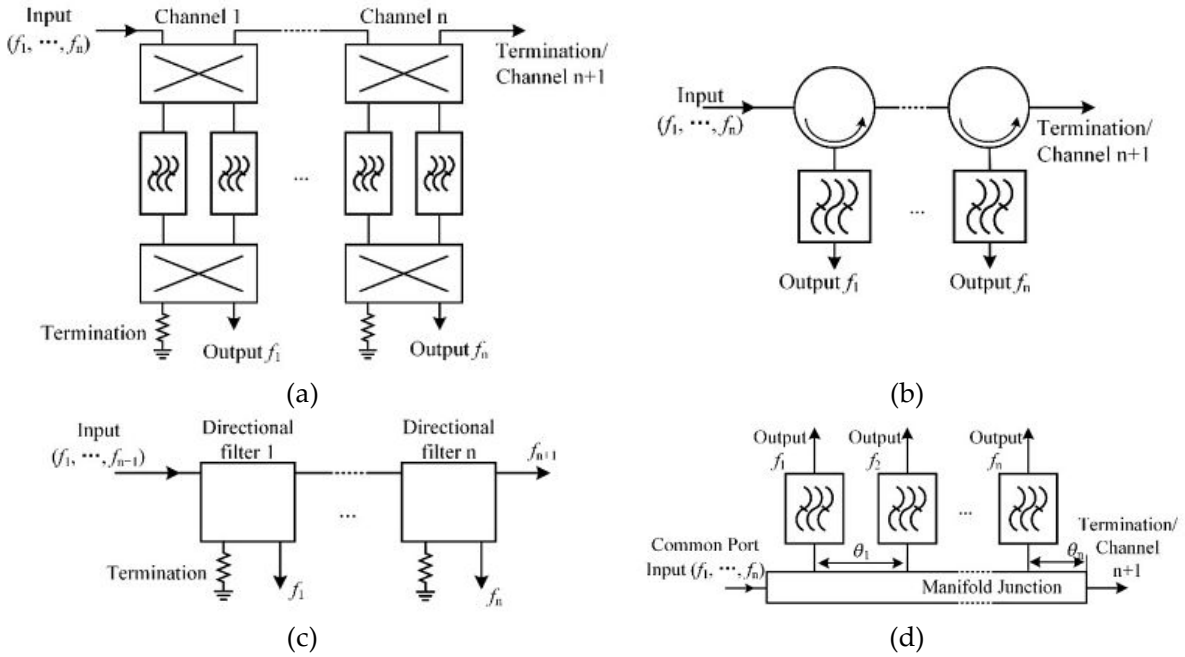


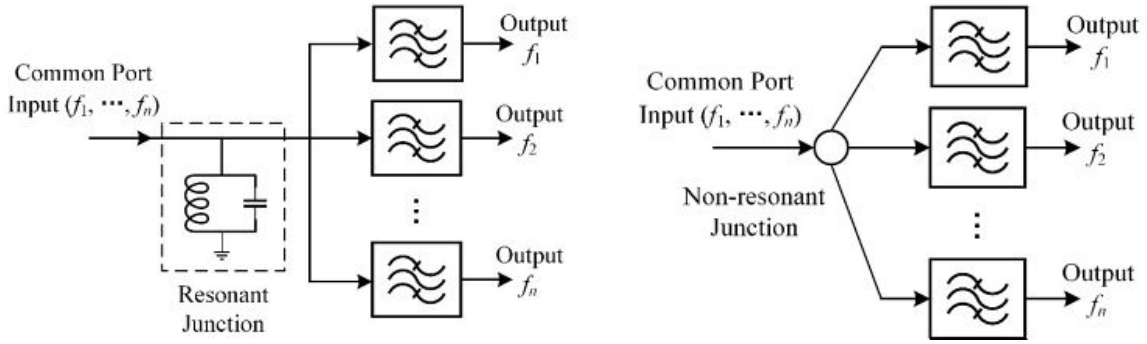

Fig. 2.1 Diagrams of commonly used configurations for multiplexers. (a) Diagram of a hybrid-coupled multiplexer; (b) Diagram of a circulator-coupled multiplexer; (c) Diagram of a directional filter multiplexer; (d) Diagram of a manifold coupled multiplexer [1].

However, its overall insertion loss is higher due to the use of circulators.

***The directional filter multiplexer*** (Fig. 2.1 (c)) consists of $n$ cascaded directional filters to separate $n$ frequency bands from the input signal. A directional filter is a four-port device in which one port is terminated by a load. The other three ports operate as a circulator connected to a bandpass filter. The directional filter multiplexers are limited to narrow-band applications and restricted to single-mode filters.

The multiplexers with the previous three configurations can be designed by a modular approach. Although this brings convenience in the design and tuning, high losses and bulky volume are the main shortcomings for their applications in communication systems.

***The manifold-coupled multiplexer*** (Fig. 2.1 (d)) is a relatively optimal solution by




(a) (b)

Fig. 2.2. Typical configurations for the star-junction multiplexers. (a) Resonant-junction multiplexer; (b) Non-resonant junction multiplexer [2].

considering the overall volume and absolute minimum insertion loss of the channels. As shown in Fig. 1(d), in a manifold multiplexer, the channel filters are periodically connected to a manifold junction by a certain separation $\theta_i$ $(i = 1, \ldots, n)$. Each channel occupies a frequency band with the centre frequency $f_i$ $(i = 1, \ldots, n)$. Conventionally, the manifold junction is a transmission line. For non-planar microwave components, the manifold junction is usually a waveguide structure.

The manifold multiplexer is viewed as an optimal choice as it facilitates miniaturization and low insertion loss. However, the design of the manifold multiplexer mostly relies on optimisation methods. This means the multiplexer cannot be synthesized theoretically. It usually starts with the design of channel filters which are then connected to the manifold for impedance matching. Since interaction exists between channels, the overall design is very complicated, especially when the number of channels is high.

In recent years, a novel configuration, called star-junction multiplexer, has been

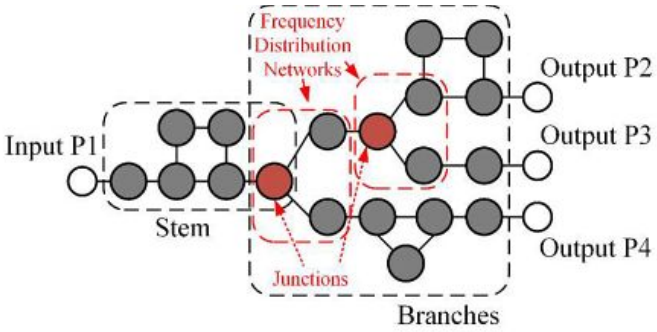



Fig. 2.3. Diagram of an all-resonator multiplexer.

employed to design diplexers and multiplexers [2]-[3]. All channel filters are combined to a resonant or a non-resonant node. A simplified diagram of the star-junction multiplexer is shown in Fig. 2.2. The coupling matrix representing the multiplexer network can be systematically obtained based on calculated characteristic polynomials of the multiplexer [2], [4]. The multiplexers are physically realized based on the initial design derived from the coupling matrix. The multiplexers have found applications in base stations for mobile communications [2]-[6].

Another relatively recent multiplexer configuration is the so-called all-resonator-based multiplexer based on resonator junctions [8]. A concept configuration is illustrated in Fig. 2.3. The multiplexer network is comprised of only coupled resonators. They can be grouped into a stem and multiple branches, where the resonators are flexibly assigned based on coupling matrix theory [8]-[13]. A tree topology [8] is usually used to minimize the number of couplings associated with any resonator to no more than three. However, the intricate frequency distribution network makes it difficult to be synthesized when the number of

channels is larger than four [8].

## 2.2 Synthesis Methods for Diplexers and Multiplexers

Most of the synthesis methods for multiplexer, proposed in recent years, aim to obtain the low-cost representation of the physical structure, e.g., lumped equivalent circuits or coupling matrix. Then, they are used for extracting the initial values for the physical realization. Before the introduction of the synthesis method, multiplexers were mostly designed by using a direct optimisation method [2]. Well-designed channel filters are connected by a combiner (e.g., manifold junction or star-junction) and then a direct "brute force" optimisation or channel-by-channel optimisation are implemented. Although these direct optimisation methods can obtain the optimal results, this process is time-consuming and prohibitive to make a quick theoretical evaluation for the design specifications [2].

The synthesis-based design method is first proposed and implemented in the star-junction multiplexers as shown in Fig. 2.2. It belongs to an analytical method [2]-[6]. The main purpose of the method is to obtain the characteristic polynomials of the network S-parameters. The whole multiplexer network is divided into multiple-channel filters. Then, the characteristic polynomials of the channel filters are synthesized. Once these polynomials are known, the multiplexer synthesis will be simplified as several filter synthesis problems. According to the characteristic polynomials of the channels, appropriate topologies of the channel filters can be selected. Then, the coupling matrix of the whole multiplexer is synthesised accordingly.

The synthesis results provide theoretical guidance to the multiplexer design, designers can quickly evaluate the design specifications, speeding up the multiplexer design and prototyping. However, the method proposed in [2] can only be suitable for the star-junction structures. When the order of resonators in the multiplexer is high, the rational polynomial for the multiplexer is difficult to be accurately solved [6]. This will attribute to large errors existing in the synthesis results. P. Zhao proposed a novel circuit equivalence called phased-inverter to frequency-invariant reactance inverter transformations [6]. The synthesis utilizing a channel-by-channel scheme resolved the high-order polynomial synthesis problem. For another, in the star-junction topology, the input ports of all the channel filters connect to a single one junction. It is more suitable for the application with a lower number of channels (2-4 channels) [7].

Another widely implemented method is optimisation-based synthesis approaches. They are mainly implemented for the multiplexers with all-resonator configurations [9]-[13] when analytical synthesis becomes unattainable. Although some analytical methods were also investigated for all-resonator multiplexer [14]-[15], their application ranges are still limited. The optimisation process is more straightforward as the polynomial synthesis can be omitted since there is a direct relationship between the coupling matrix and S-parameter responses. The “distance” (error function) between actual S-parameter responses with respect to one coupling matrix (a set of optimisation variables) and the design specifications can be calculated.

Desired coupling matrix will be obtained when the error function minimisation is realized by local optimizers or global optimisers. For example, sequential quadratic programming (SQP) method, a local optimizer, was implemented to obtain the coupling matrix for the diplexer with symmetric responses [16]. Then, this method is extended and implemented in the diplexers and multiplexers with more complex responses [8], [10]. The local optimizer is efficient, but a good initial value (starting point of the optimisation) is necessary. Otherwise, the optimisation is easily trapped into local optimal solutions when the filtering topology is complex. Further, a global optimizer, called self-adaptive differential evolution for coupling matrix synthesis (SADEC), is proposed for all-resonator diplexers [17]. The global optimizer does not depend on the initial values and has a more powerful exploration ability to avoid trapping into local optima, but its optimisation efficiency is not as good as the local one. It can be noticed that the available methods have a certain capability to solve some multiplexer with simple filtering responses, a general and stable synthesis method for real-world applications is still unavailable. In this thesis, a general optimisation-based coupling matrix synthesis method is proposed for the all-resonator multiplexers, which is detailed in Chapter IV.

Up to now, the manifold multiplexer cannot be designed based on the synthesis approaches. This is because the evaluation of characteristic polynomials is hard to be realized when the junction is constituted by distributed elements [18]. Some polynomial design method has been investigated using an optimisation procedure [18]-[19].

There are also some other investigations in the aspect of multiplexer synthesis. Zhang [20] employed extracted pole structure and frequency-variant topologies in the channel filters of a multiplexer and its synthesis problem have been solved by using the analytical method. Yang [21] proposed a singly terminated (ST) network treating each channel as a single-port network with a zero-impedance source port. The ST network is used as the initial solution to design a contiguous multiplexer.

## 2.3 Physical Dimensioning Methods

The physical dimensioning aims to extract initial geometrical parameters based on the obtained coupling matrix. It is an important step for the subsequent 3-D EM optimisation. The methods in the literature are summarised as follows.

### 2.3.1 Design Curve Method

This method has been most widely used and well-documented [22]-[23]. The initial dimensioning uses two design curves, describing the mutual couplings between resonator pairs and the external quality factor between the resonator and I/O ports. EM simulations are employed to generate these two curves as a function of an only one-dimensional parameter at a time, e.g., the coupling iris width in waveguide filters. The mutual coupling values and external quality factor values are normally calculated from either frequency-domain simulation or eigenmode simulation results by sweeping the dimension parameters with discrete samples. When changing parameters, the centre frequency of the simulation

results must be held at a specific frequency point. i.e., the centre frequency of the filter. Then, design curves would be interpolated, yielding the corresponding geometrical dimension for the desired coupling value. By using this method, the initial design for microwave filters can be obtained by using relatively few EM simulations. Experience-based estimation and tunings are often required to maintain the resonant frequency. However, there is no guideline about how many simulation samples need to be employed to ensure sufficient accuracy in the initial design. When it comes to the filters with complex structures, e.g., those with cross-couplings or multiplexer, this method may become inaccurate. Some extended works based on this method can be found in [24]-[26].

### 2.3.2 Metamodeling Method

To increase the accuracy of the physical dimensioning, some research works use more complex mathematical functions to represent the relations between the coupling values and the elements in the filter. In [27], the authors employed a quadratic function to represent the relationship between each coupling value and multiple adjacent dimensions. The same authors also adopted sparse grid interpolation schemes with adaptive sampling to generate a surface to represent the coupling value to multiple dimensions [28]. This method can surely obtain high-quality initial dimensions. However, to obtain the complex mathematical model considering more design variables, a larger number of EM simulations are required. Also, the selection of the dimensions in the modelling and the order of the modelling function has to be determined depending on the specific filter structure.

### 2.3.3 Inverse Modelling Method

The inverse modelling method means to construct a mathematical model (e.g., artificial neural network (ANN)) whose input is a specific frequency response (e.g., S-parameter), and the output is the corresponding design. In [29]-[30], the authors use a 3rd-order filter model to construct an inverse model. Since the 3-order filter contains two mutual couplings and an external quality factor, it is assumed that all situations of coupling combination in the real filter can be represented by the 3rd order filter responses. Then, the constructed inverse model can be seen as an initial design generator. The input is a set of coupling coefficients that are synthesised based on the design specification. The output is the dimensions corresponding to the set of coupling coefficients. The initial dimension generation is very fast because the constructed inverse model is reusable as long as the filters have the same resonator type. However, it is not easy and sometimes impossible to construct such an inverse model. To construct the inverse model, dimension sampling has to be performed using the 3$^{rd}$-order filter over a very wide range. Also, the inverse modelling could meet multiple-valued problems, namely for one specific frequency response, there can be two or more sets of design parameters.

## 2.4 Optimisation Methods for Diplexers and Multiplexers

### 2.4.1 Computer-aided Design Methods for Multiplexers

Nowadays, the design of the diplexer and multiplexer are routinely verified and tested

in simulation before fabrication. With the assistance of the EM simulator, it is increasingly plausible to obtain the behaviours of the microwave components close to the measurement results. However, when the component structure is very complex, especially for diplexers and multiplexers, the design process becomes less efficient in practice because of the time-consuming EM simulations.

In the early days, the manifold multiplexers were designed by analytical methods based on equivalent circuits [31]-[33]. These analytical methods are a kind of approximation rather than simulation behaviour or practical measurements of the multiplexer. Thus, inaccuracies in the initial design result in cumbersome subsequent optimisation and tuning [34].

More recently, methods using hybrid design procedures have been adopted to achieve desirable multiplexer performance. The main idea of a hybrid procedure is to introduce low-cost models, e.g., equivalent circuits, into the design process to reduce the difficulty in optimisation. These methods can be divided into three types:

**1) Utilizing low-cost models to replace parts of EM models.** The equivalent circuit model or numerical model can replace some parts of the multiplexer, e.g., channel filters. In the CAD software, these low-cost model responses are used to replace the computationally expensive EM model simulations. Accatino et al. [35] use the full-wave model to represent the manifold behaviour while the filter responses are represented by an equivalent circuit. Wang et al. [36] proposed two hybrid models to address the design and optimisation of the manifold multiplexer. The first one combines the circuitry channel filter model and EM

analysis of the coupling junction adjacent to the manifold. The second one is to build neural network models for the output couplings from the manifold junction to the first resonators of the channels [36].

**2) Accurately modelling the manifold T-junctions to obtain a good starting point for the manifold dimensions then using a circuit model [1], [37]-[38]**. The T junction is firstly simulated to obtain the sub-optimal dimensions for the manifold junction assuming reciprocity and lossless of the junction. With the designed channel filters, further optimisation is needed to fulfil the specifications [37]. Montejo-Garai et al. [38] introduced a fictitious reactive load concept to precalculated the distances between channel filters and a short circuit at the end of the manifold junction. In [1], the authors precalculated the parameters of the manifold junction by a mode-matching routine.

**3) Linking the low-fidelity model (i.e., circuit model) and high-fidelity model (i.e., EM model).** Space mapping technique has been applied to refine each filter of the multiplexer [38]-[42]. Cogollos et al. proposed a systematic method for multiplexers with contiguous and non-contiguous channel configurations, in both E-plane and H-plane configurations [42]. They employed a distributed model of the individual channel filters to build a halfway point between the lumped model and the physical structures. In this way, the computational time is saved.

In recent years, computational intelligence (CI) methods have been increasingly investigated and developed [43]. The computational intelligent methods utilize the nature-

inspired mathematical modelling techniques and optimisation methods to learn the behaviours of complex real-world problems, e.g., computer-aided design for microwave filters, and then address them. The available optimisation techniques are reviewed in the following.

### 2.4.2 Direct Optimisation and Surrogate-assisted Optimisation

It has been a long time since the numerical optimisation procedures were first applied to the RF and microwave circuit design in the 1960s [44]. In the computer-aided design method, the physical dimensions are used as the optimisation variables which are iteratively corrected to obtain a design that meets the design specifications. These can be broadly put into two categories: direct optimisation (DO) and surrogate-assisted optimisation (SAO) [45]. DO means that the high-fidelity EM prototype simulation model is directly inserted in the optimisation process as illustrated in Fig. 2.4 whereas the SAO utilises a low-cost model (surrogate) to approximate the high-fidelity EM simulation model.

DO methods for microwave filters appeared in the 1990s [46]-[50]. It utilized the optimisation method adjusting the dimensions to the desired responses after each simulation. However, when the microwave structure is very complicated, the optimisation process will be very low-efficient. Some works first achieve an optimal solution of a section of a microwave filter. Then, the rest of the filter will be progressively optimized until the simulation performance achieves the desired responses [46].

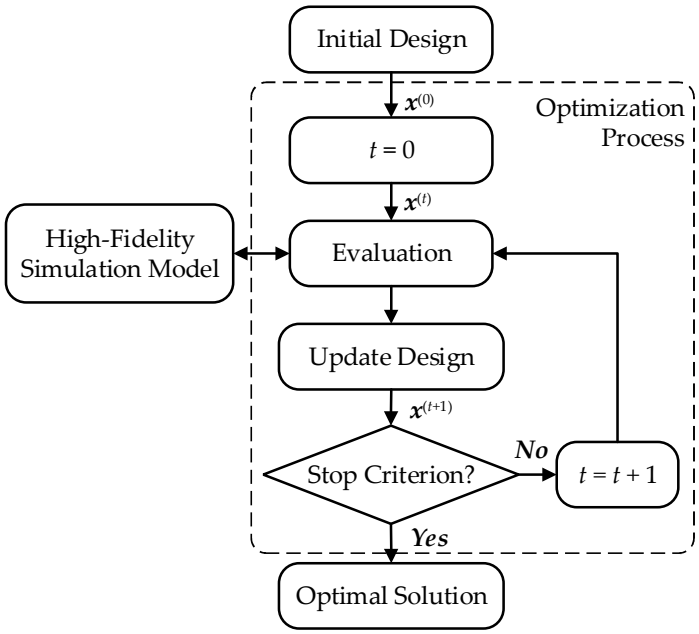



Fig. 2.4. The workflow of the direct optimization (DO) for microwave components.

The DO usually requires a large number of EM simulations during the optimisation process. SAO methods can be applied to improve the optimisation efficiency. It employs a low-cost mathematical or physical surrogate model to approximate the microwave component behaviour. The workflow of the SAO is shown in Fig. 2.5. By invoking the surrogate (fast evaluation) rather than the high-fidelity EM simulation model (slow evaluation), the optimisation can be sped up and achieve reasonable accuracy. Microwave passive filter is one of the most productive applications for SAO techniques. In 1994, the space mapping technique first introduced the concept of surrogate in the microwave engineering area [51]. It employs two types of simulation models, one is the coarse model which is efficient but not very accurate (e.g., equivalent circuit) and the other is a fine model which is very accurate but time-consuming, i.e., the full-wave EM design prototype. As the

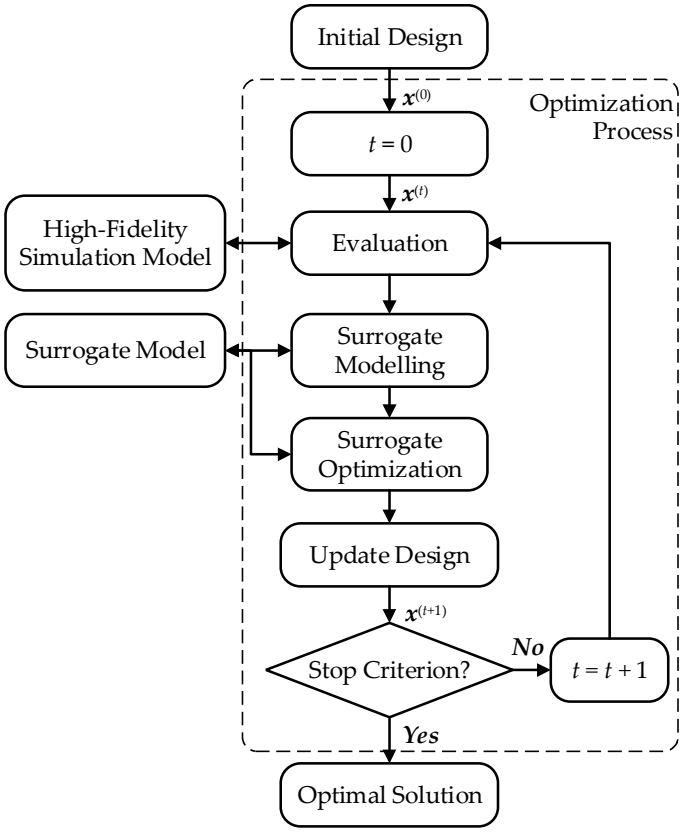



Fig. 2.5. The workflow of the SAO for microwave components.

equivalent circuit is low-cost, the space mapping method also belongs to a general type of SAO [52]-[53]. The local optimisation is performed on the coarse model, guided and corrected (the mapping process) by the simulation of the fine model. To achieve the optimal solution, multiple mapping processes are needed.

Finding an appropriate physical surrogate model is increasingly harder with the increased complexity and diversity of the microwave components [53]-[57]. Mathematical surrogate modelling methods, namely data-driven SAO methods, are increasingly employed for RF and microwave component designs. The data-driven surrogate modelling is performed based on the EM simulations. Firstly, dimensions (input) are sampled within

a preassigned range, and simulations are carried out to obtain the simulation object (output). Then, the data set of dimensions and simulation object values are used in surrogate modelling. There are many modelling methods, e.g., polynomial regression [53]-[54], Artificial neural network (ANN) [55]-[56], and Gaussian process regression (GPR) [57].

### 2.4.3 Optimisation Algorithms in SAO

The optimisation of microwave components can be seen as a minimization problem, which is formulated as [45]

$$\boldsymbol{x}^* = \arg\min_{x} F\big(\boldsymbol{y}(\boldsymbol{x})\big) \tag{2.1}$$

where $\boldsymbol{y}(\boldsymbol{x})$ represents an output simulation response vector of the EM model with a vector of input design variables $\boldsymbol{x} = [x_1, x_2, \dots, x_d]^{\mathrm{T}}$. $F(\cdot)$ is the objective function based on simple manipulations of the $\boldsymbol{y}(\boldsymbol{x})$value. $\boldsymbol{x}^*$ denotes the optimal design. The optimisation algorithm is the method to search for the optimal design satisfying the design specification. There are local optimisation-based methods [50]-[56] and global optimisation-based methods [57]-[61].

The local algorithms are suitable for searching for an optimal solution with a specific region with a linear characteristic. Due to its limited exploration ability, the searching method is easily trapped into local optima if the optimisation landscape (determined by the optimisation objective function) is multimodal (local optimal solutions exist around the global optimal solution). Fig. 2.6 illustrates the characteristic landscape of an Ackley function [62], which has a globally optimal solution around with multiple locally optimal

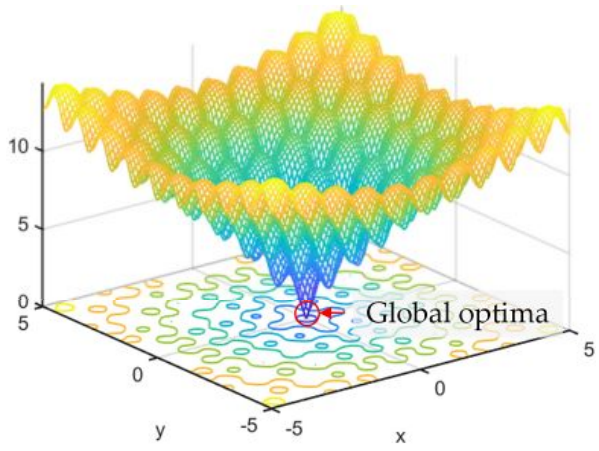



Fig. 2.6. The Ackley function [62].

solutions. Owing to the characteristics of the local optimizer, optimisation procedures are often employed in EM optimisation, such as space mapping technique [51]-[52], port tuning method [50], and step tuning method [46].

The global optimisation methods have a relatively powerful exploration ability to search the global optimal solution in a multimodal landscape independent of a good starting point. However, it has a problem with the speed of convergence. There are multiple types of global optimisation methods, e.g., evolutionary algorithms [63] and swarm intelligence [64]. These optimisation methods are computational intelligence methods that are inspired by the natural phenomenon. In the following sub-sections, some widely used optimisation methods are introduced. They are also utilized in the following Chapters.

### 2.4.3.1 Trust Region Optimisation

The trust-region method is a widely used local optimizer in engineering optimisation

[65]-[66]. It has been employed in this thesis. The trust region method iteratively produces a sequence of approximate solutions to $\boldsymbol{x}^*$ within a neighbourhood of $\boldsymbol{x}^\tau$, where $\tau$ denotes the number of iterations.

$$\boldsymbol{x}^{\tau+1} = \arg\min_{x\in\Omega^\tau} F\big(\boldsymbol{G}^\tau(\boldsymbol{x})\big) \tag{2.2}$$

where $\Omega^\tau$ is the neighbourhood of $\boldsymbol{x}^\tau$ defined as

$$\Omega^\tau = \{\boldsymbol{x} \in \mathbb{R}^d | \boldsymbol{x}^\tau_{c.l} - \Delta^\tau_l \le \boldsymbol{x}^\tau_{c.l} \le \boldsymbol{x}^\tau_{c.l} + \Delta^\tau_l\} \tag{2.3}$$

where $\boldsymbol{x}^\tau_{c.l}$ is the centre of the trust-region in $\tau$th iteration. $\Delta^\tau_l$ is the trust-region radius of $l$th variable ($l$ = 1,2,…, $d$) in $\tau$th iteration. $\boldsymbol{G}^\tau(\boldsymbol{x})$ is an approximation of $\boldsymbol{y}(\boldsymbol{x})$ in $\Omega^\tau$. Here, a first-order Taylar expansion of $\boldsymbol{y}(\boldsymbol{x})$ at $\boldsymbol{x}^\tau$ is used:

$$\boldsymbol{G}^{\tau+1}(\boldsymbol{x}) = \boldsymbol{y}(\boldsymbol{x}^\tau) + \boldsymbol{J}_y(\boldsymbol{x}^\tau)(\boldsymbol{x} - \boldsymbol{x}^\tau) \tag{2.4}$$

where $\boldsymbol{J}_y$ is the Jacobian of $\boldsymbol{y}$ obtained by the finite difference method. Starting from a predefined initial solution and a trust region radius, the trust region method works as follows:

*Step 1:* Set the updating trust-region radius $\Delta^{\tau+1}_l = \Delta^\tau_l$.

*Step 2:* Solve

$$\boldsymbol{x}^{tmp} = \arg\min_{x\in\Omega^\tau} F\big(\boldsymbol{G}^\tau(\boldsymbol{x})\big) \tag{2.5}$$

*Step 3:* Calculate the ratio $\rho$,

$$\rho = \frac{F\big(\boldsymbol{y}(\boldsymbol{x}^{tmp})\big) - F\big(\boldsymbol{y}(\boldsymbol{x}^{\tau})\big)}{F\big(\boldsymbol{G}^{\tau}(\boldsymbol{x}^{tmp})\big) - F\big(\boldsymbol{G}^{\tau}(\boldsymbol{x}^{\tau})\big)} \tag{2.6}$$

*Step 4:* Update the trust-region radius based on the ratio $\rho$ as

$$\Delta^{\tau+1} = \begin{cases} 2\Delta_l^{\tau} & \rho > 0.75 \\ \Delta_l^{\tau} & 0.25 < \rho < 0.75 \\ \Delta_l^{\tau}/3 & \rho < 0.25 \end{cases} \tag{2.7}$$

*Step 5:* Return $\boldsymbol{x}^{\tau+1} = \boldsymbol{x}^{tmp}$. Then, update $\tau = \tau + 1$ and go to step 1.

The stopping criterion includes either of the following two: (1) $\|x^{\tau} - x^{\tau-1}\| \leq \varepsilon$, where $\varepsilon$ is a predefined threshold ($10^{-4}$ is used in this research) or (2) the design specifications are satisfied.

### 2.4.3.2 Sequence Quadratic Program (SQP)

SQP is a popular local optimizer for constrained nonlinear continuous problems [67]-[68] and it is widely employed in this thesis. It is briefed in the following.

In each iteration of the SQP method, the constrained optimisation problem is modelled as a quadratic programming problem. The Lagrangian function for this problem is

$$L(\boldsymbol{x}, \lambda_1, \dots, \lambda_m) = F(\boldsymbol{x}) + \sum_{i=1}^{m} \lambda_i^T c_i(\boldsymbol{x}) \tag{2.8}$$

where $F(\boldsymbol{x})$ is the objective function, $c_i(\boldsymbol{x}), i = 1, 2, \dots, m$ are the constraints. $\lambda_1, \dots, \lambda_m$ are

the Lagrange multipliers. In the *i*th iteration of (2.8), the quadratic programming (QP) problem is defined as

$$\min_{\boldsymbol{x}} \nabla F(\boldsymbol{x}_t)^T \cdot S_t + \frac{1}{2} S_t^T \nabla^2 (L_t) \cdot S_t$$

$$s.t. \nabla c_i(x_t)^T S_t + c_i(x_t) \leq 0, i = 1, 2, ..., m. \tag{2.9}$$

where $S_t$ is the solution to the QP problem. The next iteration will be

$$\boldsymbol{x}_{t+1} = x_t + a_t \cdot S_t \tag{2.10}$$

where $a_t$ is the step length obtained by a line search method.

### 2.4.3.3 Differential Evolution (DE) Method

This thesis also adopts the differential evolution (DE) method [69]-[70] in the optimisation-based synthesis method and EM optimisation method for the diplexers and multiplexers. The DE is an effective global optimisation method in the engineering optimisation area. DE is an iterative optimisation method. Each iteration contains mutation, crossover, and selection to search for the optimal solution. The mutation is a strategy to generate a population of mutation vectors. The crossover is performed to the generated mutation vectors to generate a new population. Then, the section will be employed to select the parameter with the better objective value among the old and new populations. The workflow of DE is introduced in the following.

*Step 1*: Initialization of the population *P*. The population is a data set of *Np D*-dimensional design parameter vectors with the corresponding objective function values. The *i*th vector in the *t*th iteration can be described as $\boldsymbol{x}^i(t) = [x_1^i, x_2^i, \dots, x_D^i]$, *D* is the number of the parameters. The population is generated based on simulations of the design parameter vector within a specific range. For example, the initial parameter of the *m*th parameter of the *i*th vector is

$$x_m^i(0) = rand_m(0,1) \cdot (UB_m - LB_m) + LB_m \tag{2.11}$$

where $rand_m(0,1)$ denotes a uniformly distributed random number with the range $(0,1)$. $UB_m$ and $LB_m$ are the upper and lower bound of the *m*th parameter in the *i*th vector.

*Step 2*: *Mutation.* Once the population is initialized, the mutation will be performed to generate the mutation vectors. There are various mutation strategies. The most widely used one is DE/rand/1 [49]. In the *t*th iteration, the *i*th mutation vector can be represented as

$$\boldsymbol{v}(t+1) = \boldsymbol{x}^{r1}(t) + C \cdot \left(\boldsymbol{x}^{r2}(t) - \boldsymbol{x}^{r3}(t)\right) \tag{2.12}$$

where $\boldsymbol{x}^{r1}$, $\boldsymbol{x}^{r2}$, and $\boldsymbol{x}^{r3}$ are three different design parameter vectors randomly selected from the current population. $\boldsymbol{v}^i$ is the *i*th mutation vector. $C \in (0,2]$ is a scaling factor.

*Step 3: Crossover.* The generated mutation vector population will be performed by the crossover parameter to generate a new population or child population *U*. It has two steps:

1) Randomly select an index number $j_{rand} \in \{1, \dots, D\}$.

2) For each index *j*, a uniformly distributed random number is generated within (0,1). Then, the new population will be

$$\boldsymbol{u}_j(t+1) = \begin{cases} \boldsymbol{v}_j(t+1), & if\ (rand \le CR)\ or\ j = j_{rand} \\ \boldsymbol{x}_j(t), & otherwise \end{cases} \tag{2.13}$$

where $CR \in [0,1]$ is a constant called crossover rate.

Step 4: Selection. If one vector $\boldsymbol{u}_j$ has an equal or better objective function value than that of the vector $\boldsymbol{x}_j$, then it will replace the target vector in the next iteration, namely,

$$\boldsymbol{x}(t+1) = \begin{cases} \boldsymbol{u}(t+1) & if\ F\big(\boldsymbol{u}(t+1)\big) < F\big(\boldsymbol{x}(t)\big) \\ \boldsymbol{x}(t), & otherwise \end{cases} \tag{2.14}$$

The above process will not stop until the stop criterion or design specification is satisfied.

## 2.4.4 Objective Functions

The objective function used in the optimisation problem often has an impact on the effectiveness of the optimisation. For filtering components, the objective function in the optimisation can be various. The reported objective functions in the literature are summarised.

### 2.4.4.1 S-parameter Magnitude

The most widely used objective function is formulated based on S-parameter magnitude [63]. For instance, the objective function can be defined as

$$F_1 = (\max[S_{11}(PB)] - RL) \tag{2.15}$$

where $PB$ is the passband range of the filter. $RL$ is the desired return loss for the filter.

#### 2.4.4.2 Feature Points

Some reported works utilized the feature zeros in the filter responses as the objective function [72]-[75]. Based on the filter theory, the S-parameter responses can be mathematically represented as rational polynomials. The roots of the rational polynomials are the reflection zeros (RZs) and transmission zeros (TZs) in the filtering responses. These feature zeros can characterize the filter responses. Therefore, they can be formulated as the objective function. Some curve fitting methods, e.g., Cauchy Method and vector fitting method, are utilized to approximate the simulation curve of the filters. Then, the feature zeros are extracted from the fitted polynomials. Since only several discrete frequency points are set as the optimisation object, the optimisation would be more efficient. However, accurate extraction of the feature zeros is difficult if the initial responses are not very good, when the curve fitting algorithm may not recognize the polynomial very well. As an example, an objective function for a microwave filter can be defined as

$$F_2 = \sum_{i=1}^{n} |S_{11}(f_{RZi})| + \sum_{i=1}^{n_{tz}} |S_{21}(f_{TZi})| + \sum_{i=1}^{2} (|S_{11}(f_{BEi})| - \varepsilon) \tag{2.16}$$

where $n$ is the number of resonators in the filter. $f_{RZi}$ denotes the frequency of $i$th RZ. $n_{tz}$ is

the number of transmission zeros. $f_{TZi}$ denotes the frequency of the *i*th transmission zeros. $f_{BEi}$ denotes two band edges of the passband. $\varepsilon$ represent the maximum magnitude value of the return loss (e.g., 0.1).

#### 2.4.4.3 Coupling Matrix Extraction Method

A new objective function was recently proposed based on the distance between the extracted coupling matrix (CM) of a candidate design and the ideal CM [76]-[77]. This objective function shows improved linearity and smoothness of the design landscape. This method has been implemented in CST Filter Designer 3D. However, the main challenge is that the CM extraction method has a low success rate if a candidate design shows poor response, or when the orders of the channel filters are high.

## 2.5 Fabrication Technologies for Waveguide Components

With the requirement of an increasingly complex and changeable electromagnetic (EM) environment, modern advanced radio communication systems require high-performance and multi-functional microwave/millimetre-wave devices. In these radio communication systems, especially radio frequency front-end transceiver systems, traditional microwave/millimetre-wave passive waveguide device has advantages such as large power capacity and low RF loss [78]. Compared with planar microwave transmission systems (such as microstrip line devices and coplanar waveguides), these air-filled metal waveguide devices play an important role in applications requiring low dispersion and low RF loss [79].

### 2.5.1 Computerised Numerically Controlled (CNC) Milling Technology

Waveguide devices with complex RF functions often have complex three-dimensional (3-D) physical structures [80]. The devices are usually split into multiple parts for processing by using traditional machining technology (e.g., computerised numerically controlled (CNC) metal milling and electrical discharge machining (EDM)) which increase the occupation and weight of parts for the assembly, i.e., screws and flanges. Some 3D structures with special shapes (such as spherical surfaces or hollow structures) are difficult to be achieved. Those factors will large processing/assembly errors, high processing costs, and restriction of component design creativity. In addition, for waveguides operating at the high-frequency end of millimetre waves (such as over W-band (90 GHz)), traditional machining with very-high precision will be very expensive and high alignment accuracy is required to make sure the contact between the multiple splitting parts [79]. In addition, traditional all-metal waveguide devices are heavy with redundant junctions. They cannot fulfil the requirement of compactness and lightweight in many applications such as airborne, shipborne, aerospace, etc.

### 2.5.2 Micro-fabrication Technologies

For the waveguide component applications with high-dimensional accuracy and good surface quality, some micro-fabrication techniques also have been explored in recent years. The most concerning techniques include silicon deep reactive ion etching (DRIE), LIGA-

based thick resist electroplating, and SU-8 layered process [80]. The abovementioned techniques employ multiple silicon or polymer layers to construct waveguides. The process requires etching and metallization layer by layer, then the layers have to be assembled with very high accuracy to form the waveguide devices. The accuracy of these techniques requires very high and therefore they are suitable for the device with small feature dimensions which can be appliable for the manufacturing of millimetre devices up to WR-15 band. Relatively, the cost of micro-processing technologies is even higher, the process is complex and requires a long fabrication period. Multiple steps required for these fabrication routines are processed by a professional technician in a cleanroom. Moreover, intrinsic limitations with respect to the material and fabrication types and tolerance restrict the designs of the components.

### 2.5.3 3D Printing Technologies

In recent years, the development of 3-D printing technology offers a fresh choice for lightweight and monolithic fabrication of the microwave and millimetre-wave waveguide components [80]-[83]. 3-D printing, also well-known as additive manufacturing, is the general term grouping a variety of manufacturing processes. With computer control, three-dimensional models are built through the continuously stacking of raw materials. This process technique is the opposite process of the traditional “subtractive manufacturing". Although there are various 3-D printing approaches with various materials can be implemented, their forming mechanism is quite the same. Generally, a 3-D structure is first

"sliced" into finite layers (whose thickness is often determined by the resolution of the printer, normally several tens to hundreds micron or even higher) by software. Then, the structure will be formed layer by layer by various approaches. There are seven approaches according to the International Organization for standardization (ISO/ASTM 52900:2015) [83]: material extrusion, vat photopolymerization, powder bed fusion, material jetting, binder jetting, sheet lamination, and directed energy deposition. There is a broad range of materials that can be utilized in 3-D printing such as metal, plastic, organic material, or even food. Here, we only discuss the material for our microwave waveguide components. Therefore, a simple division is based on the material used for fabrication, namely metal printing, and non-metal printing. In the following, characteristics of some frequently used 3-D printing techniques with their material main used are introduced.

*Powder bed fusion (PBF) technology* uses a heat source, i.e., high-power laser and electron beams, to selectively fuse the powder particles layer by layer forming a solid structure. The exemplary techniques are selective laser sintering (SLS) and selective laser melting (SLM) for metal 3-D printing.

*Material Extrusion 3-D printing technology* forms the 3-D structures based on a continuous filament of a thermoplastic material. During the printing process, the filament is steadily moving into a heated printer extruder head. Then, the molten filament of material is forced out and deposited on a printing platform. The 3-D model is also formed layer by layer. The most used technique is fused deposition modelling (FDM). As stated above, the

technique is commonly used for plastic printing.

*Photopolymerization 3-D printing technology* selectively cures liquid photopolymer layer by layer by a heat source to form a 3-D object. The commonly used material is photosensitive resin, and the heat source is ultraviolet (UV) laser. Typical technologies have Stereolithography (SLA) and Digital Light Processing (DLP).

Compared with the traditional CNC milling process, the most significant advantage is that the fabrication cost in theory is only related to the volume of the printed object (raw material consumption) while independent of the geometrical complexity of the object. Therefore, fabrication costs can be greatly reduced. This makes the 3-D printing technology particularly suitable for complicated and precise structures. In recent years, 3-D printing techniques have been reported in various areas with significant practical values, e.g., mechanical manufacture [85], biology and medical area [86], and electronic communications fields [87]. In the research area of microwave/millimetre-wave circuits and systems, traditional waveguide or cavity devices usually fully employ metals materials, i.e., copper and alumina. If various non-metal materials with much lower densities are employed, e.g., photosensitive resin, plastic, nylon, and ceramics, the weight of the object with exact save structure can reduce more than half. This is of significance for modern communication systems, especially for satellite communication systems.

Compared with micro-processing techniques, the advantages of 3-D printing can be found in the following aspects. 1) 3-D printing fully employs metals to be fabricated. It is

more suitable for scenarios where higher thermal stability of the devices is required. 2) 3-D printing is more flexible than 3-D structure does not have severe constraints in depth and height. Therefore, they do not have to split the devices into several layers and re-assemble, which also reduces the losses. 3) It is more cost-effectively while modification needs to be introduced into the design. The size order from small to large can be effectively and simultaneously fabricated in one piece.

It is worth noting that not all 3-D printing technology can be used for microwave/millimetre-wave devices. Furthermore, the device operating at different frequency bands should adopt appropriate 3-D printing techniques. In the literature, 3-D printing techniques available for the microwave/millimetre wave components mainly have 4 types. 1) metalloid printing with surface metallization. 2) directly metallic printing with several post-processing processes, e.g., surface polishing. 3) dielectric material printing of complex structures, such as Lens antenna. 4) 3-D printed substrate and planar structures with coating or printing conductive material to form transmission lines or antennas.

## 2.6 Summary of this Chapter

This chapter reviewed the state-of-the-art research works of the microwave diplexers and multiplexers regarding the configurations, synthesis method, physical dimensioning method, EM optimisation methods, and micro-fabrication techniques. The advantages and disadvantages of the current techniques are concluded by the literature review. These have inspired the following works in this thesis.

# Reference


[1] R. J. Cameron, M. Yu, "Design of manifold-coupled multiplexers", *IEEE microwave magazine*, vol. 8, no. 5, pp: 46-59, Nov. 2007.

[2] G. Macchiarella and S. Tamiazzo, "Synthesis of Star-Junction Multiplexers," *IEEE Transactions on Microwave Theory and Techniques*, vol. 58, no. 12, pp. 3732-3741, Dec. 2010.

[3] G. Macchiarella, "Synthesis of Star-Junction Multiplexers," *IEEE Microwave Magazine*, vol. 12, no. 6, pp. 101-109, Oct. 2011.

[4] G. Macchiarella and S. Tamiazzo, "Novel approach to the synthesis of microwave duplexers," *IEEE Transactions on Microwave Theory and Techniques*, vol. 54, no.12, pp. 4281–4290, Dec. 2006.

[5] G. Macchiarella and S. Tamiazzo, "Design of triplexer combiners for base stations of mobile communications," *IEEE MTT-S Int. Microw. Symp. Dig.*, Anheim, CA, May. 2010, pp. 429–432.

[6] P. Zhao and K. Wu, "An Iterative and Analytical Approach to Optimal Synthesis of a Multiplexer With a Star-Junction," in IEEE Transactions on Microwave Theory and Techniques, vol. 62, no. 12, pp. 3362-3369, Dec. 2014.

[7] R. V. Snyder, A. Mortazawi, I. Hunter, S. Bastioli, G. Macchiarella and K. Wu, "Present and Future Trends in Filters and Multiplexers," in IEEE Transactions on Microwave Theory and Techniques, vol. 63, no. 10, pp. 3324-3360, Oct. 2015.

[8] X. Shang, Y. Wang, W. Xia, and M. J. Lancaster, "Novel Multiplexer Topologies Based on All-Resonator Structures," *IEEE Transactions on Microwave Theory and Techniques*, vol. 61, no. 11, pp. 3838-3845, Nov. 2013.

[9] T. Skaik, M. Lancaster, M. Ke, and Y. Wang, "A micromachined WR-3 band waveguide diplexer based on coupled resonator structures," *2011 41st European Microwave Conference*, 2011, pp. 770-773.

[10] Y. Wu, Y. Wang and E. A. Ogbodo, "Microstrip wideband diplexer with narrow guard band based on all-resonator structures," *2016 46th European Microwave Conference* (EuMC), London, 2016, pp. 1163-1166.

[11] R. Wang, J. Xu, M.-Y. Wang, and Y.-L. Dong, "Synthesis of microwave resonator diplexers using linear frequency transformation and optimisation," *Progress In Electromagnetics Research*, vol. 124, pp. 441-456, 2012.

[12] I. Llamas-Garro, F. Mira, P. Zheng, Z. Liu, L. Wu, and Y. Wang, "All-resonator based LTCC diplexer using substrate-integrated-waveguides," *Electronics Letters*, vol. 53, no. 21, pp. 1410-1412, 2017.

[13] W. Xia, X. Shang and M. J. Lancaster, "All-resonator-based waveguide diplexer with cross-couplings," *Electronics Letters*, vol. 50, no. 25, pp. 1948-1950, Dec. 2014.

[14] S. Tamiazzo and G. Macchiarella, “Synthesis of Duplexers With the Common Port Matched at All Frequencies,” in IEEE Transactions on Microwave Theory and Techniques, vol. 62, no. 1, pp. 46-54, Jan. 2014.

[15] G. Macchiarella and S. Tamiazzo, "Generation of canonical forms for multiport filtering networks," 2014 IEEE MTT-S International Microwave Symposium (IMS2014), 2014, pp. 1-3.

[16] T. F. Skaik, M. J. Lancaster, and F. Huang, “Synthesis of multiple output coupled resonator circuits using coupling matrix optimisation,” *IET Microwaves, Antennas & Propagation*, vol. 5, no. 9, pp. 1081-1088, 2011.

[17] B. Liu, H. Yang, and M. J. Lancaster, "Synthesis of coupling matrix for diplexers based on a self-Adaptive differential evolution algorithm," IEEE Transactions on Microwave Theory and Techniques, vol. 66, no. 2, pp. 813-821, 2018.

[18] G. Macchiarella and S. Tamiazzo, "Polynomial design of manifold multiplexers," 2011 IEEE MTT-S International Microwave Symposium, 2011, pp. 1-4.

[19] David Cañete Rebenaque, Giuseppe Macchiarella, "Application of polynomial design of multiplexers to the implementation of a manifold microstrip triplexer", International Journal of RF and Microwave Computer-Aided Engineering, vol. 23, pp. 690, 2013.

[20] Yong-Liang Zhang, “Direct Matrix Synthesis for in-Line Diplexers with Transmission Zeros Generated by Frequency Variant Couplings,” Progress In Electromagnetics Research Letters, Vol. 78, 45-52, 2018.

[21] Y. Yang, Q. Wu, X. Yin and M. Yu, "Singly terminated network and contiguous multiplexer design," 2018 IEEE/MTT-S International Microwave Symposium - IMS, 2018, pp. 1234-1237.

[22] J. Hong and M. J. Lancaster, *Microstrip filters for RF/microwave applications*. John Wiley & Sons; 2004.

[23] R. J. Cameron, C. M. Kudsia, and R. R. Mansour, “Design and physical realization of coupled resonator filters,” *Microwave filters for communication systems: fundamentals, design, and applications*, Wiley, 2018, pp.457-484, ch14.

[24] D. G. Swanson, “Narrow-band microwave filter design,” *IEEE Microwave Magazine*, vol. 8, no. 5, pp. 105-114, Oct. 2007.

[25] A. R. Harish and J. S. K. Raj, "A direct method to compute the coupling between nonidentical microwave cavities," *IEEE Transactions on Microwave Theory and Techniques*, vol. 52, no. 12, pp. 2645-2650, Dec. 2004.

[26] D. Swanson, G. Macchiarella, "Microwave filter design by synthesis and optimisation", *IEEE Microwave Magazine*, vol. 8, no. 2, pp. 55-69, 2007.

[27] M. Caenepeel, F. Seyfert, Y. Rolain and M. Olivi, "Parametric modelling of the coupling parameters of planar coupled-resonator microwave filters," *2015 European Microwave Conference (EuMC)*, Paris, France, 2015, pp. 538-541.

[28] M. Caenepeel, F. Ferranti and Y. Rolain, “Efficient and automated generation of multidimensional design curves for coupled-resonator filters using system identification and

metamodels," 2016 13th International Conference on Synthesis, Modelling, Analysis and Simulation Methods and Applications to Circuit Design (SMACD), 2016, pp. 1-4.

[29] L. Balewski, A. Lamecki, and M. Mrozowski, "Multivariate models of inter-resonator couplings and their application in filter design," in XXVIIIth General Assembly of International Union of Radio Science (URSI), October 2005.

[30] L. Balewski and M. Mrozowski, "Applications of Surrogate Models in Synthesis of Microwave Bandpass Filters," EUROCON 2007 - The International Conference on "Computer as a Tool", 2007, pp. 98-101.

[31] A. E. Atia, "Computer-aided design of waveguide multiplexer (short papers)", IEEE Transactions on Microwave Theory and Techniques, vol. 22, no.3, pp: 332-336, 1974.

[32] R. G. Egri, A. E. Williams, and A. E. Atia, "A contiguous-band multiplexer design", IEEE MTT-S International Microwave Symposium Digest, pp. 86-88, 1983.

[33] J. D. Rhodes and R. Levy, "Design of General Manifold Multiplexers", IEEE Transactions on Microwave Theory and Techniques, vol. 27, no.2, pp: 111-123, 1979.

[34] S. Cogollos, P. Soto, V. E. Boria, et al., "Efficient design of waveguide manifold multiplexers based on low-order EM distributed models", IEEE Transactions on Microwave Theory and Techniques, vol. 63, no. 8, pp: 2540-2549, 2015.

[35] L. Accatino, and M. Mongiardo, "Hybrid circuit-full-wave computer-aided design of a manifold multiplexers without tuning elements." IEEE Transactions on Microwave Theory and Techniques, vol. 50, no. 9, pp: 2044-2047, 2002.

[36] Y. Wang, S. Li, and M. Yu, "Hybrid Models for Effective Design and Optimisation of Large-Scale Multiplexing Networks", IEEE Transactions on Microwave Theory and Techniques, vol. 61, no. 5, pp: 1839-1849, 2013.

[37] A. Morini, T. Rozzi, and M. Morelli, "New formulae for the initial design in the optimisation of T-junction manifold multiplexers", MTT-S International Microwave Symposium Digest IEEE, vol. 2, 1997.

[38] J. R. Montejo-Garai, J. A. Ruiz-Cruz and J. M. Rebollar, "Full-wave design of H-plane contiguous manifold output multiplexers using the fictitious reactive load concept," in IEEE Transactions on Microwave Theory and Techniques, vol. 53, no. 8, pp. 2628-2632, Aug. 2005.

[39] M. A. Ismail, et al., "EM-based design of large-scale dielectric-resonator filters and multiplexers by space mapping", IEEE Transactions on Microwave Theory and Techniques, vol. 52, no.1, pp: 386-392, 2004.

[40] M. Yu, and Y. Wang, "Synthesis and Beyond", IEEE Microwave Magazine, vol.12, no.6, pp: 62-76, 2011.

[41] M. A. Ismail, and Ming Yu, "Advanced design of large scale microwave devices for space applications using space mapping optimisation", MTT-S International Microwave Symposium (IMS), IEEE, 2017.

[42] S. Cogollos, et al., “Efficient design of waveguide manifold multiplexers based on low-order EM distributed models”, IEEE Transactions on Microwave Theory and Techniques, vol. 63, no.8, pp: 2540-2549, 2015.

[43] Nazmul Siddique and Hojjat Adeli, Computational intelligence: synergies of fuzzy logic, neural networks and evolutionary computing, John Wiley & Sons, 2013.

[44] J. E. Rayas-Sánchez, S. Koziel and J. W. Bandler, “Advanced RF and Microwave Design Optimisation: A Journey and a Vision of Future Trends,” in IEEE Journal of Microwaves, vol. 1, no. 1, pp. 481-493, winter 2021.

[45] S. Koziel, X. S. Yang, and Q. J. Zhang, Simulation-driven Design Optimisation and Modelling for Microwave Engineering. London, U.K.: Imperial College Press, 2013.

[46] J.T. Alos and M. Guglielmi, “Simple and effective EM-based optimisation procedure for microwave filters,” IEEE Trans. Microwave Theory Tech., vol. 45, pp. 856-858, Jun. 1997.

[47] S. Bila et al., "Direct electromagnetic optimisation of microwave filters," in IEEE Microwave Magazine, vol. 2, no. 1, pp. 46-51, March 2001.

[48] U. Effing and I. Wolff, “A new approach to the optimisation of microwave structures on the basis of a FTDT method,” in Proc. 1998 IEEE MTT Symp., Baltimore, MD, June 1998, pp. 1787-1790.

[49] D. Baillargeat, S. Verdeyme, M. Aubourg, and P. Guillon, “CAD applying the finite element method for dielectric resonator filters,” IEEE Trans. Microwave Theory Tech., vol. 46, pp. 10-17, Jan. 1998.

[50] D. Swanson and G. Macchiarella, “Microwave filter design by synthesis and optimisation,” in IEEE Microwave Magazine, vol. 8, no. 2, pp. 55-69, April 2007.

[51] J. W. Bandler, R. M. Biernacki, Shao Hua Chen, P. A. Grobelny and R. H. Hemmers, “Space mapping technique for electromagnetic optimisation,” in IEEE Transactions on Microwave Theory and Techniques, vol. 42, no. 12, pp. 2536-2544, Dec. 1994.

[52] J. W. Bandler, R. M. Biernacki, Shao Hua Chen, R. H. Hemmers and K. Madsen, "Electromagnetic optimisation exploiting aggressive space mapping," in IEEE Transactions on Microwave Theory and Techniques, vol. 43, no. 12, pp. 2874-2882, Dec. 1995.

[53] J. L. Chávez-Hurtado and J. E. Rayas-Sánchez, "Polynomial-Based Surrogate Modelling of RF and Microwave Circuits in Frequency Domain Exploiting the Multinomial Theorem," in IEEE Transactions on Microwave Theory and Techniques, vol. 64, no. 12, pp. 4371-4381, Dec. 2016.

[54] J. E. Rayas-Sánchez, J. Aguilar-Torrentera and J. A. Jasso-Urzúa, "Surrogate modelling of microwave circuits using polynomial functional interpolants," 2010 IEEE MTT-S International Microwave Symposium, 2010, pp. 197-200.

[55] J. Jin, C. Zhang, F. Feng, W. Na, J. Ma and Q. Zhang, "Deep Neural Network Technique for High-Dimensional Microwave Modelling and Applications to Parameter Extraction of Microwave Filters," in IEEE Transactions on Microwave Theory and Techniques, vol. 67, no. 10, pp. 4140-4155, Oct. 2019.

[56] F. Feng et al., "Multifeature-Assisted Neuro-transfer Function Surrogate-Based EM Optimisation Exploiting Trust-Region Algorithms for Microwave Filter Design," in IEEE Transactions on Microwave Theory and Techniques, vol. 68, no. 2, pp. 531-542, Feb. 2020.

[57] B. Liu, H. Yang and M. J. Lancaster, "Global Optimisation of Microwave Filters Based on a Surrogate Model-Assisted Evolutionary Algorithm," in IEEE Transactions on Microwave Theory and Techniques, vol. 65, no. 6, pp. 1976-1985, June 2017.

[58] H. M. Torun and M. Swaminathan, "High-Dimensional Global Optimisation Method for High-Frequency Electronic Design," IEEE Transactions on Microwave Theory and Techniques, vol. 67, no. 6, pp. 2128-2142, June 2019.

[59] Y. Wang, Z. Zhang, Y. Yi, Y. Zhang. "Accurate microwave filter design based on particle swarm optimization and one-dimensional convolution autoencoders," Int. J. RF & Microw Comput. Aided Eng., pp: e23034, 2021.

[60] B. Liu, H. Yang and M. J. Lancaster, "Global Optimisation of Microwave Filters Based on a Surrogate Model-Assisted Evolutionary Algorithm," in IEEE Transactions on Microwave Theory and Techniques, vol. 65, no. 6, pp. 1976-1985, June 2017.

[61] N. Damavandi and S. Safavi-Naeini, "A global optimisation method for synthesis of multiple coupled resonator filters," 2002 9th International Symposium on Antenna Technology and Applied Electromagnetics, 2002, pp. 1-4.

[62] N. Damavandi and S. Safavi-Naeini, "A hybrid evolutionary programming method for circuit optimisation," in IEEE Transactions on Circuits and Systems I: Regular Papers, vol. 52, no. 5, pp. 902-910, May 2005.

[63] D. Ackley, *A connectionist machine for genetic hillclimbing.* Vol. 28. Springer Science & Business Media, 2012.

[64] A. E. Eiben and J. E. Smith, "What Is an Evolutionary Algorithm?", in Membrane Computing, Membrane Computing, 2015, pp. 25–48.

[65] J. Kennedy, "Swarm Intelligence", Handbook of nature-inspired and innovative computing, Springer, Boston, MA, 2006, pp. 187–219.

[66] A. R. Conn, N. I. M. Gould, and P. L. Toint, "Trust region methods," in MPS-SIAM Series on Optimisation. Philadelphia, PA, USA: SIAM, 2000.

[67] S. Koziel and A. Bekasiewicz, "Fast EM-Driven Size Reduction of Antenna Structures by Means of Adjoint Sensitivities and Trust Regions," in IEEE Antennas and Wireless Propagation Letters, vol. 14, pp. 1681-1684, 2015.

[68] P. T. Boggs and J. W. Tolle, "Sequential quadratic programming," Acta numerica, vol. 4, pp. 1-51, 1995.

[69] S. Wright and J. Nocedal, Numerical optimisation, Springer Science, vol. 35, no. 67-68, p. 7,1999.

[70] M. Emmerich, K. Giannakoglou, and B. Naujoks, "Single-and multi- objective evolutionary optimisation assisted by Gaussian random field metamodels," Evolutionary Computation, IEEE Transactions on, vol. 10, no. 4, pp. 421–439, 2006.

[71] K. Price, R. Storn, and J. Lampinen, Differential evolution: a practical approach to global optimisation. Springer-Verlag New York Inc, 2005.

[72] J. W. Bandler, R. M. Biernacki, Shao Hua Chen, D. G. Swanson and Shen Ye, "Microstrip filter design using direct EM field simulation," in IEEE Transactions on Microwave Theory and Techniques, vol. 42, no. 7, pp. 1353-1359, July 1994.

[73] S. Tao, H.H. Tung, K.A. Zaki, A.E. Atia, and T.G. Dolan, "Full-wave design of canonical waveguide filters by optimisation," IEEE Trans. Microwave Theory Tech., vol. 51, no. 2, pp. 504–511, Feb. 2003.

[74] A. Garcia-Lamperez, S. Llorente-Romano, M. Salazar-Palma and T. K. Sarkar, "Efficient electromagnetic optimisation of microwave filters and multiplexers using rational models," in IEEE Transactions on Microwave Theory and Techniques, vol. 52, no. 2, pp. 508-521, Feb. 2004.

[75] F. Feng et al., "Multifeature-Assisted Neuro-transfer Function Surrogate-Based EM Optimisation Exploiting Trust-Region Algorithms for Microwave Filter Design," in IEEE Transactions on Microwave Theory and Techniques, vol. 68, no. 2, pp. 531-542, Feb. 2020.

[76] F. Feng, C. Zhang, W. Na, J. Zhang, W. Zhang and Q. Zhang, "Adaptive Feature Zero Assisted Surrogate-Based EM Optimisation for Microwave Filter Design," in IEEE Microwave and Wireless Components Letters, vol. 29, no. 1, pp. 2-4, Jan. 2019.

[77] M. Sharifi Sorkherizi and A. A. Kishk, "Use of Group Delay of Sub-Circuits in Optimisation of Wideband Large-Scale Bandpass Filters and Diplexers," in IEEE Transactions on Microwave Theory and Techniques, vol. 65, no. 8, pp. 2893-2905, Aug. 2017.

[78] X. Wang, Y. Zhang, G. Shen, W. Che, H. Chen, and W. Feng, "Automated optimisation of multiplexers based on aggressive space mapping and cauchy method," 2015 International Workshop on Electromagnetics: Applications and Student Innovation Competition (iWEM), Hsinchu, 2015, pp. 1-4.

[79] D. M. Pozar, Microwave Engineering, Hoboken, NJ, USA:Wiley, 2005.

[80] I. Stil, A. L. Fontana, B. Lefranc, A. Navarrini, P. Serres, and K. F. Schuster, "Loss of WR10 waveguide across 70–116 GHz," in Proc. 22nd Int. Symp. Space Terahertz Technol., Apr. 2012, pp. 1–3.

[81] X. Shang, P. Penchev, C. Guo, M. J. Lancaster, S. Dimov, Y. Dong, M. Favre, M. Billod, E. de Rijk, "*W* -Band Waveguide Filters Fabricated by Laser Micromachining and 3-D Printing," IEEE Transactions on Microwave Theory and Techniques, vol. 64, no. 8, pp. 2572-2580, Aug. 2016.

[82] B. Zhang, Y. Guo, H. Zirath and Y. P. Zhang, "Investigation on 3-D-Printing Technologies for Millimetre- Wave and Terahertz Applications," Proceedings of the IEEE, vol. 105, no. 4, pp. 723-736, April 2017.

[83] O. A. Peverini et al., "Selective Laser Melting Manufacturing of Microwave Waveguide Devices," in Proceedings of the IEEE, vol. 105, no. 4, pp. 620-631, April 2017.

[84] C. Tomassoni, O. A. Peverini, G. Venanzoni, G. Addamo, F. Paonessa and G. Virone, "3D Printing of Microwave and Millimetre-Wave Filters: Additive Manufacturing Technologies Applied in the Development of High-Performance Filters with Novel Topologies," in IEEE Microwave Magazine, vol. 21, no. 6, pp. 24-45, June 2020.

[85] R. V. Snyder, G. Macchiarella, S. Bastioli and C. Tomassoni, "Emerging Trends in Techniques and Technology as Applied to Filter Design," in IEEE Journal of Microwaves, vol. 1, no. 1, pp. 317-344, winter 2021.

[86] M. Symes, P. Kitson, J. Yan, et al., "Integrated 3D-printed reactionware for chemical synthesis and analysis." Nature Chem., vol. 4, pp. 349-354. 2012.

[87] L. Ouyang, "3D Bioprinting and Bioink: Background", in Kinetically Controlled Stepwise Syntheses of a Heterometallic Complex and a Tetrahedral Chiral-at-Metal Complex, Kinetically Controlled Stepwise Syntheses of a Heterometallic Complex and a Tetrahedral Chiral-at-Metal Complex, 2019, pp. 7–23.

[88] Y. L. Kong, I. A. Tamargo, H. Kim, B. N. Johnson, M. K. Gupta, T.-W. Koh, H.-A. Chin, D. A. Steingart, B. P. Rand, and M. C. Mcalpine, "3D Printed Quantum Dot Light-Emitting Diodes", Nano Letters, vol. 14, no. 12, pp. 7017–7023, 2014.

# Chapter 3 Theoretical Background

In the last chapter, the state-of-the-art of microwave diplexers and multiplexers are briefly reviewed. The diplexers and multiplexers are resonator-coupled filtering networks. The coupling matrix technique is widely utilized in the synthesis and design process for these resonator-coupled structures. The theory for the resonator-coupled network is laid down in this chapter. It starts from the filter concept and then extends to diplexers and multiplexers.

## 3.1 Filter Network and Polynomials

### 3.1.1 General Characteristics for Filter Network

A microwave filter is a two-port network that can be characterised by a scattering parameter (S-parameter) [1]. The S-parameter is used to analyze and measure the state of a microwave network. Fig. 3.1 shows a two-port network with the source and load impedances of $Z_S$ and $Z_L$. $a$ and $b$ represent the voltage waves incident at and propagating

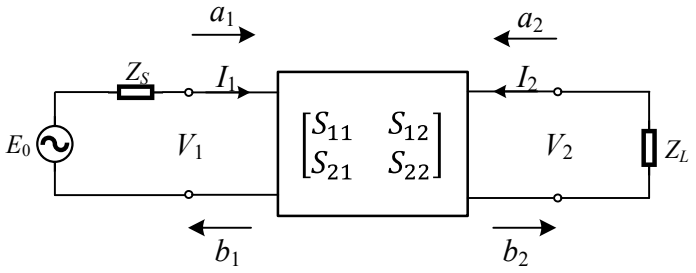



Fig. 3.1. A two-port network

away from the source port and load port (ports 1 and 2), respectively. The S-parameter matrix is represented by a block matrix [1],

$$\begin{bmatrix} b_1 \\ b_2 \end{bmatrix} = \begin{bmatrix} S_{11} & S_{12} \\ S_{21} & S_{22} \end{bmatrix} \cdot \begin{bmatrix} a_1 \\ a_2 \end{bmatrix} \tag{3.1}$$

Given that the network is passive, lossless, and reciprocal, the S-parameter fulfil conservation of energy equations [2], namely

$$S_{11}(s)S_{11}(s)^* + S_{21}(s)S_{21}(s)^* = 1, \tag{3.2}$$

$$S_{22}(s)S_{22}(s)^* + S_{12}(s)S_{12}(s)^* = 1, \tag{3.3}$$

and a unique orthogonality equation

$$S_{11}(s)S_{12}(s)^* + S_{21}(s)S_{22}(\mathrm{s})^* = 1, \tag{3.4}$$

where the *S*-parameters are assumed to be functions of $s$ $(s = \sigma + j\omega)$, the frequency variable. The asterisk in the terms of S-parameter denotes the conjugates of the corresponding parameter. Insertion loss (*IL*) and return loss (*RL*) measured in dB are defined by the reflection coefficient $S_{11}$ and the transmission coefficient $S_{21}$,

$$IL = -20\log_{10}(|S_{21}|), \tag{3.5}$$

$$RL = -20\log_{10}(|S_{11}|). \tag{3.6}$$

Mathematically, the reflection coefficient $S_{11}$ and transmission coefficient $S_{21}$ can be

expressed by two rational polynomials [2]. Assume that $N$ resonators comprise the two-port network, the $S_{11}(s)$ at port 1 is expressed as

$$S_{11}(s) = \frac{F(s)/\varepsilon_R}{E(s)} \tag{3.7}$$

where Both $E(s)$ and $F(s)$ are $N$-th degree polynomials with complex coefficients. Constant $\varepsilon_R$ normalizes the highest-degree coefficients of $E(s)$ and $F(s)$ to unity. Since it is a lossless passive network, $E(s)$ is strictly Hurwitz, namely all the roots of $E(s)$ (poles of $S_{11}(s)$) are in the left half of the complex plane. The poles are not symmetric about the real axis. Substitute the (3.7) into (3.2), a relation is found by

$$S_{21}(s)S_{21}(s)^* = 1 - \frac{F(s)F(s)^*}{\varepsilon_R^2 E(s)E(s)^*} = \frac{P(s)P(s)^*}{\varepsilon^2 E(s)E(s)^*}, \tag{3.8}$$

Then, the transfer parameter $S_{21}(s)$ is expressed as

$$S_{21}(s) = \frac{P(s)/\varepsilon}{E(s)} \tag{3.9}$$

where $P(s)P(s)^*/\varepsilon^2 = E(s)E(s)^* - F(s)F(s)^*/\varepsilon_R^2$ . $\varepsilon$ is constant which normalizes the $S_{21}(s)$ to the equal-ripple level at $s = \pm j$. For a Chebyshev filter, it is called a ripple constant expressed as

$$\varepsilon = \frac{1}{\sqrt{10^{RL/10} - 1}} \left| \frac{P(s)}{F(s)} \right|_{s=\pm j} \tag{3.10}$$

where *RL* is the prescribed passband return loss in dB. To this moment, the highest-degree

coefficients of polynomials $E(s), F(s)$ and $P(s)$ are all normalized to unity. The $E(s), F(s)$ and $P(s)$ are the polynomials composed of reflection poles (RPs), reflection zeros (RZs) and transmission zeros (TZs), respectively. Both $E(s)$ and $F(s)$ are $N$-th degree polynomials. $P(s) = \prod_{n=1}^{n_{fz}}(s - s_n)$ is of degree $n_{fz}$ which is the number of finite transmission zeros. When there are no finite-position zeros ($n_{fz} = 0$), the filtering function is known as an "all-pole" response. Since the number of the transmission zeros is incorporated in the transmission parameters, it is evident that $n_{fz} < N$. Otherwise, the $S_{21}$ will be larger than unity ($s \to \infty$), which is impossible for the passive networks [2]. The relation between the two normalization factors is,

$$\varepsilon_R = \begin{cases} 1 & n_{fz} < N \\ \dfrac{\varepsilon}{\sqrt{\varepsilon^2 - 1}} & n_{fz} = N \end{cases} \tag{3.11}$$

According to the conservation of energy equation (3.4), a relationship is obtained,

$$\varepsilon^2 \varepsilon_R^2 E(s)E(s)^* = \varepsilon_R^2 P(s)P(s)^* + \varepsilon^2 F(s)F(s)^* \tag{3.12}$$

With this relationship, any one of the polynomials can be determined when the other two are known. Then, the S-parameter can be accordingly obtained.

### 3.1.2 Filter Polynomial Synthesis

For simplicity, in $\omega$-plane and a two-port lossless network, the transmission response is related to the Chebyshev filtering function. It is derived by

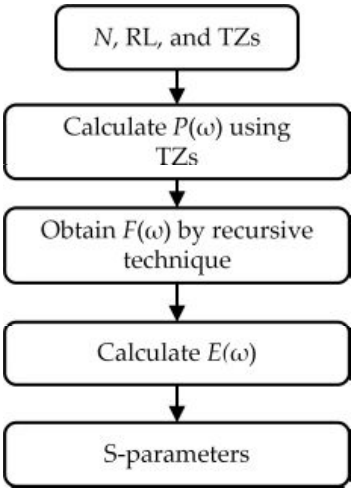



Fig. 3.2 The flowchart of the polynomial synthesis.

$$S_{21}(\omega)S_{21}(\omega)^* = \frac{P(\omega)P(\omega)^*}{\varepsilon^2 E(\omega)E(\omega)^*} = \frac{\varepsilon_R^2 P(\omega)P(\omega)^*}{[\varepsilon_R P(\omega) - j\varepsilon F(\omega)][\varepsilon_R P(\omega) + j\varepsilon F(\omega)]}$$
$$= \frac{1}{\left[1 - j\frac{\varepsilon}{\varepsilon_R}C_N(\omega)\right]\left[1 + j\frac{\varepsilon}{\varepsilon_R}C_N(\omega)\right]} = \frac{1}{1 + \frac{\varepsilon^2}{\varepsilon_R^2}C_N^2(\omega)}, \tag{3.13}$$

namely,

$$|S_{21}(\omega)|^2 = \frac{1}{1 + \frac{\varepsilon^2}{\varepsilon_R^2}C_N^2(\omega)}, \tag{3.14}$$

where $C_N(\omega) = F(\omega)/P(\omega)$ is known as the $N$th order filtering characteristic function. In this case, the poles and zeros of $C_N(\omega)$ are the roots of $P(\omega)$ and $F(\omega)$, respectively. To realize a Chebyshev filtering function, $C_N$ is defined as

$$C_N(\omega) = cosh\left[\sum_{n=1}^{N} cosh^{-1}\big(\chi_n(\omega)\big)\right], \chi_n(\omega) = \frac{\omega - 1/\omega_n}{1 - \omega/\omega_n} \tag{3.15}$$

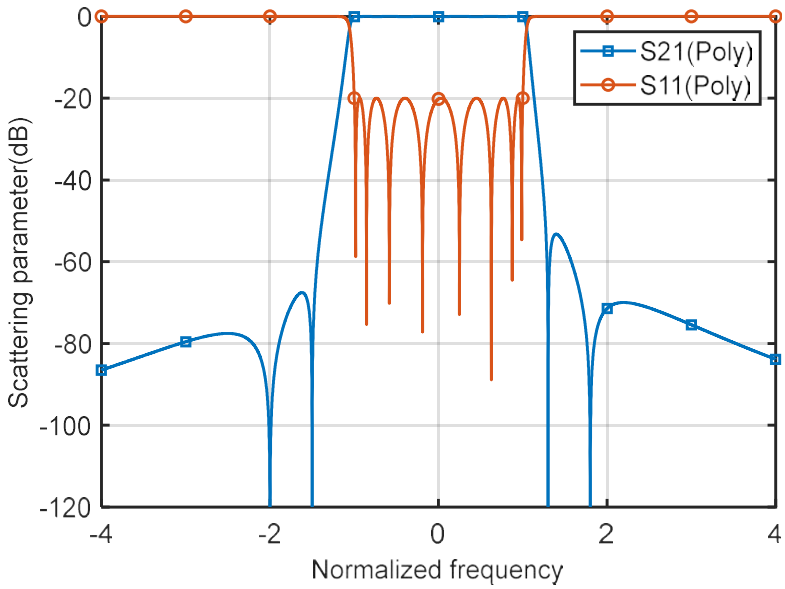



Fig. 3.3. The polynomial responses of the 8th order Chebyshev filter.

Table 3.1 The polynomial coefficients for the 8th order Chebyshev filter.

| Order | $P(s)$ | $F(s)$ | $E(s)$ |
|---|---|---|---|
| 0 | 0.0000 + 7.0200j | 0.0125 + 0.0000j | 0.1572 - 0.0347j |
| 1 | -1.1100 + 0.0000j | 0.0000 - 0.0172j | 0.7998 - 0.1519j |
| 2 | 0.0000 + 5.5100j | 0.3262 + 0.0000j | 2.1835 - 0.3482j |
| 3 | -0.4000 + 0.0000j | 0.0000 - 0.1218j | 3.9394 - 0.5461j |
| 4 | 0.0000 + 1.0000j | 1.4432 + 0.0000j | 5.4051 - 0.5913j |
| 5 | | 0.0000 - 0.2261j | 5.2809 - 0.5080j |
| 6 | | 2.1250 + 0.0000j | 4.3362 - 0.2632j |
| 7 | | 0.0000 - 0.1228j | 2.1030 - 0.1228j |
| 8 | | 1.0000 + 0.0000j | 1.0000 + 0.0000j |

where $j\omega_n$ is the position of the $n$th TZ in the complex frequency plane.

The polynomial $P(\omega)$ is calculated by using prescribed finite transmission zeros. The $F(\omega)$ is obtained by a recursive technique [2]. Then, polynomial $E(\omega)$ is obtained based on the polynomial relationship equation (3.12). The synthesis workflow is shown in Fig. 3.2.

The detailed deviation of the recursive technique is elaborated in Appendix A of this thesis.

Assume that an 8th order Chebyshev filter with four transmission zeros at −2j, −1.5j, 1.3j, and 1.8j has a return loss of 20 dB. The polynomial of the filter is synthesized based on the approach mentioned above. The calculated polynomial responses are illustrated in Fig. 3.3. The normalized coefficients of polynomial $P(s)$, $F(s)$, and $E(s)$ are listed in Table 3.1. The feature points, including TZs, RZs and RPs of the filter are listed in Table 3.1.

## 3.2 Circuit Representation of Resonator-coupled Filter

### 3.2.1 Lowpass Prototype Lumped Circuits

Despite various physical realizations of microwave filters, a resonator-coupled microwave filter can be equivalent to an electrical circuit with different basic elements: 1) Frequency-dependent elements, i.e., lumped capacitors and inductors. They form the resonators in the filter. 2) Frequency-independent elements, i.e., reactance and susceptance. They are employed to offset the resonators to be asynchronously tuned in the filter. 3) Coupling inverters. They are used for coupling elements.

With the elements mentioned above, the filter with any type of response can be realized. Fundamentally, an *n*-th order low-pass all-pole lumped filter with the ladder topologies is shown in Fig. 3.4. Each circuit is formed by resistors, capacitors, and inductors. The values of the elements are termed as "$g$ parameters". The filter order $N$ equals the number of inductors and capacitors.

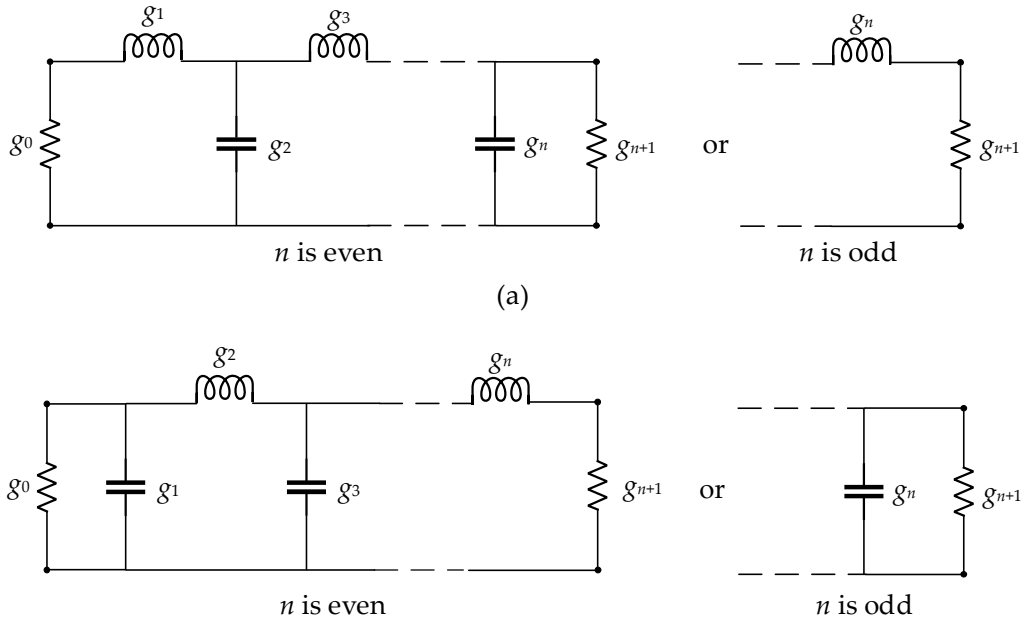



Fig. 3.4. The $n$-th order low-pass all-pole lumped filter. (a) Leading component is a series inductor; (b) Leading component is shunt capacitor.

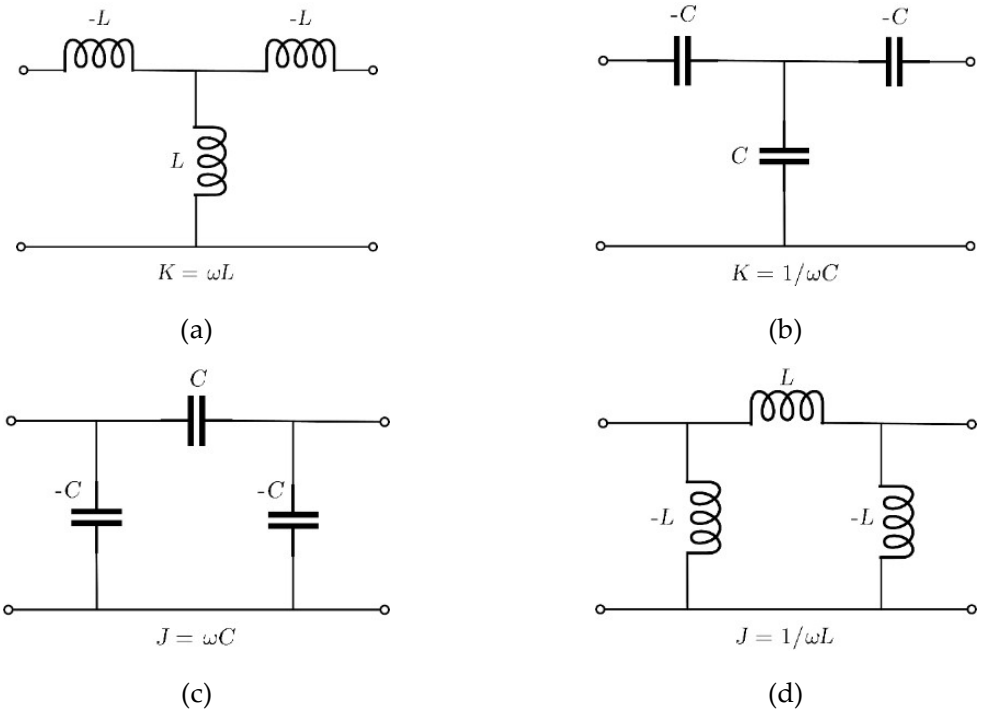
For a filter with a standard filtering function, e.g., Chebyshev, Butterworth, and Elliptic, the $g$ parameters can be calculated directly for the lumped circuit in Fig. 3.4. Assume that the lowpass prototype filter has a Chebyshev response with a passband return loss $RL$ and cut-off frequency $\Omega_C = 1$. The $g$ parameters are calculated by the following formulas.

$$
\begin{aligned}
g_0 &= 1 \\
g_1 &= \frac{2}{\gamma}\sin\left(\frac{\pi}{2n}\right) \\
g_i &= \frac{1}{g_{i-1}}\frac{4\sin\left(\frac{(2i-1)\pi}{2n}\right)\sin\left(\frac{(2i-3)\pi}{2n}\right)}{\gamma^2+\sin^2\left(\frac{(i-1)\pi}{n}\right)} \quad (i = 2 \text{ to } n) \\
g_{n+1} &= \begin{cases} 1 & n \text{ is odd} \\ \coth^2\left(\frac{\beta}{4}\right) & n \text{ is even} \end{cases}
\end{aligned}
\tag{3.16}
$$




(a) (b)

Fig. 3.5. Two-port networks of *K* and *J* inverters. (a) *K* inverter; (b) *J* inverter.




(a) (b)

(c) (d)

Fig. 3.6. The equivalent lump circuits of *K* and *J* inverters. (a) Equivalent *K* inverter using inductors; (b) Equivalent *K* inverter using capacitors; (c) Equivalent *J* inverter using capacitors; (d) Equivalent *J* inverter using inductors.

where $\beta = \ln[\coth(RL/17.37)]$ , $\gamma = \sinh(\beta/2n)$.

### 3.2.2 Immittance Inverters

Two types of immittance inverters called *K* inverter and *J* inverter, are added to the two-port networks. As shown in Fig. 3.5, they are frequency invariant two-port network

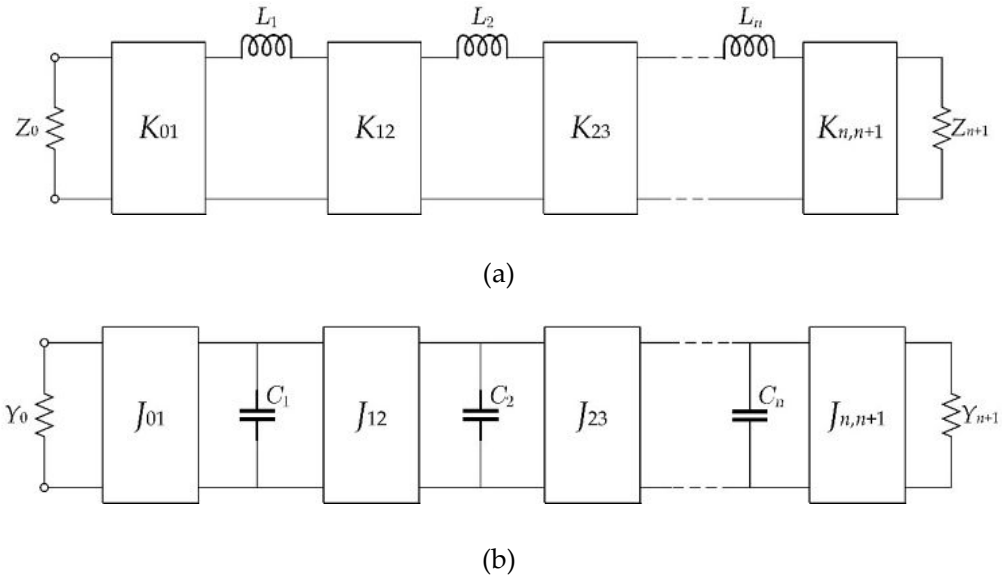



Fig. 3.7. Lowpass prototype filter formed by (a) *K* inverters and (b) *J* inverters.

converting their corresponding input immittances, given by,

$$Z_b = \frac{K^2}{Z_a}, \qquad Y_b = \frac{J^2}{Y_a} \tag{3.17}$$

where *K* and *J* are both real and defined as impedance and admittance of their network. The equivalent lumped circuits are illustrated in Fig. 3.6.

Applying the inverters, in the two-port network shown in Fig. 3.4, series (shunt) components are transformed to shunt (series) components as shown in Fig. 3.7. It can be seen that the filter can be realized by using one type of component, namely inductors or capacitors by adding the immittance inverters to the ladder circuit. It makes the filter realization feasible for different filter topologies.

With the equation (3.17), the *K* inverters in Fig. 3.4(a) are calculated by

$$K_{01} = \sqrt{\frac{Z_0 L_1}{g_0 g_1}}, K_{n,n+1} = \sqrt{\frac{L_n Z_{n+1}}{g_n g_{n+1}}},$$

$$K_{i,i+1} = \sqrt{\frac{L_i L_{i+1}}{g_i g_{i+1}}}, (i = 1 \; to \; n-1) \tag{3.18}$$

Also, the *J* inverters in Fig. 3.5(b) are obtained by

$$J_{01} = \sqrt{\frac{Y_0 C_1}{g_0 g_1}}, K_{n,n+1} = \sqrt{\frac{C_n Y_{n+1}}{g_n g_{n+1}}},$$

$$J_{i,i+1} = \sqrt{\frac{L_i L_{i+1}}{g_i g_{i+1}}}, (i = 1 \; to \; n-1) \tag{3.19}$$

### 3.2.3 Frequency Transformation

Filter design normally starts from a lowpass prototype filter operating from the normalized frequency range of −1 to 1. This is because a lowpass filter can be theoretically transformed into a band-pass filter operating at any frequencies with any bandwidths. This process is also known as a denormalization process. This process is illustrated in Fig. 3.8, where the Ω is the normalized frequency range (lowpass) and ω is the real frequency range

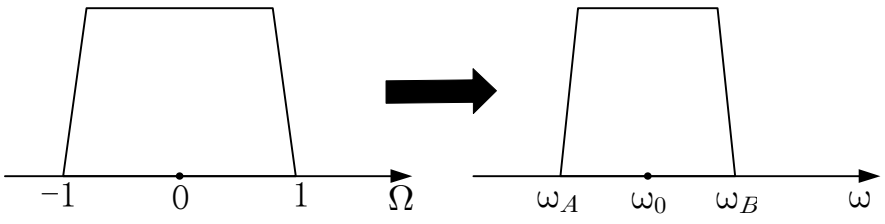



Fig. 3.8. An illustration of frequency transformation from lowpass to bandpass.

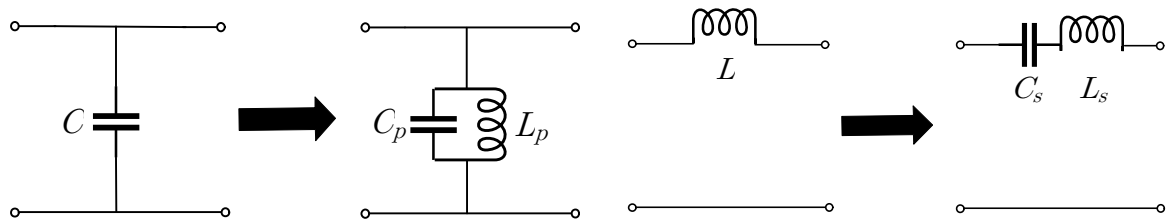



Fig. 3.9. Circuit representation of the frequency transformation for (a) capacitor and (b) inductor.

(bandpass). $\omega_A$ and $\omega_B$ are the passband edges. The frequency transformation is expressed as

$$\Omega = \frac{1}{FBW}\left(\frac{\omega}{\omega_0} - \frac{\omega_0}{\omega}\right) \tag{3.20}$$

where $\omega_0 = \sqrt{\omega_A \omega_B}$ is the centre frequency of the passband filter and $FBW = (\omega_B - \omega_A)/\omega_0$ denotes the fractional bandwidth. Substitute the frequency transformation (3.20) into the series inductor *L* and shunt capacitor *C* in Fig.3.8, they are changed as

$$j\omega \frac{L}{\omega_0 FBW} + \frac{1}{j\omega \frac{FBW}{\omega_0 L}} = j\omega L_s + \frac{1}{j\omega C_s} \tag{3.21}$$

$$j\omega \frac{C}{\omega_0 FBW} + \frac{1}{j\omega \frac{FBW}{\omega_0 C}} = j\omega L_p + \frac{1}{j\omega C_p} \tag{3.22}$$

Then, in the circuit form, the capacitor *C* and inductor *L* are changed as shown in Fig. 3.9. It can be seen that the lowpass circuit is changed into a parallel or series *LC* resonant circuit after frequency transformation. Then, Fig. 3.7 is transformed as shown in Fig. 3.10. Bandpass filters can be realized by various microwave elements, e.g., waveguide resonators.

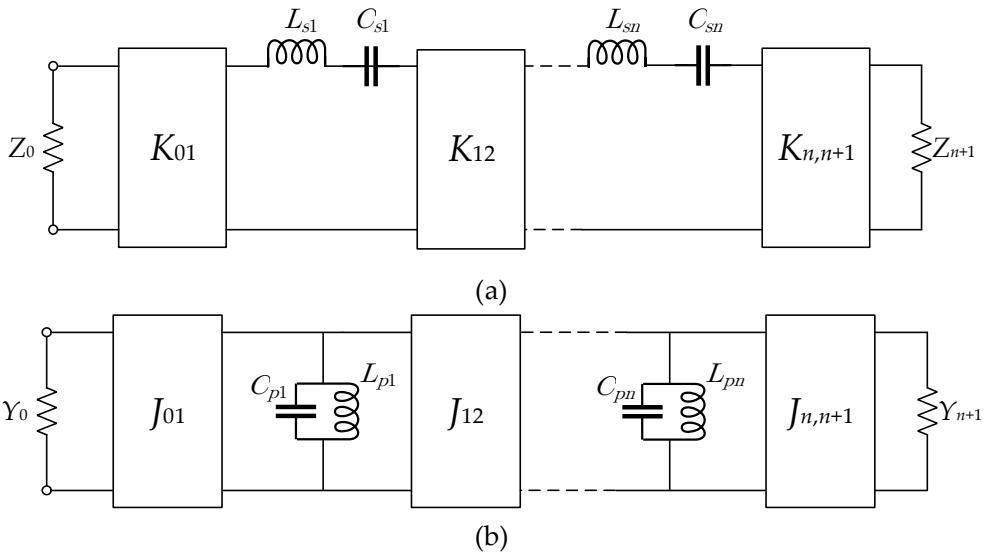



Fig. 3.10. Bandpass prototype filters formed by (a) *K* inverters and (b) *J* inverters.

## 3.3 Coupling Matrix Theory

### 3.3.1 *N*×*N* Coupling Matrix

Formed by coupled resonators, the filter circuits can be represented by a matrix called coupling matrix. Fig. 3.11 shows an *Nth* order resonator-coupled bandpass filter. Given that

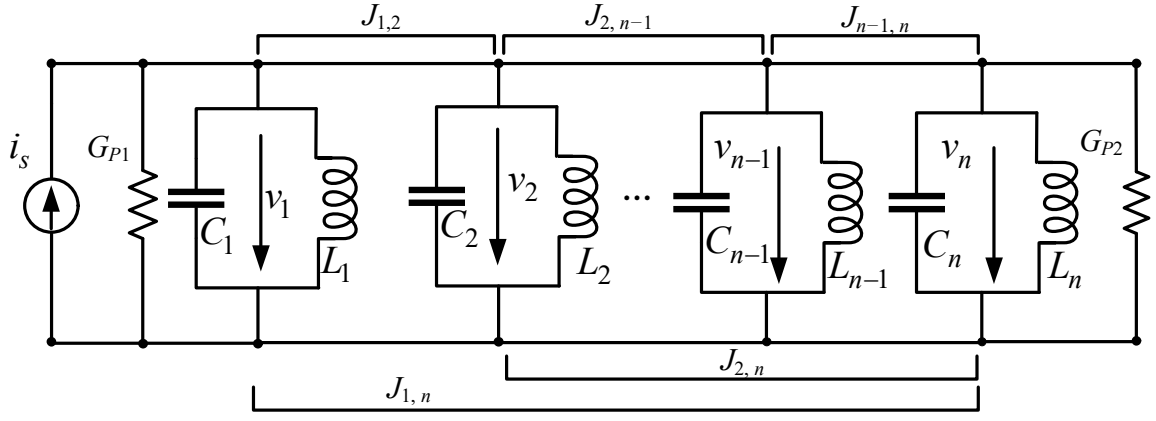



Fig. 3.11. Lumped circuit of an Nth order resonator-coupled bandpass filter.

each resonator has a capacitor of $C = 1$ F and an inductor of $L = 1$ H, the centre frequency is $\omega_0 = 1$ rad/s. $G_{P1} = G_{P2}$ are the source and load conductance. Based on Kirchoff's current law, a set of node equations are written in a matrix form as [1]

$$\begin{bmatrix} j\omega C + \frac{1}{j\omega L} + G_{P1} & -j\omega J_{1,2} & \cdots & -j\omega J_{1,n-1} & -j\omega J_{1,n} \\ -j\omega J_{2,1} & j\omega C + \frac{1}{j\omega L} & \cdots & -j\omega J_{2,n-1} & -j\omega J_{2,n} \\ \vdots & \vdots & \ddots & \vdots & \vdots \\ -j\omega J_{n-1,1} & -j\omega J_{n-1,2} & \cdots & j\omega C + \frac{1}{j\omega L} & -j\omega J_{n-1,n} \\ -j\omega J_{n,1} & -j\omega J_{n,2} & \cdots & -j\omega J_{n,n-1} & j\omega C + \frac{1}{j\omega L} + G_{P2} \end{bmatrix} \begin{bmatrix} v_1 \\ v_2 \\ \vdots \\ v_{n-1} \\ v_n \end{bmatrix} = \begin{bmatrix} i_1 \\ 0 \\ \vdots \\ 0 \\ 0 \end{bmatrix} \quad (3.23)$$

or $[Y][v] = [i]$, where $J_{p,q}$ ($p \neq q$) is the coupling coefficient between the $p$th resonator and $q$th resonator. $[Y]$ is an $N \times N$ admittance matrix. It can be normalized as

$$[Y] = \omega_0 L \bullet FBW[\bar{Y}] \quad (3.24)$$

where *FBW* is the fractional bandwidth of the bandpass filter, defined as

$$FBW = \frac{\Delta f_{3dB}}{f_0} \quad (3.25)$$

where $\Delta f_{3dB}$ and $f_0$ are the 3dB bandwidth and the centre frequency of the bandpass, respectively.

With the observation that the formulation of the normalized admittance matrix $[\bar{Y}]$ and the normalized admittance matrix $[\bar{Z}]$ have the same form [1], then the matrix formulation can be a unified immittance matrix form $[\bar{A}]$ for the resonator-coupled bandpass filters.

$$[\bar{A}] = [q] + p[U] - j[m] \tag{3.26}$$

where $[q]$ is an $N \times N$ matrix with all items zeros, expected for the $q(1,1) = 1/q_{e1}$ and $q(N,N) = 1/q_{en}$. $q_{e1}$ and $q_{en}$ are an external quality factor in the normalized frequency domain. $[m]$ is the normalized coupling matrix which is an $N$th order reciprocal matrix. $[U]$ is an $N \times N$ identity matrix. $p$ is the complex lowpass frequency variable defined by

$$p = j\frac{1}{FBW}\left(\frac{\omega}{\omega_0} - \frac{\omega_0}{\omega}\right) \tag{3.27}$$

It is worth noting that there are two different definitions of the immittance matrix $[A]$. The difference lies in the sign in front of the coupling matrix which originates from the definition of the mutual coupling coefficients of the equivalent circuit representation in (3.23). A negative sign used in this thesis has been defined in Section 8.1 of [1] while a positive sign is defined in Section 8.1.3 of [2]. It has been proved that both of them work but generate different denormalization results.

The S-parameter can be calculated by a general coupling matrix $[A]$.

$$S_{21} = \frac{2}{\sqrt{q_{e1}q_{en}}}[A]^{-1}_{n1} \tag{3.28}$$

$$S_{11} = \pm\left(1 - \frac{2}{\sqrt{q_{e1}q_{en}}}[A]^{-1}_{11}\right) \tag{3.29}$$

The coupling matrix is usually synthesized at the normalized frequency domain. Then, the coupling matrix is transformed to the real frequency. The coupling coefficients for the real

frequency can be obtained by

$$Q_e(i) = \frac{q_e(i)}{FBW}, M(p,q) = m(p,q) \times FBW \tag{3.30}$$

where $Q_e(i)$ and $M(p,q)$ represents the external quality factor and coupling coefficients for the filter in the real frequency domain. The calculation of resonant frequencies derived from self-couplings is different from the equation provided by [3], since a negative sign of the coupling matrix is defined in the immittance matrix. The resonant frequencies of each resonator can be calculated from the self-coupling by,

$$f_i = f_0 \left[ \left( \frac{m(i,i) \times FBW}{2} \right) - \sqrt{1 + \left( \frac{m(i,i) \times FBW}{2} \right)^2} \right] \tag{3.31}$$

The deviation of resonant frequency is detailed in Appendix B.

### 3.3.2 Synthesis of a Bandpass Filter with a Chebyshev Response

The bandpass filter with Chebyshev responses can be synthesized. The coupling coefficients can be directly calculated from the *g* values. The *g* values for Chebyshev in the normalized frequency domain are calculated by using (3.16). Then, the normalized coupling coefficients are calculated by

$$\begin{gathered} q_{e1} = g_0 g_1, q_{en} = g_n g_{n+1} \\ m(i,i+1) = \frac{1}{\sqrt{g_i g_{i+1}}}, \text{for } i = 1 \; to \; n-1 \end{gathered} \tag{3.32}$$

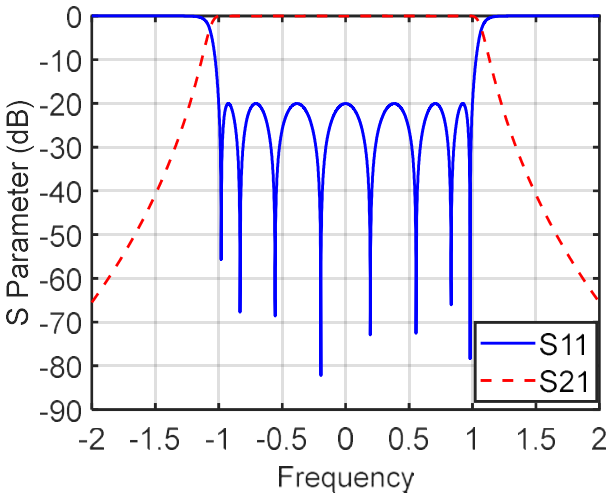



Fig. 3.12. The calculated S-parameter responses of the 10th order bandpass filter with Chebyshev responses.

Then, the S-parameter can be calculated based on the equation (3.28)-(3.29). Take a 10th order bandpass filter as an example. The return loss of the filter is 20dB. Then, the calculated g values are $g$ = {1, 1.0280, 1.4690, 1.9952, 1.6906, 2.0882, 1.7102, 2.0642, 1.6341, 1.7936, 0.8420, 1.2210}. Based on the calculations, the coupling coefficients are m(1,2) = m(9,10) = 0.8137, m(2,3) = m(8,9) = 0.5841, m(3,4) = m(7,8) = 0.5445, m(4,5) = m(6,7) = 0.5322, m(5,6) = 0.5292, $q_{e1} = q_{en} = 1.0280$. The calculated S-parameter responses are shown in Fig. 3.12.

### 3.3.3 *N*+*X* Coupling Matrix

The *N*th order resonator-coupled network with *X* (*X*⩾2) ports is shown in Fig. 3.13. To generally describe this network, a more general matrix is extended from the $N \times N$ matrix. Since the ports are parallelly connected, the *N*th order resonator-coupled network with *X* ports can be represented by using lumped circuit form as shown in Fig. 3.14. In this case,

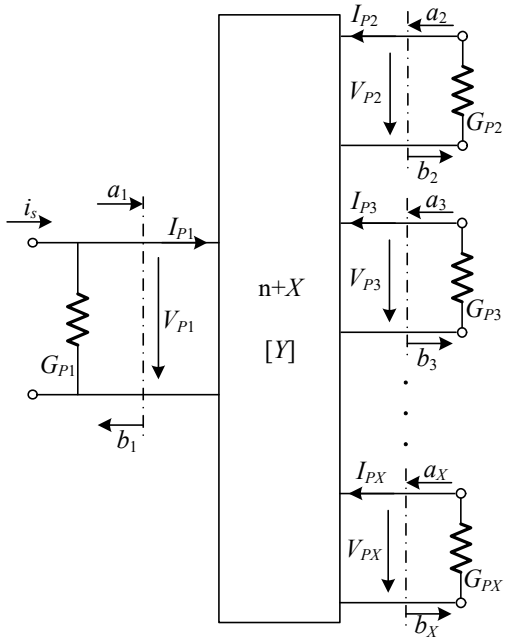



Fig. 3.13. Lumped circuit of an Nth order resonator-coupled network with $X$ ports.

the coupling matrix can be represented as a block matrix form as

$$[m] = \begin{bmatrix} [m_N] & [m_X] \\ [m_X] & [m_{XX}] \end{bmatrix} \tag{3.33}$$

where $[m_N] \in \mathbb{R}^{N\times N}$ is the general $N \times N$ coupling matrix. $[m_X] \in \mathbb{R}^{N\times X}$ is the matrix of the couplings between the ports and resonators (source and load couplings). $[m_{XX}] \in \mathbb{R}^{X\times X}$ is the couplings between ports which is normally a zero matrix. Then, a general normalized coupling matrix for the $N$th order resonator coupled network with multiple ports is given as

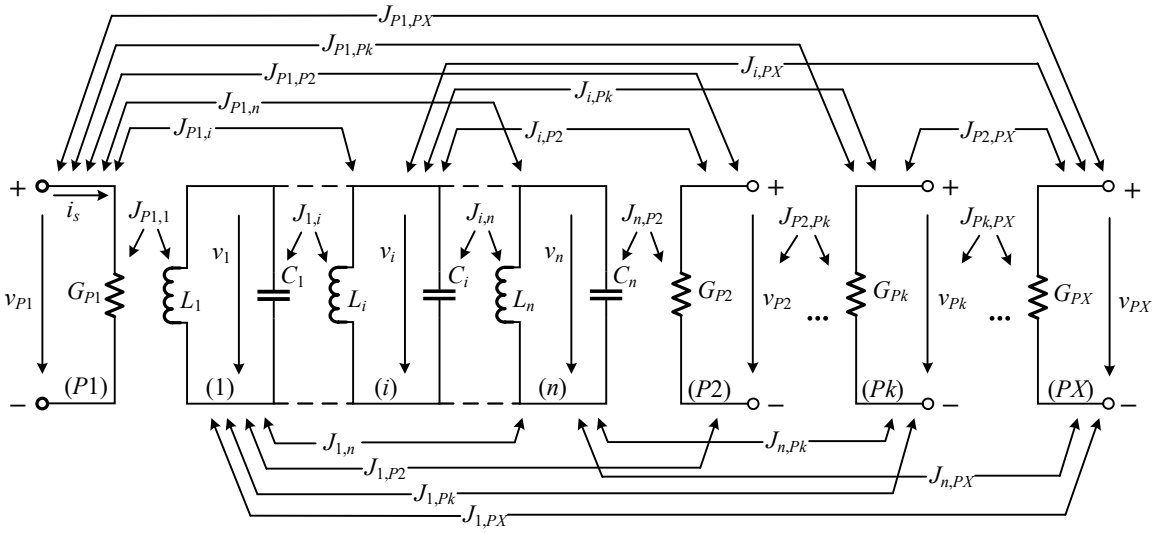



Fig. 3.14 Lumped circuit for the Nth order resonator-coupled network with $X$ ports.

$$[m] = \begin{bmatrix} m(1,1) & m(1,2) & \cdots & m(1,n) & m(1,P1) & \cdots & m(1,PX) \\ m(2,1) & m(2,2) & \cdots & m(2,n) & m(2,P1) & \cdots & m(2,PX) \\ \vdots & \vdots & \ddots & \vdots & \vdots & \ddots & \vdots \\ m(n,1) & m(n,2) & \cdots & m(n,2) & m(n,P1) & \cdots & m(n,PX) \\ m(P1,1) & m(P1,2) & \cdots & m(P1,n) & m(P1,P1) & \cdots & m(P1,PX) \\ \vdots & \vdots & \ddots & \vdots & \vdots & \ddots & \vdots \\ m(PX,1) & m(PX,2) & \cdots & m(PX,n) & m(PX,P1) & \cdots & m(PX,PX) \end{bmatrix}$$

The corresponding normalized immittance matrix $[\bar{A}]$ will be given as the form is similar to Equ. (3.26)

$$\left[\bar{A}\right] = [R] + p[U] - j[m] \tag{3.34}$$

Since port impendence or conductance has been normalized to unity. The $[R]$ and $[U]$ are two block matrices,

$$[U] = \begin{bmatrix} \boldsymbol{u} & \mathbf{0} \\ \mathbf{0} & \mathbf{0} \end{bmatrix}, [R] = \begin{bmatrix} \mathbf{0} & \mathbf{0} \\ \mathbf{0} & \boldsymbol{r} \end{bmatrix} \tag{3.35}$$

where $\boldsymbol{u}$ is an $N \times N$ identity matrix and $\boldsymbol{r}$ is an $X \times X$ identity matrix. The S-parameters of this multi-port network can be calculated as

$$S_{pq}\big|_{p\neq q} = 2[A]^{-1}_{pq} \tag{3.36}$$

$$S_{pp} = \pm(1 - 2[A]^{-1}_{pp}) \tag{3.37}$$

where $S_{pp}$ is the reflection coefficient at the port attached to the $p$th resonator, and $S_{pq}$ is the transmission coefficient between the ports attached to the $p$th and $q$th resonators.

## 3.4 Microwave Filter Design

In this thesis, the diplexers and multiplexers are implemented mainly based on rectangular waveguide technology. The rectangular waveguide, resonator, and filter design based on them are briefly introduced in the following.

### 3.4.1 Rectangular Waveguide

Rectangular waveguide is one of the most used microwave transmission media. The structure of the rectangular waveguide is shown in Fig. 3.15, where $a$ and $b$ are the geometrical dimensions, and $\mu$ and $\varepsilon$ are the permittivity and permeability of the material filled in the guide. EM waves with transverse electric (TE) and transverse magnetic (TM) modes are supported by rectangular waveguides.

Each cutoff frequency of $TE_{mn}$ mode is defined by

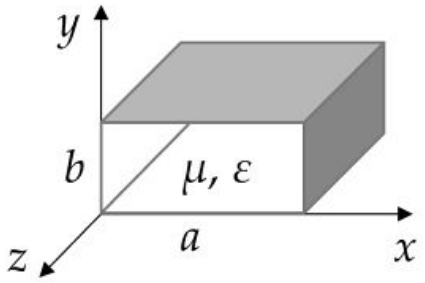



Fig. 3.15. Rectangular waveguide.

$$f_{cmn} = \frac{1}{2\pi\sqrt{\mu\varepsilon}}\sqrt{\left(\frac{m\pi}{a}\right)^2 + \left(\frac{n\pi}{b}\right)^2} \tag{3.38}$$

where $m$ and $n$ are the number of wave variations in $x$ and $y$ directions. The propagation mode with the lowest cutoff frequency is called a dominant mode. For a rectangular waveguide with $a > b$, the dominant mode is TE10 (m=1, n=0) in TE mode whose cutoff frequency is

$$f_{c10} = \frac{1}{2a\sqrt{\mu\varepsilon}} \tag{3.39}$$

The guide wavelength $\lambda_g$ is an important parameter defining the distance between two equal-phase planes along the waveguide. It is defined as

$$\lambda_g = \frac{2\pi}{\beta} \tag{3.40}$$

where $\beta = \sqrt{k^2 - (\pi/a)^2}$ is a propagation constant for TE10 mode, $k = \omega\sqrt{\mu\varepsilon}$ is a wave number.

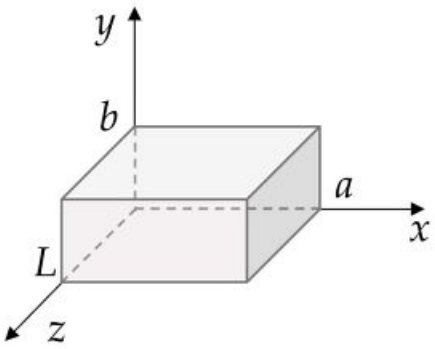



Fig. 3.16. Rectangular waveguide resonator.

## 3.4.2 Rectangular Cavity Resonator

The rectangular resonator is a closed section of a rectangular waveguide shorted at both ends. It appears as a closed box or cavity as shown in Fig. 3.16, where $L$ is the length of the resonator. The resonant frequency of the $TE_{mnl}$ or $TM_{mnl}$ mode is given by

$$f_{mnl} = \frac{c}{2\pi\sqrt{\mu_r \varepsilon_r}} \sqrt{\left(\frac{m\pi}{a}\right)^2 + \left(\frac{n\pi}{b}\right)^2 + \left(\frac{l\pi}{c}\right)^2} \tag{3.41}$$

where $m$, $n$, and $l$ represent the number of variations in $x$, $y$ and $z$ directions, respectively. $c$ = $2.99\times10^8$ m/s is the speed of light. $\mu_r$ and $\varepsilon_r$ are relative permittivity and permeability of the material filled in the resonator. The dominant resonant mode $TE_{101}$ operates at the lowest resonant frequency. Its length is corresponding to the $TE_{10}$ waveguide mode of $\lambda_g/2$.

Another important parameter for resonator is unloaded quality factor $Q_u$ defined as a ratio of stored energy and lost energy at the resonant frequency.

$$Q_u = \omega \frac{average\ energy\ stored}{energy\ loss/second} \tag{3.42}$$

The unloaded quality factor for a rectangular waveguide resonator with lossy conducting and lossless dielectric is defined as

$$Q_c = \frac{(kad)^3 b\eta}{2\pi^2 R_s} \frac{1}{(2l^2a^3b + 2bd^3 + l^2a^3d + ad^3)} \tag{3.43}$$

The unloaded Q of the cavity with a lossy dielectric filling with a perfectly electrical conducting boundary is

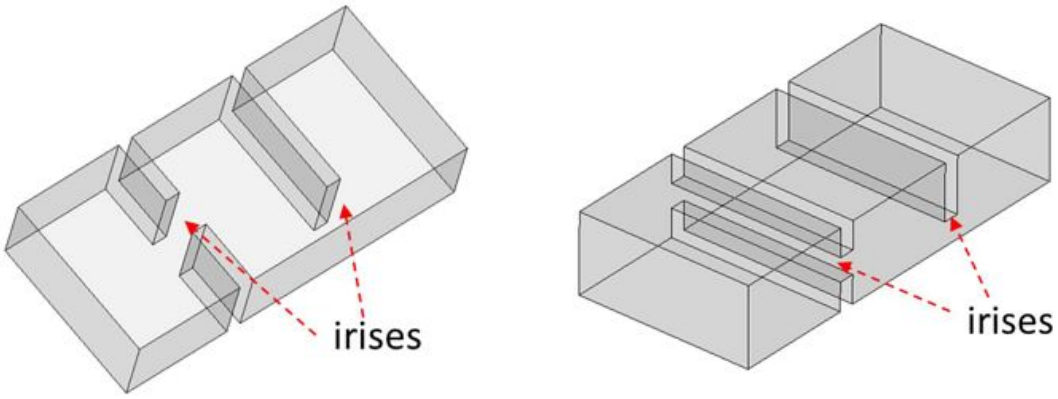
$$Q_d = \frac{1}{tan\,\delta} \tag{3.44}$$

where $\tan\delta$ is loss tangent of the material filling in the resonator. Then, the total unloaded quality factor for the resonator with lossy boundary and lossy dielectric material can be found as

$$Q_u = \left(\frac{1}{Q_c} + \frac{1}{Q_d}\right)^{-1} \tag{3.45}$$

### 3.4.3 Discontinuity between Rectangular Resonators

The rectangular resonators are coupled together via discontinuities, e.g., coupling iris and posts. Coupling iris is a widely utilized type of discontinuities. Some commonly used coupling irises are shown in Fig. 3.17. The vertical slots (Fig. 3.17(a)) are inductive irises while the horizontal slots (Fig. 3.17(b)) are capacitive irises.




(a) (b)

Fig. 3.17 The commonly used coupling irises in the rectangular waveguide. (a) Inductive irises. (b) Capacitive irises.

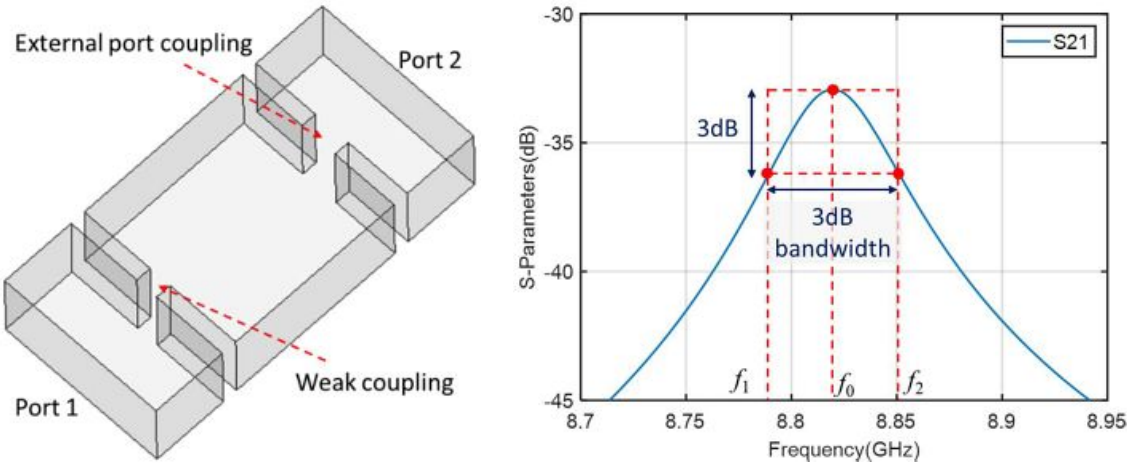
### 3.4.4 External Quality Factor Extraction in Rectangular Waveguide

The external quality factor can be extracted from simulations of a single resonator as shown in Fig. 3.18 (a). The resonator is coupled with one port via external port couplings and a weak coupling with another port. An exemplary simulated $S_{21}$ is shown in Fig. 3.18 (b).

The external quality factor can be calculated by

$$Q_e = \frac{f_0}{BW_{3d}} \tag{3.46}$$

where $f_0$ is the centre frequency resonant frequency. $BW_{3dB}$ is the 3dB bandwidth of the $S_{21}$. Then, by scaling the width of the external port coupling $d$ (mm) with different values and adjusting the resonator length $L$ (mm) to keep the centre frequency unchanged (assuming 9 GHz in this example), different external quality factors can be obtained as shown in Table




(a) (b)

Fig. 3.18. Extraction of external quality factor. (a) The single resonator simulation model. (b) $S_{21}$ responses in dB for simulation of a single resonator.

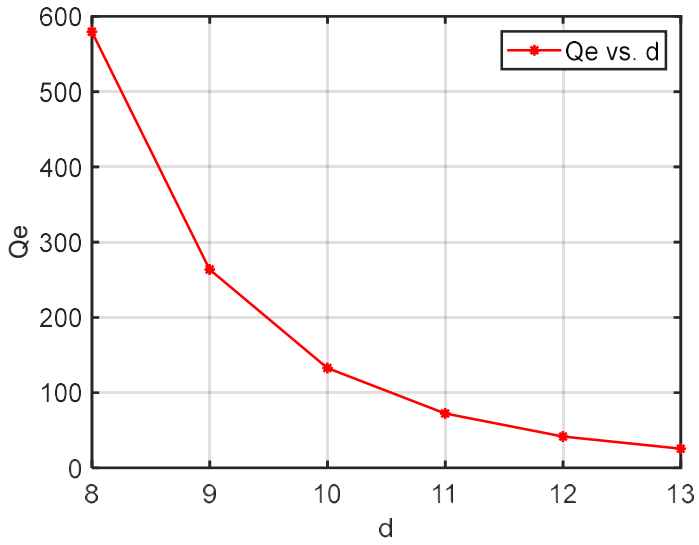



Fig. 3.19. The relationship between iris width *d* and *Qe*.

3.3. A relation curve can be plotted based on the obtained data as shown in Fig. 3.19. With the curve, the coupling dimension corresponding to an external quality factor can be obtained.

Table. 3.3. The Qe values for different coupling iris width at 9 GHz.

| $d$ (mm) | 8 | 9 | 10 | 11 | 12 | 13 |
|---|---|---|---|---|---|---|
| $Qe(10^4)$ | 0.0580 | 0.0264 | 0.0133 | 0.0072 | 0.0042 | 0.0026 |

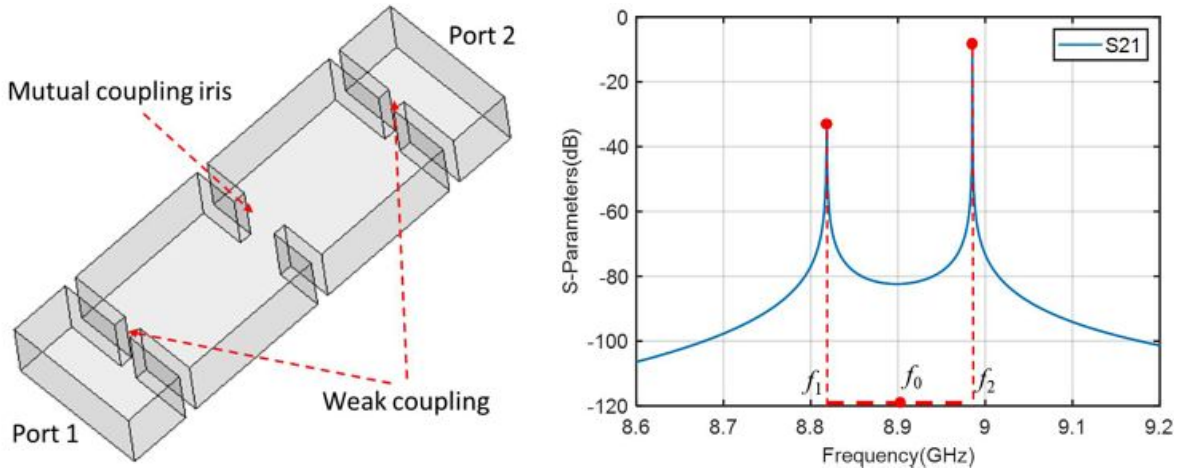
### 3.4.5 Mutual Coupling Extraction between Rectangular Resonators

The mutual coupling between two resonators can also be extracted based on the simulated $S_{21}$ response. The simulation model of two coupled resonators is modelled as shown in Fig. 3.20 (a). An exemplary simulated S21 response is shown in Fig. 3.20 (b).

The mutual coupling can be calculated by

$$k_c = \frac{f_2^2 - f_1^2}{f_2^2 + f_1^2} \tag{3.47}$$

where $f_1$ and $f_2$ are frequency points of two resonant peaks in the $S_{21}$ response. $f_0$ is the centre frequency between $f_1$ and $f_2$. Similarly, scaling the mutual coupling iris $w$ (mm) with different values, and adjusting the resonator length $L$ (mm) to keep the centre frequency




(a) (b)

Fig. 3.20. Extraction of mutual coupling coefficients. (a) The simulation model of the coupled waveguide cavities. (b) S21 responses in dB for simulation of two coupled resonators.

Table 3.4. The mutual coupling values for different coupling iris width at 9 GHz.

| $w$(mm) | 5 | 6 | 7 | 8 | 9 | 10 | 11 | 12 | 13 |
|---|---|---|---|---|---|---|---|---|---|
| $k_c$ | 0.0035 | 0.0072 | 0.0131 | 0.0205 | 0.0291 | 0.0428 | 0.0584 | 0.07788 | 0.09813 |

unchanged (assume 9 GHz), different external quality factors can be obtained as shown in Table 3.4. The relationship between the coupling iris width $w$ and coupling values can be plotted in a curve as shown in Fig. 3.21. For a given coupling value, the physical dimension of the coupling iris can be obtained based on the curve.

With the above two steps, the initial dimensions for the rectangular resonator-coupled bandpass filter can be obtained. Connecting the rectangular resonator, the coupled-resonator filter can be formed. The next step is EM simulation-based optimisation.

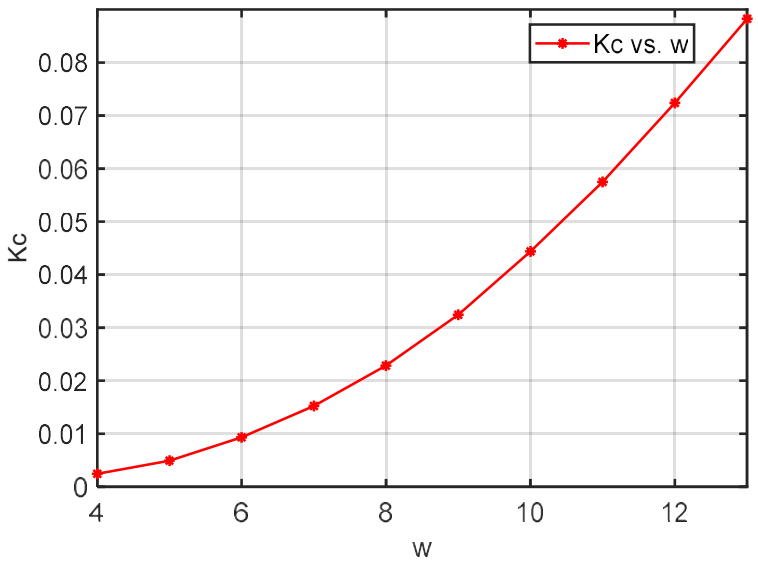



Fig. 3.21. The relationship between mutual coupling iris width $w$ and $k_c$.

### 3.4.6 Example of a 3rd order Filter Design

A specific 3rd order filter is taken as an example to illustrate the abovementioned design process. Assume that the filter operates at the centre frequency of 9GHz with 0.5GHz bandwidth. Maximum S11 within the passband is −20dB. The denormalized coupling coefficients for this filter can be calculated as M(1,2) = M(1,2) = 0.0573, M(3,4) = M(4,3) =

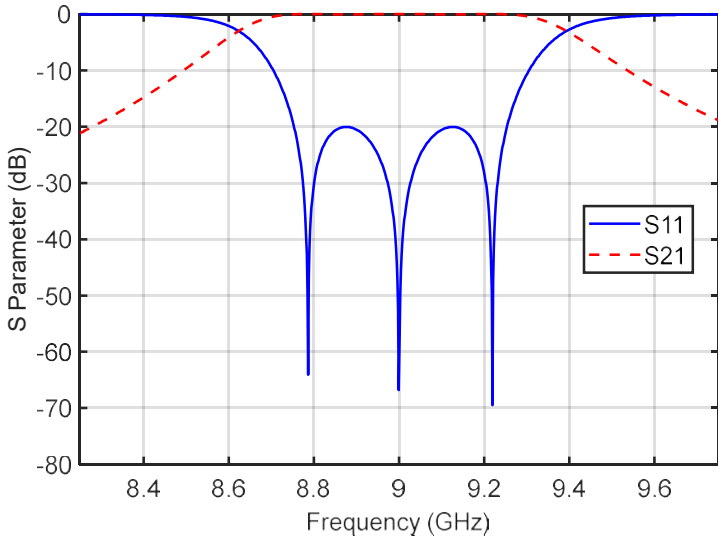



Fig. 3. 22. The calculated S-parameter responses from the denormalized coupling coefficients.

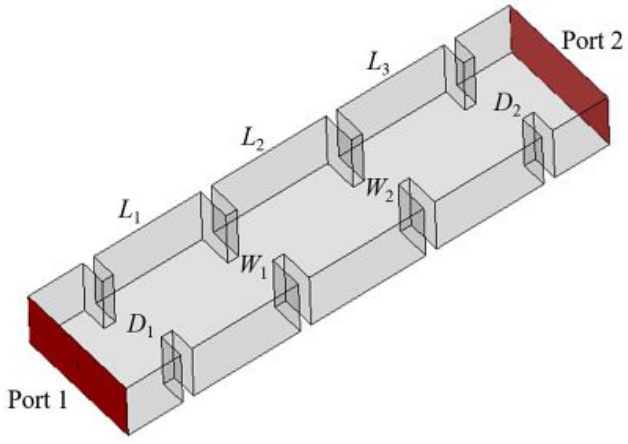



Fig. 3.23. The air cavity model of a 3rd order mode.

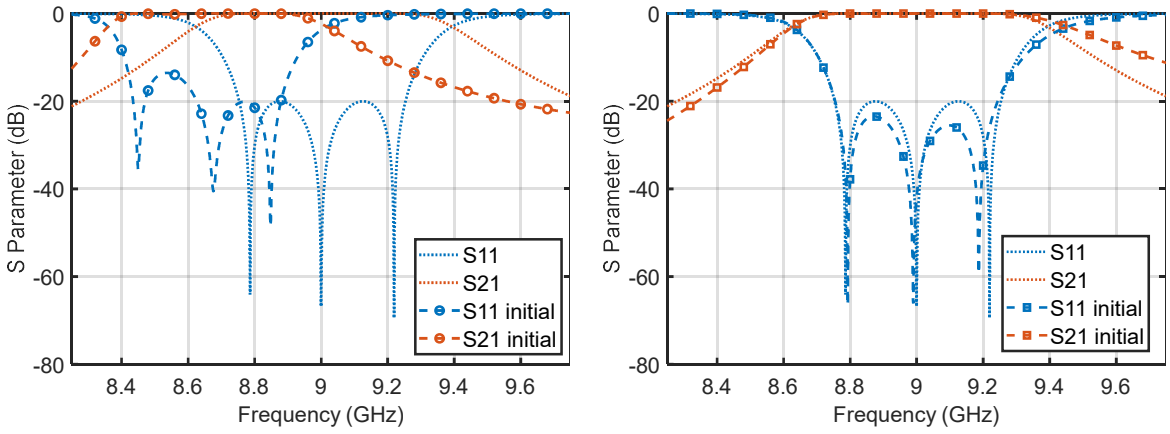



Fig. 3.24. The simulated S-parameter responses comparing with the the theoritical S-parameter responses. (a) The initial ones vs. theoritical ones. (b) The optimal ones vs. theoritical ones.

0.0573 and Qe = 15.3284. The calculated S-parameter responses are shown in Fig. 3.22. The air cavity model of the 3rd order filter is shown in Fig. 3.23. $L_1$, $L_2$ and $L_3$ are the resonator lengths. $D_1$ and $D_2$ are coupling iris widths between the waveguide port and the corresponding resonator. $W_1$ and $W_2$ are the coupling widths between two resonators. The dimensions in this filter are symmetrical, namely, $D_1 = D_2$, $W_1 = W_2$, and $L_1 = L_3$. Using the abovementioned physical dimensioning method, the initial design for this 3rd order filter can be obtained as $D_1 = D_2 = 14$ mm, $W_1 = W_2 = 10.7$ mm, $L_1 = L_3 = 20.1$ mm, and $L_2 = 22.3$ mm. The filter is modelled by using CST studio suite. Trust region framework optimizer in CST is employed for the filter optimization. After the EM optimisation, the optimal dimensions are $D_1 = D_2 = 14.25$ mm, $W_1 = W_2 = 10.68$ mm $L_1 = L_3 = 17.84$ mm, and $L_2 = 19.98$ mm. The simulated S-parameter responses of initial design and optimal design compared with the theoretical S-parameter responses are shown in Fig. 3.24.

## 3.5 Summary of this Chapter

In this chapter, some necessary theoretical backgrounds of the microwave filters and multiplexers are introduced. The coupling matrix theory plays an important role in the designs of resonator coupled filters and multiplexers. Some entry-level examples are provided to illustrate the significance of the coupling matrix in the design process of a filter component.

## Reference

[1] J. Hong and M. J. Lancaster, Microstrip filters for RF/microwave applications. John Wiley & Sons; 2004.

[2] R. J. Cameron, C. M. Kudsia, and R. R. Mansour, Microwave filters for communication systems: fundamentals, design, and applications, Wiley, 2018.

[3] D. Swanson and G. Macchiarella, "Microwave filter design by synthesis and optimisation," in IEEE Microwave Magazine, vol. 8, no. 2, pp. 55-69, April 2007.

# Chapter 4 Coupling Matrix Optimisation Method for All-resonator Multiplexers

As mentioned in Chapter 3, multiplexers can be systematically designed based on coupling matrix (CM) theory. The coupling matrix for the all-resonator multiplexer is normally synthesized based on the optimisation method. This chapter provides a general coupling matrix optimisation method for all-resonator multiplexers. This is the so-called General All-resonator diplexer/multiplexer Coupling Matrix Synthesis (GACMS) method. The optimisation workflow is elaborated first. Then, the proposed method is demonstrated by using six all-resonator diplexer and multiplexer examples. The work in this Chapter has been published in IEEE Transactions on Microwave Theory and Techniques [1].

## 4.1 Challenges in Optimisation

The challenges are mainly from the characteristic landscape (objective function variation with respect to the variables) of the optimisation [1]. In the existing CM methods of all-resonator diplexers and multiplexers, the S-parameter magnitude-based objective function is often employed. The variation of the objective function as a function of one variable can be depicted as an optimisation landscape as shown in Fig. 4.1. It can be noticed that this optimisation task would be very difficult. The global optimal valley is located among multiple local optimal valleys. The optimal valleys are very narrow. Many local optimal solutions (black circles) exist in the narrow valleys [1]. The optimisation searching

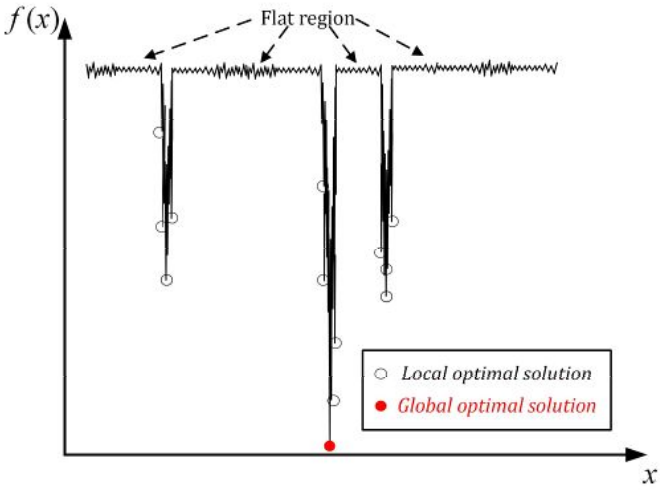



Fig. 4.1. An illustrative landscape for the all-resontor multiplexer CM optimization. $x$: coupling coefficients, $f(x)$: S-parameter magnitude based objective function

is easily entrapped into these local optima which will result in a sub-optimal or even unusable solution. This can be attributed to two main reasons: 1) The number of coupling coefficients (variables) is very large. It is hard to find an optimal solution without a reasonable starting point. 2) The existing optimisation method is not powerful enough to converge in such a narrow optimal valley.

To deal with these challenges, three schemes are employed. Firstly, the optimisation search space can be narrowed down to the near-optimal range by utilizing the information provided by channel filter synthesis. Secondly, the optimisation is carried out channel by channel. In channel optimisation, the searching space can be reduced. The successful rate of optimisation can be improved. Thirdly, a local optimizer and a global optimizer are incorporated in the optimisation. The global optimizer helps avoid local optima while the local optimizer speeds up the convergence. The optimisation framework is elaborated in the

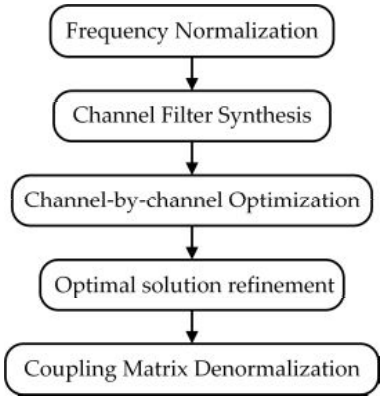



Fig. 4.2 The high-level workflow of the optimization framework.

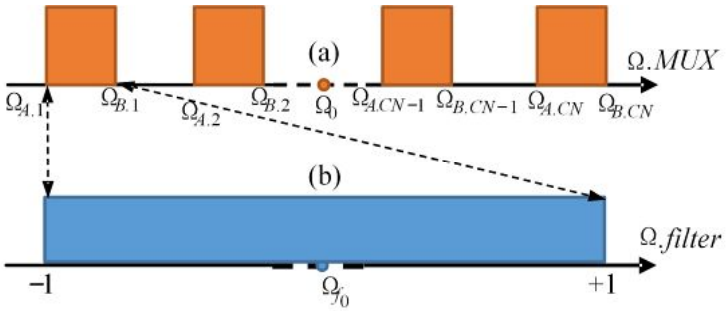



Fig. 4.3. Linear frequency transformation between (a) the normalized frequency domain of the multiplexer and (b) the lowpass prototype for each channel filter.

following.

## 4.2 The Proposed GACMS Optimisation Workflow

The proposed GACMS optimisation workflow is shown in Fig. 4.2.

***Step 1: Frequency normalization***

The specifications for the real frequency range are first normalized as shown in Fig. 4.3(a). Then, the overall passband of the multiplexer will be within [−1, +1]. $\Omega_{A,j}$ and $\Omega_{B,j}$, $j$ ($j$ = 1, …, $CN$) are the two edges of the $j$th channel. Obviously, $\Omega_{A,j} = -1$ and $\Omega_{B,CN} = 1$.

***Step 2: Channel filter synthesis***

The coupling values from channel filter synthesises can provide a high-quality starting point in the overall optimisation. They narrow down the search range. The filter is synthesized by using the classical method as described in Chapter 3. Then, coupling values of the lowpass filter are transformed into the normalized frequency domain of multiplexer as shown in Fig. 4.3.

The mutual couplings in the multiplexer are obtained by

$$m_{u,v}^{Ch} = m_{u,v}^{LP} \cdot \frac{\left|\Omega_{A.j} - \Omega_{B,j}\right|}{2} (j = 1 \; to \; CN, u \neq v) \tag{4.1}$$

where $m_{u,v}^{Ch}$ and $m_{u,v}^{LP}$ are the mutual couplings of the channel filter and the corresponding lowpass prototype filters, respectively. The self-couplings in the branches are obtained by:

$$m_{u,u}^{Ch} = m_{u,u}^{LP} + \frac{\Omega_{A.j} + \Omega_{B,j}}{2} (j = 1 \; to \; CN) \tag{4.2}$$

where $m_{u,u}^{Ch}$ and $m_{u,u}^{LP}$ are the self-couplings of the channel filter and the corresponding lowpass prototype filters, respectively.

Here, a simple diplexer example shown in Fig. 4.4 illustrates the above manipulation. Two channels of the diplexer are (−1 to −0.5) and (0.6 to 1), respectively. The maximum return loss levels for the two channels are both 20dB. The channel filter division and the corresponding responses are shown in Fig. 4.5. Since the junction resonator has influences on all channel responses of the diplexer, both the divided channel filters contain the junction resonator. The initial coupling values for the diplexer are listed in Table 4.1. The port

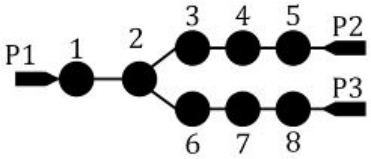
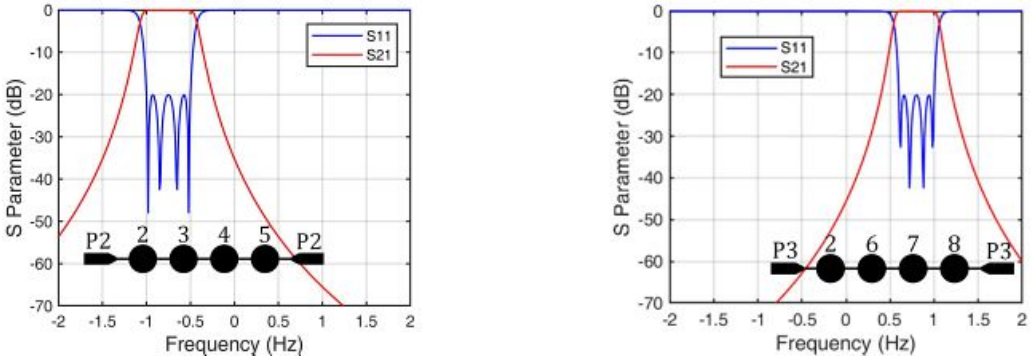



Fig. 4.4. An exemplary diplexer with 8 resonators.




(a) (b)

Fig. 4.5 The S-parameter responses of the two branches of filters

Table 4.1 Initial coupling values of the diplexer

| *Variables* | $m(2, 3)$ | $m(3,4)$ | $m(4,5)$ | $m(3,3)$ | $m(4,4)$ | $m(5,5)$ |
|---|---|---|---|---|---|---|
| *Values* | 0.2279 | 0.1751 | 0.2279 | −0.75 | −0.75 | −0.75 |
| *Variables* | $m(2,6)$ | $m(6,7)$ | $m(7,8)$ | $m(6,6)$ | $m(7,7)$ | $m(8,8)$ |
| *Values* | 0.1823 | 0.1401 | 0.1823 | 0.8 | 0.8 | 0.8 |

couplings $m(1, P1) = 0.1035$, $m(5, P2) = 0.2329$ and $m(9, P3) = 0.1863$ which are calculated based on the equations in Chapter 3.

***Step 3: Channel-by-channel optimisation***

Firstly, the coupling coefficients are divided into different groups as shown in Fig. 4.6, depending on the channel that couplings belong to. Note that all the groups contain some couplings from the stem part, since they influence all channels. For the simple diplexer example shown in Fig. 4.4, two optimisation groups are formed as listed in Table 4.2. The

Table 4.2 Coupling coefficients in each group

| Group | Coupling coefficients |
|---|---|
| *Group* 1 | ***m*(1, 2)**, *m*(2, 3), *m*(3, 4),*m*(4, 5); ***m*(1, 1)**, ***m*(2, 2)**, *m*(3, 3), *m*(4, 4), *m*(5, 5). |
| *Group* 2 | ***m*(1, 2)**, *m*(2, 6), *m*(6, 7), *m*(7, 8); ***m*(1,1)**, ***m*(2, 2)**, *m*(6, 6), *m*(7, 7), *m*(8, 8). |

Note: The bold ones are simultaneously in both groups.

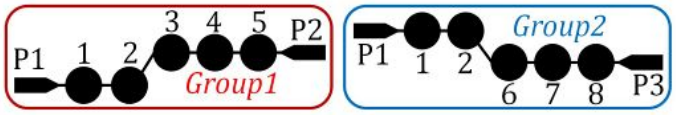



Fig. 4.6. Coupling coefficients grouping

coupling division is illustrated in Fig. 4.6.

After group division, channel by channel optimisation is implemented. The starting point of the optimisation utilizes the initial values obtained in the last step. Since the initial values are very close to the optimal, the search ranges for them are set as $[m_i - B, m_i + B]$, where $m_i$ are the initial value and $B$ denotes the boundary threshold. Here, $B$ = 0.1 is adopted. For the couplings from the stem part, they are searched in [0, 1] since there is no easily predictable initial value for them.

The optimisation is carried out the channel by channel. In each channel optimisation, the couplings in one group are optimized while the other couplings are kept at their current values. This process will not stop until all the groups are optimized. The utilized optimizer and objective function will be discussed in the next section.

***Step 4: Optimal solution refinement***

Owing to the loading effects between two channels, the coupling values after channel-by-channel optimisation are still not perfect. Therefore, final refinement is executed for all

the coupling coefficients, namely the couplings of the multiplexer are optimized in a small search range.

## 4.3 Optimisation Techniques

### 4.3.1 Objective Function

As stated in Section 4.1, the S-parameter magnitude-based objective function is often utilized for the coupling matrix optimisation. For an all-resonator multiplexer with X number of ports, the S-parameter based objective function is formulated as

$$f(\boldsymbol{x}) = \frac{\sum_{k=1}^{X-1} |\max[S_{11}(PB_k)] - RL|}{|RL|} + \frac{|\max[S_{32}(PB_1)] - IS| + \cdots + |\max[S_{X,X-1}(PB_{X-1})] - IS|}{|IS|} \tag{4.3}$$

where $PB_k$ denotes the $k^{\text{th}}$ ($k$ = 1, …, $X$−1) passband. $RL$ and $IS$ are the desired return loss and isolation levels, respectively. $S_{11}$ is the reflection coefficient from port 1 and $S_{32}$, $S_{42}$, …, $S_{X,\,X-1}$ represent the isolation performance between different channels. $\max[\cdot]$ denotes the maximum value. The optimisation minimizes the distances to the desired performance of the S-parameter responses.

### 4.3.2 Optimisation Methods

As aforementioned in the introduction, the incorporation of a local optimizer and a global optimizer can improve optimisation efficiency. In this case, a memetic optimisation

algorithm combining the global and local optimizer is adopted in channel-by-channel optimisation [3]. In the memetic algorithm, an evolutionary algorithm provides the global exploration ability whereas the local optimizer updates the population in each iteration to improve the convergence [2]. The global and local optimizers are SADEC and SQP methods, respectively. The memetic algorithm in this thesis is called Memetic SADEC (MSADEC).

SADEC is a population-based stochastic global optimisation algorithm that demonstrates good exploration ability and optimisation power in CM optimisation for diplexers without initial values [2]. It is designed based on differential evolution algorithm which has been introduced in Chapter 2. The SADEC starts from the population initialization. A parent population *P* is generated by a mutation operator DE/rand/1 [4] defined in Equation (2.12). Then, a child population is generated by a crossover operator as described in equation (2.13). Finally, a selection is implemented between the parent population and the child population as the equation (2.14) described. With the consideration of CM synthesis, SADEC utilized self-adaptive strategies in the scaling factor of the mutation operation and crossover rate of the crossover operation. The scaling factor C is defined as

$$C_{temp} = norm(0.5, 0.25)$$

$$C^i(t) = \begin{cases} 1 & \text{if } F_{temp} > 0.1 \\ 0.1 & \text{if } F_{temp} < 0.1 \\ F_{temp}, & otherwise \end{cases} \tag{4.4}$$

where $norm(0.5, 0.25)$ is a Gaussian distributed random number with a mean of 0.5 and a standard deviation of 0.25. The self-adaptive crossover rate *CR* is defined as

$$CR_{temp} = 0.1 + rand_1 \times 0.8$$
$$CR^i(t) = \begin{cases} CR_{temp} & \text{if } rand_2 < 0.1 \\ CR^i(t-1) & otherwise \end{cases} \tag{4.5}$$

where *t* is the number of iterations and *CR*(1) = 0.9. On the other hand, the SADEC utilizes a multi-population strategy. Two populations $P$ and $\bar{P}$ operate simultaneously. They have the relation

$$\bar{x}^i(t) = a + b - x^i(t) \tag{4.6}$$

where the $[a, b]^D$ is the search range, *D* is the number of the decision variables (i.e., coupling coefficients), $x^i(t)$ is the *i*th candidate solution in $P$ and $\bar{x}^i(t)$ is the corresponding candidate

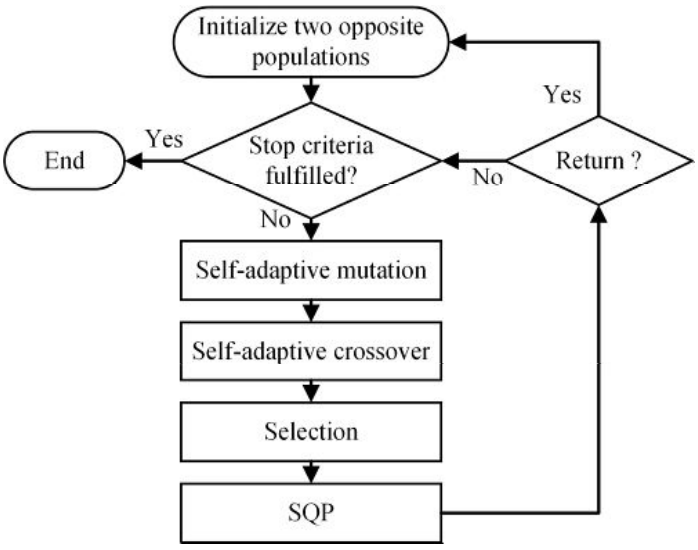



Fig. 4.7. The flowchart of MSADEC algorithm

solution in $\bar{P}$.

In SADEC, a self-adaptive return operator is implemented to avoid the optimisation trapping into the local optima. When the optimisation is judged to be trapped in local optima, another two new populations will be re-initialized and all optimisation steps will be restarted. The criteria for the optimisation to be trapped in local optima are 1) The maximum standard deviation of the variable values in the current population is smaller than a predefined threshold $\delta$ and 2) The number of reflection zeros in any passband is not correct.

The other optimizer in the memetic algorithm, SQP, is a widely used local optimizer with good convergence speed which was introduced in Chapter 2. The SQP algorithm is implemented in Matlab using the 'fmincon' function. Fig. 4.7 shows the flowchart of the memetic algorithm. In each iteration, the SQP updates the whole population obtained by SADEC.

In the final refinement, only SQP is good enough to find the desired results, since the solution after channel-by-channel optimisation is very close to the optimal.

## 4.4 Multiplexer Examples

Six complex diplexer and multiplexer examples are taken to verify the proposed optimisation framework for their coupling matrices. The topologies of the examples are shown in Fig. 4.8. The details of the optimisation are described in the following.

***Example 1*** (Fig. 4.8 (a)) is a 4-channel multiplexer with symmetric Chebyshev responses [5]. The $20^{th}$ order resonator coupled network has 15 variables owing to its symmetrical

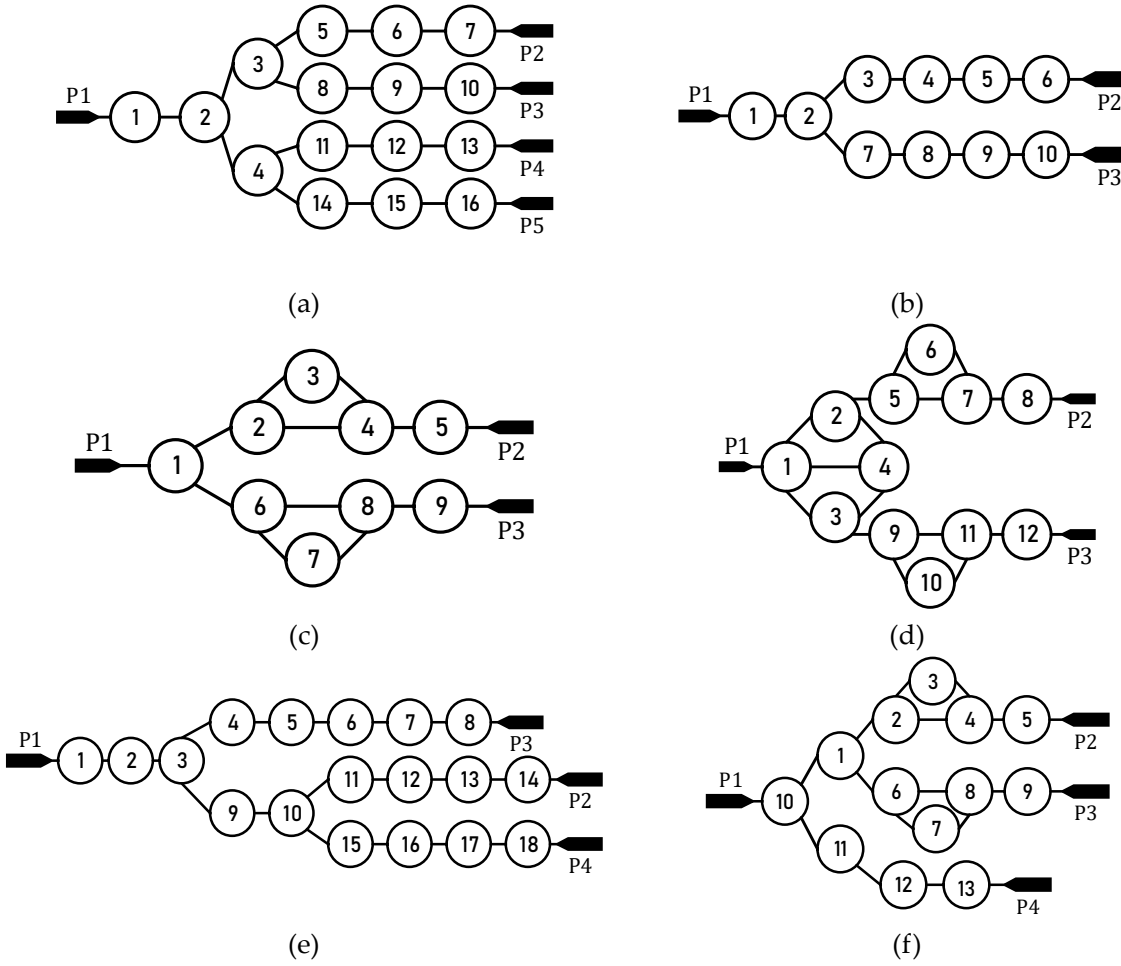



Fig. 4.8. The coupling topologies of the six test cases. (a) Example 1; (b) Example 2; (c) Example 3; (d) Example 4; (e) Example 5; (f) Example 6.

responses. The objective function is

$$f_1 = \frac{\max(PB_1 - (-20), 0)}{20} + \frac{\max(PB_2 - (-20), 0)}{20} + \frac{\max(PB_3 - (-20), 0)}{20} + \frac{\max(PB_4 - (-20), 0)}{20} + \frac{\max(IS_1 - (-30), 0)}{20} + \frac{\max(IS_2 - (-30), 0)}{20} + \frac{\max(IS_3 - (-30), 0)}{20} \tag{4.7}$$

where $PB_1 = \max(|S_{11}|)$, [−1, −0.75]; $PB_2 = \max(|S_{11}|)$, [−0.417, −0.167]; $PB_3 = \max(|S_{11}|)$, [0.167,

0.417]; $PB_4 = \max(|S_{11}|)$, [0.75, 1]; $IS_1 = \max(|S_{32}|)$, [0.167, 1]; $IS_2 = \max(|S_{43}|)$, [−0.417, 0.417]; $IS_3 = \max(|S_{54}|)$, [−1, −0.167].

***Example 2*** (Fig. 4.8 (b)) is a diplexer with two asymmetric channels. This example has 19 variables. The objective function is

$$f_2 = \frac{\max(PB_1 - (-20), 0)}{20} + \frac{\max(PB_2 - (-20), 0)}{20} + \frac{\max(IS_1 - (-80), 0)}{20} + \frac{\max(IS_2 - (-80), 0)}{20} \tag{4.8}$$

where $PB_1 = \max(|S_{11}|)$, [−1, −0.661]; $PB_2 = \max(|S_{11}|)$, [0.709, 1]; $IS_1 = \max(|S_{32}|)$, [−1, −0.661]; $IS_2 = \max(|S_{32}|)$, [0.709, 1].

***Example 3*** (Fig. 4.8 (c)) is a diplexer with one cross-coupling in each channel. The cross-couplings generate one transmission zero in the transmission response of one channel. The objective function is

$$f_3 = \frac{\max(PB_1 - (-20), 0)}{20} + \frac{\max(PB_2 - (-20), 0)}{20} + \frac{\max(IS_1 - (-30), 0)}{30} + \frac{\max(IS_2 - (-30), 0)}{30} \tag{4.9}$$

where $PB_1 = \max(|S_{11}|)$, [−1, −0.203]; $PB_2 = \max(|S_{11}|)$, [−0.026, 1]; $IS_1 = \max(|S_{32}|)$, [−1, −0.203]; $IS_2 = \max(|S_{32}|)$, [−0.026, 1].

***Example 4*** (Fig. 4.8 (d)) is a diplexer with more resonators and cross-couplings. The cross-couplings generate transmission zeros to increase the isolation between channels [6].

Table 4.3 The key features of the test cases

| Examples | No. of resonators | No. of channels | No. of cross-couplings | No. of variables (with FK values) |
|---|---|---|---|---|
| 1 | 16 | 4 | 0 | 15 (12) |
| 2 | 10 | 2 | 0 | 19 (16) |
| 3 | 9 | 2 | 2 | 19 (19) |
| 4 | 12 | 2 | 4 | 27 (24) |
| 5 | 18 | 3 | 0 | 35 (26) |
| 6 | 13 | 3 | 2 | 27 (24) |

The objective function is

$$f_4 = \frac{\max(PB_1 - (-20), 0)}{20} + \frac{\max(PB_2 - (-20), 0)}{20} + \frac{\max(IS_1 - (-60), 0)}{60} + \frac{\max(IS_2 - (-60), 0)}{60} \tag{4.7}$$

where $PB_1$ = max(|$S_{11}$|), [−1, −0.1]; $PB_2$ = max(|$S_{11}$|), [0.2, 1]; $IS_1$ = max(|$S_{32}$|), [−1, −0.1]; $IS_2$ = max(|$S_{32}$|), [0.2, 1].

***Example 5*** (Fig. 4.8 (e)) is a triplexer topology with 18 resonators. Two junction resonators distribute the three channels. The objective function is

$$f_5 = \frac{\max(PB_1 - (-20), 0)}{20} + \frac{\max(PB_2 - (-20), 0)}{20} + \frac{\max(PB_3 - (-20), 0)}{20} + \frac{\max(IS_1 - (-30), 0)}{30} + \frac{\max(IS_2 - (-30), 0)}{30} \tag{4.8}$$

where $PB_1$ = max(|$S_{11}$|), [−1, −0.6]; $PB_2$ = max(|$S_{11}$|), [−0.25, 0.25]; $PB_3$ = max(|$S_{11}$|), [0.4, 0.1]; $IS_1$ = max(|$S_{32}$|), [−1, 0.25]; $IS_2$ = max(|$S_{43}$|), [−0.25, 1].

***Example 6*** (Fig. 4.8 (f)) is a triplexer with two cross-couplings in two channels. The objective function is

$$f_6 = \frac{\max(PB_1 - (-20), 0)}{20} + \frac{\max(PB_2 - (-20), 0)}{20} + \frac{\max(PB_3 - (-20), 0)}{20} + \frac{\max(IS_1 - (-30), 0)}{30} + \frac{\max(IS_2 - (-30), 0)}{30} \tag{4.9}$$

where $PB_1$=max(|$S_{11}$|), [−1, −0.578]; $PB_2$=max(|$S_{11}$|), [−0.485, −0.051]; $PB_3$=max(|$S_{11}$|), [0.684, 0.1]; $IS_1$=max(|$S_{32}$|), [−1, 0.051]; $IS_2$=max(|$S_{43}$|), [−0.485, 1]. The key features of all the multiplexer examples are listed in Table 4.3.

## 4.5 Numerical Results and Comparison

### 4.5.1 Performance of the CM Optimisation Framework

The proposed CM optimisation framework is tested by the six numerical examples provided in the previous section. The parameter setting in the optimizer is the same as the SADEC [2]. 10 attempts are carried out for the proposed optimisation framework for each multiplexer example. For each run of all the examples, the optimisation will not stop until 250 iterations are run. In fact, 150 iterations are enough for most examples to converge. Statistical analysis for the example testing is shown in Table 4.4, where Min, Max, Mean, and STD are minimum value, maximum value, mean and standard deviation (STD) of the objective function value over the duration of the optimisation. It can be noticed that the proposed coupling matrix optimisation method can achieve excellent results for all the examples. The very small STD values for all the examples demonstrate the robustness of the proposed method. For all the examples, the CM synthesis time is around 20 to 30 minutes

Table 4.4 The statistics analysis of the CM optimization framework

| Examples | Objective function values | | | |
|---|---|---|---|---|
| | *Min* | *Max* | *Mean* | *STD* |
| 1 | 8.67E−3 | 8.76E−3 | 8.70E−3 | 3.24E−5 |
| 2 | 0.00E0 | 0.00E0 | 0.00E0 | 0.00E0 |
| 3 | 8.69E−3 | 2.19E−2 | 1.18E−2 | 3.99E−3 |
| 4 | 0.00E0 | 0.00E0 | 0.00E0 | 0.00E0 |
| 5 | 1.38E−2 | 6.09E−2 | 3.08E−2 | 1.38E−2 |
| 6 | 0.00E0 | 0.00E0 | 0.00E0 | 0.00E0 |

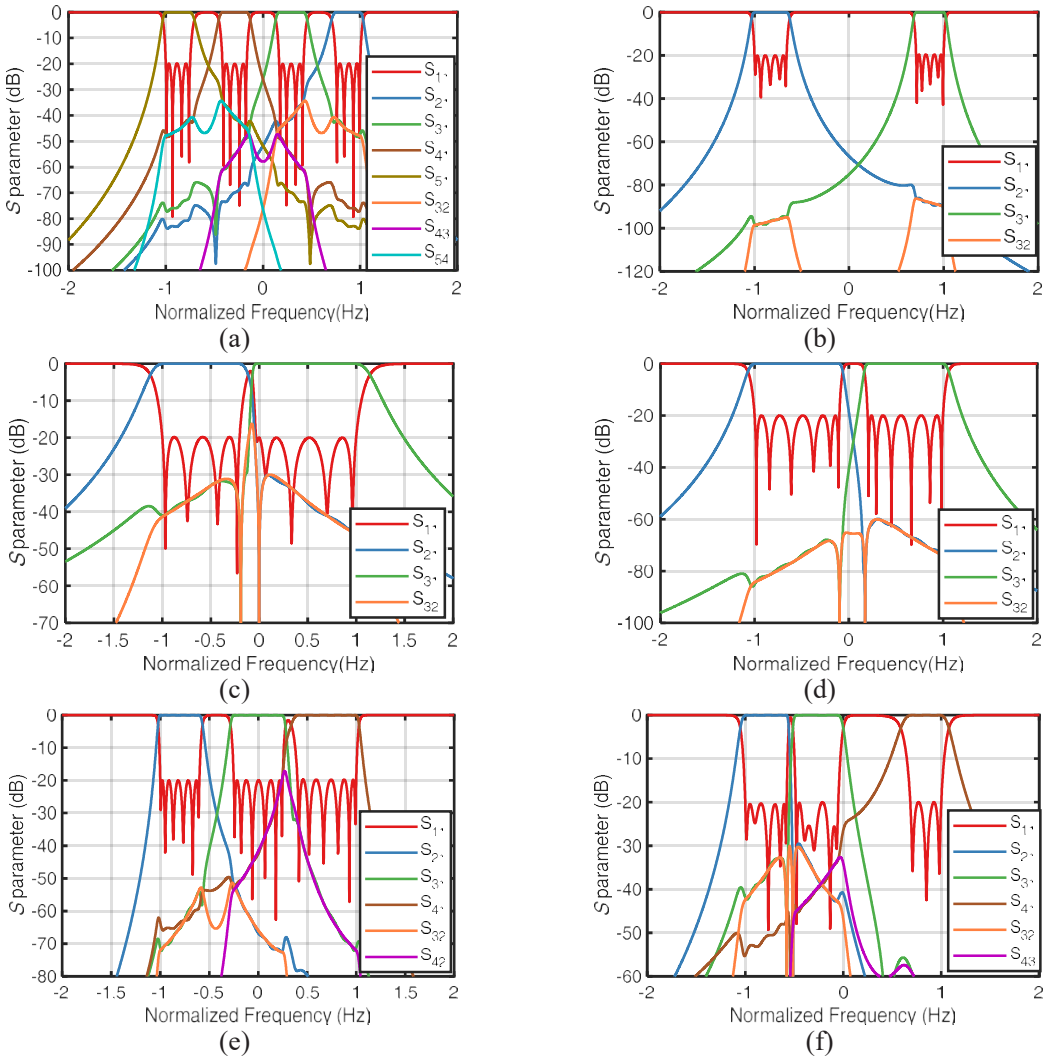



Fig. 11. Exemplary optimal responses of the six diplexer and multiplexer examples.

using a desktop computer with Intel i7-7770HQ CPU and 32 GB RAM.

### 4.5.2 Comparisons with State-of-the-art Methods

In this sub-section, the proposed optimisation framework is compared with other widely used methods. The SQP method is widely adopted for all-resonator diplexers and multiplexers. Note that the SQP method utilizes the initial coefficients obtained by using the method described as Step 2 in Section 4.2 but do not utilize the channel-by-channel scheme described as Step 3 in Section 4.2. The SQP has limited exploration ability when the number

Table 4.5 Comparison of optimal objective function values of two methods for the test cases

| Examples | Methods | Objective function values |
|---|---|---|
| 1 | SQP | 0.0128 |
| | GACMS | 0.00870 |
| 2 | SQP | 0.152 |
| | GACMS | 0.00 |
| 3 | SQP | 0.391 |
| | GACMS | 0.0118 |
| 4 | SQP | 0.996 |
| | GACMS | 0.00 |
| 5 | SQP | 0.501 |
| | GACMS | 0.0308 |
| 6 | SQP | 1.87 |
| | GACMS | 0.00 |

Table 4.6 Success rate of two methods for the test examples

| Examples | Methods | |
|---|---|---|
| | SQP | GACMS |
| 1 | 100% | 100% |
| 2 | 100% | 100% |
| 3 | 100% | 100% |
| 4 | 0% | 100% |
| 5 | 0% | 100% |
| 6 | 0% | 100% |

Table 4.7 The comparison of memetic optimizer and SADEC for numerical examples

| Examples | Methods | Optimal objective function values | | | |
|---|---|---|---|---|---|
| | | *Min* | *Max* | *Mean* | *STD* |
| 1 | SADEC | 0.0106 | 0.0360 | 0.0215 | 0.00791 |
| | Memetic | 0.00867 | 0.00876 | 0.00870 | 0.0000324 |
| 2 | SADEC | 0.0520 | 0.113 | 0.0652 | 0.0175 |
| | Memetic | 0.00 | 0.00 | 0.00 | 0.00 |
| 3 | SADEC | 0.0589 | 0.0745 | 0.0691 | 0.00439 |
| | Memetic | 0.00869 | 0.0219 | 0.0118 | 0.00399 |
| 4 | SADEC | 0.0038 | 0.0237 | 0.0128 | 0.00671 |
| | Memetic | 0.00 | 0.00 | 0.00 | 0.00 |
| 5 | SADEC | 0.117 | 0.268 | 0.179 | 0.0486 |
| | Memetic | 0.0138 | 0.0609 | 0.0308 | 0.0138 |
| 6 | SADEC | 0.0241 | 0.595 | 0.275 | 0.166 |
| | Memetic | 0.00 | 0.00 | 0.00 | 0.00 |

TABLE 4.8 The success rate of memetic optimizer and SADEC for the six examples

| Examples | Methods | |
|---|---|---|
| | SADEC | Memetic |
| 1 | 100% | 100% |
| 2 | 100% | 100% |
| 3 | 100% | 100% |
| 4 | 100% | 100% |
| 5 | 90% | 100% |
| 6 | 30% | 100% |

of optimisation variables is getting large. The success rate will decrease. The objective function values of the two methods for six testing examples are listed in Table 4.5. The success rates for them are listed in Table 4.6.

The rules for judging the success of CM synthesis are: (1) The reflection zeros are all within the channel passbands. (2) The S-parameter responses satisfy the design specifications. Based on the comparison shown in Table 4.5 and 4.6, the performance of the proposed CM optimisation framework is better than the SQP method for all the testing

examples. Especially, the SQP method cannot obtain an acceptable solution for example 4 - 6. This demonstrates that the local optimizer is easily trapped into a local optimal valley and is hard to jump out when the diplexer and multiplexer examples have complex structures.

### 4.5.3 Advantages of Memetic Optimizer

To demonstrate the advantage of the memetic optimizer, it is compared with the state-of-the-art optimizer SADEC [2]. Using the numerical examples described in 4.4, all the channel-by-channel optimisations are replaced by SADEC. For each example, 10 runs are carried out to compare with the memetic optimizer. The comparisons are shown in Tables 4.7 and 4.8. It can be noticed that optimisation solutions obtained from the SADEC optimizer are as good as the ones from the memetic optimizer. However, the success rate of SADEC is decreased when the multiplexer becomes more complex, i.e., examples 5 and 6.

## 4.6 Summary of this Chapter

This chapter presents a General All-resonator diplexer/multiplexer Coupling Matrix Synthesis (GACMS) method. The method employs filter knowledge and powerful optimisation techniques. The multiplexers are firstly divided into multiple sub-networks (filters) to obtain the initial coupling coefficients via filter synthesis. Then, a channel-by-channel optimisation scheme is utilized to relieve the optimisation burden. A powerful optimizer improves the synthesis rate. Therefore, the diplexers and multiplexers with complex configurations can be successfully and stably synthesized. The proposed method

has been verified by using six examples and the optimisation results demonstrate higher stability and superiority than the available optimisation-based method.

## Reference

[1] Y. Yu, B. Liu, Y. Wang, M. J. Lancaster, and Q. S. Cheng, "A general coupling matrix synthesis method for all-Resonator diplexers and multiplexers," IEEE Trans. Microw. Theory Techn., vol. 68, no. 3, pp. 987-999, March 2020.

[2] B. Liu, H. Yang, and M. J. Lancaster, "Synthesis of coupling matrix for diplexers based on a self-Adaptive differential evolution algorithm," IEEE Transactions on Microwave Theory and Techniques, vol. 66, no. 2, pp. 813-821, 2018.

[3] P. Moscato, "On evolution, search, optimisation, genetic algorithms and martial arts: Toward memetic algorithms," in "Caltech Concurrent Computation Program," California Inst. Technol., Pasadena, CA, Tech. Rep. 826, 1989.

[4] K. Price, R. M. Storn, and J. A. Lampinen, Differential evolution: a practical approach to global optimisation. Springer Science & Business Media, 2006.

[5] X. Shang, Y. Wang, W. Xia, and M. J. Lancaster, "Novel Multiplexer Topologies Based on All-Resonator Structures," *IEEE Trans. Microw. Theory Tech.*, vol. 61, no. 11, pp. 3838-3845, 2013.

[6] Y. Wu, R. Wu and Y. Wang, "A Compact Coupling Structure for Diplexers and Filtering Power Dividers," Progress In Electromagnetics Research, vol. 69, pp. 161-170, 2018.

# Chapter 5 Global Optimisation of Microwave Diplexers Based on a Design Knowledge-Guided Approach

The last chapter focuses on the optimisation method for the coupling matrix. In this chapter, a General Diplexer Optimisation method guided by Design Knowledge (GDODK) is proposed for the electromagnetic (EM) design of diplexers. The aim is to enable an automatic EM optimisation for diplexers without restrictions on the type of channel filters and junctions. The two key features of GDODK are: (1) High-quality initial values are extracted from the coupling matrix by using a local optimizer, facilitating the subsequent 3D EM simulation-based optimisation; (2) A new performance extraction method from S-parameters and key-performance-based objective function are proposed, which enables an effective search for the optimal design. The GDODK method is tested by two all-resonator diplexers and a Tee-junction diplexer. Successful results are shown for all cases without involving any ad-hoc design process. Through comparison, the GDODK demonstrates clear advantages over existing commercial tools in terms of generality and effectiveness.

## 5.1 Challenges and Motivations

Given a filtering topology, diplexer global optimisation aims to obtain the optimal 3D design (i.e., geometric parameter values) which satisfies a set of predefined performance specifications. Other microwave devices such as antennas, for which, a direct global

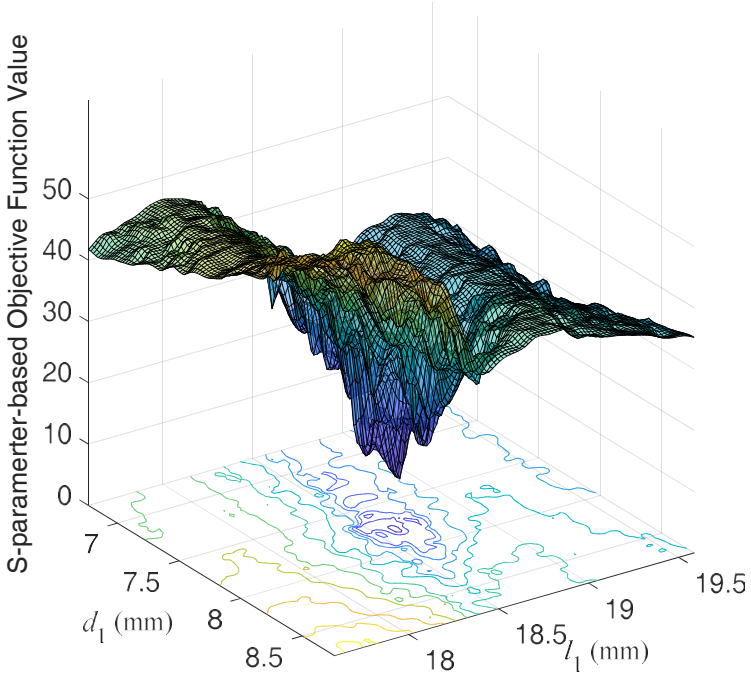



Fig. 5.1. An illustrative figure of design landscape characteristics of microwave diplexers (the example in Section IV (A)), where $l_1$ and $d_1$ represent two diplexer geometric parameters (Fig. 5.5) and the objective function value based on $\max(|S_{11}|)$ within the required bandwidth.

optimisation in the provided search range is often feasible [1]. However, popular optimisation techniques, including global optimizers, are facing significant challenges with respect to optimizing diplexers [2]-[3]. The $\max(|S_{11}|)$ in the required bandwidth-based objective function is arguably the most widely used, but this leads to a complex design landscape. Fig. 5.1 shows a typical design landscape of a diplexer based on this objective function [2]. In Fig. 5.1, the global optimal design lies in a narrow valley, among many other narrow valleys. Even in this optimal region, many local optima still exist as can be observed from the contour map of the landscape. These typical landscape characteristics make diplexer global optimisation almost intractable for many popular optimisation algorithms.

The proposed generic diplexer global optimisation process aims to address this design

challenge in two main phases: (1) Obtaining a high-quality initial 3D design and (2) Optimisation from the initial design using full-wave EM simulations.

As discussed in Chapters 2 and 3, the most common technique in acquiring the initial design is the design curve method. However, when this method is applied to diplexers, especially diplexers having a relatively wide bandwidth, the obtained initial 3D design often shows insufficient quality [4]-[5]. This is usually the case for designs having more than two couplings associated with one resonator (i.e., for non-adjacent cross-couplings or junction resonators [4]). The design curve method often fails in the second phase, even when global optimisation is employed.

For diplexers, an additional challenge is the larger number of design variables and the mutual influence between channels. A linear increase in the number of design variables leads to an exponential increase in the design space, and the valley in Fig. 5.1 ultimately becomes narrower [2]. Due to the mutual influence, some well-matched channels may prohibit the other channels from reaching their performance specifications. Hence, the exploration ability of a global optimisation algorithm may be insufficient. This asserts the importance of a high-quality initial 3D design for diplexer optimisation. Note that even if the high-quality initial design is still not good enough, it at least eases the burden of the second phase (i.e., 3D EM simulation-based optimisation) to a large extent. Therefore, a systematic local optimisation-based physical dimension approach is proposed to obtain high-quality initial dimensions.

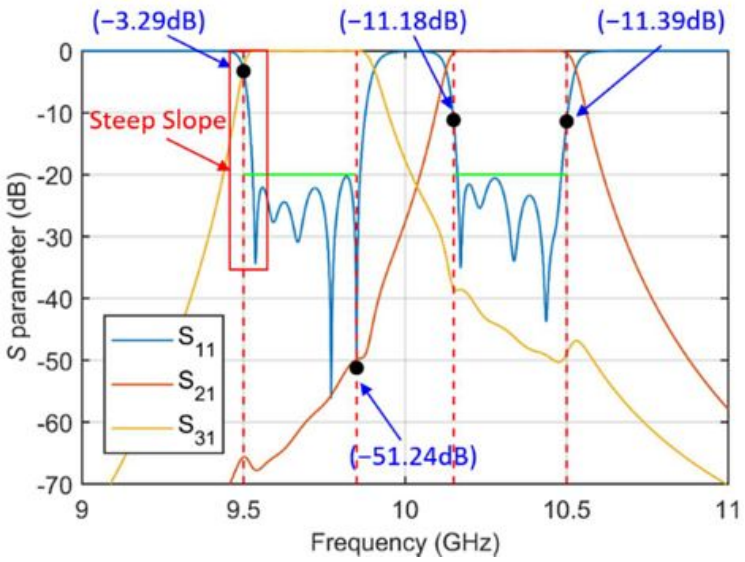



Fig. 5.2. The response of a design with good potential.

Even with a reasonable quality initial design, the second phase remains a challenging task for diplexers. At this phase, the objective function and the optimisation algorithm are two key factors.

When using the traditional max(|$S_{11}$|)-based objective function, the induced design landscape makes it difficult to identify high potential candidates. In Fig. 5.2, the design specifications are indicated by the green solid lines and red dashed lines: two passbands (channel 1 from 9.5 to 9.85 GHz and channel 2 from 10.15 to 10.5 GHz), and the in-band maximum return loss level of 20 dB. Intuitively, the response (solid line in Fig. 5.2) shows a good potential solution. However, if assessed using max(|$S_{11}$|)-based objective function, the function value is actually very poor for this response, i.e., −3.29 dB in the lower and −11.18 dB in the higher channels, respectively, as shown in Fig. 5.2. This is because of the steep slopes of the $S_{11}$ response. The steep slopes indicate that the objective function value is very

sensitive to the $S_{11}$ response. In other words, a small frequency shift leads to a large degradation of the in-band max($|S_{11}|$) value, and this phenomenon is common to many diplexers. To address this problem, key performance indicators (KPIs) are extracted from the S-parameter response to formulate the objective function. The KPIs include return loss level, bandwidth and centre frequency. The design landscape induced by the new objective function is simplified, and the identification of high potential solutions becomes much easier. This objective function does not require the extraction of the CM as carried out in [6]-[8], as the CST Filter Designer 3D does.

In terms of optimisation algorithms for the filter design, both local and global optimisation methods are available. A widely used local optimisation algorithm is the trust-region method [9], e.g., the trust-region framework in CST Studio Suite [10]. The method has been introduced in Chapter 3. Due to the limited exploration ability of local optimisation algorithms, despite some successful cases for filters, they are easily trapped in local optima and fail in many cases [3], [11]. When applying local optimisation algorithms to diplexers, our investigation shows that even with a reasonably good initial design, the trust region method finds it very difficult to obtain a reasonable result without an experience-based ad-hoc design process. Considering the complex design landscape in Fig. 5.1, this difficulty is expected. Another local optimisation algorithm with an enhanced exploration ability is the so-called 'Extreme Optimizer'. It is implemented in Mician μWave Wizard [12], and it combines gradient and random optimisation methods. However, it shows similar problems

with the trust region method for diplexers.

Recently, a global optimisation algorithm, a surrogate model-assisted evolutionary algorithm for filter optimisation (SMEAFO) [3] was proposed. Compared with standard global optimisation algorithms, SMEAFO is capable of obtaining comparable design quality, while significantly reducing the number of EM simulations by 30 times for filters [3]. Given that local optimisation algorithms have limited exploration ability for diplexer optimisation, SMEAFO is employed in this work despite the fact that it usually takes long time to obtain optimal solution [3]. Its efficiency still has room for improvement.

Until now, there is no generic and systematic diplexer global optimisation method. This chapter presents a new *general* diplexer global optimisation method guided by design knowledge (GDODK). The main contributions of this method are:

(1) A systematic and efficient method, in place of the conventional interpolation-based method, is proposed to obtain high-quality initial 3D designs.

(2) A new performance extraction method and key-performance-based objective function for 3D EM simulation-based optimisation are introduced to significantly simplify the complex design landscape of Fig. 5.1, leading to a high success rate.

## 5.2 The GDODK Method

The flow diagram of GDODK is shown in Fig. 5.3. Starting from the CM, the blocks on the left-hand side of Fig. 5.3 show the flow of the initial 3D design generation method based on local optimisation, and the blocks on the right-hand side of Fig. 5.3 show the flow of key

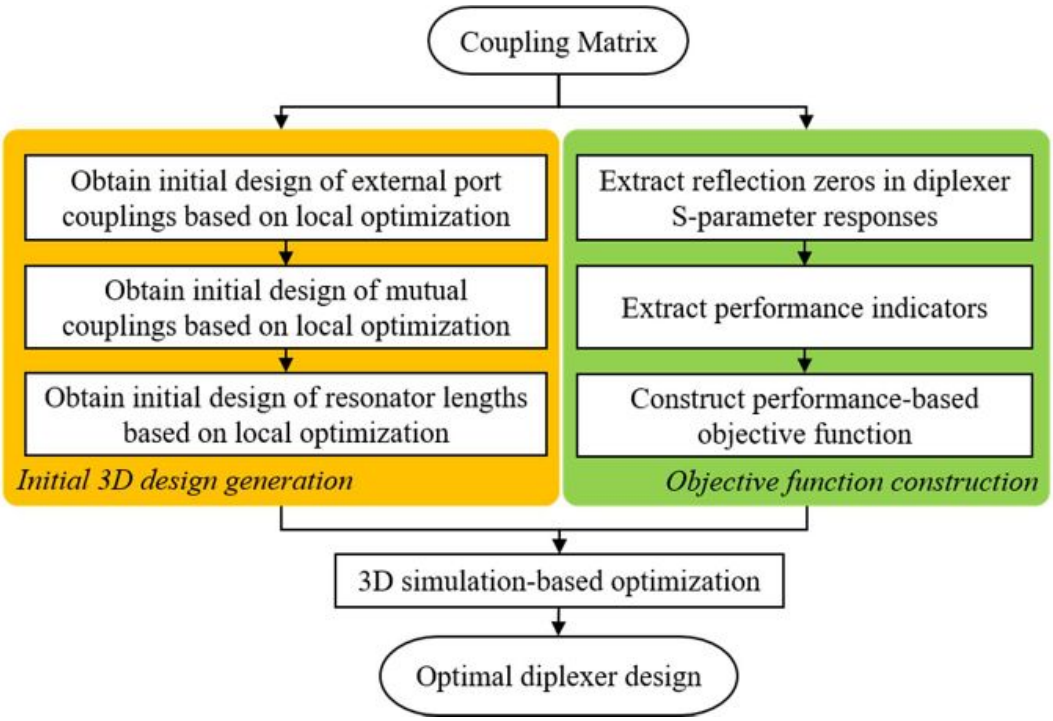



Fig. 5.3. The flow diagram of GDODK

performance extraction and the performance-based objective function construction method. The 3D simulation-based optimization in Fig. 5.3 can use any kind of EM simulation-based optimization algorithm. Here, the SMEAFO is employed. The initial 3D design generation method and the performance-based objective function are detailed in the next two subsections and both substantially assist the 3D optimizer, SMEAFO.

### 5.2.1 Surrogate Model-assisted Evolutionary Algorithm for Filter Optimisation (SMEAFO)

SMEAFO is a surrogate model-assisted optimisation technique for filter global optimisation [3]. In SMEAFO, Gaussian process machine learning and differential

evolution-based global optimisation is employed. An overview of how SMEAFO works is provided in this subsection. More details can be found in [3].

The SMEAFO design exploration works as follows:

Step 1: Create an initial database by performing full-wave EM simulations of $\alpha$ sampled candidate designs.

Step 2: Generate a population $P$ by selecting $\lambda$ best designs in the initial database based on the simulated result.

Step 3: Generate $\lambda$ child solutions by applying the selected differential evolution mutation and the crossover operators in [3] on $P$.

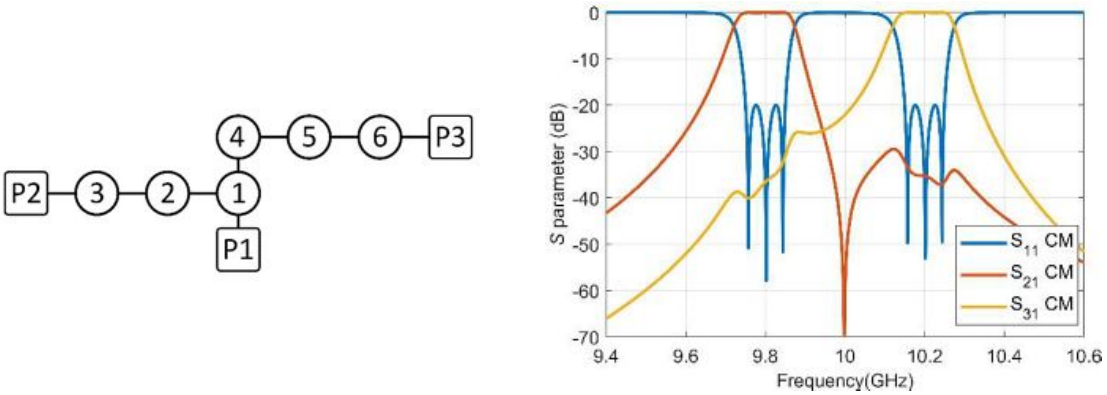
Step 4: Select training data points and construct a local Gaussian process surrogate model [3] for each child solution.

Step 5: Prescreen the $\lambda$ child solutions generated in Step 3 using the lower confidence bound method [13]. Estimate the best child solution based on the lower confidence bound values.

Step 6: Perform EM simulation to the estimated best child solution from Step 5. Add this design and its performance (full-wave EM simulation result) to the database. Go back to Step 2.

### 5.2.2 Initial 3D Design Generation Method

The initial 3D design generation method is illustrated using an X-band diplexer




(a) (b)

Fig. 5.4. The diplexer topology and S-parameter response of the optimal CM for example 1 in Section IV.

Table 5.1 The optimal coupling coefficients for the diplexer example

| | | | |
|---|---|---|---|
| $m(1, P1)$ | 0.1531 | $m(5, 6)$ | 0.0103 |
| $m(3, P2)$ | 0.1094 | $m(1, 1)$ | −0.0006 |
| $m(6, P3)$ | 0.1072 | $m(2, 2)$ | −0.0398 |
| $m(1, 2)$ | 0.0147 | $m(3, 3)$ | −0.0402 |
| $m(2, 3)$ | 0.0105 | $m(4, 4)$ | 0.0054 |
| $m(1, 4)$ | 0.0403 | $m(5, 5)$ | 0.0379 |
| $m(4, 5)$ | 0.0135 | $m(6, 6)$ | 0.0398 |

example. The diplexer is designed using a WR-90 waveguide. The filtering topology and optimal S-parameter response are shown in Fig. 5.4. The optimal CM is obtained by using the method described in Chapter 4, and the optimal coupling coefficients are listed in Table 5.1. The air cavity EM model of the diplexer is shown in Fig. 5.5. To improve the accuracy of the conventional physical dimensioning method, objective functions are formed, and trust region optimisation is used. The typical design process is as follows:

1) ***Port couplings***. Take $m_{1,P1}$ as an example. The coupling structure is modelled as shown in Fig. 5.6. The optimisation variables are the iris width ($w_1$), and the coupled

resonator length ($l_1$). The objective function is

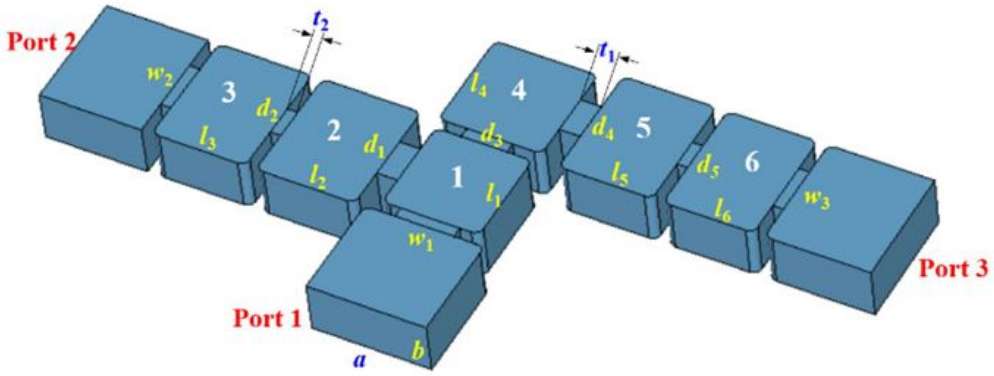



Fig. 5.5. The resonator topology and an air cavity model of a 6th order diplexer.

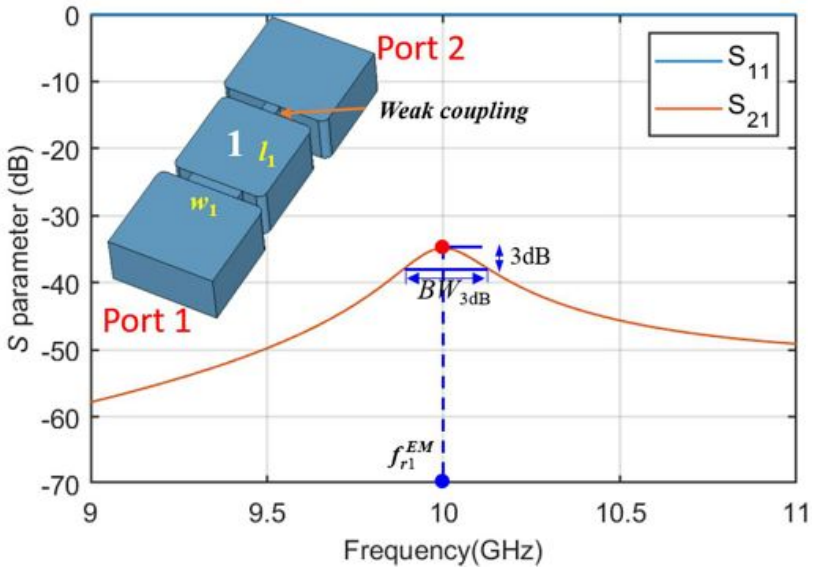



Fig. 5.6. The EM modelling and the corresponding optimal response of $m_{1,P1}$.

$$F_1 = (\xi_1 |m_{1,P1}^{EM} - m_{1,P1}| + \xi_2 |f_{r1}^{EM} - f_{r1}|) - \varepsilon_T \tag{5.1}$$

where $m_{1,P1}^{EM}$ is the simulated external port coupling value operating at $f_{r1}^{EM}$ which is calculated by [14]

$$m_{i,Pk}^{EM} = \sqrt{f_{r1}^{EM} / BW_{3d}} \tag{5.2}$$

where $BW_{3dB}$ is the 3 dB bandwidth extracted from the simulated $S_{21}$ response. $f_{r1}^{EM}$ is the simulated resonant frequency corresponding to the maximum value of $S_{21}$ (Fig. 5.6). $m_{1,P1}$, and $f_{r1}$ are the theoretical external port coupling coefficient and the resonant frequency of resonator 1, respectively. $m_{1,P1}$ is provided by the coupling matrix (Table 5.1). The theoretical resonator frequencies are calculated from the self-couplings as described in Chapter 3.3. $\xi_1$and $\xi_2$ are the weights, which are set to 1000 and 1, respectively. These weights make the two items in (5.1) comparable to each other. $\varepsilon_T$ is the convergence threshold, which is set as $10^{-6}$, making the result very close to the theoretical value.

2) Mutual couplings. Take the $m_{1,2}$ as the example (Fig. 5.7), the design variables to be optimized include $d_1$, $l_1$, and $l_2$. The objective function is formed as

$$F_2 = \left(\xi_3 \left| m_{1,2}^{EM} - m_{1,2} \right| + \xi_4 \left| f_0^{EM} - f_{ch.lo} \right.\right) - \varepsilon_T \tag{5.3}$$

where $m_{1,2}^{EM}$ is the simulated coupling value operating at $f_0^{EM}$, $m_{i,j}^{EM}$ $(i \neq j)$ is calculated by

$$m_{i,j}^{EM} = \frac{(f_1^{EM})^2 - (f_2^{EM})^2}{(f_1^{EM})^2 + (f_2^{EM})^2} \tag{5.4}$$

where $f_1^{EM}$ and $f_2^{EM}$ are two resonant frequencies corresponding to the first and second maximum values of simulated $S_{21}$, respectively, within the targeted frequency range (Fig. 5.7). $f_0^{EM}$ is calculated by $f_0^{EM} = (f_1^{EM} + f_2^{EM})/2$. $m_{1,2}$ and $f_{ch.low}$ are the theoretical coupling coefficient (Table 5.1) and centre frequency of channel passband, respectively. (The resonator with $d_1$ as its iris length belongs to the lower frequency channel.) $\xi_3$ and $\xi_4$ in

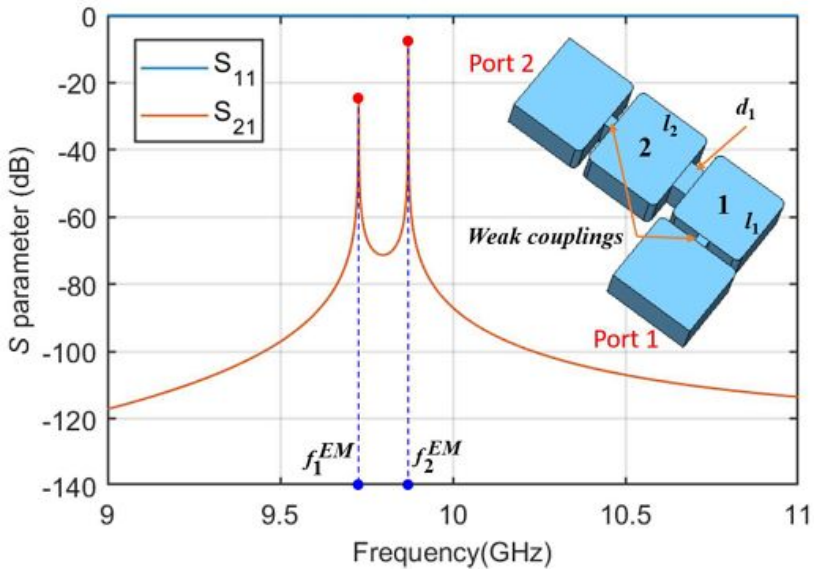



Fig. 5.7. The EM modelling and the corresponding optimal response of $m_{1,2}$.

equation (5.4) are weights, which are set as 1000 and 1, respectively. The rationale for the values of the weights and their effect on $F_2$ is similar to $F_1$ as explained earlier.

The loading effect of the coupling on the resonance frequency is critical and should be taken into account. Particularly, for the junction resonator or the resonator with more than two couplings (cross-coupling) in the diplexer, this makes the length of the junction resonator much smaller than the rest [16]. In our approach, all the resonator lengths are separately optimized using the trust region method with the starting points from the above method. Take junction resonator 1 as an example. As shown in Fig. 5.8, the resonator is modelled with all the dimensional values obtained for the iris from the previous steps. Now, the only optimisation variable is $l_1$ and the objective function is:

$$F_3 = (\xi_5 | f_{r1}^{EM} - f_{r1}|) - \varepsilon_T \tag{5.5}$$

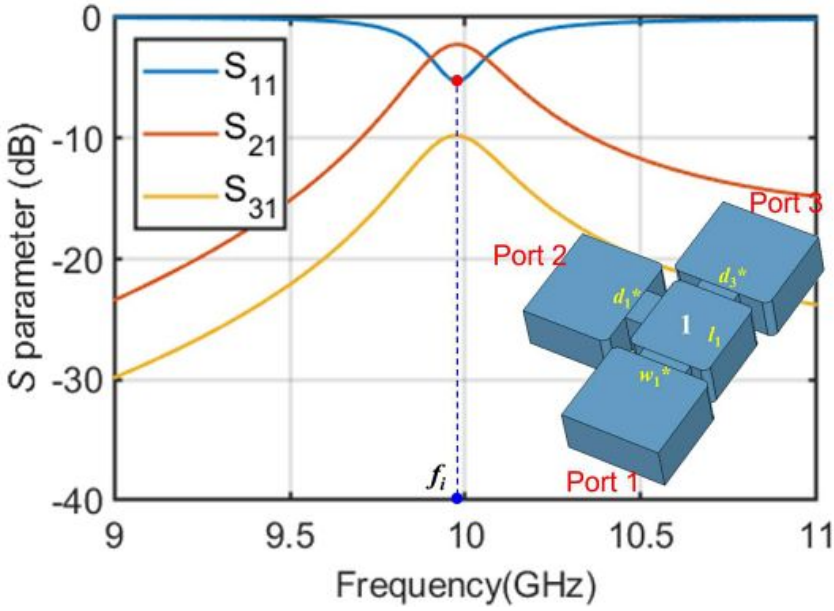



Fig. 5.8. The EM modelling and the corresponding optimal response of resonator 1.

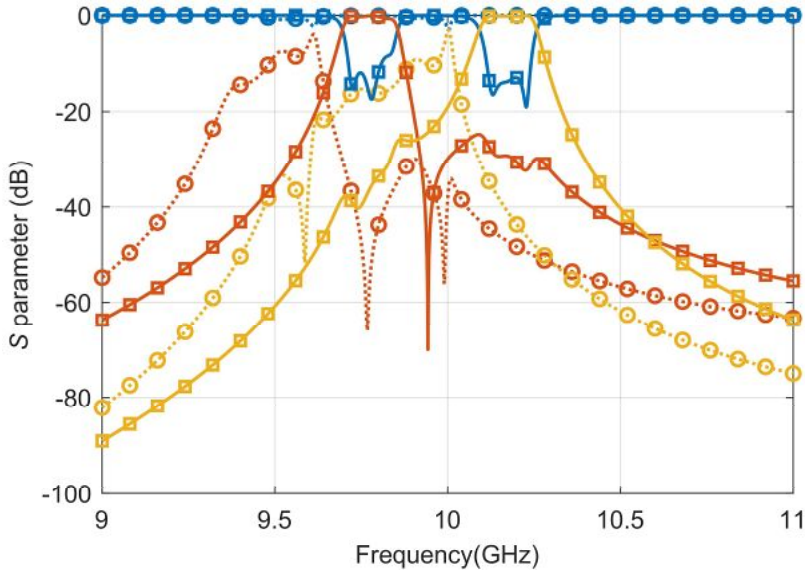



Fig. 5.9. The S-parameter response comparison of the initial design from the conventional interpolation-based method (circle marked dotted line) and the proposed method (square marked solid line).

where $f_{r1}^{EM}$ and $f_{r1}$ are the same as before. $\xi_5$ is the weight and it is set as 1.

Fig. 5.9 compares the responses of the initial designs obtained using the proposed improved method and the conventional interpolation-based method. It can be seen the

improvement offered by the proposed method is significant.

### 5.2.3 Performance-based Objective Function

The Performance-based objective function is formulated based on the KPIs from S parameters. From the $S_{11}$ response, the return loss level (RLL), the centre frequency (CF), and the bandwidth (BW) of each channel are extracted. The stopband performance described by the magnitudes of $S_{21}$ and $S_{31}$ are also directly used in the objective function (e.g., $\max(|S_{21}|) \leq -40$ dB from 10 GHz to 10.5 GHz). The reason for this choice is that the steep slope problem (see Fig. 5.2) that appears in the $S_{11}$ response often does not exist in $S_{21}$ and $S_{31}$ responses. Some diplexers have transmission zeros (TZs) and the frequency locations of the TZs can also be used as KPIs. Prior to the extraction of the KPIs, the reflection zeros (RZs) which are critical in determining other filtering performances must be obtained.

***1) Extraction of the reflection zeros (RZs)***

Although in many cases the RZs are easy to observe from the $S_{11}$ response (e.g., Fig. 5.10), other more complex cases often appear during the optimisation process. An example is shown in Fig. 5.11, which appears in the optimisation of a $10^{th}$ order diplexer (Section 5.3.2). When the *findpeaks* function in MATLAB is used, only 4 and 3 RZs are identified in the lower and higher frequency channels (i.e., the red circles in Fig. 5.11), respectively, while others (black circles) are missing.

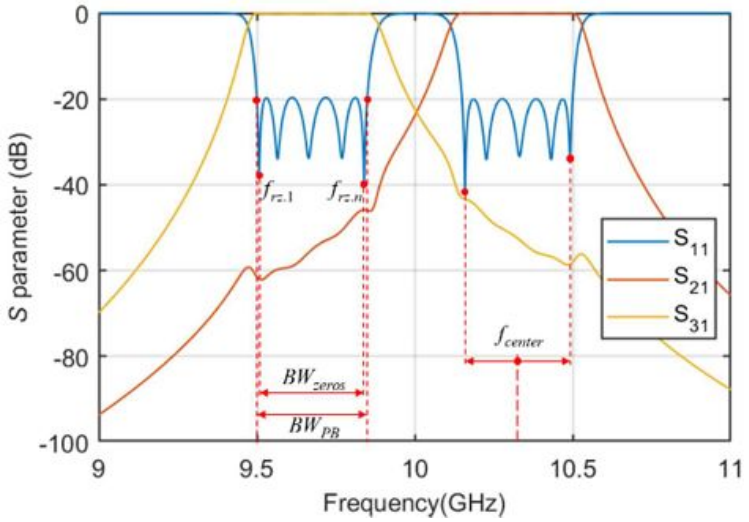



Fig. 5.10. The S-parameter response of the optimal CM for example 2 in Section IV.

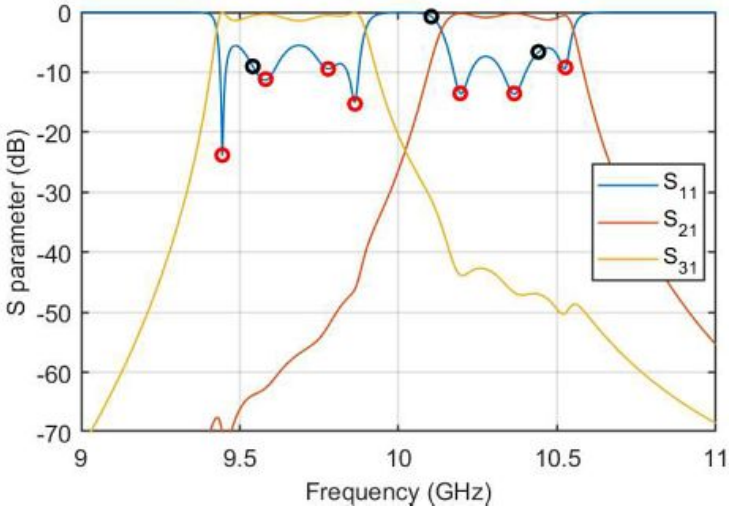



Fig. 5.11. A typical response during the optimisation of a 10th-order diplexer in Section IV (B).

To address this problem, the vector fitting method [17] is used. This method adopts a rational polynomial to fit the S-parameter response. When the fitted polynomial is sufficiently accurate compared to the response, the poles and zeros of the fitted polynomial are often accurate approximations to the poles and zeros of the diplexer. This method has been successfully used in identifying poles and zeros for microwave filters [18], [19]. It is

also successful in extracting RZs for the diplexer in our experiments, with all the 10 RZs correctly extracted, as shown in Fig. 5.11.

***2) Extraction of bandwidths (BWs)***

The BW refers to the bandwidth defining the passband of the $S_{11}$ response, as shown in Fig. 5.10 (i.e., $BW_{PB}$). When all the RZs reach or are below the desired value, i.e., −20 dB, it is straightforward to extract BWs. However, some *RZ*s often do not reach −20 dB. In this case, a BW is defined as $BW = |f_{rz.n} - f_{rz.1}| + \Delta BW_{shift}$, where $f_{rz.n}$ and $f_{rz.1}$ are the highest and lowest *RZ* frequencies in one channel, as shown in Fig. 5.10 (i.e., $BW_{zeros}$). $\Delta BW_{shift}$ is the difference between the *BW* and $BW_{zeros}$, and it is estimated using the ideal response from the optimal CM.

When some RZs are located outside the passband (e.g., the case shown in Fig. 5.11), the extracted BW could be much larger than the specifications, so they are penalized in the objective function. On the other hand, the traditional max($|S_{11}|$)-based objective function would not be able to identify such cases when the performance in the required bands satisfies the S-parameter specifications. This attribute may cause the optimisation to converge to the wrong solution.

***3) Extraction of return loss levels (RLLs)***

By comparing the extracted BWs and the 3 dB bandwidth with respect to the $S_{21}$ and $S_{31}$ responses, the locations of the RZs in relation to the passband can be identified. When all the RZs are within the passband, the RLL is defined as max($|S_{11}(f_{rz.1}:f_{rz.n})|$). In other words,

it is the maximum $|S_{11}|$ value of all the poles between $f_{rz.1}$ and $f_{rz.n}$. This definition avoids the steep slope problem (see Fig. 5.2) that occurs when the max($|S_{11}|$) in the required bands is used instead.

When some RZs lie outside the passband, the RLL is defined as max($|S_{11}$(PB)$|$), where PB is the specified passband. This is the same as the traditional method. The reason to use this setting is that such cases provide a wrong candidate design which is penalized by the bandwidth performance function. Defining an RLL using $\max(|S_{11}(f_{rz.1}: f_{rz.n})|)$ is for identifying solutions with good potential, which does not apply to these cases.

***4) Extraction of the centre frequency (CF) of each channel***

The centre frequency is defined as $CF = (f_{rz.1} + f_{rz.n})/2$ due to the equiripple characteristic of the Chebyshev response [14].

In summary, the key performance indicators include *RLL*, *BW*, *CF*, frequencies of TZs (if any), isolation performance described by the magnitudes of $S_{21}$ and $S_{31}$ (e.g., max($|S_{21}|$) in the stopbands). Note that the frequencies of the RZs are not performance indicators, but essential in the condition-controlled extraction of the performances.

Employing the extracted performance indicators, the key-performance-based objective function can be defined as:

$$F_{diplexer} = \sum_{1}^{n} \beta_j \left[ \left| min(FE_j - FES_j + \Delta_{LB.j}, 0) \right| + max(FE_j - FES_j + \Delta_{UB.j}, 0) \right] \quad (5.6)$$

where $FE_j$ represents the *j*th extracted performance function value, and $FES_j$ is the

corresponding requirement from the design specifications.

For diplexers, due to the mutual influence of the channel filters, a frequency shift often occurs. Solutions that exactly meet the design specifications (e.g., the frequency range) are difficult to obtain in many cases. This indicates that allowing small acceptable design margins (e.g., a slight frequency shift, or a slightly narrower or wider bandwidth) may be necessary for diplexer optimisation in some applications. Hence, tolerance ( $\Delta_j$ ) is introduced in (5.6). $\Delta_j$ is a user-defined threshold for the acceptable range of the *j*-th performance, and it is case dependent or application-specific. In principle, $\Delta_j$ can be set to zero which means that an exact match of the required frequency ranges is imposed. Example 1 shows a case of zero tolerance, and examples 2 and 3 present cases for the performance of GDODK when using a small tolerance. Note that the use of tolerance cannot be easily realized when using the traditional max(|$S_{11}$|)-based objective function.

The weight ($\beta_1$, …, $\beta_n$) is set so that quantities summed in (5.6) are comparable in their contributions to $F_{diplexer}$ in the optimisation process. By employing the key performance indicators discussed above, the challenges associated with the narrow valleys in the design landscape are largely mitigated, and the weights are shown to be much less sensitive compared to the traditional max(|$S_{11}$|)-based objective function. The recommended setting is that the weights corresponding to the S-parameters, bandwidth, central frequency, and transmission zeros are 1, 500, 100, 100, respectively.

## 5.3 Numerical Results and Comparisons

In this section, three diplexer examples are used to verify GDODK. These include a low-order and a high-order all-resonator diplexer, and a Tee-junction diplexer. Comparisons with optimizers in existing commercial tools, specifically, CST Microwave Studio and Mician μWave Wizard, are carried out. The numerical experiments are carried out on a desktop computer with an Intel i9-9900K 3.6 GHz CPU and 64 GB RAM.

In terms of parameter settings, two sets of parameters are involved:

(1) Algorithmic parameters: GDODK does not introduce new parameters other than the parameters in the trust region optimisation and SMEAFO. Both methods have clear parameter setting rules and they are insensitive to algorithmic parameters when following the rules.

(2) Diplexer 3D optimisation initialization parameters: In Step 1 of SMEAFO, the initial database is generated by adding a Gaussian distributed random number, $N(0, \sigma)$, to the initial 3D design. The value of $\sigma$ is related to the quality of the initial design. For example, when the initial design is poor, $\sigma$ should be large to promote exploration. For resonator lengths and iris widths in the all-resonator diplexers, $\sigma$ is 0.2% and 1% of the wavelength of centre frequency, respectively. This is because, the EM simulation responses of the initial design are often located within or very near to the required passbands, while the ripple depth and bandwidth are not far off but are still not satisfactory. For the Tee-junction diplexers, $\sigma$ for resonator dimension values associated with the junction and channel filters

is 3% of the wavelength at the centre frequency. This is because the dimensions are calculated based on the equations in [20], which may carry a relatively large error due to the mutual influence between the channels. For other dimensional values, the setting of $\sigma$ is the same as the all-resonator diplexers as described above. These values are empirical, but they are applicable generally. In other words, once set, they do not change for different diplexers.

For the reference methods, i.e., optimisation algorithms from CST Microwave Studio and Mician μWave Wizard, the default algorithmic parameters are used. For the CST trust-region framework (TRF), the global search mode [10] is used to promote its exploration ability.

### 5.3.1 Example 1

Example 1 has been introduced in Section 5.2. There are 14 design variables as shown in Fig. 5.5. The iris widths $w_1$, $w_2$, $w_3$ represent the external port couplings, $l_1$, …, $l_6$ are the resonator lengths, and $d_1$, …, $d_5$ are the iris widths. In Fig. 5.5, the cavity resonators are coupled together via inductive irises and they are operating in the TE101 mode. The resonators 1 and 4 form the stem, while the rest of the resonators form the branches in the all-resonator diplexer. Here resonators 2 and 3 cover the lower channel, while resonators 5 and 6 cover the higher channel. The cavities 1 and 4 in the stem are square structures, while all other cavities are standard waveguide cavity resonators. The thickness, $t_1$, of irises between the stem and the branches is 4 mm. All other irises have the same thickness, $t_2$ = 2 mm.

The design specifications are as follows: channel 1 covers 9.75-9.85 GHz and channel 2 covers 10.15-10.25 GHz. The return loss levels in both channels are 20 dB and the objective function is,

$$\begin{aligned} F_{ex1}(x) = {} & \beta_1(|\min(RLL_l - 20, 0)| + \max(RLL_l - 20,0)) \\ & +\beta_1(|\min(RLL_h - 20, 0)| + \max(RLL_h - 20,0)) \\ & +\beta_2(|\min(BW_l - 0.1, 0)| + \max(BW_l - 0.1,0)) \\ & +\beta_2(|\min(BW_h - 0.1, 0)| + \max(BW_h - 0.1,0)) \\ & +\beta_3(|\min(CF_l - 9.8, 0)| + \max(CF_l - 9.8,0)) \\ & +\beta_3(|\min(CF_h - 10.2, 0)| + \max(CF_h - 9.8,0)) \\ & +\beta_3(|\min(TZ - 10, 0)| + \max(TZ - 10,0)) \end{aligned} \tag{5.7}$$

where $RLL_l$ and $RLL_h$ are the extracted return loss levels of the lower and higher frequency channels, respectively. $BW_l$ and $BW_h$ are the extracted bandwidths of the lower and higher channels, respectively. $CF_l$ and $CF_h$ are the extracted centre frequencies of both channels, respectively. $TZ$ is the frequency of the transmission zero and it is located centrally between the two channels.

SMEAFO is a stochastic optimisation method. 5 runs are carried out for GDODK. The same initial design obtained by the proposed approach is used for all 5 runs. To converge, 800 iterations are used in each run. The whole optimisation costs about 67.6 hours. About 50 minutes of this cost is used for obtaining the initial 3D design, and the remaining time is used for key-performance-based optimisation (794 EM simulations). Note that after about

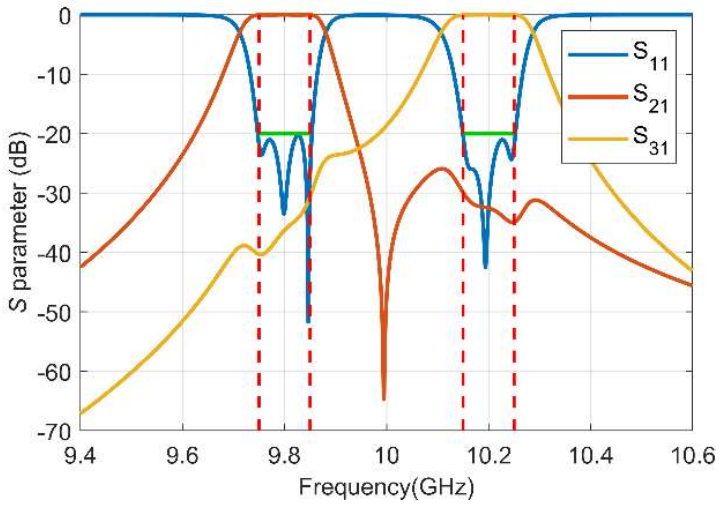



Fig. 5.12. The response of a typical optimal solution by GDODK (example 1).

TABLE 5.2 Performance function values for GDODK (5 runs)

| Performance indicators | Specifications | 1st | 2nd | 3rd | 4th | 5th |
|---|---|---|---|---|---|---|
| $RLL_1$ (dB) | 20 | 20.31 | 20.47 | 19.8 | 21.58 | 22.89 |
| $RLL_2$ (dB) | 20 | 21.03 | 19.85 | 20.68 | 20.22 | 22.56 |
| $BW_l$ (GHz) | 0.1 | 0.1063 | 0.102 | 0.097 | 0.099 | 0.1 |
| $BW_h$ (GHz) | 0.1 | 0.1032 | 0.099 | 0.098 | 0.099 | 0.1 |
| $CF_l$ (GHz) | 9.8 | 9.799 | 9.799 | 9.80 | 9.81 | 9.8 |
| $CF_h$ (GHz) | 10.2 | 10.20 | 10.20 | 10.21 | 10.2 | 10.2 |
| $TZ$ (GHz) | 10 | 9.99 | 10.02 | 10.0 | 10.02 | 10.01 |

50 hours, practically useful designs start to emerge (i.e., RLLs for both channels are better than 18 dB, and other performance values meet the required specifications). The results are shown in Table 5.2. The response of a typical solution is shown in Fig. 5.12. The optimisation is successful in all 5 runs.

To verify the advantages of the key-performance-based objective function over the traditional method using the $S_{11}$ magnitude-based objective function, 5 runs are carried out using the same initial 3D design, but without performance extraction. In other words, only SMEAFO is used to optimize the following objective function:

$$F_{S1}(x) = \max(\max(S_{11.dB}(PB_l)) - (-20), 0) + \max(\max(S_{11.d}\ \ (PB_h)) - (-20), 0)$$
$$+\max(\max(S_{21.d}\ \ (SB_{l.1})) - (-18), 0) + \max(\max(S_{21.}\quad (SB_{l.2})) - (-18), 0)$$
$$+\max(\max(S_{21.dB}(SB_{h.1})) - (-18), 0) + \max(\max(S_{21.dB}(SB_{h.2})) - (-18), 0) \quad (5.8)$$

where $S_{11.dB}$, $S_{21.dB}$, and $S_{31.dB}$ represent the decibel magnitude of the S-parameter values. $PB_l$ and $PB_h$ are the required passbands of the two channels. $SB_{l.1}$ and $SB_{l.2}$ are the two stopbands for the lower frequency channel, defined as 9 GHz to 9.64 GHz and 9.93 GHz to 11 GHz, respectively. $SB_{h.1}$ and $SB_{h.2}$ are the two stopbands for the higher frequency channel, defined as 9 GHz to10 GHz and 10.35 GHz to 11 GHz, respectively. The frequency ranges of the stopbands and the goal values in (5.8) are set based on the desired response of the optimal CM.

Again, 800 iterations are used. Using the obtained optimal designs in 5 runs, the average extracted performance values are shown in the 4th column of Table 5.3. We define a successful run as one meeting the following: (1) All the RZ, extracted by the vector fitting method (Section 5.2.3), are within the passbands, and (2) the design specifications are (almost) satisfied. It can be seen that without the proposed performance extraction method and the corresponding objective function, the success rate decreases by 60%. The main degradation happens in the return loss level and the bandwidth.

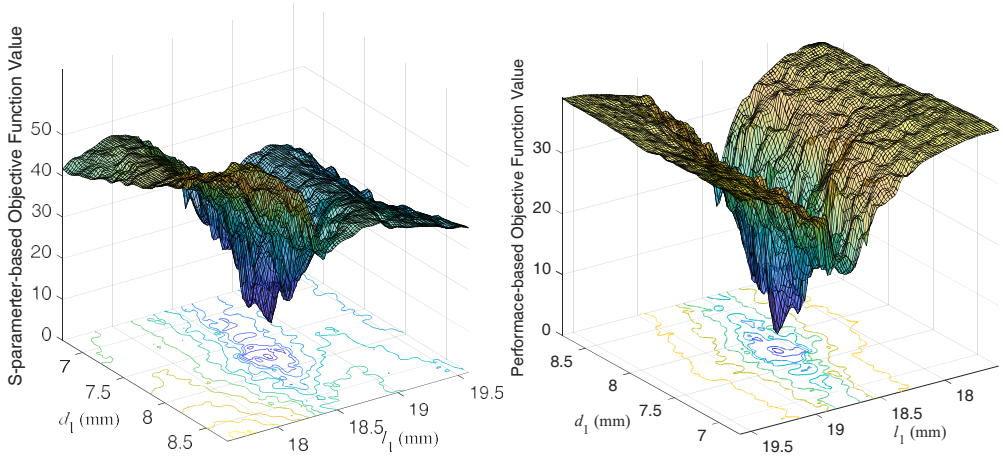



Fig. 5.13. The design landscape of example 1 with respect to the changes of $l_1$ and $d_1$ using the performance-based objective function (Eqn (16)).

Recall that Fig.5.1 shows the design landscape characteristics for using max(|$S_{11}$|) values around the initial design of this example when $d_1$ and $l_1$ are swept within +/− 0.1 mm, while the remaining design parameters are unaltered. Fig.5.13 shows a sweeping in the same range and step size, but the performance-based objective function in (5.7) is employed. It can be seen that the number of local optima considerably decreases by observing the contour map of the landscape. Note that only two design variables are considered here and the advantages of using the performance-based objective function will be more significant when considering all the 14 design variables.

To verify the advantages of the initial 3D design generation method, 5 runs are carried out using the conventional interpolation-based method [14] for comparison. The objective function is (5.8) and SMEAFO is used. Again, 800 iterations are used. Using the obtained optimal designs in all 5 runs, the average extracted performance values are shown in the 5$^{th}$ column of Table 5.3. It can be seen that all runs fail, and the results are far from satisfactory.

TABLE 5.3 Comparisons between GDODK and reference methods (example 1)

| Performance indicators | Specifications | GDODK | GDODK without performance extraction | Interpolation + SMEAFO | Interpolation + CST TRF | CST filter designer 3D + optimal initial design | Mician μWave Wizard |
|---|---|---|---|---|---|---|---|
| Success rate | | 100% | 40% | 0 | N.A. | N.A. | N.A. |
| $RLL_1$ (dB) | 20 | 21.01 | 18.01 | 0.01 | 14.35 | N.A. | 16.42 |
| $RLL_2$ (dB) | 20 | 20.868 | 19.56 | 0 | 16.63 | N.A. | 0.08 |
| $BW_l$ (GHz) | 0.1 | 0.1 | 0.1 | 0.4744 | 0.53 | N.A. | 0.09 |
| $BW_h$ (GHz) | 0.1 | 0.1 | 0.07 | 0.3256 | 0.34 | N.A. | 0.56 |
| $CF_l$ (GHz) | 9.8 | 9.8 | 9.8 | 9.7830 | 10.04 | N.A. | 9.80 |
| $CF_h$ (GHz) | 10.2 | 10.2 | 10.2 | 10.1144 | 10.07 | N.A. | 10.34 |
| $TZ$ (GHz) | 10 | 10 | 10 | 10.24 | 10.13 | N.A. | 10.89 |

Note: Because the reference methods from CST and Mician are deterministic, the success rate does not apply to them. This also applies to the following tables.

Note that SMEAFO performs global optimisation and experiments show that it needs more than 2000 iterations to obtain a reasonably good result from a low-quality initial design for this example. Hence, the clear advantages of the two proposed approaches (Section 5.2.2 and 5.2.3) are evidenced.

CST Microwave Studio and Mician μWave Wizard are then compared. Both converge before 800 iterations. Because there is no built-in function in CST to generate an initial 3D design, the conventional interpolation-based method [14] is used. Two methods in CST Microwave Studio have been widely used: (1) the trust-region framework [9], which is arguably the most popular CST optimisation algorithm; and (2) CST Filter Designer 3D, which extracts the CM from the response and carries out optimisation with CM-based objective function. The result of the former method is shown in the 6$^{th}$ column of Table 5.3. The obtained result is far from satisfactory because it is trapped in a local optimum and fails the optimisation. The same algorithm still traps the optimisation in a local optimum, even

when the initial design approach in Section 5.2.2 is used. For CST Filter Designer 3D, the initial design obtained by our approach is employed. However, the CST Filter Designer 3D is not able to successfully extract the CM for this example because the CST Filter Designer 3D does not apply to the diplexers with an all-resonator structure. The above experiments show the shortcomings of the conventional initial 3D design generation method, the trust-region local optimisation method, and the CM extraction method for diplexer 3D optimisation.

Following the suggested process of Mician μWave Wizard, two-channel filters are firstly obtained using built-in analytical functions, which serve as the initial 3D design. Then, the Mician Extreme optimizer [12] is employed. The result is shown in the 8$^{th}$ column of Table 5.3, which is far from satisfactory. Table 5.3 demonstrates the efficacy of GDODK, compared to alternative popular tools, for this example. The simulation is performed on the laptop computer with i7-7700HQ CPU @ 2.80GHz and 16 GB RAM. The simulation time of the Example 1 is 2m 28s by using CST and 13s by using Mician μWave Wizard.

### 5.3.2 Example 2

Example 2 is a 10$^{th}$ order all-resonator diplexer operating in the X-band using a WR90 waveguide. Fig. 5.14 shows a top view of the air model of the diplexer. The cavity resonators are coupled together via inductive irises in a folded configuration. The thickness $t$ of all irises is equal to 2 mm. There are 22 design variables in total as shown in Fig. 5.14: $l_1$, …, $l_{10}$ are the lengths of the resonators, $d_1$, …, $d_9$ are the iris widths of the mutual couplings, $w_1$, $w_2$,

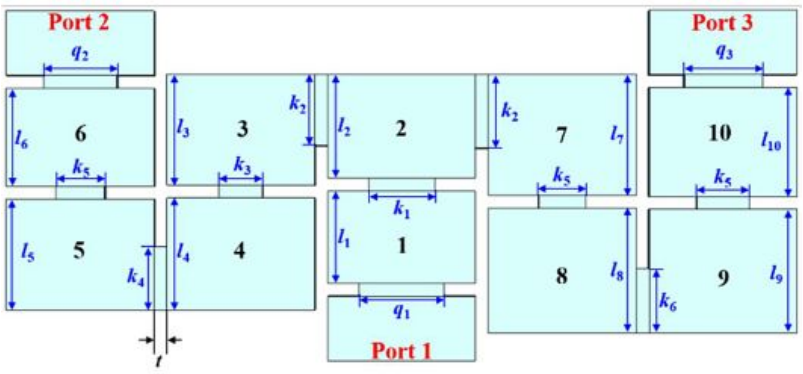



Fig. 5.14. A 10th order waveguide diplexer.

Table 5.4 The optimal coupling coefficients for example 2

| | | | |
|---|---|---|---|
| $m(1, P1)$ | 0.2687 | $m(1, 1)$ | −0.0043 |
| $m(6, P2)$ | 0.1930 | $m(2, 2)$ | 0.0020 |
| $m(10, P3)$ | 0.1869 | $m(3, 3)$ | 0.0597 |
| $m(1, 2)$ | 0.0799 | $m(4, 4)$ | 0.0652 |
| $m(2, 3)$ | 0.0344 | $m(5, 5)$ | 0.0659 |
| $m(3, 4)$ | 0.0220 | $m(6, 6)$ | 0.0660 |
| $m(4, 5)$ | 0.0218 | $m(7, 7)$ | −0.0547 |
| $m(5, 6)$ | 0.0303 | $m(8, 8)$ | −0.0624 |
| $m(2, 7)$ | 0.0389 | $m(9, 9)$ | −0.0633 |
| $m(7, 8)$ | 0.0239 | $m(10,10)$ | −0.0635 |
| $m(8, 9)$ | 0.0230 | | |
| $m(9, 10)$ | 0.0306 | | |

$w_3$ are the iris widths of the external port couplings.

The diplexer is designed to meet the following specifications: channel 1 covering 9.5-9.85 GHz and channel 2 covering 10.15 -10.5 GHz; return loss levels for both channels are 20 dB. The CM is obtained by the GACMS CM synthesis method [21], and the optimal coupling coefficients are listed in Table 5.4. The ideal S-parameter response is shown in Fig. 5.10. According to the design specifications, the key-performance-based objective function is

defined as follows:

$$\begin{aligned} F_{ex2} = {} & \beta_1(\min(RLL_l - 20 + 1,0) + \max(RLL_l - 20 - 2,0)) \\ & + \beta_1(\min(RLL_h - 20 + 1,0) + \max(RLL_2 - 20 - 2,0)) \\ & + \beta_2(\min(BW_l - 0.35 + 0.02,0) + \max(BW_l - 0.35 - 0.02,0)) \\ & + \beta_2\Big(\min\Big(BW_h - 0.35 + 0.02,0\Big) + \max(BW_h - 0.35 - 0.02,0)\Big) \\ & + \beta_3(\min(CF_l - 9.675 + 0.035,0) + \max(CF_l - 9.675 - 0.035,0)) \\ & + \beta_3(\min(CF_h - 10.325 + 0.035,0) + \max(CF_h - 10.325 - 0.035,0)) \end{aligned} \tag{5.9}$$

The description of (5.9) is similar to (5.7), so it is not restated here. Different from example 1 where zero tolerance is used, a small tolerance is used in this example. This shows that GDODK can also find acceptable solutions when designs that exactly match the specifications are difficult to obtain. This is hard to be realized when using the traditional max($|S_{11}|$)-based objective function.

Five runs of GDODK are carried out with the same initial design obtained by the proposed method in Section 5.2.2. To make GDODK converge, 1300 iterations are used in each run. The whole optimisation costs about 102 hours. Among these, 77 minutes is used to obtain the initial 3D design, and the remaining time is used for key-performance-based optimisation (i.e., 1210 EM simulations). Note that after about 76 hours, practically useful designs start to appear. The results are shown in Table 5.5. The response of a typical solution is shown in Fig. 5.15. It can be seen that all 5 runs obtain acceptable designs.

The GDODK result is compared with the same reference methods as in example 1. The

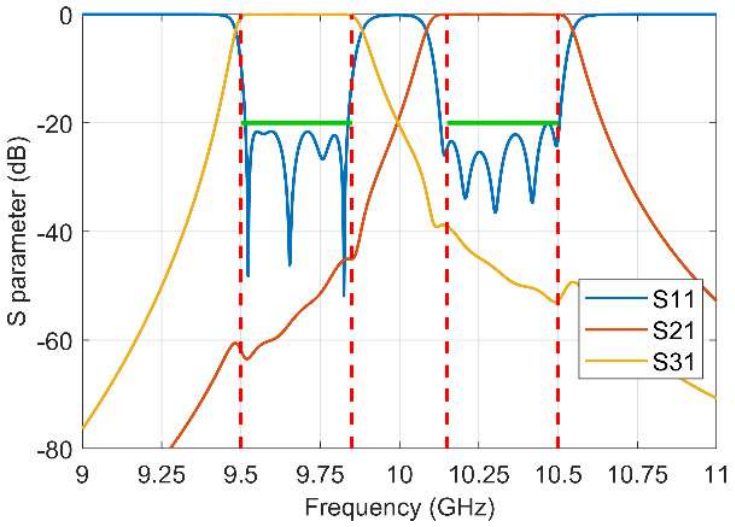



Fig. 5.15. The response of a typical optimal solution by GDODK (example 2).

TABLE 5.5 Performance function values for GDODK (1300 iterations)

| Performance indicators | Specifications | 1st | 2nd | 3rd | 4th | 5th |
|---|---|---|---|---|---|---|
| $RLL_1$ (dB) | 20 | 21.60 | 20.29 | 19.09 | 20.20 | 21.56 |
| $RLL_2$ (dB) | 20 | 21.38 | 20.55 | 19.86 | 19.02 | 20.06 |
| $BW_l$ (GHz) | 0.35 | 0.33 | 0.33 | 0.33 | 0.33 | 0.33 |
| $BW_h$ (GHz) | 0.35 | 0.36 | 0.33 | 0.34 | 0.33 | 0.37 |
| $CF_l$ (GHz) | 9.675 | 9.708 | 9.694 | 9.691 | 9.704 | 9.674 |
| $CF_h$ (GHz) | 10.325 | 10.316 | 10.320 | 10.348 | 10.337 | 10.318 |

settings for the comparison are exactly the same as example 1, except for the number of iterations which is set to 1300 for the global optimisation-based methods. Eqn. (5.8) in example 1 using the max($|S_{11}|$)-based objective function is still adopted. The required passbands $PB_l$ and $PB_h$ are changed to 9.5 - 9.85 GHz and 10.15 - 10.5 GHz, respectively. The two stopbands for the lower frequency channels, $SB_{l.1}$ and $SB_{l.2}$, are 9 - 9.42 GHz and 9.98 - 11 GHz, respectively. The two stopbands for the higher frequency channels, $SB_{h.1}$ and $SB_{h.2}$, are 9 - 10.02 GHz and 10.62 - 11 GHz, respectively. These are based on the desired response of the optimal CM.

The comparison is shown in Table 5.6. The simulation is also performed on the laptop

Table 5.6 Comparisons between GDODK and reference methods (example 2)

| Performance indicators | Specifications | GDODK | GDODK without performance extraction | Interpolation + SMEAFO | Interpolation + CST TRF | CST filter designer 3D + optimal initial design | Mician μWave Wizard |
|---|---|---|---|---|---|---|---|
| Success rate | | 100% | 0 | 0 | N.A. | N.A. | N.A. |
| $RLL_1$ (dB) | 20 | 20.55 | 15.30 | 17.2167 | 19.4328 | N.A. | 0 |
| $RLL_2$ (dB) | 20 | 20.17 | 19.54 | 18.5088 | 6.8917 | N.A. | 0.01 |
| $BW_l$ (GHz) | 0.35 | 0.33 | 0.34 | 0.3163 | 0.3592 | N.A. | 0.8553 |
| $BW_h$ (GHz) | 0.35 | 0.344 | 0.35 | 0.3317 | 0.4844 | N.A. | 1.4573 |
| $CF_l$ (GHz) | 9.675 | 9.694 | 9.673 | 9.6838 | 9.6644 | N.A. | 9.9 |
| $CF_h$ (GHz) | 10.325 | 10.328 | 10.323 | 10.3309 | 10.3929 | N.A. | 9.93 |

workstation with i7-7700HQ CPU @ 2.80GHz and 16 GB RAM. The simulation time of the Example 2 are 3m 43s by using CST and 1m 51s by using Mician μWave Wizard. The same conclusions made for example 1 can be drawn for this example. The advantages of the two approaches (Section 5.2.2 and 5.2.3) are demonstrable. It is worth noting that without using the key-performance-based objective function, the local optimisation algorithm and the SMEAFO method can only converge to a design with good RLL for one channel out of the two. The optimisation also gets trapped in a local optimum. Again, this is due to the steep slope (as shown in Fig. 5.2 and Fig. 5.15) of the design landscape which is a common issue for high-order diplexers.

### 5.3.3 Example 3

Example 3 is an 8$^{th}$ order Tee-junction diplexer operating in the Ku-band. The diplexer is designed using a WR62 waveguide. Fig. 5.16 shows the air model of the diplexer. The WR62 waveguide has the standard dimensional values of $a$ = 15.799 mm and $b$ = 7.899 mm,

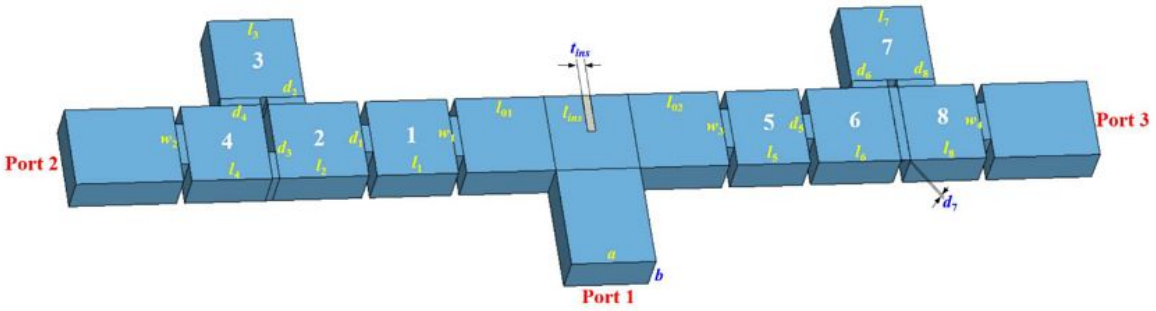



Fig. 5.16. An 8th order Tee-junction waveguide diplexer.

and there are 23 design variables in total. Resonators 3 and 7 are square structures and all others are standard waveguide cavity resonators. All the resonators are operating in the TE101 mode. $l_1$, …, $l_8$ are their lengths, $w_1$, $w_2$, $w_3$ are the widths related to the external port couplings, $d_1$, …, $d_8$ are the widths of the coupling irises. This diplexer structure contains two cross-couplings, $d_3$ and $d_7$, which are used to generate two TZs to improve the rejection between the channels. Except for the capacitive iris, $d_7$, all other irises are inductive. The iris thickness of $d_3$ and $d_7$, depends on the values of $d_2$, $d_4$, $d_6$, and $d_8$, while the thickness of all other irises is 1.5 mm. A ridge Tee-junction is implemented to improve the matching of the ports [22]. The metal ridge thickness, $t_{ins}$ is 1.5 mm, the height is $b$ and the insertion depth, $l_{ins}$, is a design variable. $l_{01}$ and $l_{02}$ are lengths of the reference sections of channel filters and their initial dimensional values are calculated according to the equations in [6]. The initial dimensional value of $l_{ins}$ is optimized to satisfy max($S_{21.dB}$) > -3 dB and max($S_{31.dB}$) > −3 dB within the passbands. The initial values of all other variables are obtained by the proposed method in Section 5.2.2.

The Tee-junction diplexer is designed based on the following specifications: channel 1

Table 5.7 The optimal coupling coefficients for example 3

| | | | | | |
|---|---|---|---|---|---|
| m(1, 2) | 0.0174 | m(1, 1) | 0.0444 | m(1, P1) | 0.1454 |
| m(2, 3) | 0.0133 | m(2, 2) | 0.0398 | m(5, P1) | 0.1430 |
| m(3, 4) | 0.0175 | m(3, 3) | 0.0328 | m(4, P2) | 0.1456 |
| m(2, 4) | 0.0044 | m(4, 4) | 0.0391 | m(6, P2) | 0.1428 |
| m(5, 6) | 0.0167 | m(5, 5) | −0.0451 | | |
| m(6, 7) | 0.0128 | m(6, 6) | −0.0405 | | |
| m(7, 8) | 0.0168 | m(7, 7) | −0.0339 | | |
| m(6, 8) | −0.0041 | m(8, 8) | −0.0398 | | |

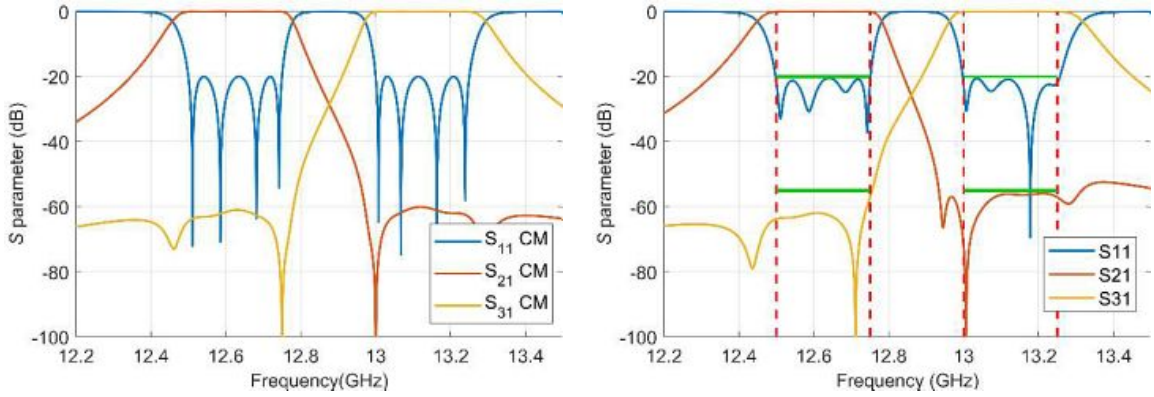
covering 12.5 - 12.75 GHz and channel 2 covering 13 - 13.25 GHz; return loss levels in both channels are 20 dB. The isolation performance within the passbands for both channels is better than 55 dB, namely {max($S_{31.dB}$(12.5:12.75)) < −55 dB} ∪ {max($S_{21.dB}$(13:13.25)) < −55 dB}.

The CM is obtained by the junction-based diplexer CM synthesis method in [20]. The obtained coupling coefficients are listed in Table 5.7 and the desired S-parameter response is shown in Fig. 5.17 (a). According to the design specifications, the key-performance-based objective function can be defined as follows.

$$
\begin{aligned}
F_{ex} &= \beta_1(|\min(RLL_l - 20 + 1,0)| + \max(RLL_l - 20 - 2,0)) \\
&+\beta_1(|\min(RLL_h - 20 + 1,0)| + \max(RLL_h - 20 - 2,0)) \\
&+\beta_2(|\min(BW_l - 0.25 + 0.01,0)| + \max(BW_l - 0.25 - 0.01,0)) \\
&+\beta_2(|\min(BW_h - 0.25 + 0.01,0)| + \max(BW_h - 0.25 - 0.01,0)) \\
&+\beta_3(|\min(CF_l - 12.625 + 0.025,0)| + \max(CF_l - 12.625 - 0.025,0)) \\
&+\beta_3(|\min(CF_h - 13.125 + 0.025,0)| + \max(CF_h - 13.125 - 0.025,0))
\end{aligned}
$$

$$+\beta_4|\min(IS_l - 55,0)| + \beta_4|\min(IS_h - 55,0)| \tag{5.10}$$

In addition to the symbols appearing in examples 1 and 2, $IS_l$ and $IS_h$ are included to account for isolation performance. They are defined by $IS_l$ = max($|S_{31}(PB_l)|$) and $IS_h$ = max($|S_{21}(PB_h)|$).




(a) (b)

Fig. 5.17. The S-parameter response: The response of (a) the coupling matrix for example 3, (b) a typical optimal solution by GDODK for example 3.

5 runs of GDODK are carried out. To make the algorithm converge, 1500 iterations are used in each run. The whole optimisation process costs about 125 hours. About 76 minutes of this time cost is used for obtaining the initial 3D design, and the remaining time is used for the key-performance-based optimisation (about 1418 EM simulations). Note that after about 70 hours, practical useful designs start to appear. The results are shown in Table 5.8 The response of a typical solution is shown in Fig. 5.17 (b). It can be seen that 4 acceptable designs are obtained in the 5 runs. Our investigation shows that the failed run could be a result of the initial size of resonators connecting with the junction and channel filters,

Table 5.8 Performance function values for GDODK (1500 iterations)

| Performance indicators | Specifications | 1st | 2nd | 3rd | 4th | 5th |
|---|---|---|---|---|---|---|
| RLL1 (dB) | >20 | 20.41 | 20.04 | 19.91 | 20.37 | 20.47 |
| RLL2 (dB) | >20 | 20.56 | 19.94 | 20.83 | 19.51 | 7.11 |
| BWl (GHz) | 0.25 | 0.25 | 0.25 | 0.25 | 0.26 | 0.24 |
| BWh (GHz) | 0.25 | 0.26 | 0.25 | 0.26 | 0.26 | 0.23 |
| CFl (GHz) | 12.625 | 12.626 | 12.622 | 12.623 | 12.629 | 12.59 |
| CFh (GHz) | 13.125 | 13.128 | 13.122 | 13.123 | 13.122 | 13.11 |
| ISl (dB) | >55 | 57.27 | 55.14 | 55.44 | 57.79 | 54.99 |
| ISh (dB) | >55 | 56.25 | 56.46 | 55.64 | 55.97 | 60.42 |

Table 5.9 Comparisons between GDODK and reference methods (example 3)

| Performance indicators | Specifications | GDODK | Interpolation + CST TRF | CST filter designer 3D + optimal initial design |
|---|---|---|---|---|
| Success rate | | 80% | N.A. | N.A. |
| RLL1 (dB) | 20 | 20.18 | 19.1124 | 9.2747 |
| RLL2 (dB) | 20 | 20.21 | 1.9325 | 12.3501 |
| BWl GHz) | 0.25 | 0.2525 | 0.2516 | 0.2990 |
| BWh GHz) | 0.25 | 0.2575 | 0.3032 | 0.2744 |
| CFl (GHz) | 12.625 | 12.625 | 12.6269 | 12.6168 |
| CFh (GHz) | 13.125 | 13.124 | 12.8767 | 13.1297 |
| ISl (dB) | 55 | 56.41 | 26.4795 | 61.1267 |
| ISh (dB) | 55 | 56.08 | 50.0792 | 58.7472 |

Note: The values of GDODK are based on the average 4 successful runs

approximated by equations in [6], being too far away from the optimum.

Since the advantages of the two approaches (i.e., Section 5.2.2 and 5.2.3) are already shown in examples 1 and 2, only comparisons with existing tools are considered here. The Mician μWave Wizard can only generate standard waveguide filters without cross-couplings. Therefore, it is not included in the comparison. CST Microwave Studio is considered. The CST trust-region framework, CST Filter Designer 3D, and average extracted performance values from 5 runs of GDODK are compared (the settings are exactly the same as examples 1 and 2). The results are shown in Table 5.9. It can be seen that CST Microwave Studio fails to obtain acceptable designs. Unlike examples 1 and 2, the CST Filter Designer

3D can extract the CM, but the optimisation fails to converge to the desired performance. Specifically, the return loss levels and bandwidths of the CST Microwave Studio generated designs are far from satisfactory. This example again shows the efficacy of GDODK for this Tee-junction diplexer.

### 5.3.4 Discussion

From the two all-resonator diplexers and the Tee-junction diplexer design optimisation, the following observations are made: (1) The performance extraction and performance-based objective function are vital for successful optimisation. Using the same SMEAFO optimizer, but without employing these techniques, the success rate either decreases substantially or the optimisation simply cannot succeed due to trapping in a local optimum. This verifies that the above technique enables global optimisation for diplexers. (2) The systematic local optimisation-based initial 3D design generation method contributes to the efficiency and success rate. When the initial design obtained by the conventional interpolation-based method is used, SMEAFO needs to use 2 to 3 times more EM simulations to obtain a practically useful design, while deterministic local optimisation methods in CST and Mician are not successful. This verifies the importance of the initial design in the diplexer global optimisation and the efficacy of the proposed method. The main drawback of the proposed optimisation method is the efficiency of the surrogate modelling and optimisation. Although the optimisation results can be stably obtained, the optimisation cost a very long time. This attributes to the global optimisation method used

in SMEAFO. It needs further improvement in future works.

## 5.4 Summary of this Chapter

This chapter presents an EM optimisation method for microwave diplexers called a General Diplexer Optimisation method guided by Design Knowledge (GDODK). This optimisation process can be fully automatic without the supervision of designers once it starts. A local-optimisation based physical dimensioning method is utilized to provide a high-quality starting point for the diplexer optimisation, narrowing down the search ranges. On the other, a novel performance-based objective function is proposed for the diplexer optimisation, smoothing the characteristic landscape. Three examples demonstrate the effectiveness of the proposed optimisation method.

## References

[1] M. O. Akinsolu, B. Liu, V. Grout, P. I. Lazaridis, M. E. Mognaschi, and P. D. Barba, "A parallel surrogate model assisted evolutionary algorithm for electromagnetic design optimisation," IEEE Trans. Emerg. Topics Comput. Intell., vol. 3, no. 2, pp. 93-105, April 2019.

[2] B. Liu, H. Yang, and M. J. Lancaster, "Synthesis of coupling matrix for diplexers based on a self-Adaptive differential Evolution Algorithm," IEEE Trans. Microw. Theory Techn., vol. 66, no. 2, pp. 813-821, Feb. 2018.

[3] B. Liu, H. Yang, and M. J. Lancaster, "Global optimisation of microwave filters based on a surrogate model-assisted evolutionary algorithm," IEEE Trans. Microw. Theory Techn., vol. 65, no. 6, pp. 1976–1985, 2017.

[4] X. Shang, W. Xia, and M. J. Lancaster, "The design of waveguide filters based on cross-coupled resonators," Microwave and Optical Technology Letters, vol. 56, no.1, pp. 3-8, Jan., 2014.

[5] P. Zhao and K. Wu, "Homotopy optimisation of microwave and millimetre-wave filters based on neural network model", IEEE Trans. Microw. Theory Techn., vol. 68, no. 4, pp. 1390-1400, April 2020.

[6] M. Sharifi Sorkherizi and A. A. Kishk, "Use of group delay of sub-circuits in optimisation of wideband large-scale bandpass filters and diplexers," IEEE Trans. Microw. Theory Techn., vol. 65, no. 8, pp. 2893-2905, Aug. 2017.

[7] X. Wang, Y. Zhang, G. Shen, W. Che, H. Chen, and W. Feng, "Automated optimisation of multiplexers based on aggressive space mapping and cauchy method," 2015 International Workshop on Electromagnetics: Applications and Student Innovation Competition (iWEM), Hsinchu, 2015, pp. 1-4.

[8] T. S. Beukman, C. Gahete, C. Vicente, and M. Wild, "Simulation enabled design of microwave filters and multiplexers," 2019 IEEE 20th Wireless and Microwave Technology Conference (WAMICON), Cocoa Beach, FL, USA, 2019, pp. 1-4.

[9] A. R. Conn, N. I. M. Gould, and P. L. Toint, "Trust region methods," MPS-SIAM Series on Optimisation. Philadelphia, PA, USA: SIAM, 2000.

[10] Dassault Systèmes, 64289 Darmstadt, Germany. CST Studio Suite® 2019.

[11] C. Zhang, F. Feng, V.-M.-R. Gongal-Reddy, Q. J. Zhang, and J. W. Bandler, "Cognition-driven formulation of space mapping for equal-ripple optimisation of microwave filters," IEEE Trans. Microw. Theory Techn., vol. 63, no. 7, pp. 2154–2165, 2015.

[12] Mician μWave Wizard, "The user manual 8.5", 2019.

[13] M. Emmerich, K. Giannakoglou, and B. Naujoks, "Single-and multi- objective evolutionary optimisation assisted by Gaussian random field metamodels," IEEE Trans. Evol. Comput., vol. 10, no. 4, pp. 421–439, 2006.

[14] J. Hong and M. J. Lancaster, Microstrip filters for RF/microwave applications. John Wiley & Sons; 2004.

[15] D. Swanson and G. Macchiarella, "Microwave filter design by synthesis and optimisation," in IEEE Microwave Magazine, vol. 8, no. 2, pp. 55-69, April 2007.

[16] X. Shang, Y. Wang, W. Xia, and M. J. Lancaster, "Novel multiplexer topologies based on all-resonator structures," IEEE Trans. Microw. Theory Techn., vol. 61, no. 11, pp. 3838–3845, Nov. 2013.

[17] B. Gustavsen and A. Semlyen, "Rational approximation of frequency domain response by Vector Fitting", IEEE Trans. Power Del., vol. 14, no. 3, pp. 1052-1061, July 1999.

[18] F. Feng, W. Na, W. Liu, S. Yan, L. Zhu, J. Ma, and Q.-J. Zhang, "Multifeature-assisted neuro-transfer function surrogate-based EM optimisation exploiting trust-region algorithms for microwave filter design," IEEE Trans. Microw. Theory Techn., vol. 68, no. 2, pp. 531-542, Feb. 2020.

[19] F. Feng, C. Zhang, W. Na, J. Zhang, W. Zhang, and Q. Zhang, "Adaptive Feature Zero Assisted Surrogate-Based EM Optimisation for Microwave Filter Design," IEEE Microw. Wireless Compon. Lett., vol. 29, no. 1, pp. 2-4, Jan. 2019.

[20] G. Macchiarella and S. Tamiazzo, "Novel approach to the synthesis of microwave diplexers," IEEE Trans. Microw. Theory Techn., vol. 54, no. 12, pp. 4281–4290, Dec. 2006.

[21] Y. Yu, B. Liu, Y. Wang, M. J. Lancaster, and Q. S. Cheng, "A general coupling matrix synthesis method for all-Resonator diplexers and multiplexers," IEEE Trans. Microw. Theory Techn., vol. 68, no. 3, pp. 987-999, March 2020.

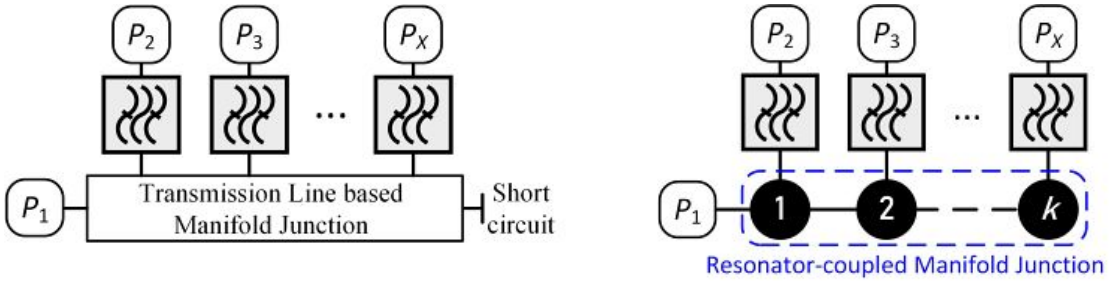
[22] J. Bornemann and M. Mokhtaari, "The bifurcated E-plane T-junction and its application to waveguide diplexer design", Proc. German Microwave Conf., 1a-5, 4 p., Karlsruhe, Germany, Mar. 2006.

# Chapter 6 Resonant Manifold Multiplexers

This chapter presents a new compact multiplexer structure and its design approach, based on a novel resonant manifold. Different from typical transmission-line-based manifold multiplexers, the proposed manifold junction is formed of coupled-resonators, so that the manifold also contributes to the filtering poles and selectivity in the passbands. The all-resonator configuration achieves a more compact footprint than the conventional manifold. This multi-port filtering network can be represented by a single coupling matrix which can be obtained by using a robust optimisation-based method. A tailored channel frequency allocation scheme is presented for the proposed multiplexers with different numbers of channels. To validate the proposed concept, a triplexer, and a 5-channel multiplexer, both at X-band, is designed and tested using the rectangular waveguide technology. The work in this chapter has been published in [1].

## 6.1 Introduction

As introduced in Chapter 2, several configurations have been used to implement frequency multiplexers [2]. Some configurations combine hybrids or circulators with channel filters to simplify design and tuning as well as to improve the isolation performance between channels [2]. However, these configurations lead to relatively high losses and large footprints due to the use of hybrids and circulators [2]-[3], [5]. To make the signal distribution network in multiplexes more compact, manifold-junction and star-junction




(a) (b)

Fig. 6.1. (a) Schematic diagram of a conventional manifold multiplexers; (b) Schematic diagram of the proposed resonant manifold multiplexer.

configurations were developed and eventually became the mainstream [2], [5]. The star-junction multiplexers combine all the channel filters to a resonant or a non-resonant node. A coupling matrix representing the multiplexer can be systematically obtained based on the calculated characteristic polynomials of the multiplexer [2], [6]. The multiplexers are physically realized based on the obtained coupling matrix and have been applied in base station applications for mobile communications [2], [6]-[8].

Manifold multiplexers are usually designed using optimisation-based methods rather than synthesis-based approaches [5], [9]. In a typical manifold multiplexer, as illustrated in Fig. 6.1(a), multiple channel filters are connected with a transmission-line-based manifold junction (normally a waveguide) with optimized separations between them [3]. There exists relatively strong interaction between each channel filter, compared with those using hybrids or circulators. The manifold has to be integrally designed to compensate for the mutual influence between channels [3]. This also means any change in frequency allocation of channels will require a new multiplexer design [3].

As an alternative configuration, the all-resonator-based configuration has also been

applied to design multiplexers [15]. As introduced in Chapter 2, the configuration is very flexibly designed based on coupling matrix theory [16]-[21]. However, when the number of the channels becomes larger (e.g., > 4) [23], the multiplexer design will become difficult and complex.

A new multiplexer configuration using a novel resonant manifold structure based exclusively on coupled resonators is proposed in this chapter. The topology is shown in Fig.6.1(b). It can be noticed that the transmission-line-based manifold junction is replaced by an "all-resonator" manifold junction which contributes to the transmission poles and therefore frequency selectivity. The overall structure can be represented by a single integral coupling matrix. In the following, the coupling matrix synthesis method will be discussed with a tailored channel frequency allocation method. The proposed multiplexer can be dimensioned by using the obtained coupling matrix. Then, a step-tuning based EM optimisation method is employed to address the extensive EM optimisation tasks [28]-[29]. To demonstrate the design concept, two exemplary prototypes, including a triplexer and a pentaplexer, are synthesized, designed, and fabricated.

## 6.2 Resonant Manifold Triplexer

Firstly, a triplexer is employed to demonstrate the synthesis of the coupling matrix and the design. The topology of the triplexer with a 3-rd order resonant manifold (Resonator-1, 4 and 7) is shown in Fig. 6.2(a). Frequency channels are at 9.7 - 9.8 GHz (Channel 1), 9.95 -

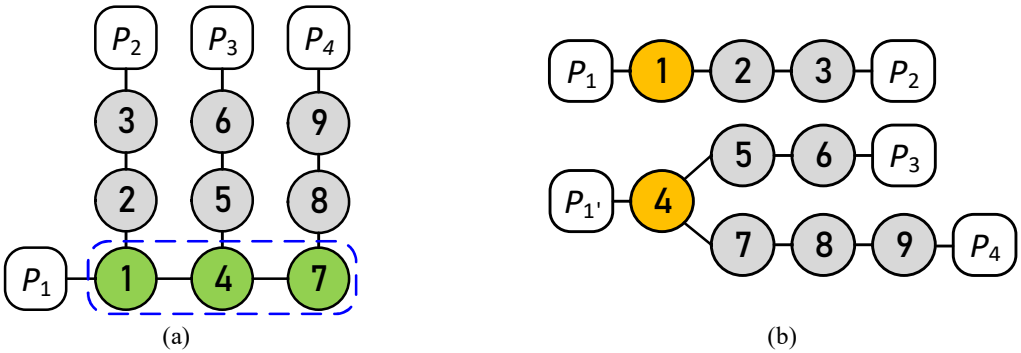


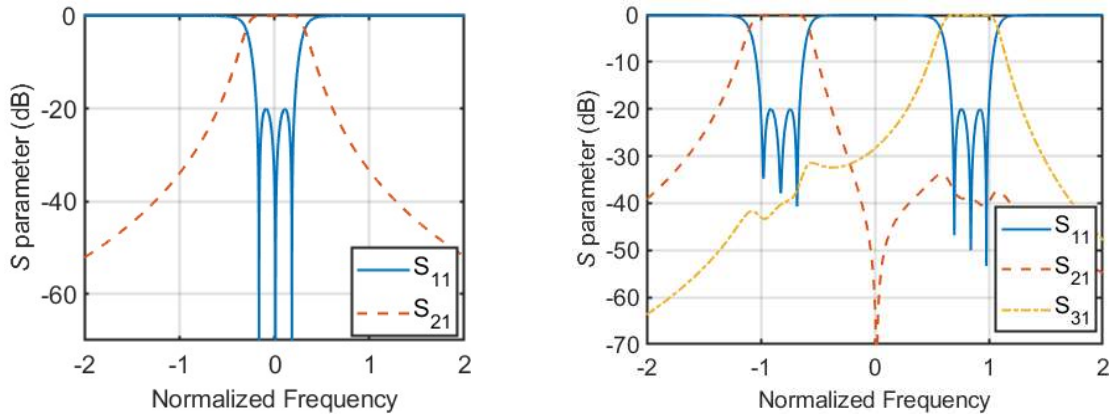

Fig. 6.2. (a) Coupling topology of the resonant manifold triplexer, where the green circles indicate the resonant manifold. (b)The segment scheme for the triplexer. The synthesis results for the subcircuits are employed as the initial coupling values for the triplexer synthesis.

10.05 GHz (Channel 2), and 10.2 - 10.3 GHz (Channel 3), respectively. Return loss levels (*RLL*s) in the passbands are at 20 dB. The coupling matrix is first obtained with an appropriate channel frequency allocation to be discussed in more detail in Appendix C. Then, the physical dimensioning is implemented according to the obtained coupling matrix. Finally, the triplexer is optimized starting from the initial dimensions. The details of the design procedure are as follows.

## 6.2.1 Coupling Matrix Synthesis

To begin with, the passbands are normalized to $CH_1$: [−1, −0.5919], $CH_2$: [−0.1879, 0.2119], and $CH_3$: [0.6079, 1]. The coupling matrix synthesis uses the GACMS method provided in Chapter 4. For the effective use of the GACMS method, high quality starting values of the matrix and a reasonable channel frequency allocation are desired. Segmenting is first conducted to generate the starting coupling coefficients for the triplexer.

In the resonant manifold shown in Fig. 6.2(a), the junction resonators (Resonator-1 and




(a) (b)

Fig. 6.3. The S-parameter corresponding to the coupling coefficients of the filter and the diplexer in Fig. 6.2(b), used as the initial values for the triplexer.

4) are the basic frequency distribution elements. By segment of the connection between the two junction resonators1 and 4, as shown in Fig. 6.2(b), the triplexer is divided into a filter and a diplexer. The starting coupling values for the triplexer come from the synthesis of a filter (Resonator 1 to 3) and a diplexer (Resonator 4 to 9).

For the proposed resonant multiplexer, there are various ways to allocate frequencies to the channels. For this triplexer, there can be six different frequency allocation schemes. But not all lead to satisfactory responses. In this thesis, scheme 3 shown in Appendix C is chosen for the design, where $CH_2$, $CH_1$, and $CH_3$ are sequentially assigned to the three branches of the triplexer. The synthesis approach is illustrated in the following.

The starting coupling coefficients are taken from the 3rd-order filter and the 6th-order diplexer with the responses shown in Fig. 6.3. Optimisation on the coupling matrix of the triplexer is then executed using a method similar to [23]. The S-parameter-based objective function is formulated as

Table 6.1 THE OPTIMAL COUPLING COEFFICIENTS FOR THE TRIPLEXER

| Mutual Couplings | Values | Self-couplings | Values | Input/output Couplings | Values |
|---|---|---|---|---|---|
| $m(1, 2)$ | 0.2982 | $m(1, 1)$ | 0.0042 | $m(1, P1)$ | 0.7662 |
| $m(2, 3)$ | 0.1706 | $m(2, 2)$ | 0.0138 | $m(3, P2)$ | 0.4424 |
| $m(1, 4)$ | 0.7113 | $m(3, 3)$ | 0.0138 | $m(6, P3)$ | 0.4478 |
| $m(4, 5)$ | 0.2346 | $m(4, 4)$ | −0.0127 | $m(9, P4)$ | 0.4368 |
| $m(5, 6)$ | 0.1780 | $m(5, 5)$ | −0.7970 | | |
| $m(4, 7)$ | 0.5616 | $m(6, 6)$ | −0.8240 | | |
| $m(7, 8)$ | 0.2957 | $m(7, 7)$ | 0.1533 | | |
| $m(8, 9)$ | 0.1838 | $m(8, 8)$ | 0.7163 | | |
| | | $m(9, 9)$ | 0.8154 | | |

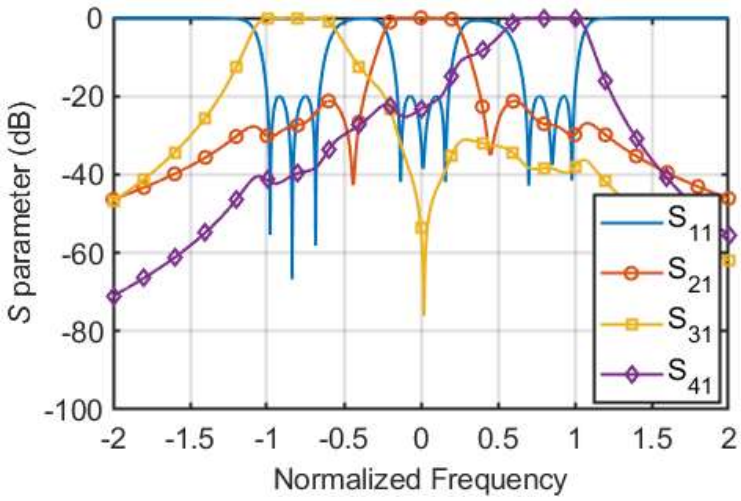



Fig. 6.4. The S-parameter responses corresponding to the optimized coupling coefficients for the triplexer.

$$O_1 = \frac{\max(PB_1 - (-20), 0)}{20} + \frac{\max(PB_2 - (-20), 0)}{20} + \frac{\max(PB_3 - (-20), 0)}{20} \tag{6.1}$$

where $PB_1 = max(|S_{11}(CH_1)|)$ ; $PB_2 = max(|S_{11}(CH_2)|)$ and $PB_3 = max(|S_{11}(CH_3)|)$ . Note that for all the frequency allocation schemes are shown in Appendix C, the same objective function (6.1) is utilized. The obtained optimal coupling coefficients are listed in Table 6.1 and the corresponding S-parameter responses for the triplexer are shown in Fig.

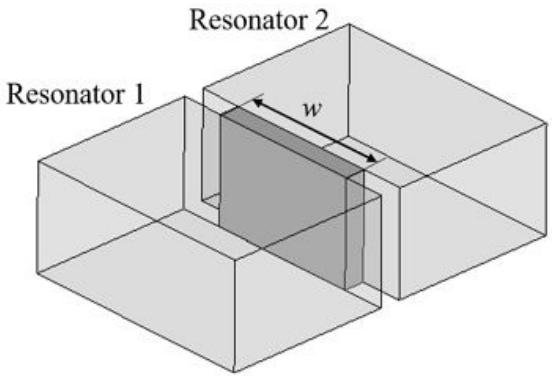



Fig. 6.5. Structure used to extract the coupling between two waveguide resonators.

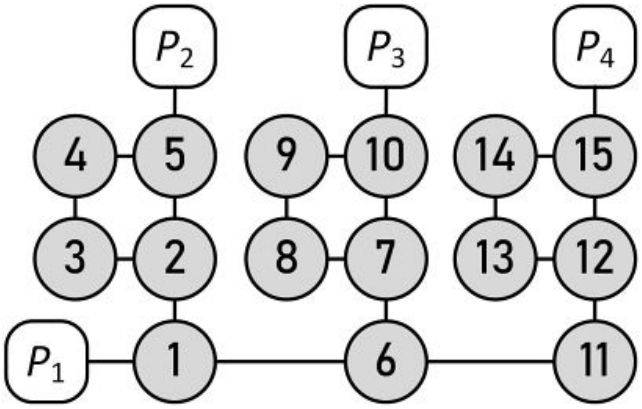



Fig. 6.6. The coupling topology of the Ku-band triplexer with contiguous channels.

6.4. It can be seen that transmission zeros are generated in $S_{21}$ and $S_{31}$. This is because resonators 4 and 7 can be seen as two frequency attenuation structures for Channel 1 whereas resonator 7 is an attenuation structure for Channel 2 [26].

It is worth noting that the mutual coupling values within the resonant manifold junction are much stronger than those in the branches, as they are required to allow the subsequent channels to pass through. The maximum realizable coupling limits the overall

Table 6.2 Coupling Coefficients for The Triplexer with Contiguous Channels

| Mutual couplings | | | | | |
|---|---|---|---|---|---|
| m(1,2) | 0.4809 | m(6,7) | 0.2904 | m(11,12) | 0.2821 |
| m(2,3) | 0.1874 | m(7,8) | 0.1867 | m(12,13) | 0.1850 |
| m(3,4) | 0.2162 | m(8,9) | 0.2312 | m(13,14) | 0.2282 |
| m(4,5) | 0.2656 | m(9,10) | 0.2811 | m(14,15) | 0.2786 |
| m(2,5) | -0.0444 | m(7,10) | -0.0445 | m(12,15) | -0.0443 |
| m(1,6) | 0.6684 | m(6,11) | 0.6404 | | |
| Self couplings | | | | | |
| m(1,1) | 0.0022 | m(6,6) | 0.0065 | m(11,11) | 0.1268 |
| m(2,2) | 0.0031 | m(7,7) | -0.6667 | m(12,12) | 0.6430 |
| m(3,3) | 0.0036 | m(8,8) | -0.6811 | m(13,13) | 0.6753 |
| m(4,4) | 0.0059 | m(9,9) | -0.6732 | m(14,14) | 0.6726 |
| m(5,5) | 0.0081 | m(10,10) | -0.6742 | m(15,15) | 0.6597 |
| Input/output Couplings | | | | | |
| $m(1, P1)$ | 0.9933 | $m(3, P2)$ | 0.5812 | $m(6, P3)$ | 0.5812 |
| $m(9, P4)$ | 0.5812 | | | | |

bandwidth the resonant manifold structure can render. Typically coupling matrix used in the synthesis is considered for a narrowband network, i.e., normally less than 20% in fractional bandwidth [31]. The overall bandwidth of the two examples given in this paper is much smaller than this.

As a thought experiment, if we scale the triplexer to have a fractional bandwidth of 20%, the largest coupling value required would be m(1,4) = 0.7113 in the normalized frequency domain. The coupling M(1,4) in the real frequency domain will be 0.1423. To achieve this coupling between two X-band rectangular waveguide resonators, as shown in Fig. 6.5, the width of the coupling window would be about 16.154 mm (out of the broad wall width of 22.86 mm). This is still feasible for the X band but starting to approach the limit. In short, it is possible to increase the overall bandwidth of the resonant manifold multiplexer, but the

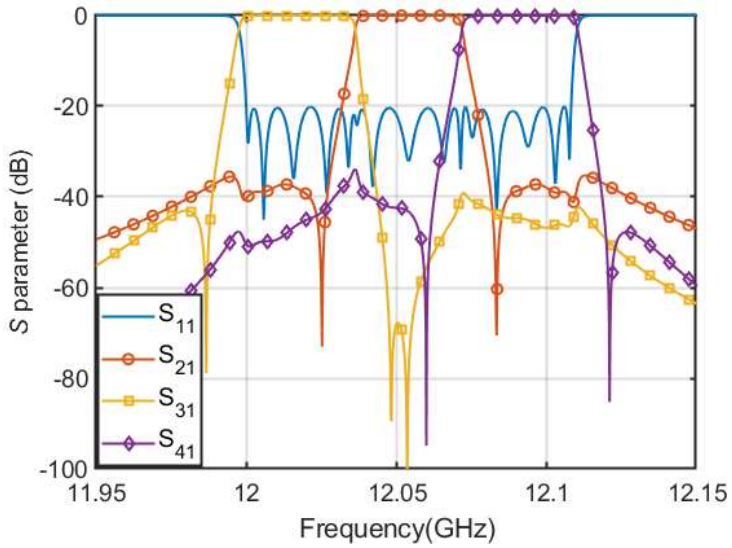



Fig. 6.7. The S-parameter responses of the contiguous-channel triplexer calculated from the coupling matrix.

maximum allowable coupling in the resonant manifold structure is the limiting factor.

In the triplexer example, the guard bands between channels are comparable to the channel bandwidth. The developed approach can also obtain a coupling matrix of the multiplexers with contiguous channels or other complex channel configurations. A Ku-band contiguous-channel triplexer is illustrated as an example in Fig. 6.6, using cascaded quadruplets in the channel filters. The passbands are from 12 GHz to 12.108 GHz and each channel is 36 MHz. Using the same synthesis procedure, the obtained coupling values are listed in Table 6.2 and the S-parameter responses are shown in Fig. 6.7. The synthesis procedure developed in this work is robust and effective enough to generate coupling matrices for resonant manifold multiplexers with complex filtering structures.

### 6.2.2 Physical Realization of the 9th-order Triplexer

Physical realization is implemented using the denormalized coupling values and resonant frequencies obtained from the equations shown in Section 3.3.1. The triplexer is designed based on X-band waveguide technology. The structural configuration is shown in Fig. 6.8. All the resonators are coupled via inductive irises. The triplexer is optimized using CST Studio Suite [27]. The optimized dimensions are given in Fig. 6.8. Fig. 6.9 shows the simulated responses of the 9th-order waveguide triplexer in comparison with those from the coupling matrix. A very good agreement between them has been achieved.

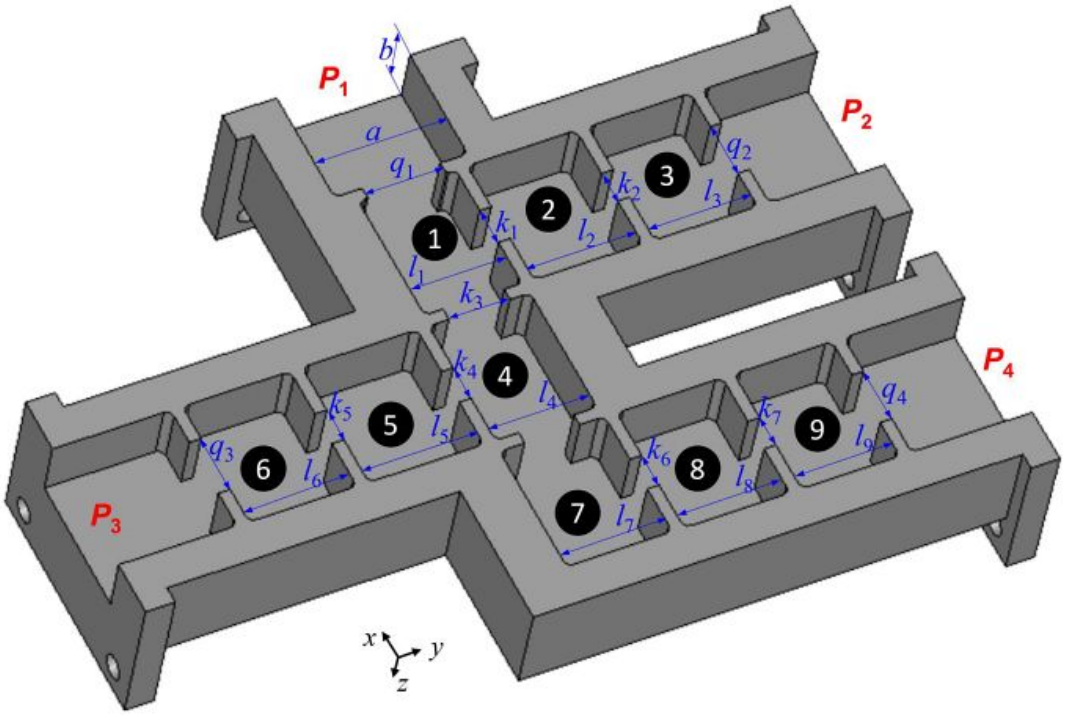



Fig. 6.8. Configuration of the 9th-order X-band triplexer. $a$ = 22.86, $b$ =10.16, $l_1$ = 16.70, $l_2$ = 18.72, $l_3$ = 17.72, $l_4$ = 17.30, $l_5$ = 19.60, $l_6$ = 18.27, $l_7$ = 18.00, $l_8$ = 18.09, $l_9$ = 16.89, $d_1$ = 6.43, $d_2$ = 5.53, $d_3$ = 10.46, $d_4$ = 6.10, $d_5$ = 5.87, $d_6$ = 9.43, $d_7$ = 5.84, $d_8$ = 5.44, $q_1$ = 13.39, $q_2$ = 9.43, $q_3$ = 10.05, $q_4$ = 9.45. Unit: millimetres. The thicknesses of all the irises are 2 mm. The radiuses of all the blended corners are 1.2 mm. The footprint is 94.58 × 143.31 mm in $x$ and $y$ direction for the above configuration.

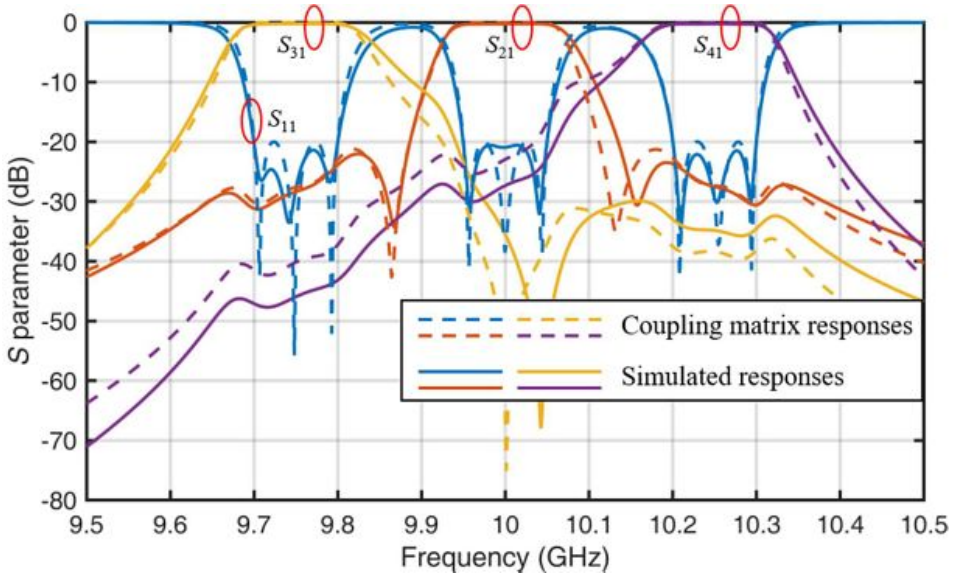



Fig. 6.9. Simulated S-parameter responses of the 9th-order waveguide triplexer comparing with the ideal S-parameter responses from coupling matrix.

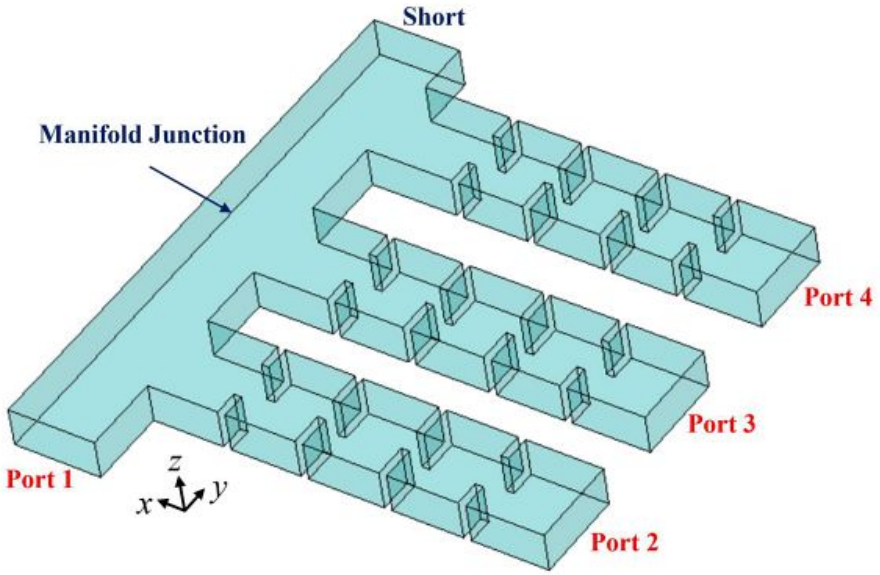



Fig. 6.10. Air cavity model of a conventional waveguide manifold triplexer. The footprint is 124.89 × 140.41 mm in $x$ and $y$ direction for the above configuration.

To objectively evaluate the resonant manifold multiplexer, a conventional waveguide manifold multiplexer is designed for comparison, with the same order filtering responses and using the conventional manifold configuration in [1]. Fig. 6.10 shows the air-cavity

model of the multiplexer where the manifold junction is a standard waveguide. Channel filters are connected to the manifold with intervals of about $\lambda_g/2$, where $\lambda_g$ is the guided wavelength. Comparing the occupied area of the air cavity (including cavity resonator, manifold junction and coupling irises), this traditional multiplexer takes 84 $cm^2$, whereas the resonant manifold multiplexer only takes half of the area, 42 $cm^2$.

The optimisation of multiplexers is usually difficult and time-consuming, especially when the number of channels and resonators is large. The design of the resonant manifold multiplexer follows a different routine from the conventional manifold multiplexer. For the latter, the design normally starts from the channel filters and they are then connected together and optimised. The design of the channel filter can provide a reasonable starting point for the multiplexer optimisation, but it cannot guarantee the quality of the starting responses. The optimisation is still complicated since a large number of EM optimisations are needed [1], [11]-[14]. For the resonant manifold multiplexers, the interaction between channels is much stronger than the conventional one. This presents an optimisation challenge. Direct optimisation on the resonant manifold would be more difficult than that on the conventional structure. However, the resonant manifold multiplexer can be designed from a single coupling matrix. Physical dimensioning can be implemented using the coupling extraction method widely adopted in filters [24]-[25]. The physical dimensions can provide a high-quality initial design for the subsequent optimisation. Fig. 6.11. shows the

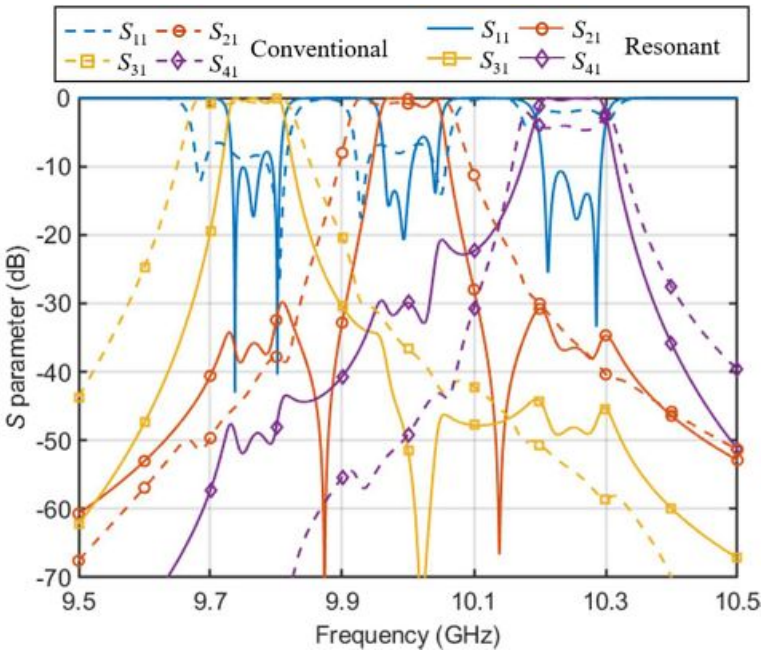
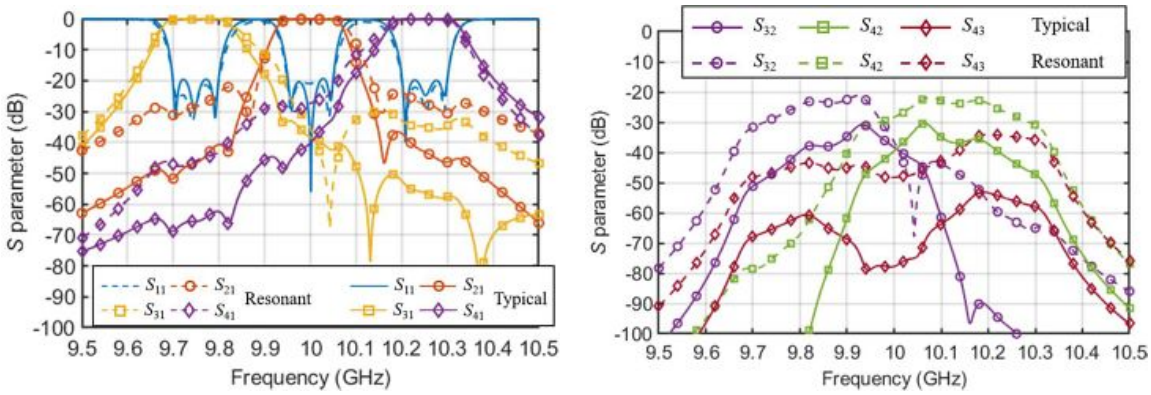



Fig. 6.11. The starting responses in the design of the two types of triplexers.

comparison of the initial design between the two types of triplexers. It can be noticed that the initial S-parameters of the resonant manifold triplexer, extracted using the coupling matrix, can be better than those of the initial design of the conventional one. Furthermore, the coupling matrix can be used to guide the optimisation. In this thesis, a simple but robust optimisation routine, the so-called step-tuning method [28]-[29], is used. The optimisation is effective and fast. It is executed by manually controlling the CST Studio Suite. This process could be accelerated if this can be fully automated.

Fig. 6.12 shows the response comparison between the two types of manifold multiplexers. As Fig. 6.12(a) shows, their reflection coefficients are very similar. However, the isolation performance ($S_{32}$, $S_{34}$ and $S_{24}$ in Fig. 6.12(b)) of the all-resonator one is not as




(a) (b)

Fig. 6.12. Comparison of S-parameter responses between the two types of triplexer configurations. (a) Reflection and transmission; (b) Isolation.

Table 6.3 COMPARISONS BETWEEN TWO TYPES OF MANIFOLD MULTIPLEXERS

| Type | max($\|S_{11}\|$) | max($\|S_{32}\|$) | max($\|S_{42}\|$) | max($\|S_{43}\|$) | Occupied area |
|---|---|---|---|---|---|
| Resonant | −20dB | −21.19dB | −34.02dB | −21.77dB | 42cm² |
| Typical | −20dB | −30.85dB | −53.32dB | −30.61dB | 84cm² |

good as that of the traditional manifold. The isolation is reduced by about 10 dB. As expected, this is attributed to the increased interaction between the channels through coupling. Table 6.3 compares the performance of the two types of multiplexers.

Fig. 6.13 compares the out-of-band spurious performance of the two manifold triplexers. It can be observed the resonant manifold triplexer has a clearer harmonic response. Its out-of-band spurious response is at least not inferior to, if not better than, the conventional manifold design used in this work.

We also investigated the two triplexers' sensitivities to fabrication tolerance. This is evaluated using a Monte Carlo sampling (MCS) method [32]-[33]. In this analysis, the resonant manifold triplexer has 21 parameters including the dimensions of all the coupling

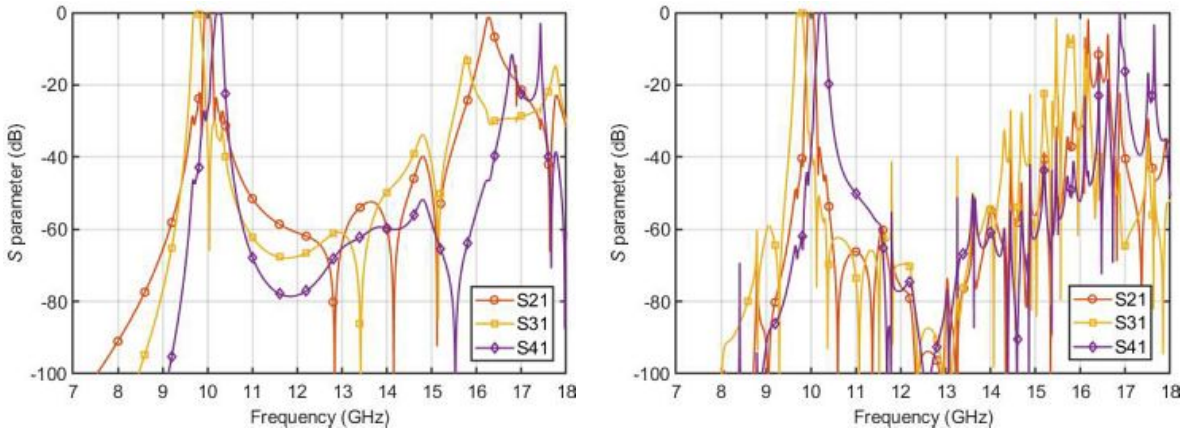



Fig. 6.13. Out-of-band spurious performance of: (a) The resonant manifold triplexer, (b) The conventional manifold triplexer.

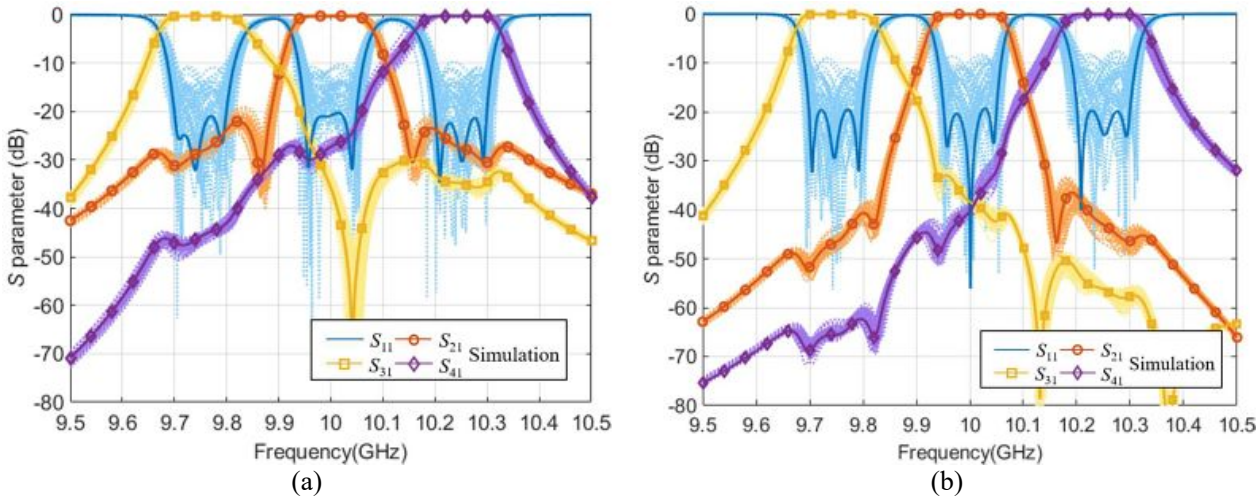



Fig. 6.14. Tolerance analysis of the two triplexers. (a) Resonant manifold triplexer. (b) Conventional manifold triplexer.

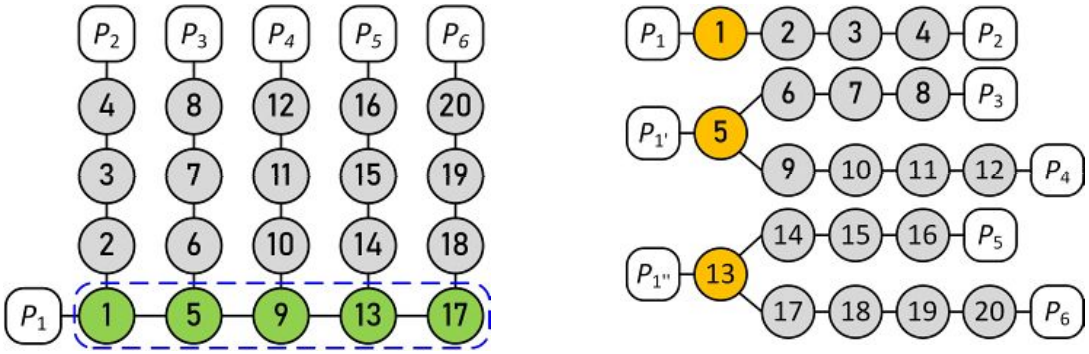
irises and resonator lengths while the conventional one has 27 parameters including the dimensions of coupling iris, resonator lengths and waveguide section lengths in the manifold junction. The manufacturing tolerance is assumed to be ±50 μm. The sampling number is 500 for each triplexer with uniformly random distributed dimensions. 50 curves of each triplexer are randomly selected to be compared as shown in Fig. 6.14. As expected,

both triplexers are sensitive to the manufacturing tolerance. Seen from the return loss level, the return losses in three channels for the resonant manifold triplexer are larger than 10 dB while the return losses for the conventional design are 7 - 9 dB. Therefore, the resonant manifold multiplexer has slightly less sensitive to the tolerance than the conventional design used in this thesis. However, they have similar bandwidth performance. The bandwidths of three channels of two triplexers shrink to 70-80 MHz. From this comparison, it can be noticed that the resonant manifold triplexer is not more sensitive to dimensional tolerance than the conventional design. Instead, the variation of the manifold dimensions in the conventional manifold seems to have a more pronounced effect on the performance. It should be noted that the structure of the conventional manifold used here could be optimized further. We do not intend to generalize the conclusion from this specific comparison. If we were to tune the resonant manifold multiplexer with screws, we expect to face a similar challenge as with conventional multiplexer tuning.

## 6.3 Resonant Manifold Pentaplexer

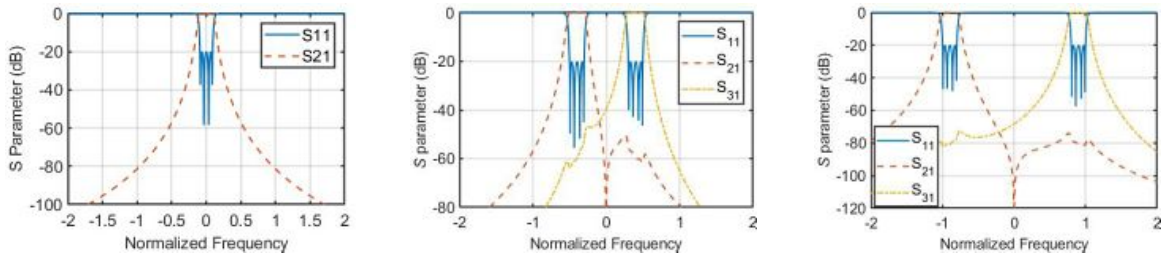
### 6.3.1 Coupling Matrix Synthesis

More channels can be designed and implemented using a similar approach. Here a 5-channel resonant manifold multiplexer is demonstrated. The coupling topology of the multiplexer is shown in Fig. 6.15. It consists of 20 coupled resonators wherein resonators 1, 5, 9, 13, and 17 (marked in green) constitute the resonant manifold. The channels are




(a) (b)

Fig. 6.15. (a) Coupling topology of the 5-channel resonant manifold multiplexer. (b) The separation scheme for the multiplexer. Sub-circuits are used to find the initial coupling values of the multiplexer.




(a) (b) (c)

Fig. 6.16. S-parameter responses corresponding to the coupling coefficients of the sub-circuits in Fig. 6.15(b).

specified as $CH_1$: 9.55 - 9.65 GHz; $CH_2$: 9.85-9.95 GHz; $CH_3$: 10.05 - 10.15 GHz; $CH_4$: 10.25 - 10.35 GHz; and $CH_5$: 10.55 - 10.65 GHz. The return losses for all the channels are designed to be larger than 20 dB.

The normalized passbands are: (−1, −0.8088), (−0.4324, −0.2471), (−0.0638, 0.1178), (0.2976, 0.4756), and (0.8268, 1). The larger number of channels and coupling coefficients present a great challenge to the coupling matrix optimisation. High-quality starting values with a suitable frequency allocation scheme are required to facilitate the optimisation. Inspired by the successful implementation of the triplexer, the 5-channel multiplexer is divided into a filter and two diplexers, by splitting the coupling $m(1, 5)$ and $m(9, 13)$ between

Table 6.4 Optimized Coupling Coefficients for The 5-channel multiplexer

| Mutual Couplings | Values | Self-couplings | Values | Input/output Couplings | Values |
|---|---|---|---|---|---|
| $m(1, 2)$ | 0.1820 | $m(1, 1)$ | −0.0060 | $m(1, P1)$ | 0.6987 |
| $m(2, 3)$ | 0.0601 | $m(2, 2)$ | 0.0220 | $m(4, P2)$ | 0.3122 |
| $m(3, 4)$ | 0.0794 | $m(3, 3)$ | 0.0219 | $m(8, P3)$ | 0.3204 |
| $m(1, 5)$ | 0.6640 | $m(4, 4)$ | 0.0215 | $m(12, P4)$ | 0.3049 |
| $m(5, 6)$ | 0.1284 | $m(5, 5)$ | −0.0074 | $m(16, P5)$ | 0.3154 |
| $m(6, 7)$ | 0.0670 | $m(6, 6)$ | −0.8976 | $m(20, P6)$ | 0.3092 |
| $m(7, 8)$ | 0.0869 | $m(7, 7)$ | −0.9041 | | |
| $m(5, 9)$ | 0.6081 | $m(8, 8)$ | −0.9040 | | |
| $m(9, 1)$ | 0.1305 | $m(9, 9)$ | 0.0521 | | |
| $m(10, 11)$ | 0.0619 | $m(10, 10)$ | 0.8941 | | |
| $m(11, 12)$ | 0.0800 | $m(11, 11)$ | 0.9108 | | |
| $m(9, 13)$ | 0.3979 | $m(12, 12)$ | 0.9117 | | |
| $m(13, 14)$ | 0.1231 | $m(13, 13)$ | 0.0237 | | |
| $m(14, 15)$ | 0.0670 | $m(14, 14)$ | −0.3300 | | |
| $m(15, 16)$ | 0.0847 | $m(15, 15)$ | −0.3390 | | |
| $m(13, 17)$ | 0.2817 | $m(16, 16)$ | −0.3366 | | |
| $m(17, 18)$ | 0.1348 | $m(17, 17)$ | 0.0882 | | |
| $m(18, 19)$ | 0.0683 | $m(18, 18)$ | 0.3383 | | |
| $m(19, 20)$ | 0.0823 | $m(19, 19)$ | 0.3804 | | |
| | | $m(20, 20)$ | 0.3855 | | |

junction resonators as shown in Fig. 6.15(b). Similarly, as for the channel frequency allocation (Appendix C), the first filter occupies the centre channel, namely Channel 3 (−0.0638, 0.1178). The two diplexers occupy the rest of the four channels. Diplexer 1 takes up Channel 1 and 5, while Diplexer 2 takes Channel 2 and 4. The coupling matrices of these three sub-circuits are first synthesized, as shown in Fig. 6.16, and used to form the initial matrix for the 5-channel multiplexer. This matrix is also optimized using the GACMS method [23]. The optimisation goal only contains the passband constraints similar to (9). Since there are a large number of coupling coefficients, group by group optimisation is employed in GACMS. Each variable group contains the coupling coefficients related to the

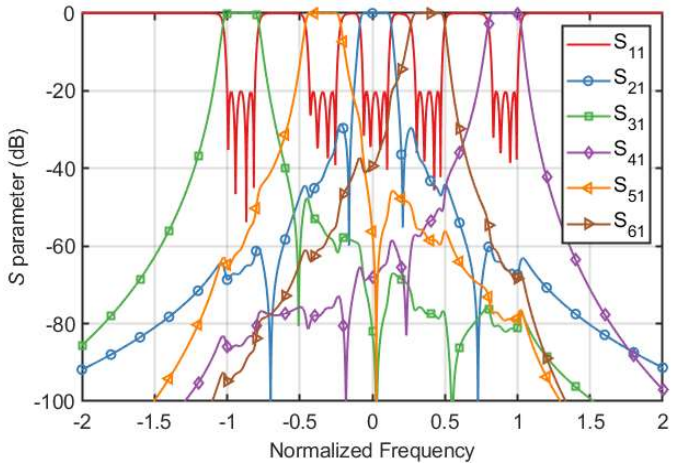



Fig. 6.17. Calculated S-parameter responses corresponding to the optimized coupling matrix for the 5-channel multiplexer.

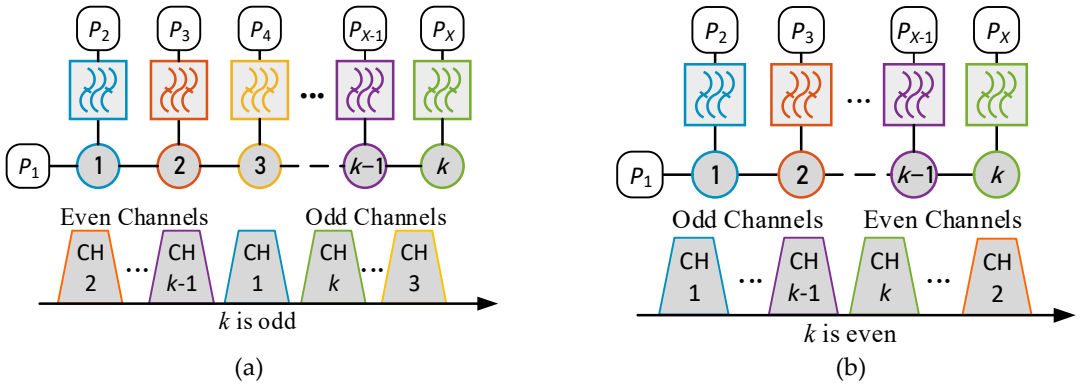



Fig. 6.18. Channel extension scheme for the manifold multiplexer.

initial coupling values of each diplexer. The convergence time is highly related to the number of variables in the optimisation. For this multiplexer, the time cost is within 30 minutes. The optimized matrix is given in Table 6.4. The corresponding S-parameter responses are shown in Fig. 6.17.

From the two successful coupling-matrix syntheses, a general channel extension and frequency allocation scheme can be derived for the resonant manifold multiplexers with $k$ ($k \geqslant 3$) channels, as illustrated in Fig. 6.18. With this scheme, the multiplexer can be split into

multiple sub-circuits (filters and diplexers) for preparing the starting coupling values. The whole coupling matrix for the multiplexer can be obtained by using the GACMS optimisation framework [23]. Robust convergence has been exhibited. It should be noted that there are other potential frequency allocations as listed in Appendix C of this thesis.

### 6.3.2 Physical Realization for 20$^{th}$-order Multiplexer

Again, the real coupling values and resonator frequencies are denormalized and calculated based on (6)-(8). The structural configuration of the multiplexer is shown in Fig. 6.19. All the resonators are coupled via inductive irises. In this structure, $d_1$, $d_2$ … $d_{19}$ denote the coupling iris widths between resonators. $q_1$, …, $q_6$ denote the input/output coupling iris widths. $l_1$, …, $l_{20}$ represent the lengths of resonators.

The initial dimensions are extracted based on the classical dimensioning method [24]-[25]. Due to mutual interference between channels and a large number of design variables in the multiplexer structure, it is almost impossible to directly optimize the structure as a whole. Again, the step-tune method [28]-[29] has been adopted. The optimisation starts from the port away from the manifold in each branch. Resonators are added one by one to execute the optimisation until the couplings to the resonant manifold are optimized. The optimisation goal is to match the simulated responses to the ideal responses from the sub-coupling matrix. In each optimisation step, only the length and the output coupling of the added resonator are altered. Therefore, the optimisation is fast to converge. After the optimisation of all the branches, a similar progressive optimisation for the resonant

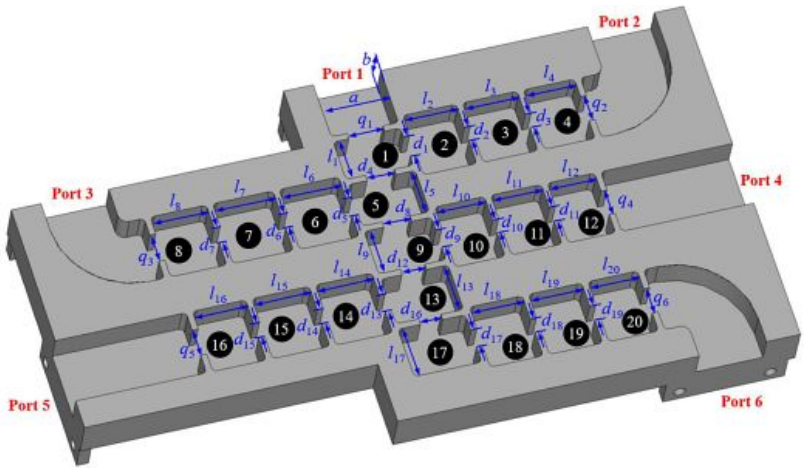



Fig. 6.19. Structural configuration of the 5-channel resonant manifold multiplexer. $a$ = 22.86, $b$ =10.16, $l_1$ = 14.18, $l_2$ = 18.20, $l_3$ = 18.73, $l_4$ = 17.37, $l_5$ = 15.88, $l_6$ = 20.24, $l_7$ = 20.47, $l_8$ = 18.98, $l_9$ = 16.16, $l_{10}$ = 17.03, $l_{11}$ = 17.28, $l_{12}$ = 16.12, $l_{13}$ = 16.96, $l_{14}$ = 19.15, $l_{15}$ = 19.37, $l_{16}$ = 18.01, $l_{17}$ = 17.97, $l_{18}$ = 17.93, $l_{19}$ = 18.09, $l_{20}$ = 16.90, $d_1$ = 7.59, $d_2$ = 4.91, $d_3$ = 5.35, $d_4$ = 9.85, $d_5$ = 6.67, $d_6$ = 5.26, $d_7$ = 5.71, $d_8$ = 9.53, $d_9$ = 6.43, $d_{10}$ = 4.79, $d_{11}$ = 5.11, $d_{12}$ = 8.33, $d_{13}$ = 6.41, $d_{14}$ = 5.09, $d_{15}$ = 5.46, $d_{16}$ = 7.48, $d_{17}$ = 6.43, $d_{18}$ =5.07, $d_{19}$ = 5.28, $q_1$ = 12.43 $q_2$ = 9.56, $q_3$ = 10.02, $q_4$ = 9.01, $q_5$ = 9.65, $q_6$ = 9.19. Unit: millimeters. The thicknesses of all the irises are 2 mm. The radiuses of all the rounded corners are 1.5 mm.

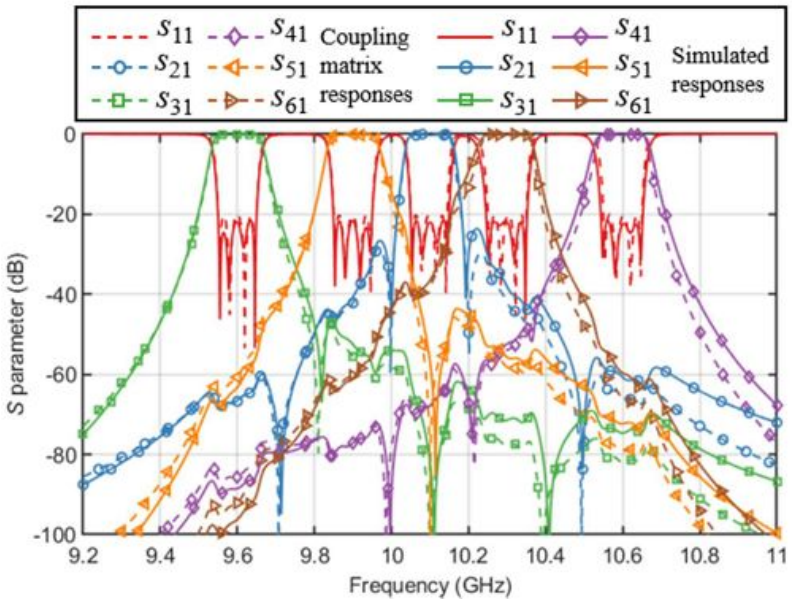



Fig. 6.20. Comparison of the S-parameter responses between the coupling matrix and simulation.

manifold is performed. This step-tune approach ensures more robust convergence in the optimisation. Fig. 6.20 shows the optimized solution, compared with the S-parameter responses calculated by the coupling matrix. A very good agreement between simulation and theory has been achieved. All 20 reflection zeros are clearly visible.

## 6.4 Fabrication and Measurements

### 6.4.1 Triplexer

The triplexer is machined from aluminium shown in Fig. 6.21. It is cut along the top edges of the resonators. This cutting plane is prone to leakage so good contact is essential. Two parts of the triplexer are assembled and tightened together by metal screws. No tuning is applied.

The triplexer is measured by using a Keysight E5071C network analyser. The measured S-parameter responses compared with the simulation results using the dimensions from

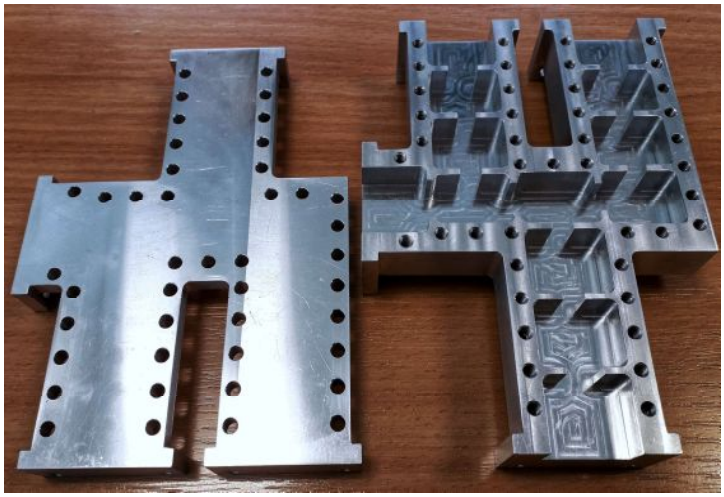


Fig. 6.21. Photograph of the fabricated resonant manifold triplexer.

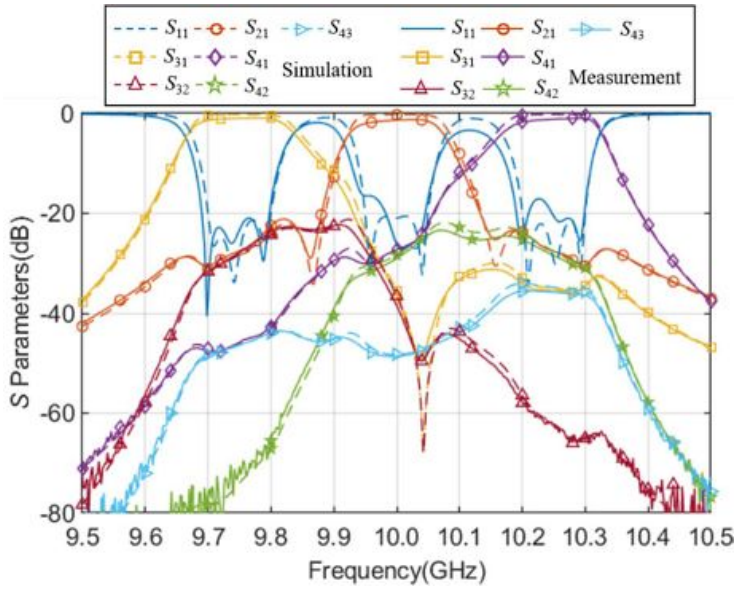



Fig. 6.22. Measured S-parameter responses of the triplexer in comparison with the simulated results.

EM-simulation based design are shown in Fig. 6.22. A good agreement has been achieved between them. The insertion losses on average for the three channels are 0.96 dB, 1.33 dB and 1.31 dB, respectively. The simulated insertion losses are about 0.7dB. The higher-than-expected insertion loss is believed to be a result of contact losses from the unfavourable split plane.

### 6.4.2 Five-channel Multiplexer

The 5-channel multiplexer is fabricated using aluminium with a natural oxidation process on the surface as shown in Fig. 6.23. The measured S-parameter responses, in comparison with simulations using the dimensions from EM-simulation based design, are illustrated in Fig. 6.24. Aluminium is used in the simulation, where the electrical conductivity is $\sigma_{AL} = 3.56\text{e}7$ S/m. Again, reasonably good agreement has been achieved

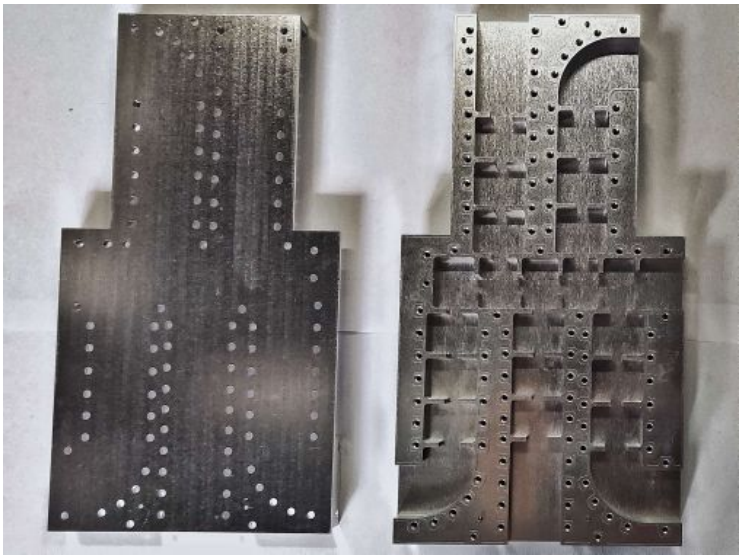


Fig. 6.23. Photograph of the fabricated 5-channel resonant manifold multiplexer

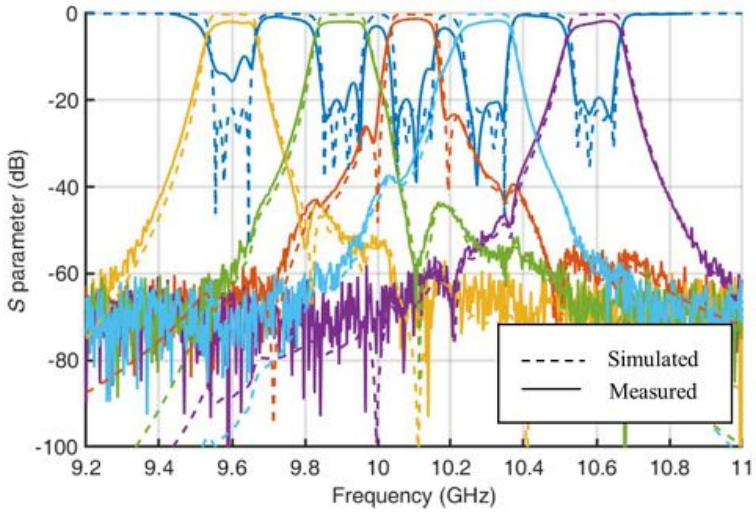
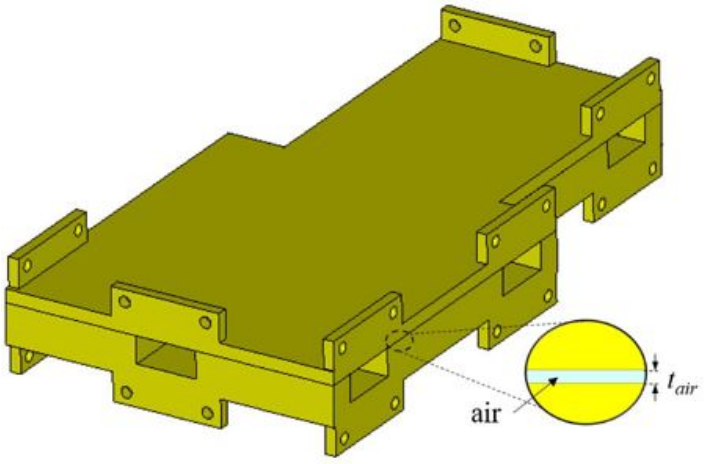


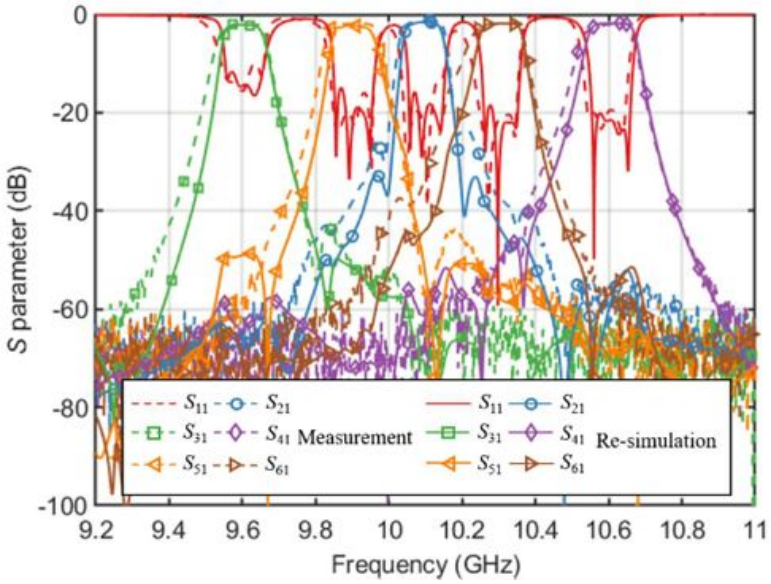

Fig. 6.24. Measured S-parameter responses of the 5-channel resonant manifold multiplexer, comparing with the simulated results.

between them without applying any tuning. The insertion losses on average for the five channels are 1.89 dB, 1.86 dB, 1.22 dB, 1.87 dB, and 2.11 dB, respectively. The simulated insertion losses obtained by using CST simulation is around 0.7dB.

The measured losses for the two multiplexers are higher than simulation results and




(a)




(b)

Fig. 6.25. Investigation on the effect of poor contact of the 5-channel multiplexer. (a) The modified model with an air gap. (b) Simulation responses showing a much better agreement with the measurement responses when air layer thickness equals to $t_{air}$ = 3.5 μm.

uneven for different channels. This is mainly attributed to the H-plane cut design. As mentioned before, this cut plane is prone to contact losses. The large contact areas of the multiplexer exacerbated the imperfect connection between the two pieces. The 5-channel multiplexer is re-simulated with a thin layer of air added between the cap and multiplexer

body. It has been found the re-simulation responses match the measurement responses much better when the air gap is assumed to be 3.5 μm, which is plausible, as shown in Fig. 6.25. In practice, an E-plane cut structure, which is entirely possible with the resonant manifold topology, can be used and better performance is expected. Also, to avoid electromagnetic losses, the contact surface needs to be fastened between the cap and the multiplexer main body. Usually, small lips are arranged at the edges of all the resonators and screw holes on the contact surface as shown in Fig. 6.23. In this multiplexer example, 1mm is employed for both the lip height and width.

### 6.4.3 Discussion

As a design guideline, for a multiplexer with an odd number of channels, both Scheme 2 and 3 (See Appendix C of this thesis) can be considered for similar performance. One can make a further selection based on the physical constraint of the layout and any specific isolation or rejection requirement. It should also be noted that the required coupling levels are similar for both schemes. For multiplexers with an even number of channels, the scheme shown in Fig. 6.18(b) is recommended, where the consecutive pair of topological channels can be assigned with two symmetrically located frequency channels. The coupling matrices for all the schemes can be effectively synthesized by using the proposed optimisation method. The general coupling matrix synthesis procedure is given in the following.

*Step 1*: Transform the frequency specifications into normalized frequency channels.

*Step 2*: If the number of channels is even, jump to Step 3. If the number of channels is odd,

assign the middle-frequency channel to the first topological channel, such as the CH1 shown in Fig. 18 (a).

*Step 3*: Every two frequency channels located at two outer sides are assigned to the following every consecutive pair of topological channels, as shown in Fig. 6.18 (a) and (b).

*Step 4*: Divide the multiplexer into multiple sub-circuits, including a filter and multiple diplexers.

*Step 5*: Synthesis of the sub-circuits using the allocated frequency specifications in Steps 2 and 3.

*Step 6*: Take the coupling values obtained in Step 5 as the starting point. Optimize the coupling matrix of the multiplexer using the GACMS method [23].

*Step 7*: Transform the optimal coupling matrix into the real frequency domain.

## 6.5 Summary of this Chapter

This chapter presented a novel concept to design compact manifold multiplexers based on an all-resonator structure. Therefore, the proposed multiplexer can be designed based on the coupling matrix synthesis-based design method. To address the coupling matrix synthesis, a recommended frequency allocation scheme is presented for the proposed multiplexers. Then, the coupling matrix can be successfully obtained by using the method proposed in Chapter 4. A triplexer and a pentaplexer are designed and fabricated to demonstrate the design concept of the proposed multiplexer design concept.

## References

[1] R. J. Cameron, C. M. Kudsia, and R. R. Mansour, "Multiplexer Theory and Design," Microwave Filters for Communication Systems: Fundamentals, Design, and Applications, Wiley, 2018, pp.569-608, ch18.

[2] G. Macchiarella and S. Tamiazzo, "Synthesis of Star-Junction Multiplexers," IEEE Trans. Microw. Theory Techn., vol. 58, no. 12, pp. 3732-3741, Dec. 2010.

[3] R. I. Cameron and M. Yu, "Design of manifold-coupled multiplexers," IEEE Microw. Mag., vol. 8, no. 5, pp. 46-59, Oct. 2007.

[4] C. Kudsia, R. Cameron, and W.-C. Tang, "Innovations in microwave filters and multiplexing networks for communications satellite systems," IEEE Trans. Microw. Theory Techn., vol. 40, no. 6, pp. 1133–1149, Jun. 1992.

[5] S. Cogollos et al., "Efficient Design of Waveguide Manifold Multiplexers Based on Low-Order EM Distributed Models," IEEE Trans. Microw. Theory Techn., vol. 63, no. 8, pp. 2540-2549, Aug. 2015.

[6] P. Zhao and K. Wu, "An Iterative and Analytical Approach to Optimal Synthesis of a Multiplexer with a Star-Junction," in IEEE Transactions on Microwave Theory and Techniques, vol. 62, no. 12, pp. 3362-3369, Dec. 2014.

[7] G. Macchiarella and S. Tamiazzo, "Novel approach to the synthesis of microwave duplexers," IEEE Trans. Microw. Theory Tech., vol. 54, no. 12, pp. 4281–4290, Dec. 2006.

[8] G. Macchiarella and S. Tamiazzo, "Design of triplexer combiners for base stations of mobile communications," in IEEE MTT-S Int. Microw. Symp. Dig., Anheim, CA, May 2010, pp. 429–432.

[9] R. V. Snyder, A. Mortazawi, I. Hunter, S. Bastioli, G. Macchiarella and K. Wu, "Present and Future Trends in Filters and Multiplexers," IEEE Transactions on Microwave Theory and Techniques, vol. 63, no. 10, pp. 3324-3360, Oct. 2015.

[10] A. Morini, G. Venanzoni, M. Farina and M. Villa, "A Method for Fast and Reliable Analysis and Optimisation of Side-Coupled Cavity Filters and Multiplexers," IEEE Trans. Microw. Theory Techn., vol. 66, no. 8, pp. 3847-3856, Aug. 2018.

[11] M. Ismail, D. Smith, A. Panariello, Y. Wang, and M. Yu, "EM-based design of large-scale dielectric-resonator filters and multiplexers by space mapping," IEEE Trans. Microw. Theory Techn., vol. 52, no. 1, pp. 386–392, Jan. 2004.

[12] M. Yu and Y. Wang, "Synthesis and beyond," IEEE Microw. Mag., vol. 12, no. 6, pp. 62–76, Oct. 2011.

[13] M. Ismail, Y. Wang, and M. Yu, "Advanced design and optimisation of large-scale microwave devices," in IEEE MTT-S Int. Microw. Symp. Dig., Jun. 2012, pp. 1–3.

[14] Z. C. Hao, X. P. Huo, W. Q. Ding, and W. Hong, "Efficient design of compact contiguous-channel SIW multiplexers using the space mapping method," IEEE Trans. Microw. Theory Techn., vol. 63, no. 11, pp. 3651–3662, Nov. 2015.

[15] X. Shang, Y. Wang, W. Xia, and M. J. Lancaster, "Novel Multiplexer Topologies Based on All-Resonator Structures," IEEE Trans. Microw. Theory Techn., vol. 61, no. 11, pp. 3838-3845, 2013.

[16] T. Skaik, M. Lancaster, M. Ke, and Y. Wang, "A micromachined WR-3 band waveguide diplexer based on coupled resonator structures," 2011 41st European Microwave Conference, 2011, pp. 770-773.

[17] Y. Wu, Y. Wang and E. A. Ogbodo, "Microstrip wideband diplexer with narrow guard band based on all-resonator structures," 2016 46th European Microwave Conference (EuMC), London, 2016, pp. 1163-1166.

[18] R. Wang, J. Xu, M.-Y. Wang, and Y.-L. Dong, "Synthesis of microwave resonator diplexers using linear frequency transformation and optimisation," Progress In Electromagnetics Research, vol. 124, pp. 441-456, 2012.

[19] I. Llamas-Garro, F. Mira, P. Zheng, Z. Liu, L. Wu, and Y. Wang, "All-resonator based LTCC diplexer using substrate-integrated-waveguides," Electronics Letters, vol. 53, no. 21, pp. 1410-1412, 2017.

[20] W. Xia, X. Shang and M. J. Lancaster, "All-resonator-based waveguide diplexer with cross-couplings," Electronics Letters, vol. 50, no. 25, pp. 1948-1950, 4 12 2014.

[21] T. F. Skaik, M. J. Lancaster, and F. Huang, "Synthesis of multiple output coupled resonator circuits using coupling matrix optimisation," IET Microwaves, Antennas & Propagation, vol. 5, no. 9, pp. 1081-1088, 2011.

[22] B. Liu, H. Yang, and M. J. Lancaster, "Synthesis of Coupling Matrix for Diplexers Based on a Self-Adaptive Differential Evolution Algorithm," IEEE Transactions on Microwave Theory and Techniques, vol. 66, no. 2, pp. 813-821, 2018.

[23] Y. Yu, B. Liu, Y. Wang, M. J. Lancaster and Q. S. Cheng, "A General Coupling Matrix Synthesis Method for All-Resonator Diplexers and Multiplexers," IEEE Transactions on Microwave Theory and Techniques, vol. 68, no. 3, pp. 987-999, March 2020.

[24] J. -S. G. Hong and M. J. Lancaster, Microstrip Filters for RF/Microwave Application, vol. 167. Hoboken, NJ, USA: Wiley, 2004.

[25] Richard J. Cameron; Chandra M. Kudsia; Raafat R. Mansour, "Design and Physical Realization of Coupled Resonator Filters," in Microwave Filters for Communication Systems: Fundamentals, Design, and Applications , Wiley, 2018, pp.457-484, ch14.

[26] S. Llorente Romano and M. Salazar Palma, "Implementation of extracted pole filters in rectangular waveguide," 2014 44th European Microwave Conference, Rome, 2014, pp. 616-619.

[27] CST Studio Suite – EM Simulation Software. [Online]. Available: http://www.cst.com/Content/Products/CST_S2/Overview.aspx, 2011.

[28] M. Guglielmi, "Simple CAD procedure for microwave filters and multiplexers," IEEE Transactions on Microwave Theory and Techniques, vol. 42, no. 7, pp. 1347-1352, July 1994.

[29] X. Shang, W. Xia, and M. J. Lancaster, "The design of waveguide filters based on cross-coupled resonators," Microwave and Optical Technology Letters, vol. 56, pp. 3-8, 2014.

# Chapter 7 D-band Waveguide Diplexers Fabricated Using Micro Laser Sintering and CNC Machining

In this chapter, a D-band waveguide diplexer has been designed and fabricated using micro laser sintering (MLS) based metal additive manufacturing. As a comparison, the same diplexer design fabricated using high-precision computer numerical controlled (CNC) milling is also presented.

## 7.1 Introduction

Due to the generously available bandwidth (up to several tens of GHz) and relatively low attenuation, D-band has found many applications in high-capacity backhaul links for 5G and beyond, and space-based receivers for earth observation [1]-[3]. D-band has a 2 dB lower rain attenuation than W-band and the attenuation is almost flat [4]. According to a group report provided by the millimetre-wave (MWT) industry specification group (ISG) in European Telecommunications Standards Institute (ETSI) [4], link distances of several hundred meters are practical at D-Band frequencies with antenna sizes comparable to those at E-Band.

As introduced in Chapter 1, the diplexer is an essential component in the communication system. With the advantage of low-loss and high power handling capability, the waveguide technology is still the best choice for the high mm-wave and sub-THz system

(90~300GHz). However, the fabrication of the diplexers over 100 GHz is still a challenge. The waveguide size is very small (e.g., The waveguide dimensions for the D-band frequency range is WR-6 standard waveguide with the dimensions of 1.65mm × 0.83mm.) and the filtering performance of the diplexer is highly sensitive to the manufacturing tolerance [5]. Therefore, high-precision fabrication accuracy of 5 μm is required.

In recent years, additive manufacturing (AM) techniques, also known as 3D printing, has become a fresh choice for RF and microwave components. This Chapter presents a diplexer operating at D-band fabricated using a high-resolution micro laser sintering (MLS) technique on stainless steel [6]. Comprehensive measurements are conducted on the electrical performance and surface quality.

## 7.2 Diplexer Design

### 7.2.1 Filtering Topology and Synthesis

The diplexer is designed with the following specifications which meet the scope for future communication links provided by European Telecommunications Standards Institute (ETSI) [4] and frequency bands allocated to fixed service by ITU Radio Regulation 2020 [7].

- *Channel A* passband ($f_{A.1}$ - $f_{A.2}$): 130 - 134 GHz. Return loss ⩾ 20 dB.
- *Channel B* passband *($f_{B.1}$ - $f_{B.2}$):* 151.5-155.5 GHz. Return loss ⩾ 20 dB.
- Isolation within the passband (IP) ⩾ 60 dB.

To minimize the transmitter power loss and maintain receiver sensitivity, a minimum

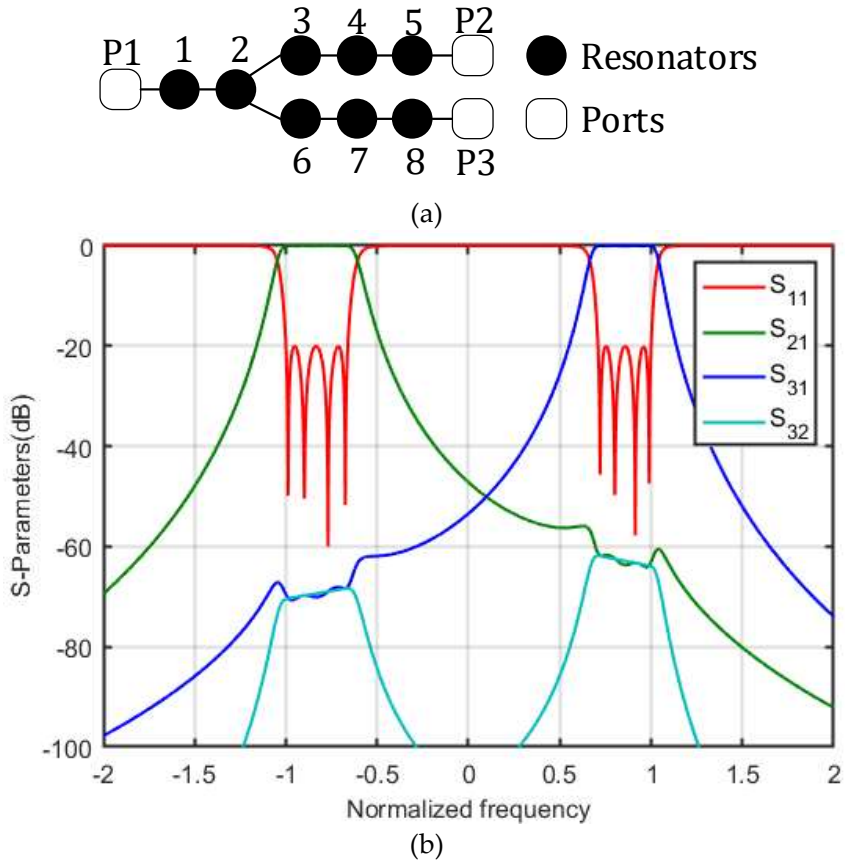



Fig. 7.1. (a) The coupling topology of the diplexer and (b) The calculated S-parameter response from the coupling matrix.

loss is required in the passbands. Based on the evaluation of different filter orders and topologies, an 8th order all-resonator structure is adopted as illustrated in Fig. 7.1 to meet the design specifications. Without the need for a junction-based frequency distribution network, the diplexer can be realized in a more compact size. Note that resonator 2 not only plays a role in frequency distribution but also provide a transmission pole in the passband.

The all-resonator diplexer is designed based on coupling matrix theory. The synthesis is performed with the optimisation-based synthesis approach presented in Chapter 4. The optimal coupling matrix and corresponding normalized scattering parameter responses are

Table 7.1 The Optimal Coupling Coefficients for The Diplexer

| Mutual Couplings | | Self-couplings | |
|---|---|---|---|
| $m(1, 2)$ | 0.8677 | $m(1, 1)$ | −0.0537 |
| $m(2, 3)$ | 0.2203 | $m(2, 2)$ | 0.0635 |
| $m(3, 4)$ | 0.1200 | $m(3, 3)$ | −0.8021 |
| $m(4, 5)$ | 0.1548 | $m(4, 4)$ | −0.8279 |
| $m(2, 6)$ | 0.1767 | $m(5, 5)$ | −0.8290 |
| $m(6, 7)$ | 0.1026 | $m(6, 6)$ | 0.8368 |
| $m(7, 8)$ | 0.1330 | $m(7, 7)$ | 0.8524 |
| | | $m(8, 8)$ | 0.8537 |
| Input/output Couplings | | | |
| $m(1, P1)$ | 0.5817 | $m(5, P2)$ | 0.4265 |
| $m(8, P3)$ | 0.3956 | | |

shown in Table 7.1 and Fig. 7.1 (b), respectively. It can be seen that both transmission and rejection requirements are theoretically satisfied. For the following physical realization, the coupling matrix is first transformed into the real-frequency domain. The physical dimensioning uses the initial design generation method presented in Chapter 5.

## 7.2.2 Structural Design and Simulation

The air cavity configuration of the diplexer is illustrated in Fig. 7.2(a). The diplexer is designed on standard WR-6 waveguide cavities. Two channels are folded for a compact configuration. Channel A is designed in a staircase configuration, which not only makes the overall diplexer more compact but also increases the higher frequency rejection performance in Channel B [8]. As shown in Fig. 7.2(b), to find the coupling coefficient, two TE101 mode cavities are coupled with a slot in a staircase configuration. Their coupling coefficients vary with the changes of relative distances. Considering the fabrication resolution of the additive manufacturing, the height and width of the slot are kept constant

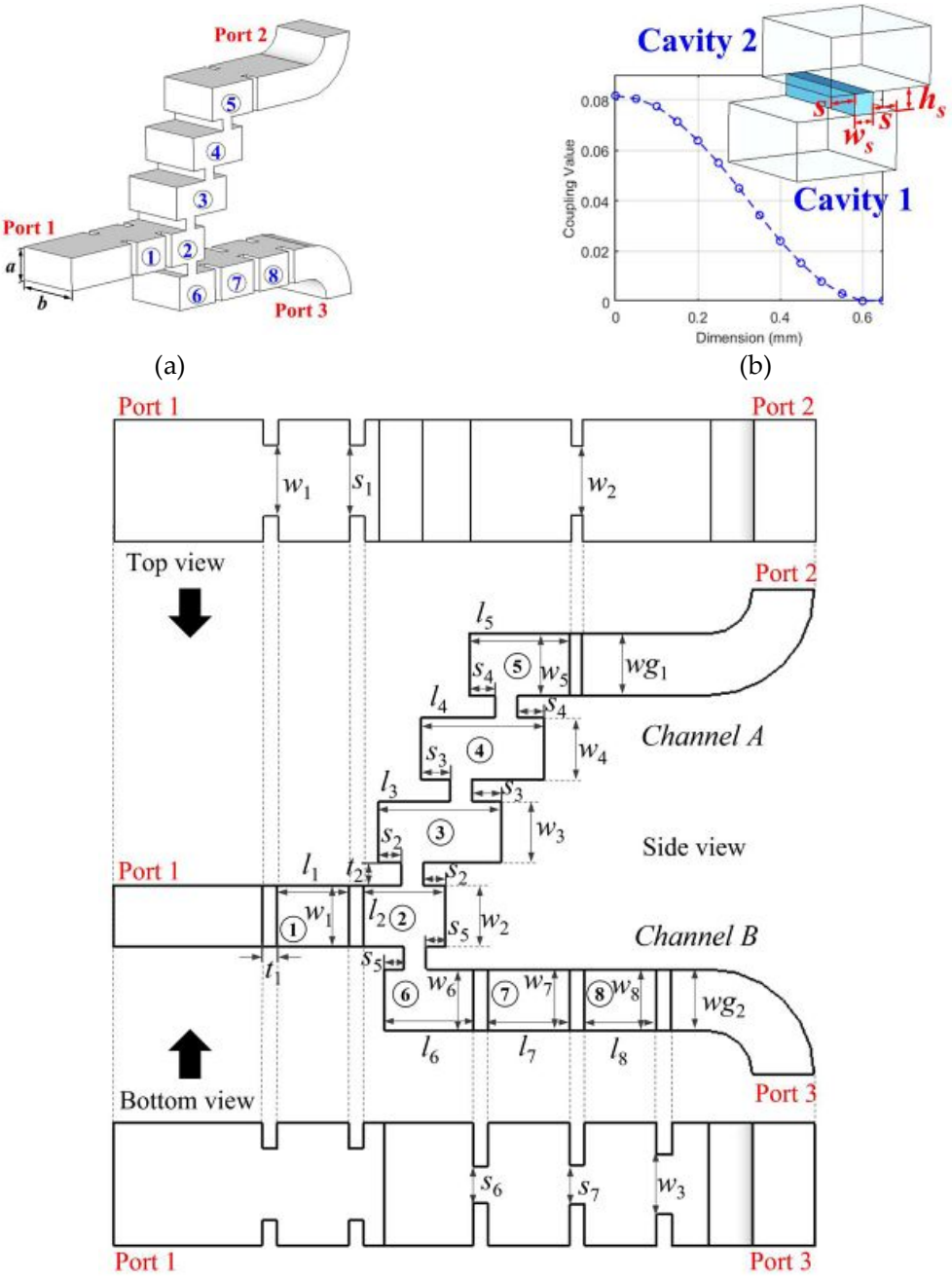



Fig. 7.2. Structures of the diplexer design. (a) The core air cavity model of the diplexer, $a$ = 1.651 and $b$ = 0.826. (b) Coupling coefficients of two waveguide cavities coupled in a staircase configuration, as a function of $s$. $w_s$ = 0.3 and $h_s$ = 0.3. (c) Schematic diagram of the diplexer with top view, side view and bottom view. The resonator length: $l_1$ = 0.9576, $l_2$ =1.1071, $l_3$ = 1.6538, $l_4$ = 1.6459, $l_5$ = 1.3554, $l_6$ = 1.1842, $l_7$ = 1.0958, $l_8$ = 0.9692. The dimensions related to couplings: $s_1$ = 0.9583, $s_2$ = 0.3039, $s_3$ = 0.3899, $s_4$ = 0.3495, $s_5$ = 0.2609, $s_6$ = 0.4869, $s_7$ = 0.5222. Input/output couplings: $w_1$=0.9594, $w_2$=0.9262, $w_3$= 0.7948. The thickness for all the irises $t_1$ = 0.2. Unit: mm.

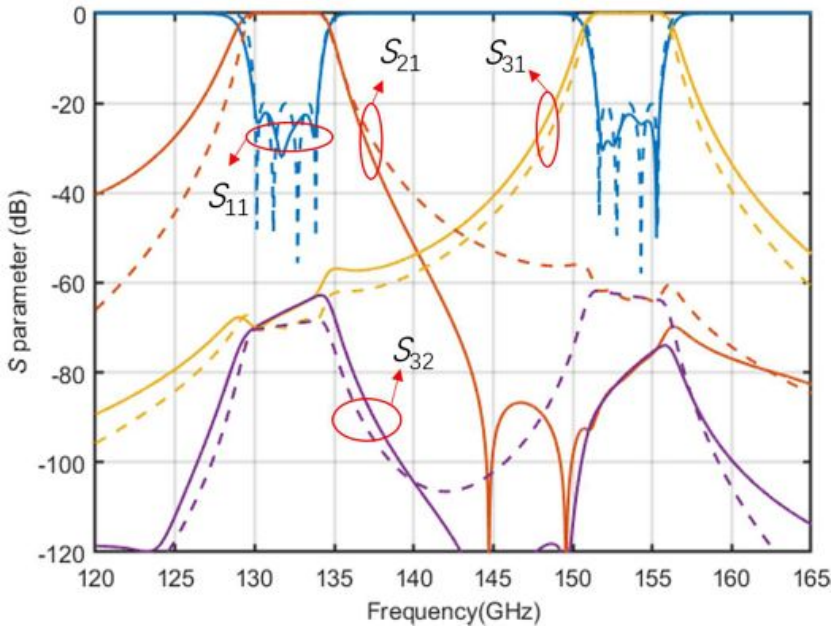



Fig. 7.3. Simulated S-parameter response of the 8th order diplexer shown in Fig. 4, compared with the theoretical responses calculated from coupling matrix. The dash line denotes the theoretical responses, and the solid line denotes the simulated responses.

at 0.3 mm. The coupling value range provided by the slot can fulfil the requirement of the diplexer design. The physical dimensions are illustrated in Fig. 7.2(c). Fig. 7.3 shows the simulated S-parameter responses, as compared with the responses calculated with the coupling matrix. The S-parameter responses between the staircase coupled structure and regular inductive iris coupled structure of Channel A are compared in Fig. 7.4. It can be seen that the simulated isolation performance is much improved to over 60 dB. The diplexer structure for MLS with UG-387 flange [9] is shown in Fig. 7.5(a) where the three-waveguide ports are extended and bent along the H-plane for interface with external devices. The diplexer model in Fig 7.5(a) is divided into two halves to be printed. Limited by the printing volume of the printer, parts of the flanges have to be removed. The profile of the diplexer

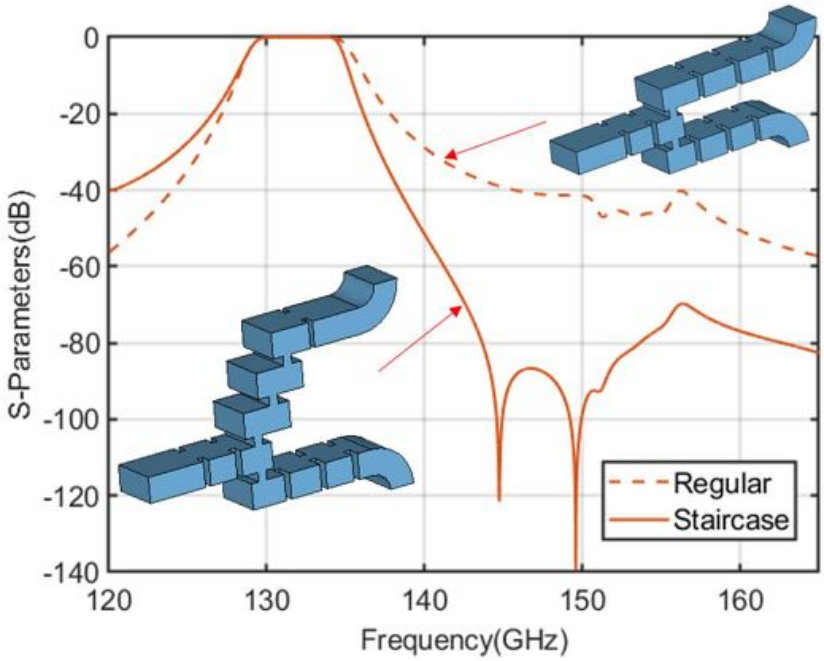
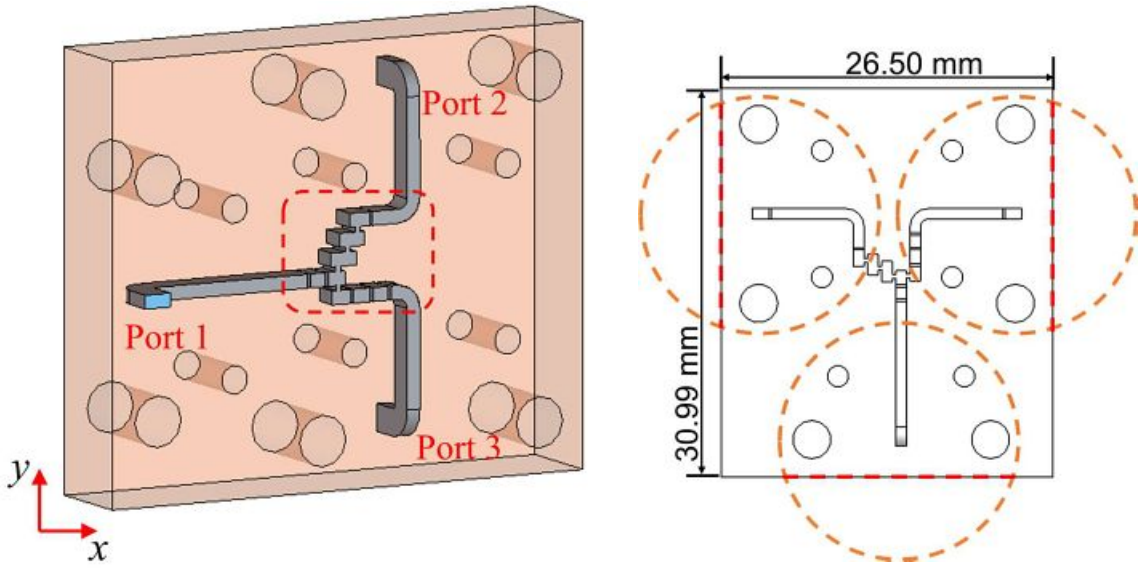



Fig. 7.4. S-parameter comparison between two diplexers with different configurations in Channel A - a regular inductive iris structure versus a staircase coupled structure.




(a) (b)

Fig. 7.5. (a) The diplexer model, with H-plane bends and UG-387 flanges, for MLS fabrication. (b) The top-view profile of the MLS model.

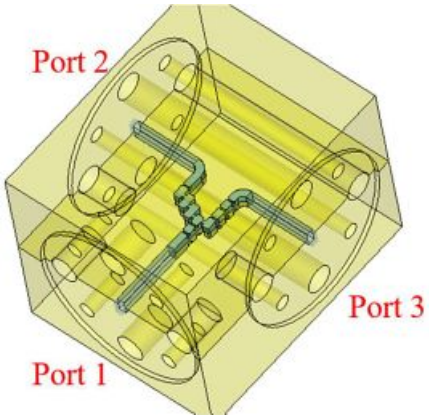



Fig. 7.6. The diplexer 3D model for CNC milling. The modified dimensions are: the resonator length $l_1$ = 0.9238, $l_2$ =1.1303, $l_3$ = 1.6719, $l_4$ = 1.6650, $l_5$ = 1.3781, $l_6$ = 1.2010, $l_7$ = 1.1002, $l_8$ = 0.9598. The dimensions related to couplings, $s_1$ = 0.9747, $s_2$ = 0.3030, $s_3$ = 0.3918, $s_4$ = 0.3537, $s_5$ = 0.2571, $s_6$ = 0.5156, $s_7$ = 0.5559. Input/output couplings, $w_1$=0.9908, $w_2$=0.9172, $w_3$= 0.8369. Unit: mm.

model is shown in Fig. 7.5(b).

As for the diplexer design for CNC milling, all three ports are extended in three directions to allow connection with UG387 flanges as shown in Fig. 7.5. Meanwhile, the air cavities are modified with rounded corners with a radius of 0.15mm to be convenient for CNC milling. The other dimensions are modified as listed in Fig. 7.6.

## 7.3 Fabrication and Surface Treatment

### 7.3.1 Diplexer Fabricated by MLS and CNC

The diplexer was printed using stainless steel in an inert argon atmosphere by MLS technology. The 3D printing service is provided by a Germany company called 3D MicroPrint GmbH [6]. The MLS is one of the most accurate metal 3D printing technology

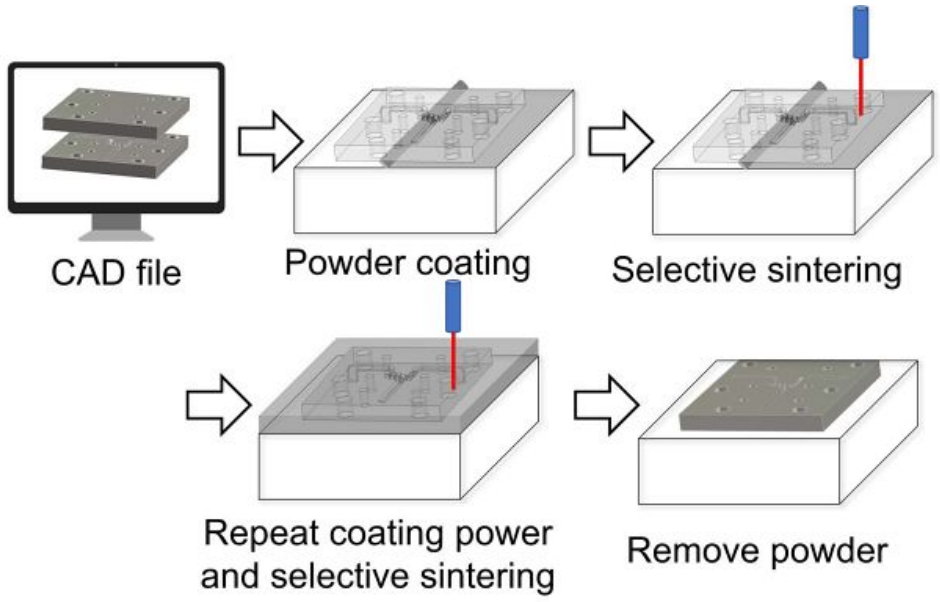
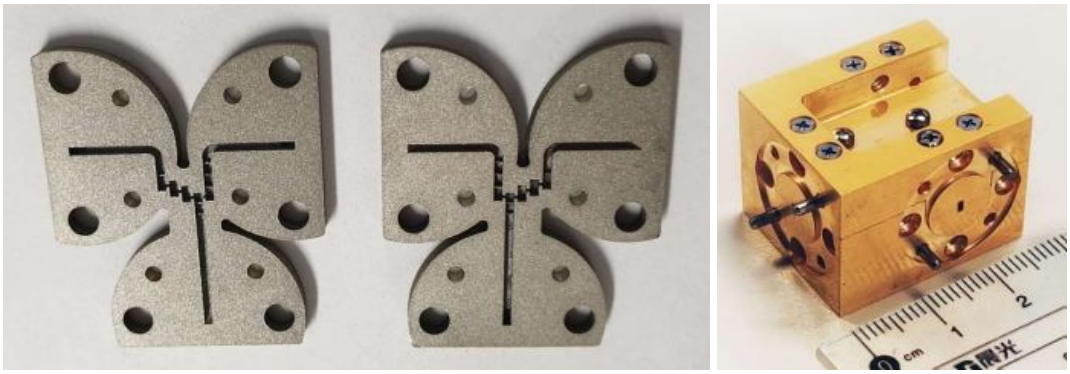



Fig. 7.7. The fabrication process of the MLS.

technologies for small size metal structures. The fabrication process is illustrated in Fig. 7.7. Firstly, the CAD model is sliced into layers. During the fabrication, the platform is coated by a thin layer of metal powder and one layer is selectively sintered by a laser beam. The laser source was an IR fibre laser with a 50W laser average power. The laser spot diameter is focused down to 30 μm and was operated in continuous wave mode. After the construction of one layer, the platform is lowered down, and the fabrication process repeats power covering and selective sintering until all the component is finished. The type of stainless steel was 1.4542 (17-4PH) according to ASTM 564, which is a chromium-nickel copper alloyed stainless steel, containing 17% chromium, 4% nickel, 4% copper and 0.3% niobium. Each layer thickness is around 5 μm. The powder particle sizes had d80 smaller than 5 μm (d80 smaller than 5 μm: The powder has 80% of the particles are less than 5 μm



(a) (b)

Fig. 7.8. The fabricated diplexer (a) by using the MLS technique (b) by using the high-precision CNC machining.

in diameter) and had an electrical conductivity of $1.35 \times 10^6$ S/m [6]. The print took about 16 hours, but this could be considerably reduced by optimizing the build process further. The fabricated diplexer is shown in Fig. 7.8. The flanges are built with the diplexer.

As for the diplexer fabricated by using CNC milling shown in Fig. 7.8(b), the precision of the CNC machining is up to 10 μm. The fabrication is provided by a commercial CNC provider in China. The diplexer is split into two halves with the E-plane cut. They are milled separately. Gold plating is performed to the milled diplexer to improve the surface quality.

### 7.3.2 Surface Treatment

To improve the surface quality and performance of the diplexer, the printed diplexer is plated with gold. The gold plating has done by Millimeter Wave Technology Group with Rutherford Appleton Laboratory (RAL). Fig. 7.9 shows the printed diplexer after gold plating. The diplexer with tiny dimensions and complex structures is hard to be coated. Also, stainless steel forms an oxide layer on the surface preventing corrosion of the base metal but

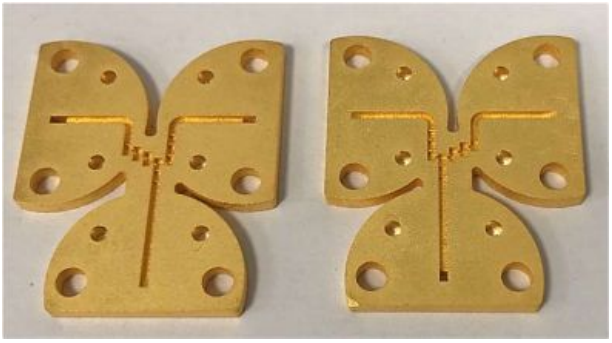


Fig. 7.9. The MLS printed diplexer with gold plating.

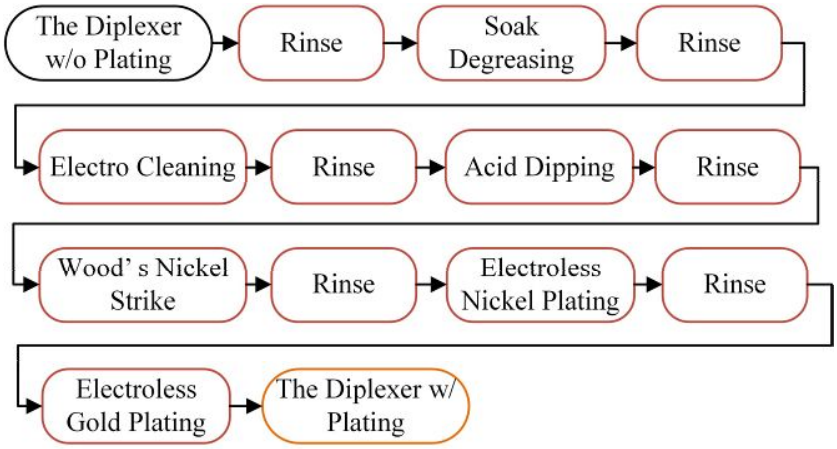



Fig. 7.10. The workflow of the gold plating process.

also good adhesion of the surface coating. In this case, the surface coating process utilizes an unconventional electroless plating process which is a gold plating with a nickel undercoat on the diplexer surface. To achieve a well-adhered uniform plating layer, removal of oxide layer on the surface is critical. Conventionally, an excellent and proven method to remove the oxide layer and apply a thin layer of nickel at the same time is to use a Wood's nickel strike followed by electroless nickel plating and then the final gold plating. If there is a time delay, nickel will get passivated and further plating will be impossible resulting in unreliable gold adhesion on the nickel strike. Moreover, both the cathodic cleaning and

Wood's nickel strike process [11] works on the principle of electro-polishing/plating requiring an anode, cathode and direct current (DC). This set-up would require an anode inside the diplexer cavity which was not achievable with the given structures. In our work, the diplexer was plated using a novel electroless plating method which provides an adequate surface finish albeit with a low adhesion strength in combination with gold plating procedure. The workflow of the gold plating is illustrated in Fig. 7.10. The skin-depth of gold operating at D-band frequency range is about 0.2 μm. However, there exist uncertainties during gold plating according to the experiments. The corners of the diplexer cavity are difficult to be plated if thinner plating layer is used. To ensure a sufficient coverage, the thickness of the nickel undercoat is about 3 $\mu$m and the gold layer is about 2 $\mu$m.

The novelty of this electroless plating process lies in its capability to build up a relatively thick gold deposit. In general, conventional methods are difficult to reach a thickness in excess of a micron. In theory, this electroless (autocatalytic) plating process could build over 3 μm gold if an ideal condition can be achieved with careful pH, temperature, and contamination control. What is more critical is the control of the flow (agitation) of the plating solution around and inside the sample. This is highly geometry dependent, not defined by the supplier and can only be optimized by trial-and-error. A careful balance has to be found between minimum flow required to replace depleted solution from the sample surface with fresh solution and turbulent flow that doesn't allow

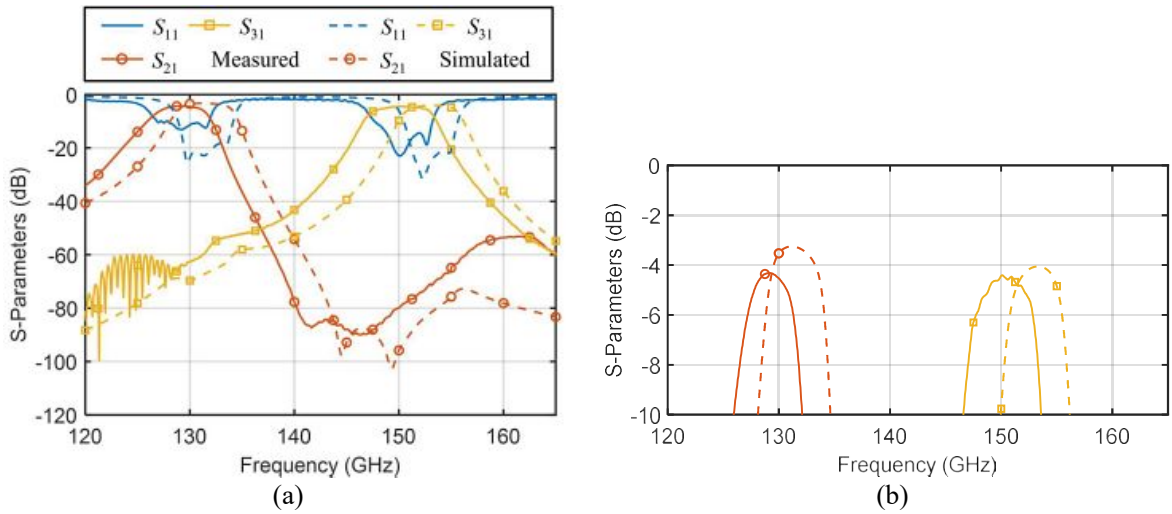



Fig. 7.11. Measured S-parameter responses for the MLS diplexer before gold plating.

enough time for the gold to adhere to the surface. Experiments in regular waveguides show over 3 μm of gold can be realized. The plating process usually takes over 2 hours to plate 1 μm.

## 7.4 Measurement and Discussion

### 7.4.1 Electrical Performance

The S-parameter performance of the as-printed MLS diplexer was measured by using a Keysight network analyser. Two ports of the diplexer connect with a pair of OML VNA extension modules, and the third port of the diplexer is terminated by a matched load. The measured S-parameter responses, compared with the simulated ones, are shown in Fig. 7.11. The simulation assumed the surface roughness of Sa = 2 μm (the surface characterization will be elaborated in Section 7.4.2). With the nominal conductivity of the stainless steel, the effective conductivity will come down to $3.9 \times 10^5$ S/m due to the surface roughness [12]-[13].

The effective conductivity can be calculated by using CST Studio Suite. The simulated average insertion losses are 3.65 dB and 4.41 dB within the passbands for the Channel A and B, respectively. The simulated 3 dB bandwidths are 5.35 GHz and 5.23 GHz.

To compare with the simulation results, the measurement has the minimum insertion losses for two channels are 4.2dB and 4.4 dB, respectively. The frequency shifts of the two channels are 2.8 GHz (2.1%) and 3.3 GHz (2.1%), respectively. Since it is hard to compare the bandwidth from the reflection responses ($S_{11}$), 3dB bandwidth from the transmission responses ($S_{21}$/$S_{31}$) are compared. The 3dB bandwidths for two channels in the simulation results are 5.58 GHz and 5.46 GHz. The measured 3dB bandwidths are 4.96 GHz (−11.1%) and 6.04 GHz (+10.6%).

## 7.4.2 Surface Characterisation and Dimensional Measurement

To investigate the influence of the fabrication on the measurement results, the surface roughness and dimensions of the MLS diplexer have been measured using an Alicona optical system with a magnification of 50X [14]. The system has specified that the minimum arithmetical mean height variation of the surface (Sa) is 0.06 μm and the root-mean-square deviation of the surface is 0.03 μm.

The surface roughness of the bottom surface of the waveguide cavity is measured as shown in Fig. 7.12. The measured Sa is 2.1 μm and Sq is 2.8 μm. It can be noticed that a hatching pattern is discernible. However, it should be noted that no polishing was applied to the cavity for fear of damage to the fine iris structures. The surface roughness of 2 μm

used in the simulation is an average from these measurements.

The widths *W* and lengths *L* of cavities shown in Fig. 7.4(c) are also measured using Alicona optical system. The dimensions are given in Table 7.2 and compared to design values. It is noticed that the dimensions are generally 0.2 - 3.9% larger than the design which caused the frequency shift as shown in Fig. 7.11.

In addition to lateral dimensions, the depths of the cavities were also measured using the Alicona system. Fig. 7.13(a) shows a composite image formed by measurements with the Alicona system on different levels. Here the measured quantity is *h*, half of the cavity/waveguide height as indicated in Fig. 7.13(b). The vertical dimension at the numbered locations is given in Fig. 7.13. The measured dimensions are larger than the target values ($a/2$ = 825.5 μm) by less than 11 μm. This indicates that good dimensional accuracy is

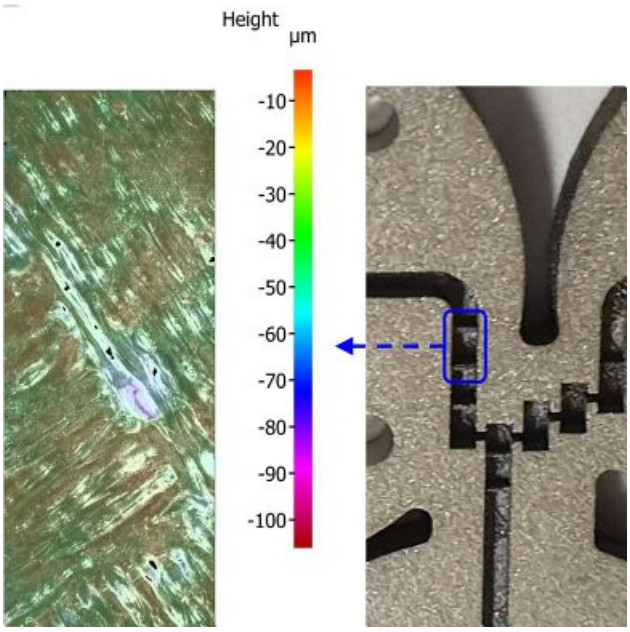
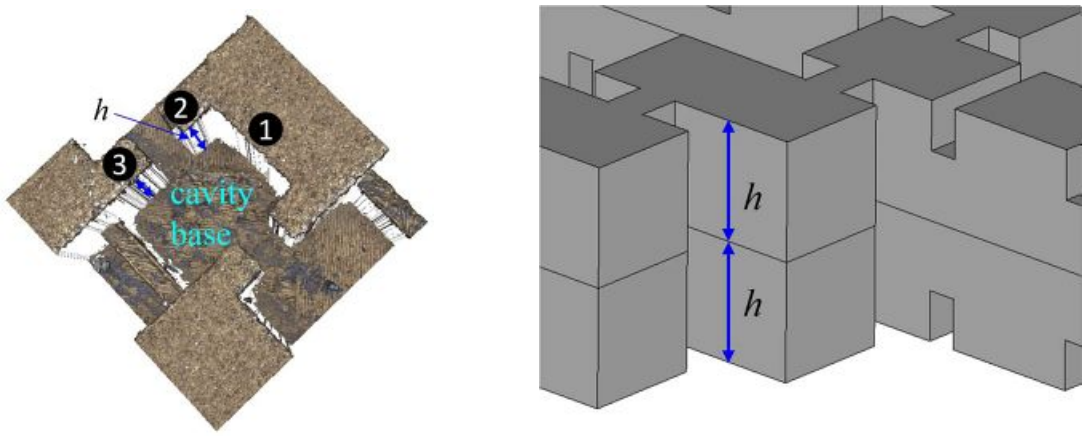



Fig. 7.12. Surface roughness measurement on the bottom area of a selected waveguide cavity.




(a) (b)

Fig. 7.13. Vertical dimension h measurement at locations 1, 2 and 3 (mm): 0.828, 0.834 and 0.837, respectively. Note the photograph is after gold coating.

achieved due to the small layer thickness (7 μm) and powder particle size (5 μm).

By considering the measured surface roughness and fabrication tolerances, we can refine and update the simulation model. All the design values are changed to the values shown in Table 7.2. The unavailable values $L_1$, $L_2$ and $L_5$ are assumed to be 1.8% larger than the design values. The re-simulated response is shown in Fig. 7.14. Now that the insertion loss level and frequency band more match with the measurement, the discrepancy in return loss is still significant. Parameter study shows that this may be attributed to the imperfect assembly contact between two half blocks of the diplexer. Using a model with a thin air gap between the two half blocks (Fig. 7.15), it has been found that the re-stimulated responses match the measurement responses, including return loss, much better when this air gap is assumed to be $t_{gap} = 4\ \mu\text{m}$, as shown in Fig. 7.14. It is not easy to measure the gap precisely, but such an air gap is plausible because no polishing has been applied to the contact surfaces for fear of damaging the fine iris structures.

Table 7.2. Measured Dimensions of the Diplexer in Comparison with Their Design values

| Dimension (μm) | Design values (μm) | Measured values (μm) | Deviations (μm) |
|---|---|---|---|
| W1 | 825.5 | 835 | +9.5 |
| W2 | 825.5 | 849 | +23.5 |
| W3 | 825.5 | 845 | +19.5 |
| W4 | 825.5 | 835 | +9.5 |
| W5 | 825.5 | 835 | +9.5 |
| W6 | 825.5 | 847 | +21.5 |
| W7 | 825.5 | 858 | +32.5 |
| W8 | 825.5 | 856 | +30.5 |
| WG1 | 825.5 | 831 | +5.5 |
| WG2 | 825.5 | 827 | +1.5 |
| $L_1$ | 958 | N/A | N/A |
| $L_2$ | 1107 | N/A | N/A |
| $L_3$ | 1654 | 1672 | +18 |
| $L_4$ | 1646 | 1658 | +12 |
| $L_5$ | 1355 | N/A | N/A |
| $L_6$ | 1184 | 1204 | +20 |
| $L_7$ | 1096 | 1120 | +24 |
| $L_8$ | 969 | 984 | +15 |

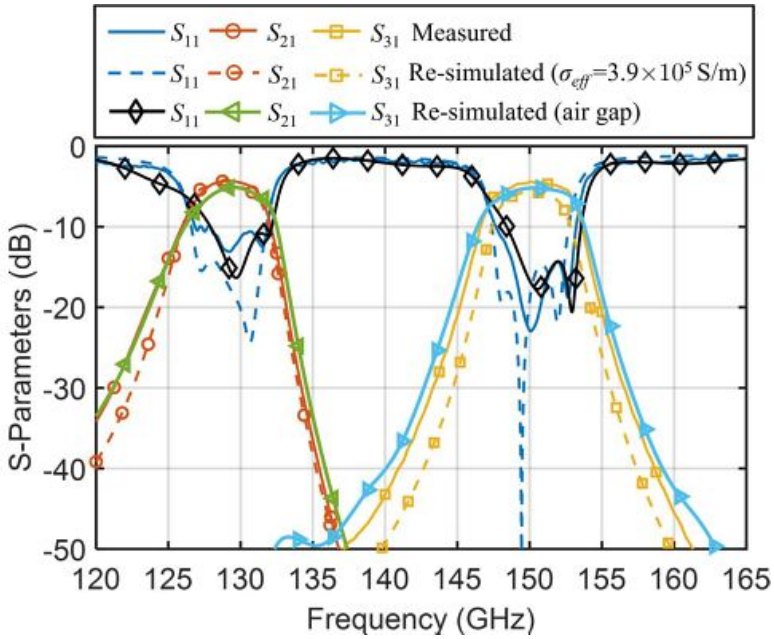



Fig. 7.14. Re-simulated S-parameter responses by considering the measured surface roughness, geometric dimensions and also the imperfect assembly contact, before gold coating.

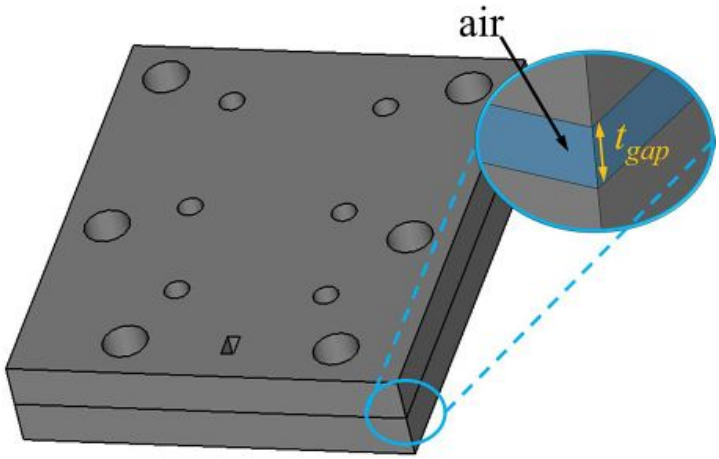



Fig.7.15. The diplexer simulation model with an added air gap to investigate the effect of the assembly contact.

### 7.4.3 Fabrication Tolerance Analysis

To investigate the influence of fabrication tolerance on the performance of the diplexer, an analysis has been performed based on simulation. The $x$ and $y$ directions of the diplexer shown in Fig. 7.5(a) are increased by 0-5%. Latin Hypercube sampling [15] with random distribution is utilized to collect 500 sets of design data. The 3 dB bandwidth, centre

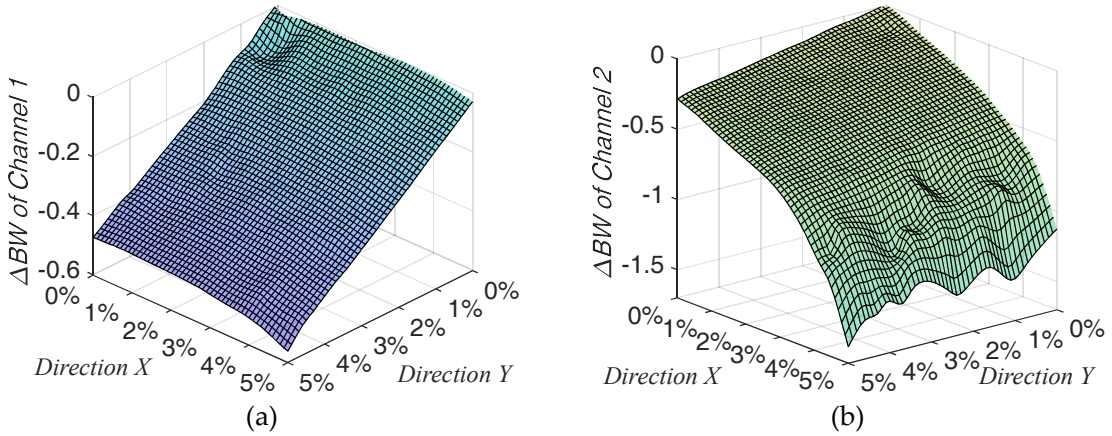
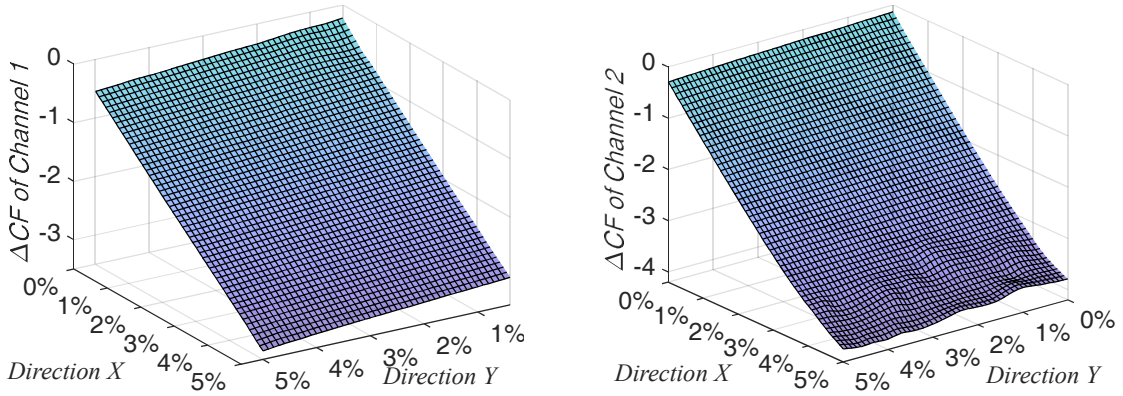
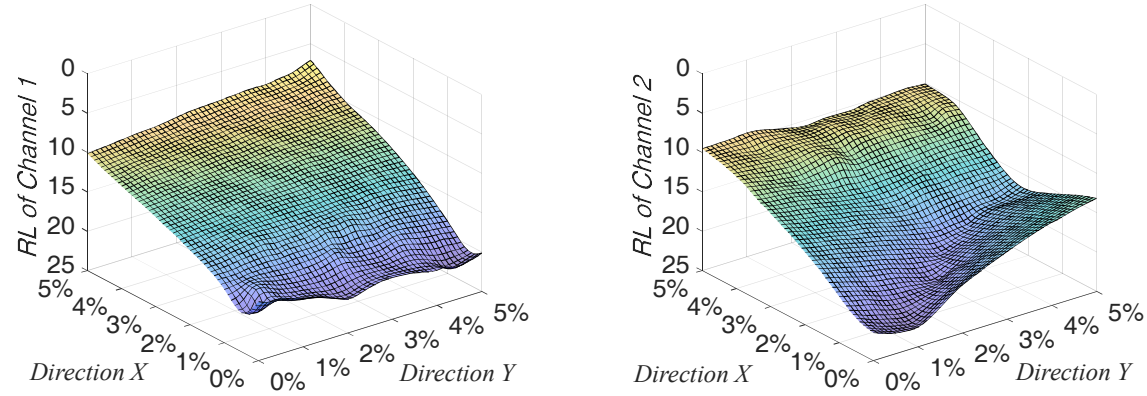



Fig. 7.16. Tolerance analysis of the bandwidth deviation with regard to dimensional scaling. (a) Channel A and (b) Channel B. H: horizontal direction, V: vertical direction.




(a) (b)

Fig. 7.17. Tolerance analysis of the centre frequency shift with regard to dimensional scaling. (a) Channel A and (b) Channel B.




(a) (b)

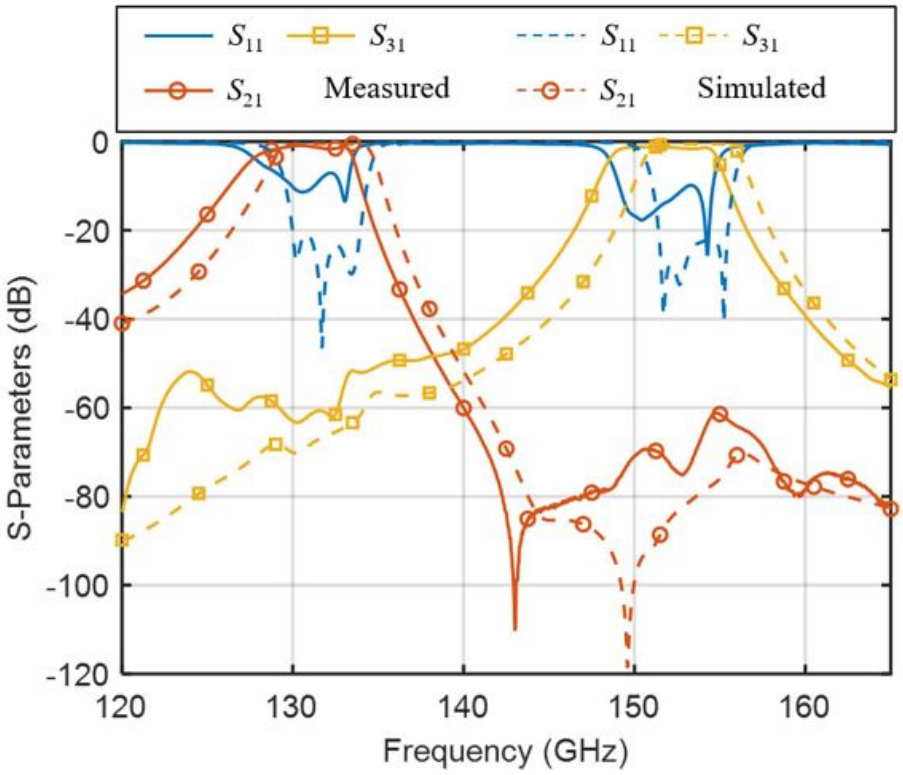
Fig. 7.18. Tolerance analysis of the return loss with regard to dimensional scaling. (a) Channel A and (b) Channel B.

frequencies and return loss (*RL*) levels for the sets are extracted and compared with the simulated responses. Their variation $\Delta BW$, $\Delta CF$ and *RL* for the two channels with respect to the scale (*x* and *y* directions) are shown in Fig. 7.16, 7.17 and 7.18. The surface fitting employs the biharmonic spline interpolation method implemented in Matlab. It can be noticed that the bandwidth of channel A is more sensitive to *y*-direction scaling while that of channel B is more sensitive to the *x*-direction. This is because the scaling affects the inter-resonator couplings. The centre frequencies of both channels are sensitive to *x*-direction scaling. The

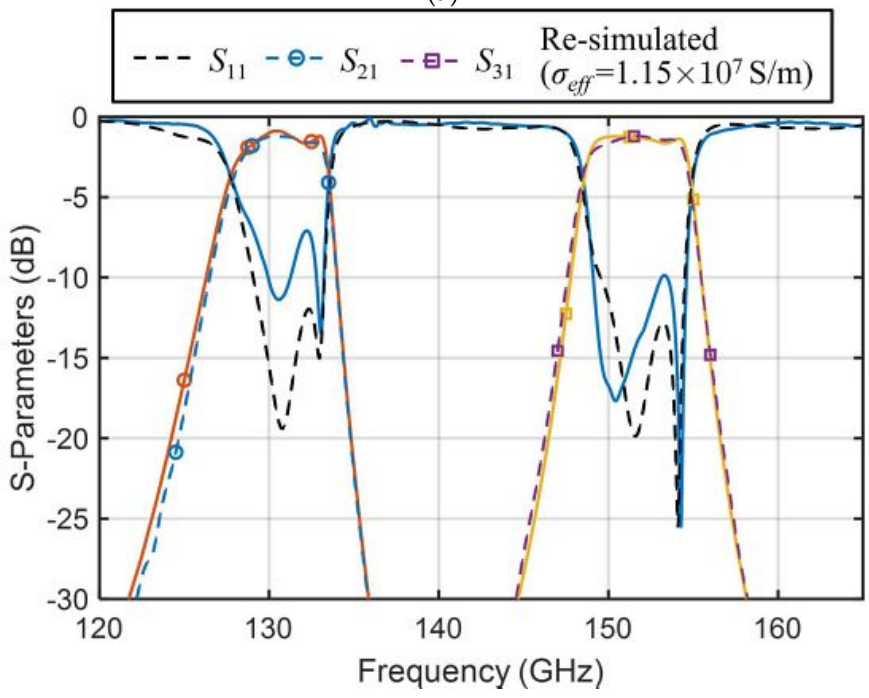
return losses of both channels are sensitive to the *x*-direction scaling. The *RL* of channel B is more sensitive to the *y*-direction scaling than that of channel A.

### 7.4.4 Measurement After Gold Plating

After gold plating, the diplexer S-parameter were measured again using a pair of VDI frequency extension modules. The measured S-parameter responses comparing the simulation responses are shown in Fig. 7.19(a). In the simulation, the ideal conductivity of gold ($4.6\times10^7$ S/m) is firstly used. The minimum simulated insertion losses for the two channels are 0.49 dB and 0.57 dB, respectively. The corresponding measurement values are 1.31 dB and 1.37 dB. These are averaged over the range of 4 GHz around the measured centre frequency. Note that gold coating has significantly reduced the insertion loss. It also reduces the frequency shift by half to 1.22 GHz (0.9 %) and 1.69 GHz (1.1 %). The simulated 3 dB bandwidths are 5.66 GHz and 5.55 GHz while the measured 3dB bandwidths are 5.88 GHz (+3.9 %) and 6.39 GHz (15.1%). Using the model in Fig. 14, simulation is repeated considering the measured surface roughness of 2 μm, measured geometric dimensions, and the imperfect assembly contact. It has been found again that the re-stimulated S-parameter responses appear well-matched with the measured ones when the air gap is assumed to be $t_{gap} = 3.5\ \mu m$, as shown in Fig. 7.19(b).




(a)



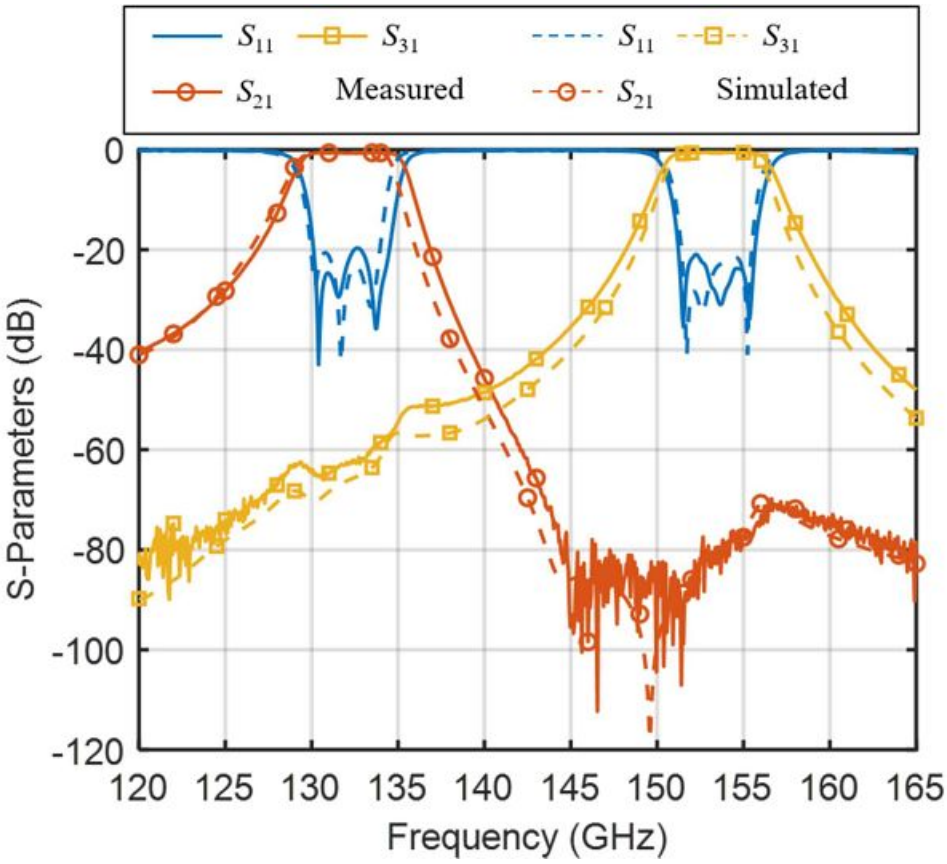

(b)

Fig. 7.19. (a) Measured and simulated S parameter responses for the MLS diplexer after gold plating. (b) Measured and re-simulated S-parameter responses considering the surface roughness after gold coating, measured geometric dimensions and imperfect assembly contact.

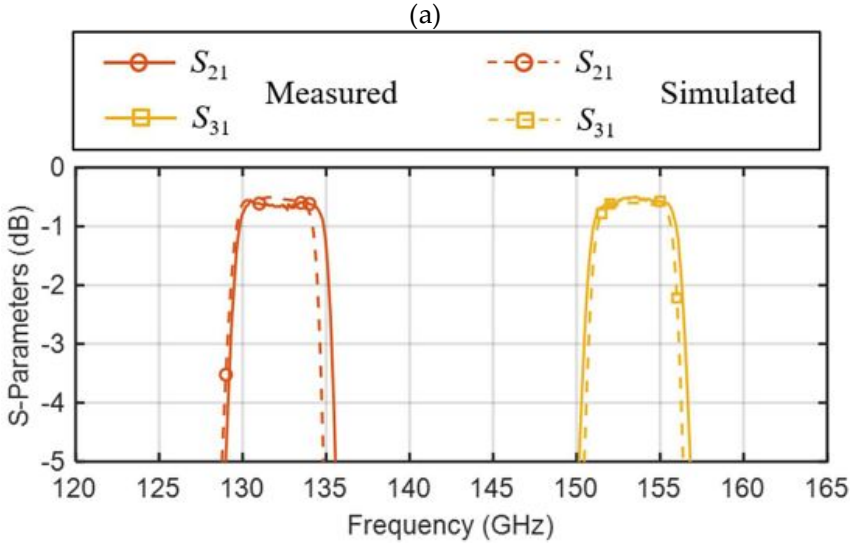
### 7.4.5 Measurement of CNC Milled Diplexer

As a comparison, the measurement setup using VDI extension modules for the diplexer fabricated by CNC. The measured S-parameter responses of the diplexer fabricated by CNC are shown in Fig. 7.20. The simulation results utilized were also obtained by using a gold cavity. The minimum insertion losses for the two channels are 0.60 dB and 0.49 dB. The centre frequency shifts are very small which can be ignored while the bandwidths for the two channels are slightly enlarged 0.51GHz (+8.2%) and 0.63GHz (10.1%) respectively.

To compare with the state of the arts listed in Table 7.3, the performance of both MLS printed, and CNC milled diplexer show very good performance in terms of insertion loss, frequency shift, and bandwidth variation.




(a)




(b)

Fig. 7.20. Measured S parameter responses of the CNC milled diplexer comparing with the simulated responses.

Table 7.3 Comparison with Reported Narrowband Filters and Diplexers

| Ref. | $f_0$ (GHz) | $\Delta f_0$ (%)* | $BW$ | $\Delta BW$(%)* | $IL$(dB) | Fabrication |
|---|---|---|---|---|---|---|
| [6] | 132/145 | 0.7/1 | 3/5.1 | 7.5/8 | 1.2/0.8 | DRIE |
| [7] | 190/220 | 1.6/1.4 | 2.1/2.7 | 25/33 | 1.5/1.5 | CNC |
| [9] | 265/300 | 3/1.67 | 7.5/6.7 | N/A | 7.6/8 | SU-8 |
| T.W. | 132/153.5 | 0.92/1.1 | 4/4 | 3.9/15.1 | 1.31/1.37 | MLS |
| T.W. | 132/153.5 | 0.2/0.17 | 4/4 | 8.2/10.1 | 0.60/0.49 | CNC |

*$\Delta f_0$ means centre frequency shift, $\Delta BW$ is the bandwidth variation comparing with the simulation results.

## 7.5 Summary of this Chapter

This chapter presents a D-band diplexer fabricated using MLS micro additive manufacturing technology. Also, a sample diplexer design has been fabricated by using high-precision CNC milling technology as a comparison. The diplexer is designed in an all-resonator structure using the coupling matrix synthesis-based design method. To balance the trade-off between the filtering performance and fabrication constraints, the diplexer is designed in a novel configuration. To improve the electrical performance of the diplexer, the MLS fabricated diplexer is plated with gold via an irregular electroless plating technique. Both the MLS printed diplexer and the CNC milled one show very good performance in terms of insertion loss, frequency shift, and bandwidth variation. Based on comprehensive measurements, the reason for the deterioration of the MLS printed diplexer has been found. Although the diplexer fabricated by additive manufacturing still exists limitations, e.g., unstable fabrication tolerance and limited fabrication size, there still provides a new possibility to fabricate the diplexers and multiplexers in the future.

# References


[1] C. Jansen et al., “Applications for THz systems: Approaching markets and perspectives for an innovative technology,” Opt. Photon., vol. 3, no. 4, pp. 26–30, 2008.

[2] S. Koenig et al., “Wireless sub-THz communication system with high-data rate,” Nature Photon., vol. 7, no. 12, pp. 977–981, Dec. 2013.

[3] M. G. L. Frecassetti et al., "D-Band Radio Solutions for Beyond 5G Reconfigurable Meshed Cellular Networks," 2019 16th International Symposium on Wireless Communication Systems (ISWCS), Oulu, Finland, 2019, pp. 427-431.

[4] D. Gentina et al., “Millimetre Wave Transmission; Analysis of Spectrum, License Schemes and Network Scenarios in the D-band” ETSI GR mWT 008 V1.1.1, Aug. 2018. Available: http://www.etsi.org/standards-search.

[5] X. Zhao et al., "Silicon Micromachined D-Band Diplexer Using Releasable Filling Structure Technique," in IEEE Transactions on Microwave Theory and Techniques, vol. 68, no. 8, pp. 3448-3460, Aug. 2020.

[6] 3D Micro Print Gmbh. Accessed: Jul. 10, 2021. [Online]. Available: http://www.3dmicroprint.com/

[7] ITU-R Radio Regulation 2020. [Online]. Available: https://www.itu.int/en/myitu/Publications/2020/09/02/14/23/Radio-Regulations-2020

[8] J. F. V. Sullca, M. Guglielmi, S. Cogollos, and V. E. Boria, “Hybrid Wideband Staircase Filters in Rectangular Waveguide With Enhanced Out-of-Band Response”, IEEE Transactions on Microwave Theory and Techniques, pp. 1–1, 2021.

[9] A. R. Kerr, E. Wollack, and N. Horner, “Waveguide flanges for ALMA instrumentation,” ALMA Memo. 278, Nov. 1999 [Online]. Available: http://www.alma.nrao.edu/memos/

[10] China Electronics Technology Group Corporation 13th Research Institute (CETC 13). Accessed: Feb. 12, 2022. [Online]. Available: http://www.cetc13.cn/

[11] H. Deng, and P. Moller, “Effects of pretreatment on the structure and properties of electroless nickel coatings.” Plating and surface finishing, vol.81, no. 3, pp: 71-7, 1994.

[12] G. Gold and K. Helmreich, “A Physical Surface Roughness Model and Its Applications,” IEEE Trans. Microw. Theory Techn., vol. 65, no. 10, pp. 3720-3732, Oct. 2017.

[13] K. Lomakin, G. Gold, and K. Helmreich, “Analytical Waveguide Model Precisely Predicting Loss and Delay Including Surface Roughness,” IEEE Trans. Microw. Theory Techn., vol. 66, no. 6, pp. 2649-2662, June 2018.

[14] “Alicona optical system” [Online]. Available: https://www.alicona.com/our-technology/focus-variation/. [Accessed: 12-Aug-2021].

[15] J. F. Swidzinski and K. Chang, “Nonlinear statistical modelling and yield estimation technique for use in Monte Carlo simulations [microwave devices and ICs],” IEEE Trans. Microw. Theory Techn., vol. 48, no. 12, pp. 2316-2324, Dec. 2000.

# Chapter 8 Conclusions and Future Work

## 8.1 Conclusions

This thesis focuses on the new design methodologies, novel configurations, and new fabrication techniques for microwave diplexers and multiplexers.

In Chapter 4, an optimisation-based coupling matrix synthesis method for all-resonator diplexers and multiplexers has been proposed for complex coupling topologies that are not directly synthesizable. The proposed method is believed to be the first general method to effectively tackle the coupling matrix of all-resonator diplexers and multiplexers with complex configurations. Six numerical case studies have been carried out to verify the proposed method. Statistical comparisons show that the proposed method has a higher optimisation ability and robustness in the complex coupling matrix synthesis problems. The proposed method takes advantage of prior design knowledge of channel filters and implements a powerful memetic optimisation algorithm. The information provided from the channel filters reduces the search ranges. In addition, the channel-by-channel optimisation scheme simplifies the optimisation difficulties. The utilized Memetic optimizer balances the exploration and exploitation, which effectively tackles the characteristic landscape of the all-resonator multiplexers.

While Chapter 4 focused on the synthesis of coupling matrices, Chapter 5 proposed an EM optimisation method for microwave diplexers. This is the so-called GDODK (general

diplexer global optimisation method guided by design knowledge) method. It is a general and automatic EM optimisation method for diplexers. It combines the generality (i.e., the method is suitable for diplexers with different types of channel filters and junctions) and the powerful optimisation ability. The proposed method has been demonstrated in three practical design cases. This method employs the high-quality initial design generation method and key performance-based objective functions. The high-quality initial design narrows down the search range and reduces the complexity of the optimisation. The performance-based objective function further simplifies the characteristic landscape of the diplexer optimisation problem, which enhances the efficacy of the EM simulation-based optimisation.

Chapter 6 presented a novel manifold multiplexer configuration using an all-resonator structure, based on the new concept of a 'resonant manifold'. The proposed configuration has the advantage of a compact footprint over conventional manifold multiplexers. The proposed multiplexer has been represented and designed based on coupling matrix theory. For every filtering topology, there can be various frequency allocation schemes. An appropriate frequency allocation scheme is suggested for the proposed multiplexer configuration. The coupling matrix for the multiplexer can be effectively obtained by using the method proposed in Chapter 4. To verify the resonant manifold design concept, two waveguide multiplexers operating at X-band are synthesized and prototyped. According to the measurement results of the triplexer and the pentaplexer, good agreements have been

shown with respect to the simulations. The resonant manifold provides a more compact multiplexer topology. It is worth noting that the proposed concept is not restricted to waveguide technology but more generally for applications such as mobile base stations or satellite payload systems. One drawback for the resonant manifold multiplexer is its isolation performance, in comparison with the conventional manifold multiplexer. To address this shortcoming, one potential method is to increase the order of the channel filter. The other one is to appropriately assign the transmission zeros by using the cross-couplings or extracted pole structures in the channel filters.

Chapter 7 investigated a sub-terahertz diplexer, its design and manufacture. A D-band diplexer was fabricated by using MLS micro-printing technique. As a comparison, the diplexer with the same design was also fabricated by using high-precision CNC milling. The diplexer has an all-resonator structure. It has been designed using the coupling matrix theory. The diplexer structure has been tailored for the filtering performance and fabrication constraints. To improve the electrical performance of the diplexer, the MLS fabricated diplexer is plated with gold using a newly-developed electroless plating technique. Comprehensive measurements have been carried out to characterise the fabricated diplexers. Both the MLS printed diplexer and the CNC milled one show very good performance in terms of insertion loss and frequency response. Comprehensive measurements have revealed the reason for the performance deterioration of the MLS printed diplexer. Despite its inferior performance to the CNC machined counterpart, the 3D printed diplexer offers a

new possibility to fabricate the diplexers and multiplexers in the future. The additive manufactured diplexers have high potentials in several aspects. 1) Simple and rapid prototyping process, 2) More variation and flexibility in the structure design, 3) Possibility of co-manufacture with other components, and 4) Monolithic build with no or reduced assemblies.

## 8.2 Future Work

Built on this thesis, possible future work may be in the following directions:

1) General Coupling Matrix Synthesis of Multi-Port Networks with Mixed Topology

The proposed optimisation-based synthesis method in Chapter 4 can deal with coupling matrix problems of all-resonator multiplexers. In practice, non-resonant T-junction, star-junction, and manifold junction are widely employed. These junctions can be treated as non-resonant nodes in the multiplexer topology and the corresponding coupling matrix. On the other hand, one non-resonant node can form an extracted pole structure with a resonator to generate transmission zeros in the filtering responses. Theoretically, a multiport network with resonators, non-resonant nodes, and ports can be represented by using a single coupling matrix. The synthesis of such a more general coupling matrix may be the subject of future research.

2) General EM optimisation method for multiplexers

In this thesis, the EM optimisation method proposed in Chapter 5 addressed the optimisation tasks for diplexers without configuration restrictions. However, this method

still has its limitations when applied to multiplexers. This can be attributed to several reasons. First, the multiplexer has more channels than the diplexer. The mutual influence between the channels will be more complex, which presents a great challenge to the overall optimisation. Moreover, multiplexers normally have much more design variables than diplexers. The design space is enlarged exponentially with the increase of the design variables. Full-wave EM simulation will also be more time-consuming and less efficient. Further investigation is needed to extend the automatic EM optimisation technique from diplexers to multiplexers.

3) Multiplexers with novel configurations

The proposed novel multiplexer configuration in Chapter 6 has realized a more compact footprint than that of the conventional ones. However, the prototyped multiplexers have relatively simple configurations. To improve the filtering performance, cross-couplings or extracted pole structures can be added to the channel filters. On the other hand, multiple-mode resonators can be employed in multiplexer designs. For example, multiple-mode resonators can be used in the resonant manifold. It is expected this can improve the bandwidth of the multiplexer. However, none of these will be straightforward. This increases the difficulty of the multiplexer design and optimisation. Therefore, the multiplexers with novel configurations can be further studied.

# Appendix

## A. Recursive Techniques

In the following, the recursive technique is detailed. Substituting the identities,

$$acosh\, x = ln\left(x + \sqrt{x^2 - 1}\right), cosh\, x = \frac{e^x + e^{-x}}{2} \tag{A. 1}$$

Then, the filtering characteristic function in equation (3.15) is transformed as

$$C_N(\omega) = cosh\left[\sum_{n=1}^{N} ln(a_n + b_n)\right] \tag{A. 2}$$

where $a_n = \chi_n$, $b_n = \sqrt{\chi_n^2 - 1}$. In this case, $a_n^2 - b_n^2 = 1$. Then, (A. 2) can be derived by

$$\begin{aligned} C_N(\omega) &= \frac{1}{2}\left\{\exp\left[\sum_{n=1}^{N}\ln(a_n + b_n)\right] + \exp\left[-\sum_{n=1}^{N}\ln(a_n + b_n)\right]\right\} \\ &= \frac{1}{2}\left[\prod_{n=1}^{N}(a_n + b_n) + \frac{1}{\prod_{n=1}^{N}(a_n + b_n)}\right] \\ &= \frac{1}{2}\left[\prod_{n=1}^{N}(a_n + b_n) + \frac{1}{\prod_{n=1}^{N}(a_n + b_n)} \bullet \frac{\prod_{n=1}^{N}(a_n - b_n)}{\prod_{n=1}^{N}(a_n - b_n)}\right] \\ &= \frac{1}{2}\left[\prod_{n=1}^{N}(a_n + b_n) + \prod_{n=1}^{N}(a_n - b_n)\right] \end{aligned} \tag{A. 3}$$

Substitute $a_n$ and $b_n$ into (A. 3),

$$C_N(\omega) = \frac{1}{2}\left[\frac{\prod_{n=1}^{N}(c_n + d_n) + \prod_{n=1}^{N}(c_n - d_n)}{\prod_{n=1}^{N}\left(1 - \frac{\omega}{\omega_n}\right)}\right] \tag{A. 4}$$

where $c_n = \omega - \frac{1}{\omega_n}, d_n = \omega' \sqrt{1 - 1/\omega_n^2}\,, \omega' = \sqrt{\omega^2 - 1}$. From (A. 5), it can be seen that the numerator of $C_N$ can be formulated as

$$num[C_n(\omega)] = F_N(\omega) = \frac{1}{2}[G_N(\omega) + G'_N(\omega)] \tag{A.5}$$

with

$$G_N(\omega) = \prod_{n=1}^{N}(c_n + d_n) = \prod_{n=1}^{N}\left(\left(\omega - \frac{1}{\omega_n}\right) + \omega'\sqrt{1 - \frac{1}{\omega_n^2}}\right)$$

$$G'_N(\omega) = \prod_{n=1}^{N}(c_n - d_n) = \prod_{n=1}^{N}\left(\left(\omega - \frac{1}{\omega_n}\right) - \omega'\sqrt{1 - \frac{1}{\omega_n^2}}\right)$$

where $G_N$ can be expressed as a sum of two polynomials $U_N(\omega)$ and $V_N(\omega)$ as

$$G_N(\omega) = U_N(\omega) + V_N(\omega) \tag{A.6}$$

with

$$U_N(\omega) = u_0 + u_1\omega + u_2\omega^2 + \cdots + u_N\omega^N,$$

$$V_N(\omega) = \omega'(v_0 + v_1\omega + v_2\omega^2 + \cdots + v_N\omega^N).$$

The recursive process starts from prescribing the first TZ $\omega_1$, namely, substitute $N = 1$ into (3.21). Then, $G_1$ can be obtained as

$$G_1 = c_1 + d_1 = \left(\left(\omega - \frac{1}{\omega_1}\right) + \omega'\sqrt{1 - \frac{1}{\omega_1^2}}\right) = U_1(\omega) + V_1(\omega) \tag{A.7}$$

Then, when $N = 2$, $G_2(\omega)$ is calculated by

$$\begin{aligned} G_2(\omega) &= G_1(\omega)[c_2 + d_2] \\ &= [U_1(\omega) + V_1(\omega)] \left[ \left( \omega - \frac{1}{\omega_2} \right) + \omega' \sqrt{1 - \frac{1}{\omega_2^2}} \right] \\ &= U_2(\omega) + V_2(\omega) \end{aligned} \tag{A.8}$$

Since the $U_2(\omega)$ is a polynomial of $\omega$, $V_2(\omega)$ is the polynomial of $\omega$ with the term of $\omega'$. Thus, $\omega' V_1(\omega)$ is a polynomial without the term of $\omega'$. $\omega' V_n(\omega) = (\omega^2 - 1)(v_0 + v_1\omega + v_2\omega^2 + \cdots + v_N\omega^N)$. Therefore, we have

$$U_2(\omega) = \omega U_1(\omega) - \frac{U_1(\omega)}{\omega_2} + \omega' V_1(\omega)\sqrt{1 - 1/\omega_2^2} \tag{A.9}$$

$$V_2(\omega) = \omega V_1(\omega) - \frac{V_1(\omega)}{\omega_2} + \omega' U_1(\omega)\sqrt{1 - 1/\omega_2^2} \tag{A.10}$$

After obtaining the $U_2(\omega)$ and $V_2(\omega)$, the cycle will be repeated by using the third to $N$th transmission zeros until the $U_n(\omega)$ and $V_n(\omega)$ are calculated. There are $N - 1$ iterations.

$$U_N(\omega) = \omega U_{N-1}(\omega) - \frac{U_{N-1}(\omega)}{\omega_N} + \omega' V_{N-1}(\omega)\sqrt{1 - 1/\omega_N^2} \tag{A.11}$$

$$V_N(\omega) = \omega V_{N-1}(\omega) - \frac{V_{N-1}(\omega)}{\omega_N} + \omega' U_{N-1}(\omega)\sqrt{1 - 1/\omega_N^2} \tag{A.12}$$

For the equation of $G'_N$ in (3.20), it can be seen that $U'_N(\omega) = U_N(\omega)$ and $V'_N(\omega) = -V_N(\omega)$. $G'_N$ can be obtained via a similar process. After another $N - 1$ iterations,

$$\begin{aligned} F_N(\omega) &= \frac{1}{2}[G_N(\omega) + G'_N(\omega)] \\ &= \frac{1}{2}\{[U_N(\omega) + V_N(\omega)] + [U'_N(\omega) + V'_N(\omega)]\} \end{aligned}$$

$$= U_N(\omega) \tag{A.13}$$

Then, we can find that the zeros of $F_N(\omega)$ are the roots of the polynomial $U_N(\omega)$. Knowing the polynomial $P_N(\omega)$ and $F_N(\omega)$, $E_N(\omega)$ can be obtained.

## B. Resonant Frequencies of Denormalized Resonators

The resonant frequency of a denormalized resonator is calculated from the corresponding self-coupling in the coupling matrix. The self-coupling is seen as the resonant frequency in the normalized frequency range. Therefore, the calculation process is a frequency transformation process. Equ. 3.33 is also employed here. The self-coupling has the following relation,

$$m(i,i) = \frac{1}{FBW}\left(\frac{\omega}{\omega_0} - \frac{\omega_0}{\omega}\right) = \frac{1}{FBW}\left(\frac{f}{f_0} - \frac{f_0}{f}\right) \tag{B.1}$$

where $f$ is the resonant frequency of the resonator, $f_0$ is the centre frequency of the filter. Then, a Quadratic equation (with the form $ax^2 + bx + c = 0$) can be obtained,

$$f^2 - f \cdot \left(f_0 \cdot FBW \cdot m(i,i)\right) - f_0^2 = 0 \tag{B.2}$$

To solve the equation (B.2), two roots can be obtained based on the quadratic formula

$$f = \frac{-b \pm \sqrt{b^2 - 4ac}}{2a} = f_0 \left(\frac{FBW \cdot m(i,i)}{2} \pm \sqrt{1 + \left(\frac{FBW \cdot m(i,i)}{2}\right)^2}\right) \tag{B.3}$$

Considering the real situation, only the solution with a minus symbol is selected. Then, the resonant frequency of the resonator is expressed as

$$f = f_0 \left(\frac{FBW \cdot m(i,i)}{2} \pm \sqrt{1 + \left(\frac{FBW \cdot m(i,i)}{2}\right)^2}\right) \tag{B.4}$$

It can be noticed that the $m(i, i)$ introduce a shift in the resonant frequency in the denormalized resonator without changing their slope parameter of $1/FBW$.

# C. Frequency Allocation Schemes for Resonant Manifold Triplexer

The triplexer topology with different frequency allocation schemes can result in different filtering responses. The combinations of frequency allocations can be put into three categories and demonstrated here. In the following, Scheme 2 is chosen for the final design in Chapter 6. Note that all the coupling matrix optimisation processes utilize the same topology separation scheme to prepare the initial coupling values, as shown in Fig. 6.2. In addition, the same objective function, as expressed in (9), is used.

## C.1 Scheme 1: (a) $CH_1$-$CH_2$-$CH_3$ or (b) $CH_3$-$CH_2$-$CH_1$

In this scheme, the topological channels are assigned with frequencies sequentially either from low to high or the other way around. The S-parameter responses after optimisation are shown in Fig. C.1. The corresponding coupling values are listed in Tables C.1 and C.2. It can be observed that although the return loss responses are satisfactory, the transmission responses exhibit strong interference between the channels.

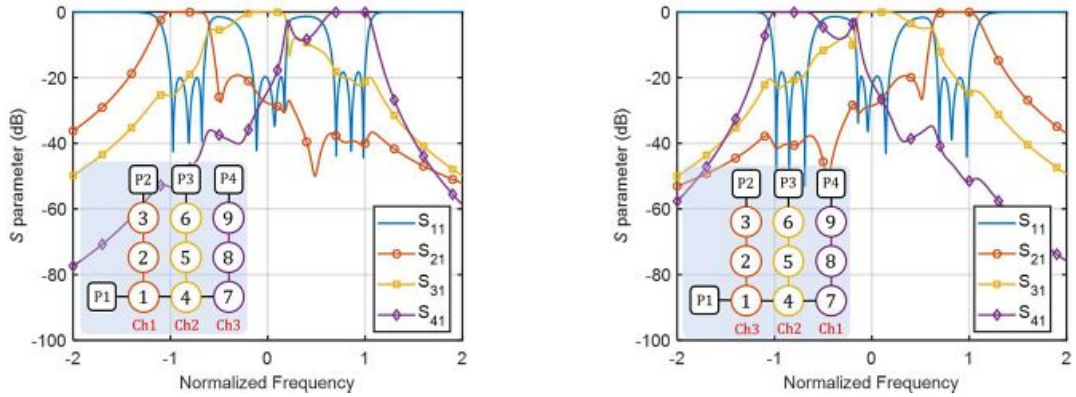
## C.2 Scheme 2: (a) $CH_2$-$CH_1$-$CH_3$ or (b) $CH_2$-$CH_3$-$CH_1$

In this scheme, the first topological channel is assigned with the middle channel frequency, where the following two are assigned with the two bands on either side, as shown in Fig. C.2 together with the S-parameter responses from the optimized coupling matrix. The coupling values are listed in Tables C.3 and C.4. The filtering responses exhibit

reasonable isolation performance. The transmission zeros appear at the appropriate place in the guard bands. This scheme is selected in this paper, consistent with the channel extension scheme proposed in Fig. 6.18.

## C.3 Scheme 3: (a) $CH_1$-$CH_3$-$CH_2$ or (b) $CH_3$-$CH_1$-$CH_2$

The assignment of Scheme 3 is similar to the one of Scheme 2. The last topological channel, rather than the first one, is assigned with the middle band frequency, as shown in Fig. C.3. The optimized coupling values are listed in Table C.5 and C.6. The filtering responses broadly match those from Scheme 2 but with slightly higher asymmetry.




(a) (b)

Fig. C.1. S-parameter responses for the resonant manifold triplexer. (a) Frequency allocation scheme 1; (b) Frequency allocation scheme 2.

Table C.1 Optimized Coupling Values for Triplexer with Allocation Scheme 1

| $m(1, 2)$ | $m(2, 3)$ | $m(1, 4)$ | $m(4, 5)$ | $m(5, 6)$ | $m(4, 7)$ | $m(7, 8)$ |
|---|---|---|---|---|---|---|
| 0.2989 | 0.1765 | 0.6936 | 0.4099 | 0.2204 | 0.2877 | 0.3019 |
| $m(8, 9)$ | $m(1, 1)$ | $m(2, 2)$ | $m(3, 3)$ | $m(4, 4)$ | $m(5, 5)$ | $m(6, 6)$ |
| 0.2125 | -0.0373 | -0.8327 | -0.8440 | 0.1440 | -0.0877 | -0.0419 |
| $m(7, 7)$ | $m(8, 8)$ | $m(9, 9)$ | $m(1, P1)$ | $m(3, P2)$ | $m(6, P3)$ | $m(9, P4)$ |
| 0.5182 | 0.5968 | 0.7917 | 0.7662 | 0.4478 | 0.4424 | 0.4368 |

Table C.2 Optimized Coupling Values for Triplexer with Allocation Scheme 2

| $m(1, 2)$ | $m(2, 3)$ | $m(1, 4)$ | $m(4, 5)$ | $m(5, 6)$ | $m(4, 7)$ | $m(7, 8)$ |
|---|---|---|---|---|---|---|
| 0.2912 | 0.1679 | 0.6979 | 0.4111 | 0.2221 | 0.2871 | 0.3136 |
| $m(8, 9)$ | $m(1, 1)$ | $m(2, 2)$ | $m(3, 3)$ | $m(4, 4)$ | $m(5, 5)$ | $m(6, 6)$ |
| 0.2317 | 0.0268 | 0.8413 | 0.8519 | -0.1395 | 0.1232 | 0.0749 |
| $m(7, 7)$ | $m(8, 8)$ | $m(9, 9)$ | $m(1, P1)$ | $m(3, P2)$ | $m(6, P3)$ | $m(9, P4)$ |
| -0.5242 | -0.5569 | -0.7732 | 0.7662 | 0.4368 | 0.4424 | 0.4478 |

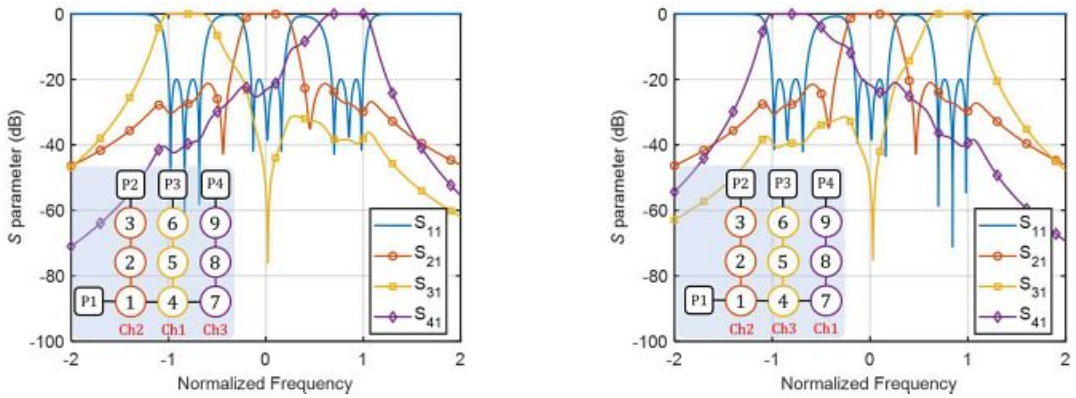


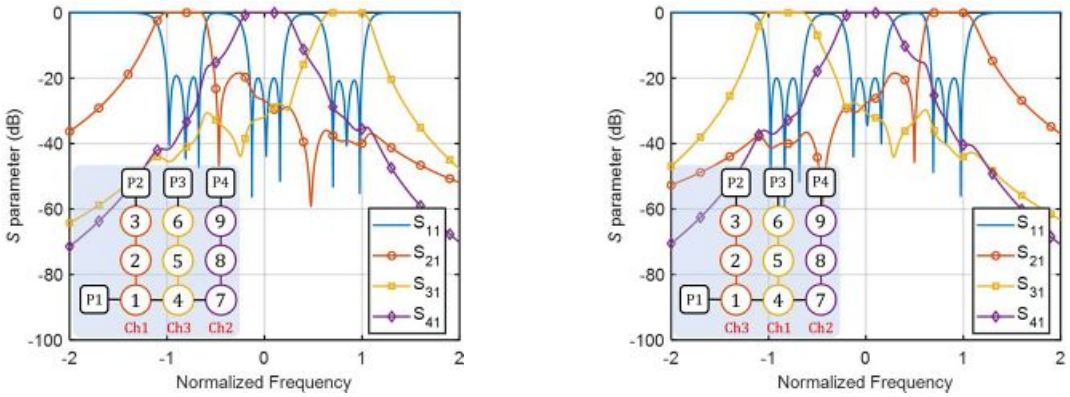

Fig. C.2. S-parameter responses for the resonant manifold triplexer. (a) Frequency allocation scheme 3; (b) Frequency allocation scheme 4

Table. C.3 Optimized Coupling Values for Triplexer with Allocation Scheme 3

| $m(1, 2)$ | $m(2, 3)$ | $m(1, 4)$ | $m(4, 5)$ | $m(5, 6)$ | $m(4, 7)$ | $m(7, 8)$ |
|---|---|---|---|---|---|---|
| 0.2982 | 0.1706 | 0.7113 | 0.2346 | 0.1780 | 0.5616 | 0.2957 |
| $m(8, 9)$ | $m(1, 1)$ | $m(2, 2)$ | $m(3, 3)$ | $m(4, 4)$ | $m(5, 5)$ | $m(6, 6)$ |
| 0.1838 | 0.0042 | 0.0138 | 0.0138 | −0.0127 | −0.7970 | −0.8240 |
| $m(7, 7)$ | $m(8, 8)$ | $m(9, 9)$ | $m(1, P1)$ | $m(3, P2)$ | $m(6, P3)$ | $m(9, P4)$ |
| 0.1533 | 0.7163 | 0.8154 | 0.7662 | 0.4424 | 0.4478 | 0.4368 |

Table C.4 Optimized Coupling Values for Triplexer with Allocation Scheme 4

| $m(1, 2)$ | $m(2, 3)$ | $m(1, 4)$ | $m(4, 5)$ | $m(5, 6)$ | $m(4, 7)$ | $m(7, 8)$ |
|---|---|---|---|---|---|---|
| 0.2980 | 0.1706 | 0.7108 | 0.2254 | 0.1692 | 0.5658 | 0.3177 |
| $m(8, 9)$ | $m(1, 1)$ | $m(2, 2)$ | $m(3, 3)$ | $m(4, 4)$ | $m(5, 5)$ | $m(6, 6)$ |
| 0.1946 | -0.0149 | 0.0152 | 0.0152 | 0.0082 | 0.8082 | 0.8328 |
| $m(7, 7)$ | $m(8, 8)$ | $m(9, 9)$ | $m(1, P1)$ | $m(3, P2)$ | $m(6, P3)$ | $m(9, P4)$ |
| -0.1201 | -0.6923 | -0.8049 | 0.7662 | 0.4424 | 0.4368 | 0.4478 |




(a) (b)

Fig. C.3. S-parameter responses for the resonant manifold triplexer. (a)Frequency allocation scheme 5. (b) Frequency allocation scheme 6.

Table C.5 Optimized Coupling Values for Triplexer with Allocation Scheme 5

| $m(1, 2)$ | $m(2, 3)$ | $m(1, 4)$ | $m(4, 5)$ | $m(5, 6)$ | $m(4, 7)$ | $m(7, 8)$ |
|---|---|---|---|---|---|---|
| 0.3035 | 0.1765 | 0.7096 | 0.2145 | 0.1688 | 0.4514 | 0.1958 |
| $m(8, 9)$ | $m(1, 1)$ | $m(2, 2)$ | $m(3, 3)$ | $m(4, 4)$ | $m(5, 5)$ | $m(6, 6)$ |
| 0.1772 | -0.0068 | -0.8309 | -0.8412 | 0.1336 | 0.8127 | 0.8341 |
| $m(7, 7)$ | $m(8, 8)$ | $m(9, 9)$ | $m(1, P1)$ | $m(3, P2)$ | $m(6, P3)$ | $m(9, P4)$ |
| -0.0170 | 0.0059 | 0.0129 | 0.7662 | 0.4478 | 0.4368 | 0.4424 |

Table C.6 Optimized Coupling Values for Triplexer with Allocation Scheme 6

| $m(1, 2)$ | $m(2, 3)$ | $m(1, 4)$ | $m(4, 5)$ | $m(5, 6)$ | $m(4, 7)$ | $m(7, 8)$ |
|---|---|---|---|---|---|---|
| 0.2950 | 0.1688 | 0.7112 | 0.2239 | 0.1772 | 0.4516 | 0.1960 |
| $m(8, 9)$ | $m(1, 1)$ | $m(2, 2)$ | $m(3, 3)$ | $m(4, 4)$ | $m(5, 5)$ | $m(6, 6)$ |
| 0.1785 | -0.0057 | 0.8384 | 0.8499 | -0.1297 | -0.8017 | -0.8247 |
| $m(7, 7)$ | $m(8, 8)$ | $m(9, 9)$ | $m(1, P1)$ | $m(3, P2)$ | $m(6, P3)$ | $m(9, P4)$ |
| 0.0596 | 0.0266 | 0.0174 | 0.7662 | 0.4368 | 0.4478 | 0.4424 |